DOCTOR OF PHILOSOPHY

Aspects of Wire arc additive manufacturing (WAAM) of alumnium alloy 5183

Derekar, Karan

Award date:
2020

Awarding institution:
Coventry University

Aspects of Wire arc additive manufacturing (WAAM) of aluminium alloy 5183

A thesis submitted in accordance with the requirements of the

COVENTRY UNIVERSITY
FACULTY OF ENGINEERING, ENVIRONMENT AND COMPUTING

for the degree of Doctor of Philosophy

by

Karan Satish Derekar

March 2020

Centre for Materials and Manufacturing Engineering
Faculty of Engineering, Environment and Computing
Coventry University

Content removed on data protection grounds

Abstract

Wire arc additive manufacturing (WAAM), a derivative of additive manufacturing (AM), has gathered attention of many researchers due to its numerous advantages such as high metal deposition rate and near-net shape production over traditional manufacturing techniques. Lightweight aluminium alloys were amongst highly experimented for WAAM products aiming widespread applications in automotive sector; however, there are some challenges which are restricting its wide spread use. In view of this, current research was directed towards better understanding of few challenges such as porosity i.e. relation between porosity formation and hydrogen dissolution, microstructural inhomogeneity, and residual stresses in WAAM produced 5183 aluminium alloy parts.

Commonly practiced technique for WAAM i.e. cold metal transfer (CMT) and conventional pulsed metal inert gas (pulsed-MIG) were used for part manufacturing and compared for porosity and microstructural variations. Samples were manufactured using 120 and 280 J/mm heat input, 50 and 100°C interlayer temperature and 30 and 120 seconds interlayer dwell time. For porosity study, computed tomography (CT) scan and dissolved hydrogen test on solid WAAM part were performed. Optical microscope and scanning electron microscope (SEM) were employed for microstructural investigation. Chosen samples were tested for mechanical properties such as tensile and hardness. Further, chemical analysis was performed to investigate possible elemental variations. Residual stress variation was measured using the newly developed contour residual stress measurement method on pulse-MIG produced WAAM samples. Substrate thickness (6 and 20 mm), interlayer temperature (50 and 100°C), heat input (120 and 280 J/mm) and deposit height (18 and 35 mm) were considered as variables for metal deposition.

Samples produced with CMT process showed smaller and lesser pores with reduced overall pore volume compared to samples from pulsed-MIG technique processed with similar conditions of heat input and temperature controls. On the contrary, CMT samples witnessed higher dissolved hydrogen in solid aluminium deposit. A peculiar trend in specific pore size and distribution drawn from probability study confirmed the influence of heat input, interlayer-temperature, and interlayer-dwell-time on WAAM type production. Further, CMT samples showed smaller grains compared to similarly processed pulsed-MIG samples. Moreover, higher heat conditioned samples i.e. processed with 280 J/mm heat input, 100°C interlayer temperature, and 30 seconds interlayer-dwell-time samples revealed relatively larger grains compared to lower heat conditioned samples i.e. 120 J/mm heat input, 50°C interlayer-temperature and 120 seconds interlayer-dwell-time. Chemical analysis of a deposit revealed loss of the elemental Mg. Tensile residual stresses dominated deposit part while substrate revealed compensating compressive residual stresses. Residual stresses with magnitude approaching the yield strength of a deposit were present. Substrate dimensions had major influence on stress distribution such that thicker substrates (20 mm) showed tensile stresses at the adjacent to deposit region and compressive in rest part, however, thinner substrates (6 mm) showed compressive stresses concentrated at extreme ends and majority of substrate portion showed tensile stresses.

High frequency oscillating motion of feed stock wire and arc on-off effects in CMT technique supported rapid reduction in temperature and increased solidification rate at solid-liquid interface that not only

resulted into lesser hydrogen absorption but also produced finer grains compared to pulsed-MIG. Continuous ignited arc of pulsed-MIG method showed increased overall energy, hotter deposit, higher arc penetration and lower cooling and solidification rates that supported in increased hydrogen absorption, easy movement and coalescence of atomic hydrogen, thus formation larger pores compared to CMT. The condition also supported in formation of larger and columnar grains. In either of the metal deposition condition, temperature of at least penultimate layer was increased above the recrystallization temperature of an alloy that affected grain formation in line with the heat flow direction. Effect of columnar grain formation in built direction was reflected in tensile properties. Vertical tensile samples showed lesser strength than horizontal samples. Similar to welding, liquid metal solidification in a layer format exerted tensile stresses. An active bending moment and firmly clamped substrate produced compressive stresses. Residual stresses as high as yield strength could be the result of high strains encountered due to multiple thermal cycles of contraction and expansion. Higher stiffness offered by 20 mm thick substrate compared to 6 mm, difference in heat flow characteristics, positive and negative strains due to repeated thermal cycles and operating bending moment collectively controlled stress distribution in processed WAAM part of 5183 aluminium alloy.

Acknowledgements

After a traumatic start of my PhD, it is a different feeling to officially express my gratitude towards all those who supported me in my PhD tenure. There are many people who directly or indirectly helped me to stay motivated.

Firstly, I would thank my supervisor, Prof Jonathan Lawrence for his continual strong support and timely valuable guidance for my research work. He was always available for resolving any issues and always stood by my side. I want to thank my industrial supervisor Geoff Melton for his endless support; not only on a basis of technical guidance but also on a personal level.

I gratefully acknowledge Adrian Addison, who is like my co-supervisor. His vision and knowledge helped me in shaping my PhD. Prof Xiang Zhang's interest into my research was phenomenal and her knowledge, experience and vision helped me in following a research path. I want to thank my friend Dr Sameehan Joshi whose excellent technical guidance and personal motivation kept me motivated. Also, I want to express my gratitude towards Dr Lei Xu who endlessly supported me on a personal ground. Over the years we have created a strong relationship and will remain same.

I would like to thank Dr Ahmad Bilal, Dr David Griffiths and Dr Rohit Kshirsagar for their guidance. I want to thank Dr Usani Ofem, Dr Vinod Kumar, Dr Ali Khan, David Howse, Dr Marcello Consonni, Robert Shaw and Dr Amina Salman for timely technical advices and guidance. I want to acknowledge Ashley, Ramin, Sally, Joshua, Imran, Robert, Dr Niall Smyth and Dr Hua Guo for their kind support for laboratory and workshop related tasks. I wish to thank my friends Dibakor, Dr Jazeel Chukkan, Kosta, Somsubhro, Hitesh, Sriharsh, Chetan and Omkar to name a few.

I want like to thank Prof Steve Jones for his unconditional and unparalleled support at the start of PhD and later continual motivation.

I am thankful to the Lloyd's Register Foundation (LRF) for providing me a sponsorship for this PhD and Dr Jan Przydatek for his important timely guidance.

I would like to thank National Structural Integrity Research Centre (NSIRC) and support staff for providing me an excellent opportunity of industrial PhD.

Along with NSIRC, I want to thank TWI Ltd. for providing me an excellent environment for my PhD and all of the supportive enthusiastic staff members who directly and indirectly supported during my tenure at TWI Ltd. as a PhD student.

I want to thank my parents for their motivation, support, and love. I express my gratitude to all my family members. Last but not the least, I want to thank one who left her job, family and nation for my studies, my wife Kshitija for her constant support, love and care!

Table of contents

List of Figures

List of Tables

Abbreviations and acronyms

3D welding	3 dimensional welding
AD	As-deposited
AM	Additive manufacturing
ASME	American Society of Mechanical Engineers
ASTM	American Society for Testing and Materials
AWS	American Welding Society
BTF	Buy-to-fly ratio
CMM	Coordinate measuring machine
CMT	Cold metal transfer technique
CMT-ADV	Advanced cold metal transfer
CMT-P	Pulsed cold metal transfer
CMT-PADV	Pulsed advanced cold metal transfer
DC	Direct current
DED	Directed energy deposition
DE-GMAW	Double electrode gas metal arc welding
EBSD	Electron Back-scatter diffraction
EBW	Electron beam welding
FE mode	Finite elemental model
GMAW	Gas metal arc welding
GMAW-P	Pulsed gas metal arc welding
GTAW	Gas tungsten arc welding
HE	Heat input (J/mm)
HH	High heat input condition
$Hnet$	Net heat input of welding process (J/mm)
HT	Heat treatment
H/W	Height to width ratio
IP	Instantaneous power
LBW	Laser beam welding
LH	Low heat input condition

MIG	Metal inert gas welding
PAW	Plasma arc wedling
Pulse-MIG	Pulsed metal inert gas welding
R15	Rolling with 15 kN load
R30	Rolling with 30 kN load
R45	Rolling with 45 kN load
RESW	Resistance electro slag welding
RP	Rapid prototyping
SAA	Surface area in contact with atmosphere
SAD	Surface area in contact under deposit
SAP	Surface area in contact with metallic platform
SAW	Submerged arc welding
SEM	Scanning electron microscope
SFF	Solid free-form fabrication
SIGMA	Shielded inert gas metal arc welding
SM	Shape melting
SMD	Shape metal deposition
SW	Shape welding
T1	Interlayer-temperature 50°C
t1	Interlayer-dwell time 30 seconds
T2	Interlayer-temperature 100°C
t2	Interlayer-dwell time 120 seconds
TIG	Tungsten inert gas welding
TS	Torch travel speed (mm/min)
TSA	Total Surface Area (mm^2)
VP-CMT	Varying polarity cold metal transfer
w	Weld bead or layer width (mm)
WAAM	Wire arc additive manufacturing
WEDM	Wire electric discharge machining
WFS	Wire feed speed
XCT	X-ray computed tomography

z	Number of values considered for calculations

Symbols

C	Specific heat of metal under consideration(J/kg°K)
E	Young's modulus (Pa)
Ĥ	Hardness (Hv)
Ii	Instantaneous current (A)
k	Thermal conductivity of metal under consideration (J/ms°K)
Ĺ	latent heat of fusion under consideration (J/m^3)
η	Efficiency of process
R	Cooling rate (°K/sec)
S	Solidification rate (mm/sec)
Ť	Temperature (°K)
Tc	Temperature (°K) at which cooling rate is calculated
T_f	Final temperatures considered (°K)
Tm	Melting temperature of metal (°K)
To	Initial temperature (°K) considered for calculations
T_s	Softening temperature of selected alloy (°K)
ν	Volume (mm^3)
ν_f	Final volume (mm^3)
ν_0	Initial volumes (mm^3)
Δν	Change in volume (mm^3)
υ	Poisson's ratio
Vi	Instantaneous voltage (V)
w	Weld bead / layer width (mm)
α	Coefficient of thermal expansion
α_{al}	Coefficient of thermal expansion of aluminium
α_{st}	Coefficient of thermal expansion of steel
ρ	Density of metal under consideration(kg/m^3)
σ_y	Yield strength (MPa)
ε	Strain

List of Publications

Related journal papers

1. K. S. Derekar, 'A review of wire arc additive manufacturing and advances in wire arc additive manufacturing of aluminium', *Mater Sci Technol (United Kingdom)*, vol. 34, no. 8, pp. 895–916, 2018.
2. K. S. Derekar, A. Addison, S.S. Joshi, X. Zhang, J. Lawrence, L. Xu, G. Melton, and D. Griffiths, 'Effect of pulsed metal inert gas (pulsed-MIG) and cold metal transfer (CMT) techniques on hydrogen dissolution in wire arc additive manufacturing (WAAM) of aluminium', *Int J Adv Manuf Technol*, vol. 107, pp. 311–331, 2020.
3. K.S. Derekar, D. Griffiths, S.S. Joshi, J. Lawrence, X. Zhang, A. Addison, G. Melton, L. Xu, Influence of interlayer temperature in microstrucutre of 5183 aluminium alloy made by wire arc additive manufacturing (WAAM), *Int J Micro Mater Prop.* (Accepted, under printing)

Related conference paper

1. K. Derekar, J. Lawrence, G. Melton and A. Addison, (2018), "Influence of interpass temperature in wire arc additive manufacturing (WAAM) of aluminium", *71st IIW Annual Assembly & International Conference*, 15-20 July 2018, Bali, Indonesia.

Related conference presentations

1. K. Derekar, J. Lawrence, G. Melton, L. Xu and A. Addison, (2018), "Effect of interpass temperature on microstructure of WAAM of aluminium", *1st International Conference on Welding & NDT, of HSNT and WGI*, 22-23 October 2018, Athens, Greece.
2. K. Derekar, X. Zhang, B. Ahmad., J. Lawrence, A. Addision, G. Melton and D. Griffiths, "Effect of deposition strategies on residual stress distribution in wire arc additive manufacturing (WAAM) of aluminium alloy", *International Congress on Welding and Additive Manufacturing (ICWAM 2019)*, 5-7 June 2019, Metz, France.

Chapter 1: Introduction

For practical application of any manufactured part, better understanding of its overall properties and structural integrity is prime important. The sound quality and structural integrity include but not limited to the behaviour under static and varying load conditions, residual stresses, microstructural properties, impact of environmental conditions and any sudden or gradual material property variation with time. The manufactured parts produced by traditional techniques such as casting, forging, rolling, machining etc. were thoroughly studied for their product quality and structural integrity over the years by many researchers from industry as well as academia. Also, some catastrophes were held responsible for opening up the new doors of research fields such as material's fracture toughness which was studied after failures of iron-based plates of war ships from Second World War. In similar manner to traditional techniques, time-to-time attention was provided to the newly developing technologies such as nanotechnology, superplastic forming, diffusion bonding, rapid solidification processing etc. The timely attention and understanding of the techniques support in reliable product development. A newly developing and highly attended additive manufacturing (AM) technique has shown a potential of replacing components produced by traditional processes [1–3]. Different studies were undertaken to understand the structural integrity of the parts produced through additive manufacturing. There are some examples of AM parts that find end user applications from different industries such as jewellery, home furniture, fashion, aero-space, medical etc. More details about additive manufacturing field discussed in following sections.

1.1 Additive manufacturing (AM)

Many researchers [1,2,4–6] predicted the possible impact of Additive Manufacturing (AM) on the manufacturing industry of future. AM is has gathered attention of many researchers due to numerous benefits ranging from its ability to handle variety of materials such as metals, polymers and ceramics, ability to produce peculiar and intricate near net shape parts eliminating the need of additional tooling and fixturing. Single-part assembly or bespoke [7] manufacturing is possible by AM because of the processes capability of reducing overall manufacturing cost by providing a focused manufacturing process reducing overall task time, material wastage hence better buy-to-fly ratio (BTF), while improving the feedback flexibility to turn wire into a commodity artefact. AM has a capability of delivering and satisfying increasing orders of customised and personalised products. As AM uses digital files for producing an object, it becomes highly convenient to transfer and modify the supporting files in the customisation of product parts.

The market for AM is speedily growing its roots in numerous fields, for instance, automobile, medical, aerospace, jewellery, fashion, high-end furniture, machine parts, electronics and many more. For AM, the estimated overall market value was £1.5billion and £3.1 billion in 2011 and 2014 respectively which

is expected a massive fivefold growth by the year 2020. From £1.4 billion in 2014 the end use parts could reach more than £7.9 billion at the end of 2020 [2]. Furthermore, Frazier [8] stated that if manufacturing difficulties are rightly addressed in shorter time frames, the market value for AM may shoot up to £80 billion *per* year by 2020; however, with all this positivity surrounding for AM, the technique currently suffers from numerous deficiencies such as lack of design principles, manufacturing guidelines and standardization of best practices when applied to high-value manufacturing. AM techniques are moderately new and substantial research is required for sustainable growth to be realised within this sector of manufacturing. Validation of mechanical, corrosive and thermal properties of the formed component, limited availability of digital designs and their acquisition cost, integration of hybrid techniques in design and production and the repair of parts are needed to be addressed in detail. To highlight and capture the current major concerns associated with AM various authorities have jointly prepared several AM roadmaps [9,10] directing focused research on critical issues.

International Organization of Standardization (ISO), British Standard Institute (BSI) and American Society for Testing of Materials (ASTM) jointly defined AM as a *'process of joining materials to make parts from 3D model data, usually layer upon layer as opposed to subtractive manufacturing and formative manufacturing methodologies'*. The ASTM International Committee F42 has categorised AM techniques into seven groups based on type and form of input material and heat source as shown in Figure 1.1. Thompson [2] has clearly identified and categorised the types of materials that particular AM processes can handle. Thus, based on feed stock material and the final required shape that to be formed, a suitable AM technique can be chosen. Figure 1.1 reveals different types of materials that a particular AM technique can handle which involves metals, thermoplastics, thermosets, ceramics and wood. Therefore, it is not surprising to find a wide spread applications of AM products in different sectors as discussed earlier.

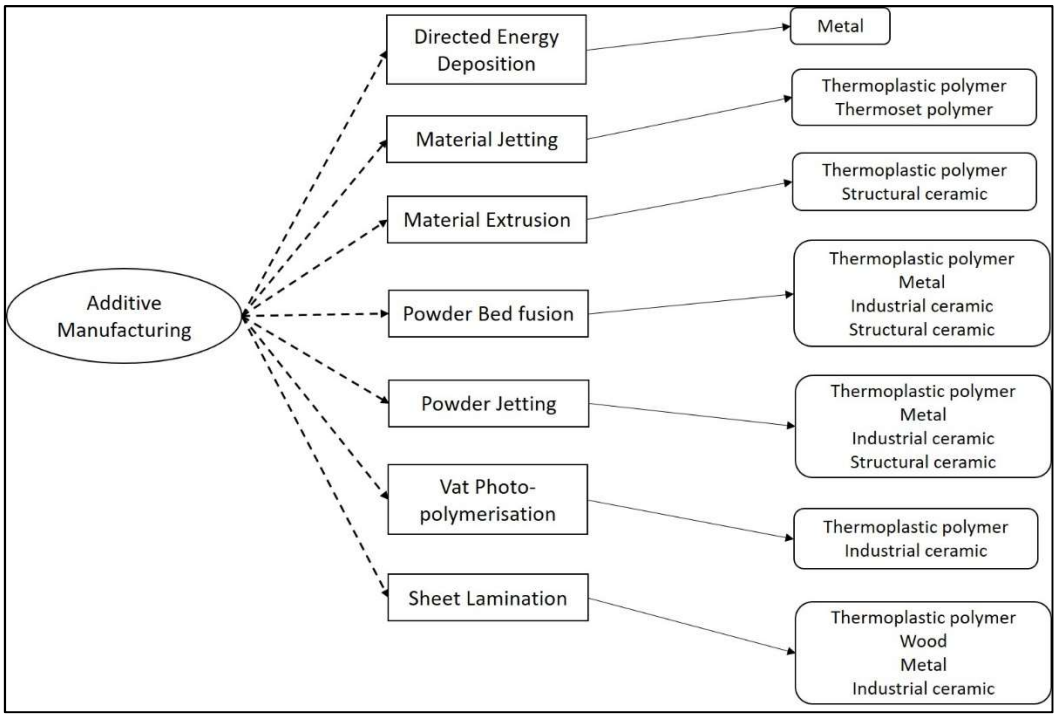

Figure 1.1 Classification of AM processes with respective material handling capabilities (adopted from [3]*).*

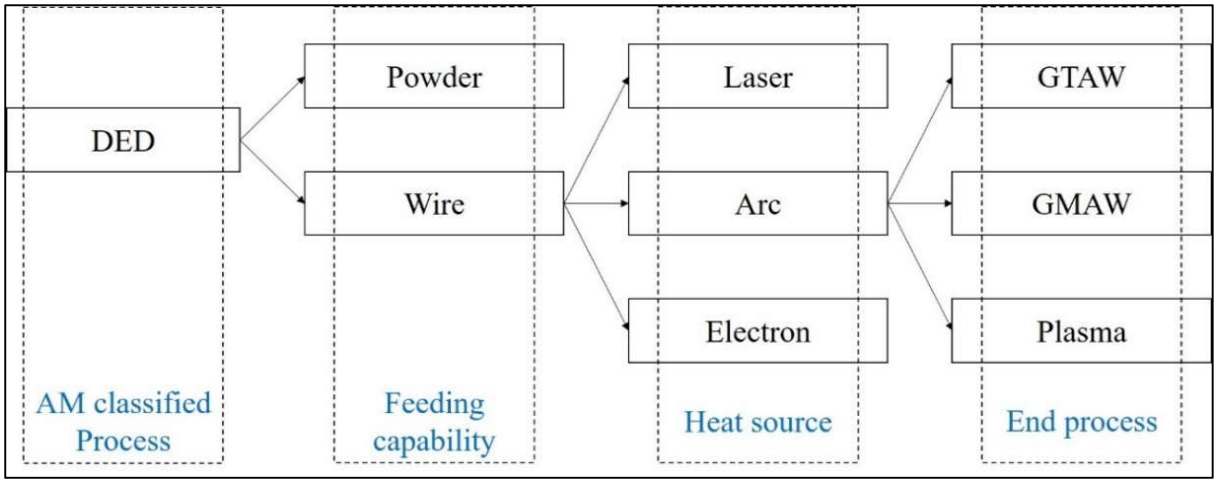

Figure 1.2 Typical classification of WAAM (adopted from [3]*).*

1.2 Wire arc additive manufacturing (WAAM)

Amongst these seven groups of AM processes, only four can produce parts using metallic material; however, only one method, Directed energy deposition (DED), is capable of handling metallic filler additions to produce an additively manufactured components. The feed capability includes powder as well as wire form. The feedstock filler wire melting using an electric arc as a heat source is typical combination of Gas metal arc welding (GMAW), Gas tungsten arc welding (GTAW) and Plasma arc welding (PAW) that is now being used to produce WAAM parts (refer Figure 1.2). Apart from wire, powder combination with laser and electron as a heat source is also the area of interests.

Further depending upon the process being used and to extend high deposition rate advantage of WAAM, different combinations and variations in the WAAM process were experimented. Thus WAAM process doe not only use GTAW, GMAW or plasma but also combinations of these with each other and with different techniques such as laser and electron beam. Also, variations with respect to feed stock chemistry, post deposition operation and many other different parameters were investigated in order to improve the productivity, product quality and production techniques which is illustrated in Figure 1.3. It is not possible to highlight all the experimented and possible combinations, however, noticeable variation of the WAAM are incorporated. Single and double wire GAMW along with combination of dip metal transfer techniques, wires of different chemistries/alloys that is formation of functionally graded part, direct and alternative current combinations in GTAW, use of specially designed wire for better product quality are some of the variations of WAAM associated with metal deposition alternatives. There are few variations that focuses on post deposition operations such as interlayer rolling (rolling of a top deposited layer immediately after deposition), unwanted metal removal by milling immediately after deposition of a layer or single step forming (such as forging) applied after formation of entire part are some examples of WAAM variations. Hybrid manufacturing that is combination of additive as well as subtractive manufacturing is one of the attractions that supports near net shape formation with increased productivity.

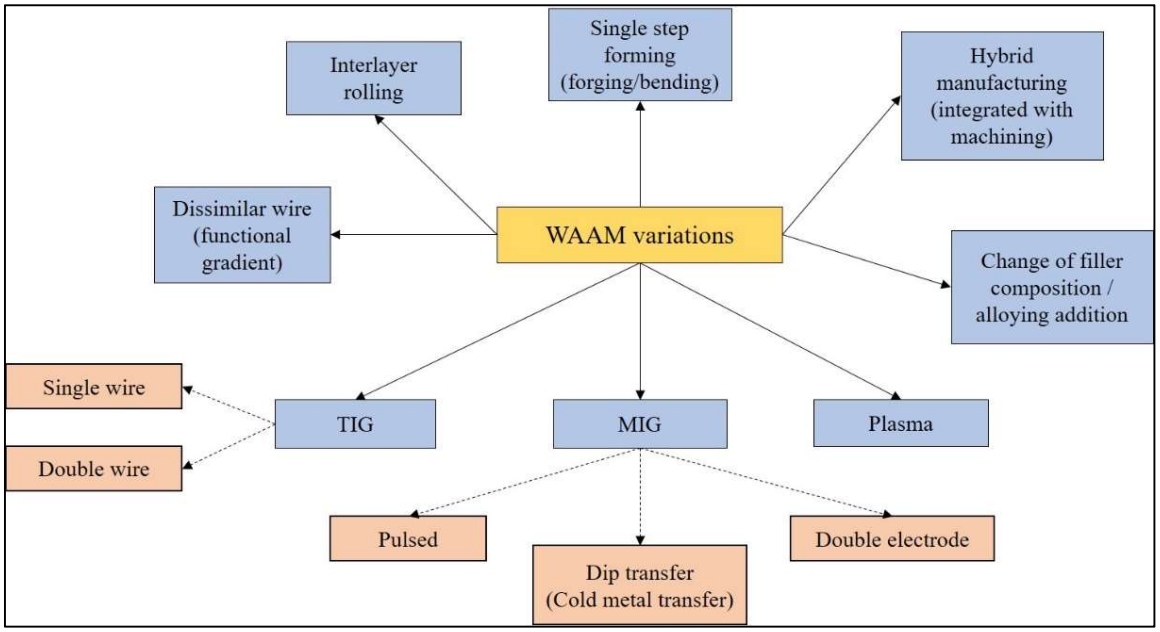

Figure 1.3 Variations of WAAM techniques.

1.3 Aluminium

1.3.1 Properties of aluminium

Aluminium is the third most abundant element in the earth's crust and is the most extensively used non-ferrous metal with numerous applications ranging from building and construction, transportation, containers and packaging, electrical, machinery, consumer durables to name but a few. The unique property combination that aluminium possesses makes it arguably the most attractive and economical metal. Aluminium is a lightweight metal (2698.8 kg/m^3) almost one-third density of the iron (7850 kg/m^3) which highlights its usefulness within the land, sea and air transportation industries. In addition to having lower density benefit the metal has a high electrical and thermal conductivity (237 W/mK) which explains its wide use in the electrical and electronics industry. Aluminium also has excellent corrosion resistance in most environments due to the instantaneous formation of an adherent oxide film. Another important aspect of aluminium is excellent formability due to good ductility and malleability along with good joining property and forgeability. Finally, aluminium possesses very good casting properties due to its low melting point (660°C). Aluminium and its alloys are manufactured in many different forms that can be broadly classified as standardized products including sheet, plate, foil, rod, bar wire, tube, pipe *etc*. and engineered products, which includes products designed for specific applications such as extruded shapes, forgings, castings, stampings, powder metallurgy parts, machined parts and metal-matrix composites.

1.3.2 Market of aluminium

To fulfil growing high demands of aluminium usage, the manufacturing industry in recent years is constantly trying to increase its production rate to newer heights. As per International Aluminium Institute [11], the aluminium production worldwide reached 64.3 million metric tonnes in 2018 from 19.5 million metric tonnes in 1990 which was around 12.3 million metric tonnes in 1975. This sharp upsurge in aluminium production clearly indicates high market demands and improved capability of

aluminium supply in recent years. It is worth noting that aluminium production in China alone is contributing a massive 56% (36.4 million metric tonnes) of the total world aluminium production. International Aluminium Institute categorises industry wise worldwide shipment of aluminium. Figure 1.4 points out the equal share of transportation and construction industry which is cumulatively exactly half of the total aluminium shipment worldwide. Electrical and electronics industries (13%) along with consumer durables and other (14%) shares aluminium shipments equally. Notably, machinery and packaging industries are also contributing to aluminium consumption. The vast expanding automobile and transportation industry assures rapid growth in aluminium consumption in the near future. The reason for such huge demands for aluminium within the transportation industry is not only related to the lightweight attributes that in turn lead to reduced fuel consumption, but also to the simultaneous reduction in CO_2 emissions thus contributing to a greener environment [12].

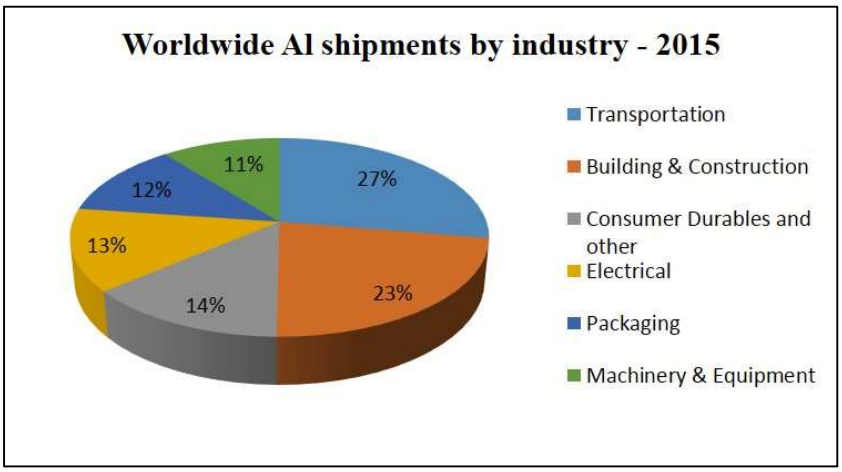

Figure 1.4 Worldwide aluminium shipments by industry in 2015.[11]

1.3.3 Deposition aspects for Wire arc additive manufacturing (WAAM) and welding

In present study, Gas metal arc welding (GMAW) process is considered for WAAM. Therefore, conditions that are present during welding that can be correlated with WAAM as same metal deposition process and material are considered. Aluminium alloys exhibit highly retentive oxide film, high coefficient of thermal expansion, high solidification shrinkage, high hydrogen solubility and relatively wide solidification temperature ranges. Strong chemical affinity of aluminium for oxygen forms aluminium oxide (Al_2O_3) instantaneously upon exposure to air. The melting point of Al_2O_3 is about 2050ºC that sometimes causes difficulties such as incomplete fusion when the oxide layer is not properly removed during arc on condition [13,14].

Porosity formation in aluminium welds is consistently being discussed amongst researchers as a need to be addressed in literature. The primary reason given for porosity formation is associated with the high hydrogen solubility in molten aluminium (7 ml/kg) and comparatively low solubility in solid form (0.4 ml/kg) [15]. Liquid aluminium absorbs large amount of hydrogen from the atmosphere due to its high temperature and as solubility of hydrogen reduces after solidification, excess hydrogen over solubility limit forms pores creating porosity problem resulting unacceptable welds. Moisture on the surface or in the form of hydrated oxide on the base metal or filler metal, lubricants on base metal or

filler metal, moisture in shielding gas, condensation inside the nozzle torch are considered as some of the sources of hydrogen that must be removed or reduced to maximum extent.

Another aspect of aluminium that needs to be considered is alloy's high thermal conductivity. Though the melting point of aluminium is much less than that of ferrous alloys, the thermal conductivity of aluminium is almost six times that of steel, which indicates the requirement of higher heat input due to loss of heat to surroundings by conduction. Relatively broad range of solidification along with high coefficient of thermal expansion and solidification shrinkage increases its susceptibility to weld cracking.

1.4 Research background and rationale

The present project is based on the concept of and partially supported by the Kraken, a Horizon 2020 project of a European Commission. Kraken involved development of hybrid manufacturing system for wire arc based additive manufacturing for aluminium alloys considering high deposition rate manufacturing. With respect to the theme of Kraken, the present study focuses on wire arc additive manufacturing (WAAM) of aluminium. Prior to the development of high deposition rate process, it was paramount to understand the mechanical, metallurgical and structural properties of the final product produced by WAAM. These properties of the part manufactured using WAAM technique are not fully understood and are under investigation. From the literature, it is clear that metallic components fabricated by WAAM method possess reduced tensile properties compared to wrought products, unique directional properties and uncommon grain structure. A detailed discussion regarding the same can be found in the literature review chapter. Apart from the discussed issues, Figure 1.5 enlists some of the deficiencies that are commonly observed in WAAM object. Although this study was linked to the Kraken project, aspect considered in this study were not completely aligned with the aim of Kraken project. A separate paths were followed focusing on the effect of metal depositing parameters on properties of deposited material as discussed in further part of this chapter.

Focusing particularly on the aluminium part formation by WAAM, imperfections such as presence of columnar grains, porosity formation and solidification cracking were reported in the literature [16]. At present, mentioned imperfections in the formed part are the prime challenges for researchers. Along with these, complex metallurgical phase formation, elemental loss and reduced mechanical properties are some of the limitations discussed in literature. A common problem in welding and WAAM structures repeatedly discussed in literature is residual stresses. The particular topic is not fully understood. Figure 1.6 illustrates the common deficiencies particularly found in WAAM processed aluminium. Thus, the WAAM of aluminium is not mature enough for manufacturing components with direct practical application; however, to raise the quality of the formed components mentioned issues need to be tackled.

In order to address the deficiencies, various parameters can be identified for tackling specific type of issues in WAAM object as shown in Figure 1.7. Thus, for minimising the defects, parameter can be handled cautiously to improve overall product quality. For example, to achieve specific three dimensional shape, peculiar deposition sequence through specific tool path planning will ensure minimum material removal from the formed part and reduced tool movement increasing the productivity.

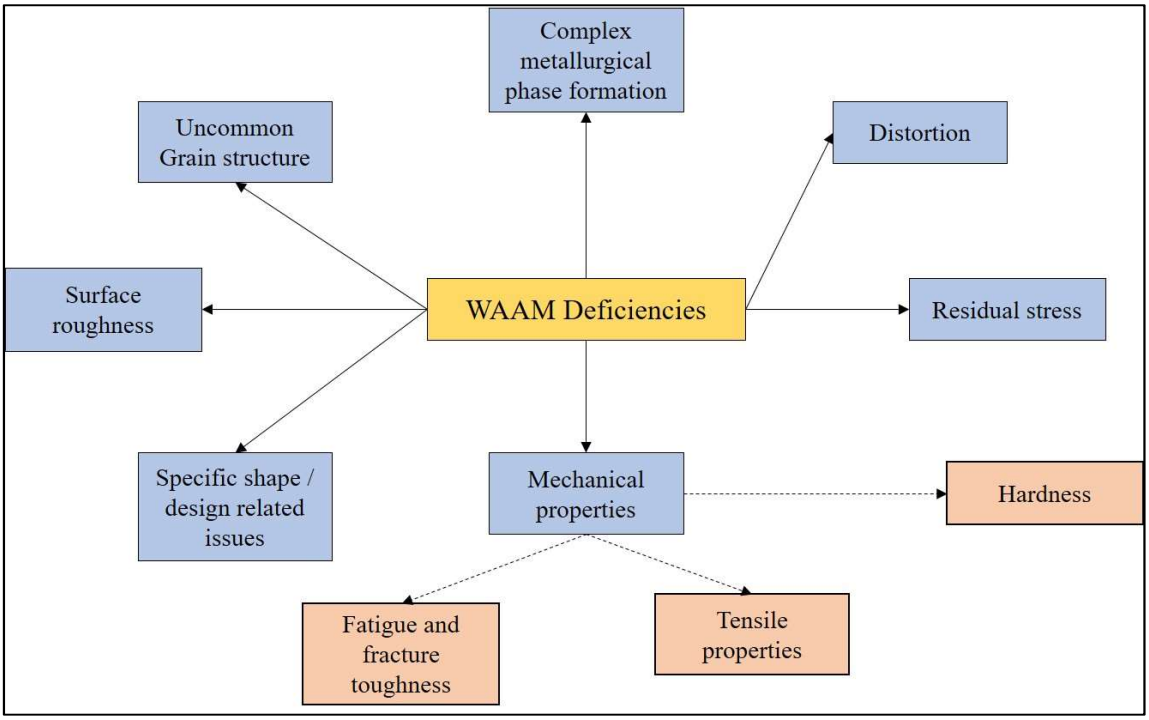

Figure 1.5 Deficiencies commonly found in an object produced using WAAM technique.

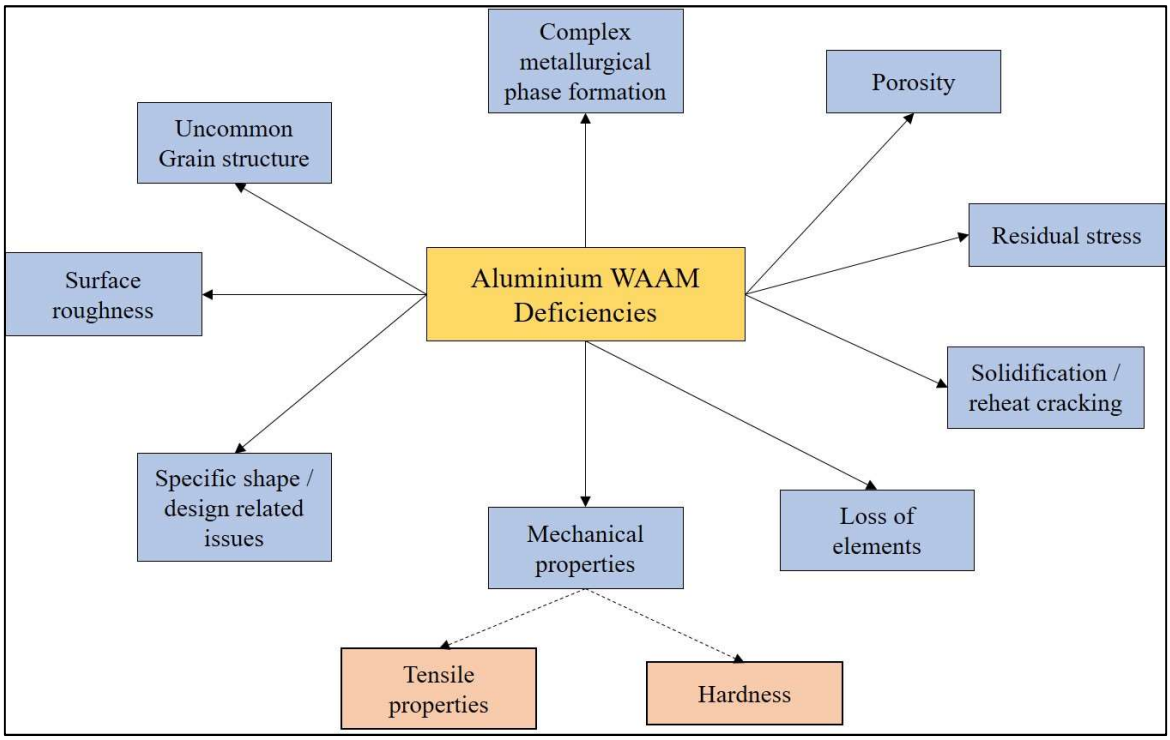

Figure 1.6 Deficiencies commonly found in an aluminium object produced using WAAM technique.

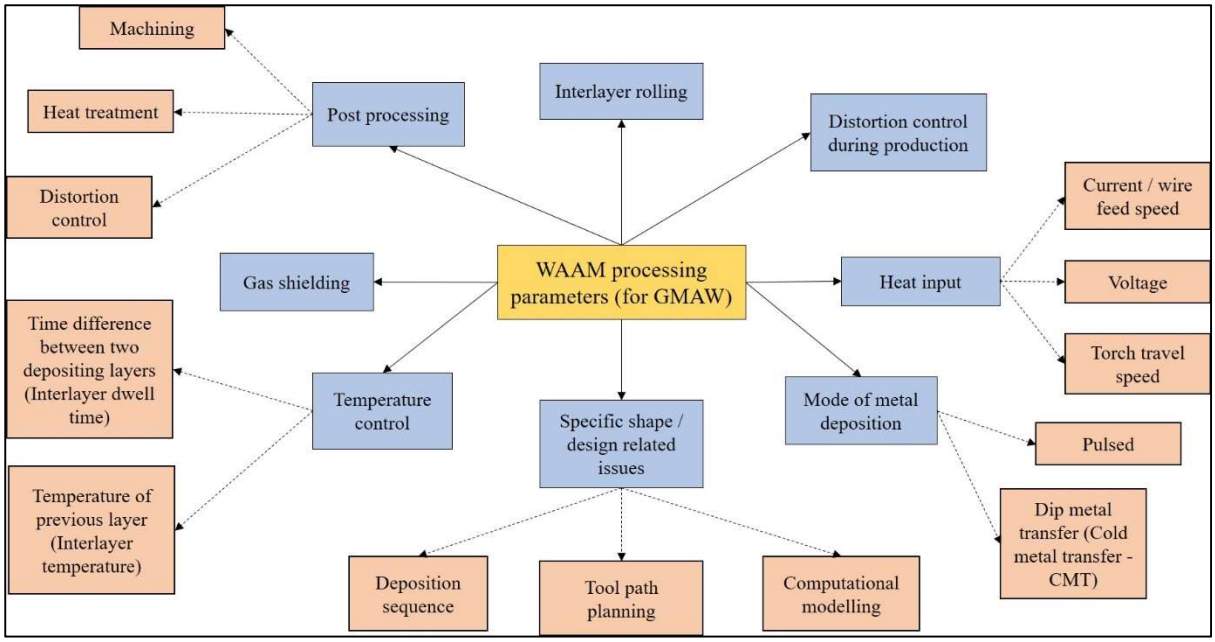

Figure 1.7 Parameters affecting WAAM product quality.

1.5 Project concept

This PhD work focuses on mainly three deficiencies mentioned previously that ultimately contribute to the structural integrity of a component produced by WAAM technique. Conventional GMAW and its variant cold metal transfer (CMT) technique are considered in this study. Aluminium wire composition AA5183 that is Al-Mg-Mn alloy is the main focused material. Unattended parameters associated with WAAM robotic metal deposition were considered such as interlayer-temperature along with variable heat input. Parameters followed are depicted in a chart format in Figure 1.8 that describes the overall project concept.

Firstly, one of the important challenges of WAAM, welding and casting of aluminium is the elimination of porosity which is correlated with hydrogen involvement in solidification process. Much of the efforts have been directed towards the understanding of pore formation in solidifying aluminium; however, it is still a major concern that needs a further in depth understanding of hydrogen dissolution and hydrogen effects in aluminium. In the present work focusing on WAAM technique, metal deposition parameters are varied in order to understand their effects on porosity formation and distribution as well as on hydrogen dissolution (refer Figure 1.8).

Second aspect of the work is microstructure of WAAM part. Microstructure has always been the critical issue that determines the mechanical properties. Presence of the epitaxial grains in build direction of WAAM processed part irrespective of metal composition (aluminium alloy, titanium alloy or nickel alloy) is not uncommon. As discussed earlier, therefore, unattended parameters in WAAM were applied for building a part. Experiments were conducted including effect of change of specific mode of metal deposition method such as pulsed GMAW and CMT in combination with heat input and interlayer temperature and time to investigate their effect on microstructure (Figure 1.8).

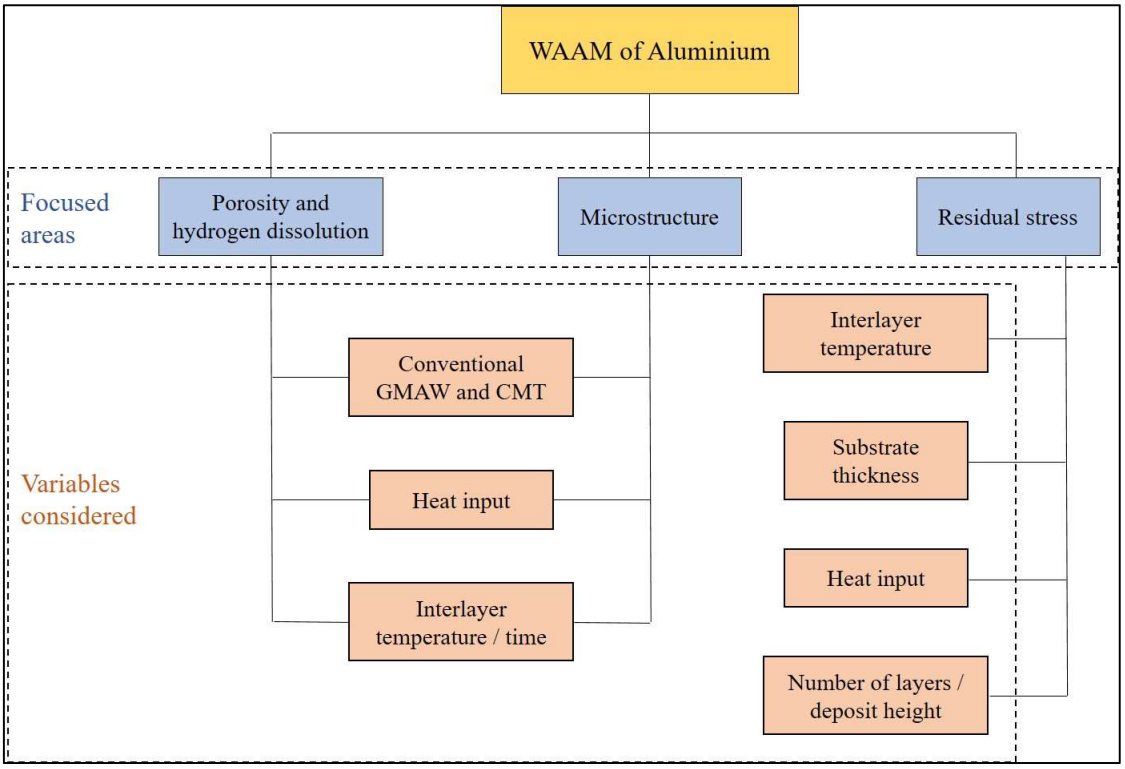

Figure 1.8 Project concept in concise flow chart.

Lastly, residual stress, a complex phenomenon in welding and WAAM is explored. Residual stress is one the prime factors that directly affects the working performance of an in-service component. Residual stresses in WAAM structures were investigated for high strength alloys namely titanium and nickel based alloys through neutron diffraction and newly developing contour method. Although, the literature included typical residual stress pattern in WAAM part for high strength alloys, the effects of different deposition strategies such as interlayer temperature, heat input and substrate thickness on residual stress distribution in WAAM deposit (described in Figure 1.8) is not investigated, particularly for relatively low strength aluminium alloys.

Conclusively, effect of mode of metal deposition, interlayer temperature and heat input on the microstructure and porosity were not discussed in open literature. Residual stress evaluation and distribution in WAAM part of aluminium along with the effect of interlayer temperature, substrate thickness, heat input and number of layers is not discussed. Therefore, the present work was carried out investigating the microstructure, porosity and residual stresses in WAAM produced aluminium part as a function of heat input, interlayer temperature and mode of metal deposition. More details about interlayer-temperature and interlayer-dwell-time deposition methods can be found in literature review, methodology and dedicated chapters on porosity, microstructure and residual stress.

1.6 Project objectives

The project is based on and research was conducted following the below mentioned research objectives that would support designers while developing a WAAM object for practical applications –

1. To determine the combined effect of interlayer-temperature, interlayer dwell time, heat input and mode of metal deposition *i.e.* pulsed MIG and CMT on the porosity formation and

distribution using the novel technique X-ray computed tomography (X-CT) scanning. Also, to study the correlation between porosity and hydrogen dissolution in WAAM processed aluminium 5183 alloy.

2. To investigate an effect of interlayer-temperature and heat input on the geometry of WAAM of aluminium alloy part.
3. To determine the combined effect of interlayer-temperature, interlayer dwell time, heat input and mode of metal deposition *i.e.* pulsed MIG and CMT on the microstructure of WAAM of aluminium 5183 alloy.
4. To find out the effects of metal deposition variations such as substrate thickness, heat input, deposition height and interlayer-temperature on residual stress formation and distribution using the newly developed contour residual stress measurement method in WAAM of aluminium 5183 alloy.

Chapter 2: Literature Review of Wire arc additive manufacturing (WAAM) and State-of-the-art of WAAM of aluminium

2.1 Introduction

Although, the acronym WAAM has become an inherent part of AM terminology in recent past, the concept of 3D welding and near-net-shape manufacturing is being exercised from almost 100 years. With the advancement of welding technology many inventors practiced contemporary welding techniques not only to join the wide variety of metal components but also to manufacture different types of shapes such as receptacles, ornaments and parts of engineering interest such as pressure vessels [17–19]. Through the innovative thought of depositing one type of metal on another to obtain enhanced surface properties such as corrosion resistance, researchers exercised the welding technique for cladding purpose to reclaim worn out machine components. These initial developments were considered as a churning factor for the manufacturing of components solely by deposition of weld metal that further gained an economic interest in manufacturing industries. Within the early stages of this technology development, researchers identified its importance in terms of low-cost and lead-time saving through using effective manufacturing process compared with the conventional subtractive and formative manufacturing processes. Though the WAAM field is yet to be fully matured appreciable amount of work is being done and potential results are advancing WAAM to a fully-fledged manufacturing process. Many techniques were developed over the years possessing inter-relation and similarities with each other that can be considered as a precursor of WAAM. Few can be named as: Shape Welding (SW); Shape Melting (SM); Rapid prototyping (RP); Solid free form fabrication (SFF); Shape Metal Deposition (SMD); and 3D welding.

2.2 History of Wire arc additive manufacturing (WAAM)

On a broader scale development of WAAM can be categorised into three timed sections. The first 'beginning phase' starting at 1920, second phase of 'building-up background' from 1970s until 1990s and the last 'development of new era' phase can be extended to date. Figure 2.1 explains notable achievements with respect to time scale and progress of WAAM over the 100 years [17,19–39].

In 1920, Baker [17] filed a patent naming '*Method of making decorative articles*' which was assigned to the Westinghouse Electric Manufacturing Company demonstrated the technique of constructing receptacles and decorative articles using non-adherent substrate as detailed in Figure 2.2. The author called the deposit as a '*superposed deposit of metal*' manufactured using manipulated helical path of a

fusible electrode. The consumable electrode path was manually controlled and the use of a suitable contour and pantograph was devised when a large number of such objects was to be produced. Baker's invention of this formation of receptacles can be considered as the foundation stone in the development of the WAAM technique which clearly showed the author's great vision that paved the way for the novel technique.

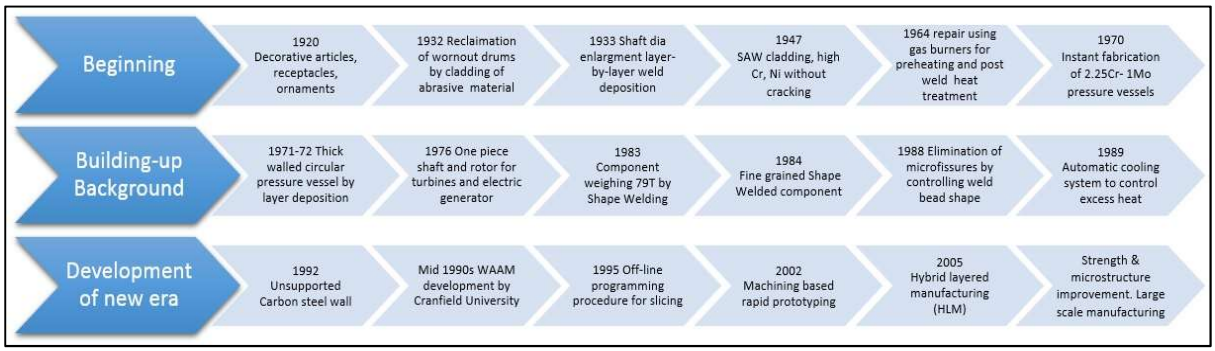

Figure 2.1 History of WAAM (adopted from [3]*).*

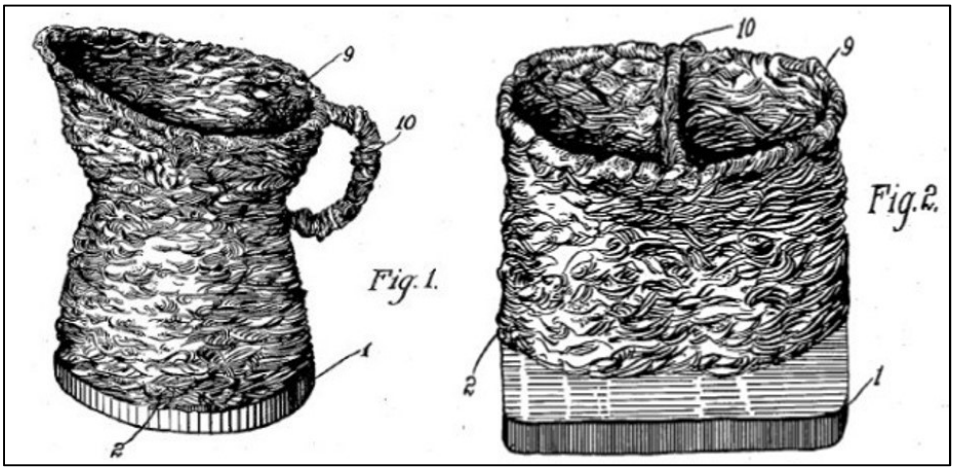

Figure 2.2 Superposed deposit [17].

In the same time period another similar patent entitling '*Ornamental arc welding*' was filed [18] which was also assigned to Westinghouse Electric Manufacturing Company (refer Figure 2.3). The author claimed the invention of a technique for deposition of metal which became an integral part of the substrate through impregnation of symbols, characters or ornamentation of a useful form and in an aesthetic manner. Further the author described the effect of welding variables such as welding current, travel speed and even torch oscillations in order to obtain desired weld bead geometry in terms of weld bead height, width and penetration. One important factor that was highlighted in this patent involved the process of heat management. The inventor mentioned the use of a base metal with high thermal conductivity such as copper that helped in rapidly dissipating the heat and thus provided desired fast cooling effect.

In 1930, Shockey [30] submitted a patent, which put forth an innovative approach to improving the life of brake drums. Repairing and reclamation of worn out drums was made possible with a cost as low as half that of the many other contemporary methods by depositing a metal by an electric arc in layers of spiral form without interruption from beginning to end to avoid any defects at start and end points (see

Figure 2.4). Shockey not only repaired worn brake drums by cladding but also improved their expected lifespan by using an abrasive resistant material as the clad overlay. Surprisingly, Shockey also studied the concept of effective weld bead overlapping and mentioned that one-third area of the previously deposited weld bead should be overlapped by the next weld bead to obtain the best results.

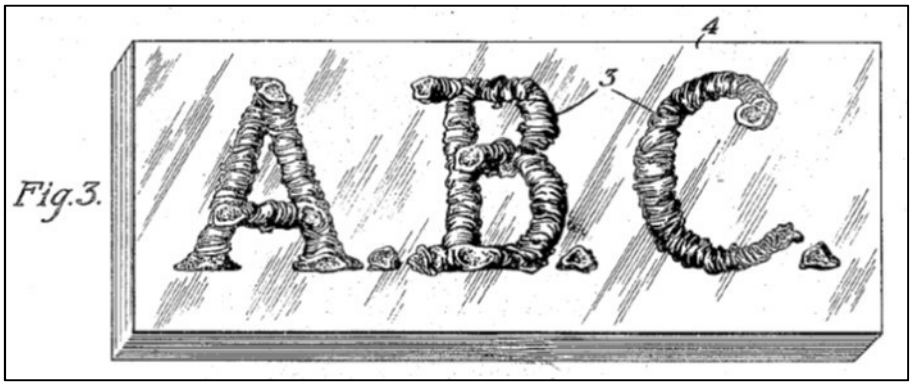

Figure 2.3 Ornamental arc welding [18].

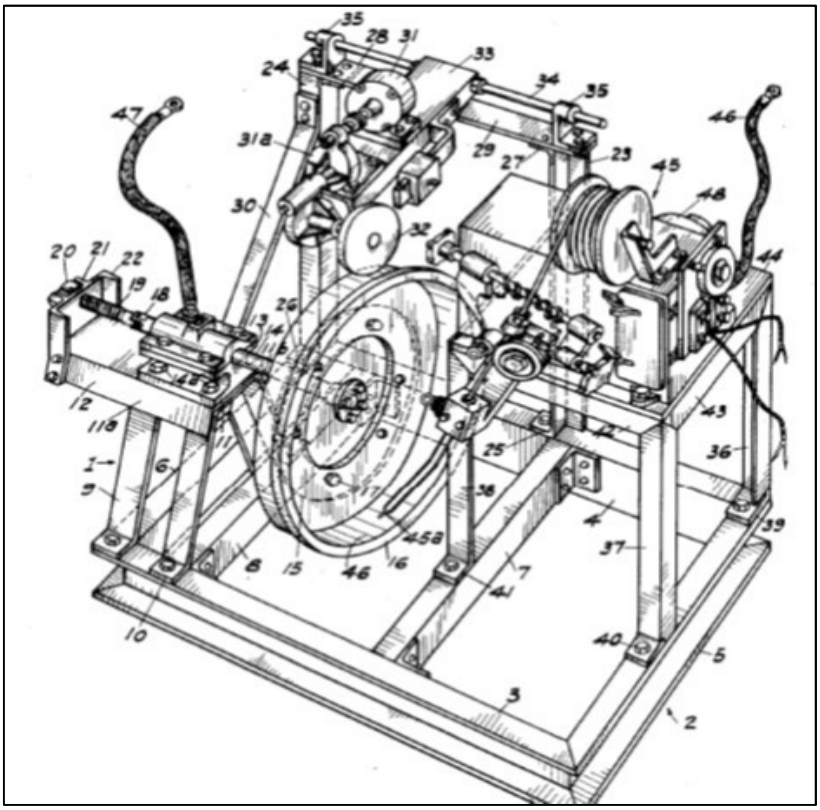

Figure 2.4 Machine for repairing and reclaimation of worn out drums [30].

In order to obtain a good and consistent weld bead geometry and higher deposition rate a continuous wire feed supply is one of the essential parameters to maintain. On the similar line Nobel [23] introduced the first known continuous wire feeding arrangement for electric arc welding; here Nobel discusses the incremental enlargement of a shaft's diameter using a layer-by-layer deposition of weld metal with a specially designed wire feeding apparatus. In another patent file by Carpenter and Kerr [24] assigned to Babcock and Wilcox Company reached a milestone in WAAM development. The important aspect of this patent was the cladding of retorts using high chromium and nickel that were normally subjected

to high temperatures during magnesium production using Submerged Arc Welding (SAW) process (refer Figure 2.5). The patent disclosed the method of successfully depositing a weld metal of desired composition required as per operational conditions by avoiding any cracks. The trend of inventing new concepts continued into 1960s when White [25] invented a method of repairing rollers using the Submerged Arc Welding (SAW) process. The notable innovative in this patent was the use of gas burners used for preheating and post-weld heat treatment, and the important influence with which such a thermal management played in controlling the shape and dimensions of the deposited bead, which is believed to be the first time such a system was used.

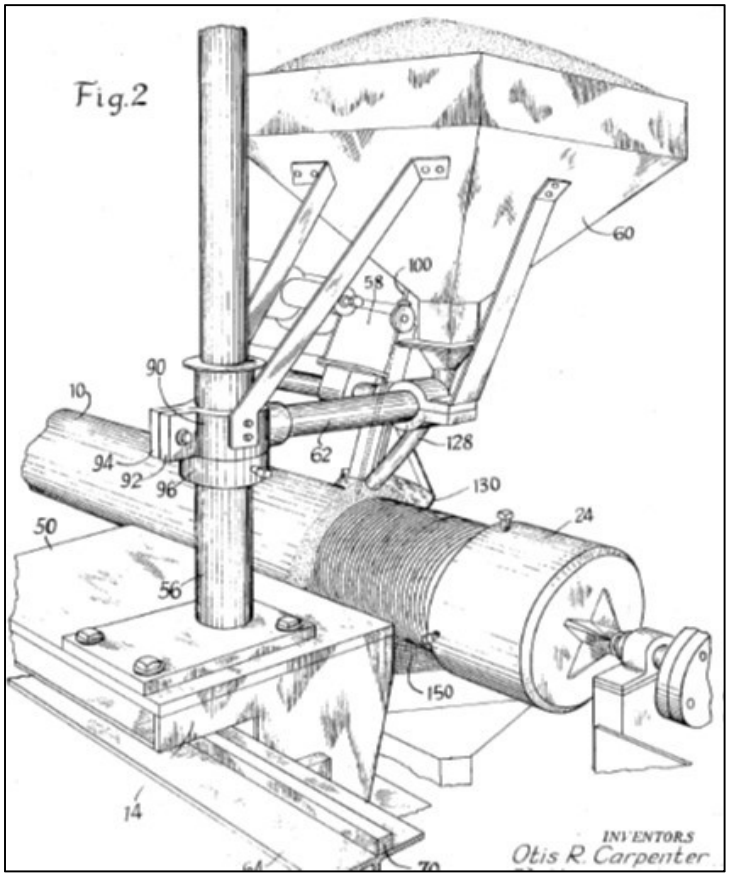

Figure 2.5 Cladding of retorts with high Cr and Ni [24].

One the most important and notable patents in the history of WAAM is considered to be the `*Method of and Apparatus for Constructing Substantially Circular Cross Section Vessel by Welding*' filed by Ujiie [19] which was assigned to Mitsubishi Iukogyo Kabushik Kaishai, Japan. The invention was used to manufacture of thick walled circular cross sectional pressure vessel solely by the deposition of weld metal as shown in Figure 2.6. In addition to this major development the patent also reveals the application and importance of the machining of inner and outer surfaces of the formed object immediately after cooling of the weld metal. This invention was considered an effective cost saving manufacturing approach to manufacture a pressure vessel when compared with the conventional approach. To achieve high deposition rates the author utilised Resistance electro slag welding (RESW) and Shielded inert gas metal arc (SIGMA) though the use of Gas tungsten arc welding (GTAW) and Submerged arc welding (SAW) were also recommended.

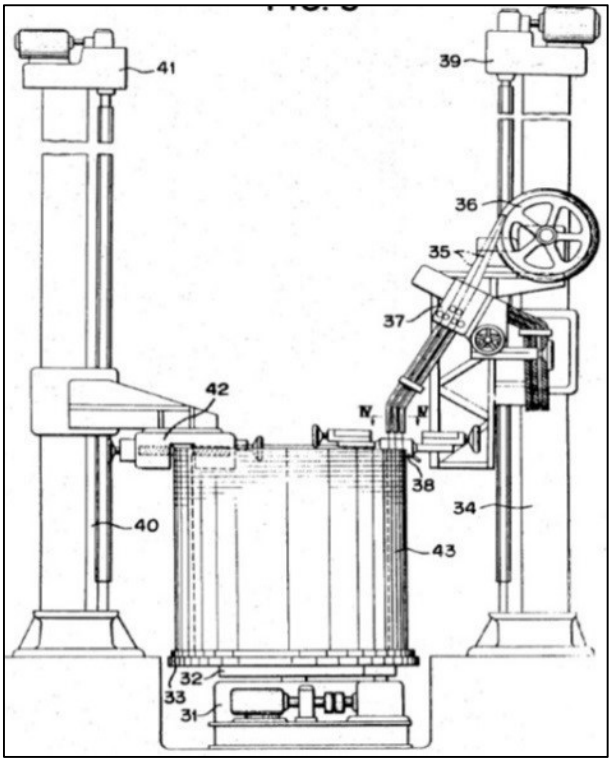

Figure 2.6 Thick walled circular cross section pressure vessel by shape welding [19].

In another patent Ujiie [33] discussed different approach of employment of three electrodes obtaining increased weld deposition rate via a short circuiting and spray mode transfer in Gas metal arc welding (GMAW). A major break-through for the WAAM technology was the fabrication of one-piece large diameter metal shafts for turbines and electric generators. The patent was filed by Brandi and Luckow [26] which was assigned to the August Thyssen-Hutte AG Company described the method of fabricating good quality product without any defects by deposition of weld metal layer by layer. An effective thermal management method had also been considered during manufacturing in which authors highlighted the need of an online monitoring system for controlling of residual stresses and distortion in a formed component. The overall process depicted the possibility of high weight product manufacturing.

To manufacture parts with Shape welding (SW), Shape melting (SM) and 3D welding techniques, it is paramount to check the integrity and overall mechanical and metallurgical properties of the formed component in order to achieve suitable in-service capability. Along with those major industries who had made huge investments in developing these techniques in 1960s many universities started showing their due interest in arc based rapid prototyping (RP). At the University of Stuttgart in 1983 Thyssen AG and the State Materials Testing Institute jointly carried out research on mechanical and microstructural properties of a SW 79t component manufactured using four SAW tandem head stations at a deposition rate of 20 kg/h in 6 weeks [34]. Refer Figure 2.7 for photographic representation of the formed component. SW research and development work was undertaken further by Thyssen AG in 1983 resulted in creating a development facility for the production of large mass components weighing up to maximum 500,000 kg with lengths up to 11m and diameters ranging between 2.5 to 5.8 m. In 1987, Million and Zimmerman [40] filed a patent that disclosed the method of formation of a fine

grained shape welded component using the 10MnMoNi5-5 grade steel through precisely controlling the weld bead profile.

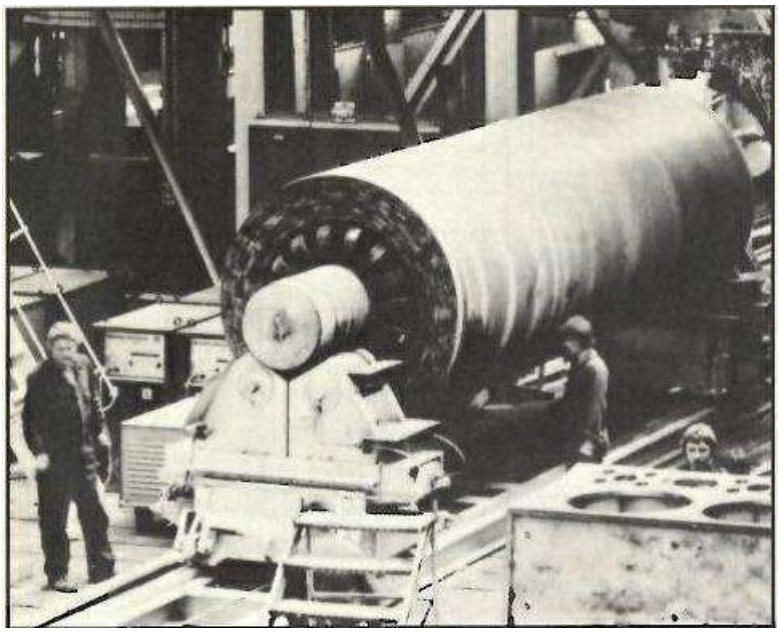

Figure 2.7 Shape welding machine with 79 metric ton cylindrical shell [34].

The work undertaken by researchers proved its difficulty during product development using MnMoNi materials due to higher susceptibility to stress-corrosion cracking. Despite stringent parameter monitoring and control of welding parameters 10CrMo9-10 shape welded pressure vessel underwent catastrophic failure, furthermore the alloy 20NiCrMoV14-5 also revealed cracks [41]. A detailed investigation revealed that both materials had low fracture toughness properties. CrMo and NiCrMoV steel grades also manifested cracks in during annealing, inferring that the re-heat cracking is also a key attribute to consider for future development. These cases adversely impacted the development of shape welding and allied techniques. This was considered a major setback for commercialisation of SW technology with respect to the manufacturing of heavy products of high alloy steels. This technique is still facing unresolved problems which need to be addressed for unrestrained growth of WAAM technique. This setback, whilst concerned with low alloyed steel could not prevent the growth of SW technology. In one patent Million and Zimmerman [40] studied the shape deposition and concluded that comparatively low deposition rate processes such as GTAW and GMAW compared to SAW and resistance welding could play a decisive role in fabrication of complex shapes. The use of GMAW and GMAW-P can precisely control the size and shape of deposited weld metal and thus can eliminate the posterior down-hand position technique.

A constant effort put by researchers in the field yielded constructive paths. Babcock and Wilcox Company filed another important patent on SW in 1987 by Ayers et al. [28]. The authors experimentally showed that if the weld bead dimensions were closely controlled by controlling welding parameters during weld deposition unwanted micro fissure which was major concern in the welding of austenitic materials can be successfully eliminated. The inventors argued that the presence of any sharp discontinuities raises the probability of micro fissure formation, and so close control over weld bead shape formation can greatly reduce or even prevent the formation of micro fissures, moreover

researchers discussed the effect that other variables had on their formation and suggested the use of optimised welding variable including heat input, travel speed, wire feed speed and torch oscillation (refer Figure 2.8). With advancement of SW technology it was not surprising that researchers precisely pointed out the need for developing an automated thermal management system during weld deposition for effective control of distortion thus final shape of the product and to obtain isotropic mechanical properties and microstructural features. With all these considerations of prior work one patent filed by Doyle and Ryan [29] who were employed by the Babcock and Wilcox Company developed an automatic cooling system by providing feedback of temperature and pressure data to a computer which regulates the flow of coolant through guiding nozzles.

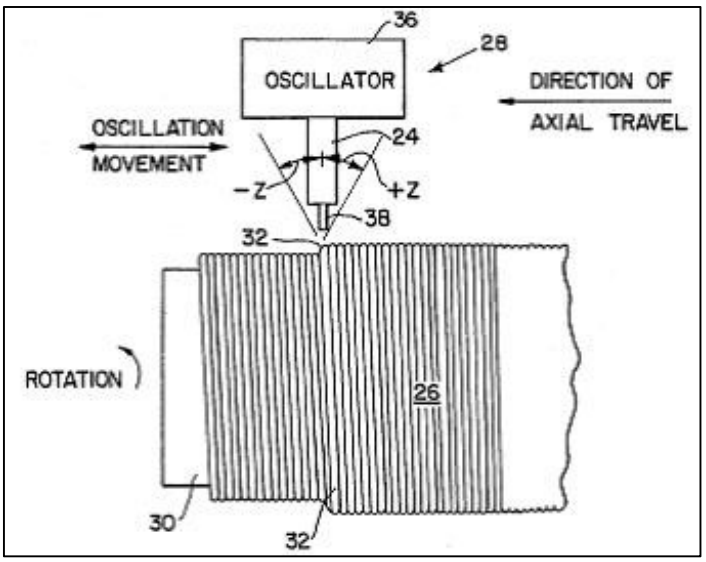

Figure 2.8 Elimination of micro-fissures by controlling welding parameters [28].

Another important milestone in the field of 3D welding was the development of unsupported walls made of carbon steel by the layer-by-layer fashion built by Dickens et al. [35] using the robotic GMAW process and on-line point to point programming. The programming was done manually which was time consuming process. Further authors studied the effect of critical welding parameters and bead dimensions on surface quality and wall thickness of built wall. The effect of variation of welding parameters such as current, voltage, torch travel speed, wire feeding rate on weld bead height and width and on the wall thickness were independently studied. The author highlighted the need of online monitoring of welding variables in order to control weld bead shape ultimately controlling the shape of the component. Temperature sensor became vital part of the SW technology when Spencer and Dickens [42] put forth study of achieving the surface quality improvement by controlling temperature and thus thermal cycles.

Rolls Royce in 1990s directed efforts in manufacturing of aero engine components. The motive behind this focused work was high manufacturing cost of the aero engine components with conventional subtractive manufacturing method which can be minimised by shape manufacturing. The material wastage was the main concern with the subtractive manufacturing which tremendously raises BTF ratio and conclusively adds up to final manufacturing cost. Rolls Royce started working with Cranfield University to find newer and cheaper routes of manufacturing of aero engine components through shape deposition. The pioneering work has been carried out at the Welding Engineering Research Centre

(WERC) in Cranfield University discovering a new area of research naming Wire arc additive manufacturing (WAAM). Initially work was highly focused on manufacturing of aerospace components mainly titanium based alloy so that material saving would result in huge cost reduction. This particular work interested many researchers who followed an extensive work on titanium alloys with WAAM technique. In 1991, McAninch et al. [43] utilised GMAW to produce functionally graded material that is components with varying mechanical and corrosion properties considered as a cost effective method at the requirement of local property variation. Ribeiro and Norrish [36] developed offline programming system for WAAM that allowed slicing of the computer-aided design (CAD) model to deposit a metal in a prescribed layered format to develop the desired final shape. Required weld bead dimensions were defined manually and system subsequently specified corresponding welding parameters automatically. In another study by Zhang et al. [44] were able to slice the final component into number of layers using the initial graphics exchange specification (IGES) format. Researchers not only advised for the need incorporate ignition time, ignition control, crater filling control and other weld parameters affecting weld quality into welding programme, but also predicted that a small wire diameter with high current carry high droplet transfer stability can produce good quality products.

The WAAM development and process complexity graph is depicted in Figure 2.9. It outlines a smooth rising curve for process development due to invention of newer techniques. From the commencement of manufacturing of ornamental objects where the process complexity was adequate researchers progressed to fabricate an entire pressure vessel using alloys such as the 10MnMoNi5-5, 20NiCrMoV14-5 grades in 1980s. At that time WAAM development could be considered at its peak and with constant process improvement, WAAM was a regular, handy and less complex manufacturing process; however, observed cracks in the formed pressure vessel impaired the process development which is showed as a plunging curve. Researchers concentrated only on the deposition rate and the shape of an object, however, the prime factor of quality and fit-for-service was out of focus. This approach restricted the prominent growth of the technique and the sector remained stagnant or even witnessed a downfall due to lack of structural and quality improvement. At similar time computer controlled systems were becoming a key in enhancing capability of the manufacturing sector due to the increased possibility of automation that could result in aiding the capability to produce high-end quality products, in an economical manner that was not possible prior to this digital renaissance. Thus WAAM re-development stage can be seen from start of 1990's along with raising complexity owing to wide research and more advanced testing availability compared to earlier times. This fact provided freedom for inventors in terms of materials handling capability, formulation of the process and conceptualisation of final shape. Further, automation omitted the use of traditional manual and machine operations which was entirely different approach in manufacturing. After due interest by Rolls Royce and Cranfield University and contemporary developments in manufacturing reinvented WAAM technique. Along with the process development, various advanced testing techniques also emerged that forced more stringent passing criteria on a shaped object. Thus, although the process has developed significantly since 1990s, this also increased process complexity in terms of satisfying different testing criteria and object readiness to operation.

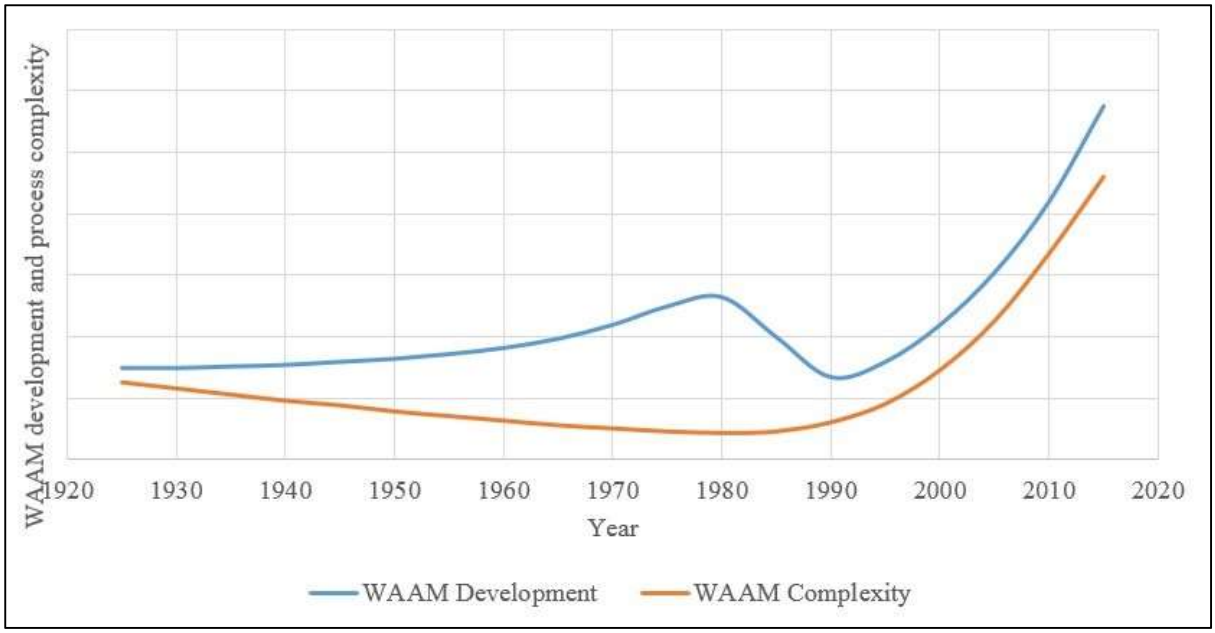

Figure 2.9 Development and complexity of the WAAM process over the years [3].

2.3 State-of-the-art of Wire arc additive manufacturing (WAAM) technique

In the following years substantial research work was carried out on possibility of using several welding processes such as electron beam welding (EBW), laser beam welding (LBW), gas tungsten arc welding (GTAW), plasma arc welding (PAW) and many more and different metals primarily Ti, Ni, Al alloys along with steels. Many theoretical and practical modelling research projects were put forth in advancement of WAAM. Up until 1995, appreciably less attention was focused on mechanical properties and microstructural features, where hardly any work was directed towards the development and enhancement of such properties. Later efforts were directed towards the development of automated techniques and quality improvement of the product through measurement of residual stresses, observation of microstructural features, computer aided simulation of WAAM process and many more. Many innovative approaches were applied to obviate structural deficiencies in WAAM component through wide variety of views but not limited to design, process variation, forming appearance, interlayer rolling, and fatigue and fracture toughness (Table 2.1a to c).

Table 2.1a Major areas of study of WAAM technique in the recent past.

Area of Study	Year	Specific area of study	Material / Filler wire	Studied by
Design	2011	▪ Cross structures ▪ Root path determination	Steel	[45]
		▪ Inclined wall preparation ▪ Preparation of horizontal wall and closed shape	Steel (ER70S-6), Aluminium (4043)	[46]
	2014	▪ Deposition patterns ▪ Cross structures	Mild steel, Titanium (Ti-6Al-4V)	[47]
		▪ Tool path planning	Mild steel	[48]
	2015	▪ Hybrid manufacturing	-	[49]
	2016	▪ T-crossin	Steel (ER70S-6)	[50]
Process variation	2005	▪ Hybrid manufacturing using milling	Steel (ER70S-6)	[22]
	2014	▪ Twin wire GMAW	Steel (ER70S-6) & Steel ER110S-6	[51]
	2016	▪ Double electrode GMAW	Steel (H08Mn2Si)	[52]
		▪ Dissimilar twin wire deposition (functionally gradient part formation)	Steel (ER70S-6) & Steel ER110S-G	[53]
		▪ Double electrode GMAW	Steel (H08Mn2Si)	[54]
	2017	▪ Hybrid manufacturing with milling	Aluminium 2325	[55]
		▪ Hybrid manufacturing	Steel (ER70S-6)	[56]
	2018	▪ Dissimilar twin wire GTAW deposition	Aluminium ER2319 and ER5087	[57]
Fatigue failure and toughness	2013	▪ Fatigue life	Titanium (Ti-6Al-4V)	[58]
	2016	▪ Fatigue crack growth propagation	Titanium (Ti-6Al-4V)	[59]
		▪ Fatigue crack path selection	Titanium (Ti-6Al-4V)	[60]
	2017	▪ Fatigue crack growth rate	Titanium (Ti-6Al-4V)	[61]

Table 2.1b Major areas of study of WAAM technique in the recent past (continued).

Area of Study	Year	Specific area of study	Material / Filler wire	Studied by
Residual stress	2007	▪ Finite elemental structural study	Steel (Simulation)	[62]
	2005	▪ Deformation modelling	Steel	[63]
	2011	▪ Computer simulation	Steel	[64]
	2013	▪ Blind-hole method and numerical modelling	Steel	[65]
		▪ Neutron diffraction	Steel	[66]
	2015	▪ Distortion control	Steel, Aluminium and Titanium (Ti-6Al-4V)	[67]
	2016	▪ Computational model for twin wire AM	Steel (ER70S-6)	[68]
		▪ Bulk deformation	Steel (ER70S-6)	[69]
		▪ Microstructure	Titanium (Ti-6Al-4V)	[70]
		▪ Finite element modelling ▪ Neutron diffraction	Titanium (Ti-6Al-4V) Steel	[71] [72]
		▪ Finite element modelling and X-ray diffraction	Steel	[68]
		▪ Neutron diffraction and Contour residual stress measurement	Titanium (Ti-6Al-4V)	[73]
	2017	▪ Neutron diffraction and coordinate measuring machine (CMM)	Stainless steel (316L)	[74]
	2019	▪ Finite element modelling	Steel	[75]
Cold metal transfer (CMT)	2010	▪ Application for Ti-6Al-4V	Titanium (Ti-6Al-4V)	[76]
	2014	▪ Parametric study with AlSi5	Aluminium (AlSi5)	[77]
		▪ Variants of CMT technique ▪ Effect on porosity	Aluminium (2319)	[78]
	2017	▪ Wall and block structure	Aluminium (ER2319)	[79]
	2018	▪ Varying polarity and microstructural considerations	Al-6Mg	[80]

Table 2.1c Major areas of study of WAAM technique in the recent past (continued).

Area of Study	Year	Specific area of study	Material / Filler wire	Studied by
Forming appearance	2014	▪ Passive vision sensor system	Steel	[81]
	2015	▪ Parametric study	Steel	[82]
		▪ Bead overlapping factor	Steel	[83]
	2016	▪ Double electrode GMAW parametric study	Steel (H08Mn2Si)	[54]
		▪ Minimum angle and curvature of radius	Aluminium 5A06	[84]
		▪ Control of arc start and end	Steel	[85]
	2017	▪ Inclined wall structure	Steel (H08Mn2Si)	[86]
Interlayer-rolling	2013	▪ Effect of different profiled rollers	Steel (ER70S-6)	[66]
		▪ Grain structure refining	Titanium (Ti-6Al-4V)	[39]
	2014	▪ Distortion	Titanium (Ti-6Al-4V)	[38]
		▪ Refined microstructure		
		▪ Reduction of residual stresses	Titanium (Ti-6Al-4V)	[87]
	2016	▪ Controlling residual stresses	Titanium (Ti-6Al-4V)	[88]
		▪ Precipitation hardenable alloy	Aluminium (ER2319)	[89]
		▪ Porosity formation behaviour in work and precipitation hardenable alloy	Aluminium (ER2319 and 5087)	[90]
		▪ β grain refinement in Ti-6Al-4V	Titanium (Ti-6Al-4V)	[20]
	2017	▪ Al-Mg4.5Mn alloy	Aluminium (ER5087)	[91]

Mehnen et al. [45,47] highlighted difficulties and discussed probable solutions for cross structures whereas Kazanas et al. [46] performed experiments to build inclined and horizontal wall first time. In order to improve the production rate, performing tools should have minimum movement and idle time was studied by Ding et al. [48]. As discussed earlier, different processes, process combinations and materials combinations such as twin wire GMAW [51], double electrode GMAW [52,54], dissimilar twin wire (functionally gradient part production) [53,57], hybrid manufacturing [22,55,56] *etc.* were experimented. Welded structures predominantly shows residual stresses due to molten metal solidification. Following similar condition, WAAM part also showed stresses however, its distribution and pattern for different shapes is not yet fully understood. Computational [62,64,68] and experimental approaches [38,66,74] were undertaken in order to study the distribution of residual stresses. Original shape of a single layer contributes towards the final shape of the WAAM part. Researchers focused on forming appearance [81,82,84,86] as discussed in Table 2.1a to d. Interlayer rolling concept was upheld my researchers owing microstructural and stress control advantages [21,39,66,87]. Low heat input process namely cold metal transfer (CMT) was widely incorporated in WAAM field irrespective of metallic alloy [76,79] used for WAAM part formation.

2.3.1 Cold metal transfer (CMT) and its application

CMT technique, advanced version of GMAW process, has been well noted and widely accepted by the industries due to its unique advantages such as less heat input, capability of production of spatter free and good quality welds [92,93]. Electro-mechanically controlled high speed metal transfer, doctored method of metal transfer, regulated arc length allowing lower heat input are the distinguishable features of CMT from conventional GMAW. Dip metal deposition remains the primary metal deposition technique in CMT operation. Cold metal transfer is a relative term that evolves from comparison to conventional GAMW processes. Periodical fluctuation of current and voltage between minimum and maximum reduces overall energy input reducing the heat average making process relatively less hot. The typical current and voltage variations in CMT process are shown in Figure 2.10. There are four variations of CMT technique namely, conventional CMT, pulsed CMT (CMTP), CMT advance (CMTADV) and CMT pulse advance (CMTPADV).

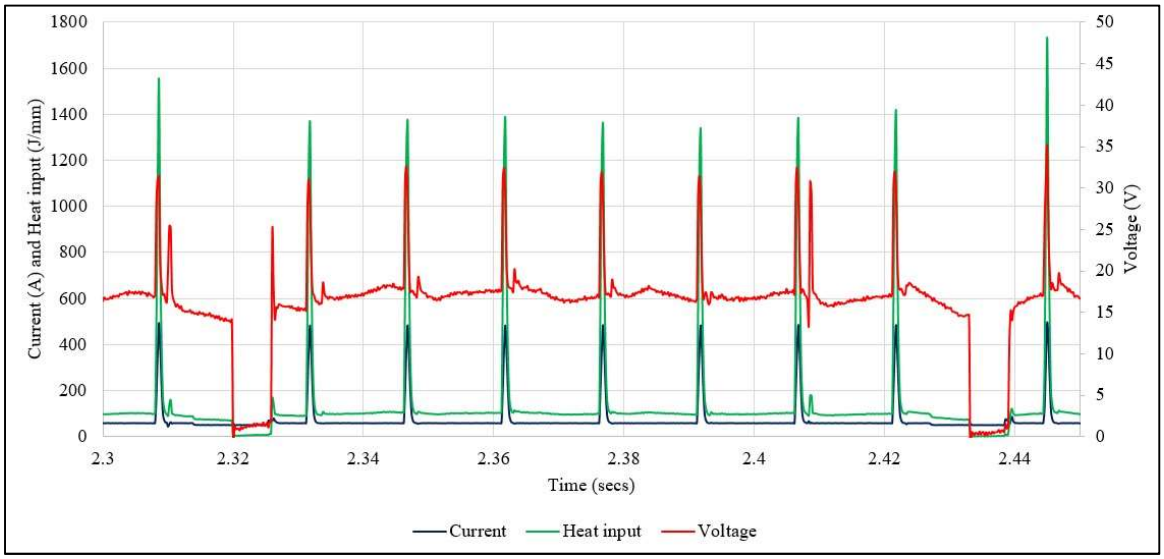

Figure 2.10 Current and voltage waveforms of the CMT process.

2.3.1.1 Cold metal transfer (CMT) operation

The difference between conventional pulsed GMAW dip metal transfer mode and CMT mode is depicted as a cyclogram of voltage versus current in Figure 2.11 and Figure 2.12. Further Table 2.2 highlights the operational differences between the two. Below are the four stages of CMT metal transfer that operates in a cyclic order.

(1) Arc burning – A hot stage with full arc ignition due to high voltage and current. A metal globule formation at the feed wire tip due to heating up to its melting temperature.

(2) Arc collapse – A cold stage in which feed wire touches liquid weld pool by extinguishing arc and supplying a liquid droplet formed at its tip.

(3) Short-circuiting – Instantaneously after wire touches weld pool in stage 2, filler wire is mechanically retracted back with the help of advanced electronic circuitry. No any resistance heating observed due to maintenance of low current during short circuiting time.

(4) Arc re-ignition – Arc re-establishes due to the increase in current and voltage as feed wire retracting. With increased distance from weld pool, electric energy increases again forming a hot phase of CMT operation.

Mechanical retraction and almost zero current flow during short circuiting is the innovative part in CMT operation. This reduces unnecessary energy supply and temperature rise with improved metallurgical properties and reduced spatter. A difference in operation between dip metal transfer of conventional MIG and CMT is shown in Figure 2.11 [94] and Figure 2.12 [Private communication with Geoff Melton, Jan 2018].

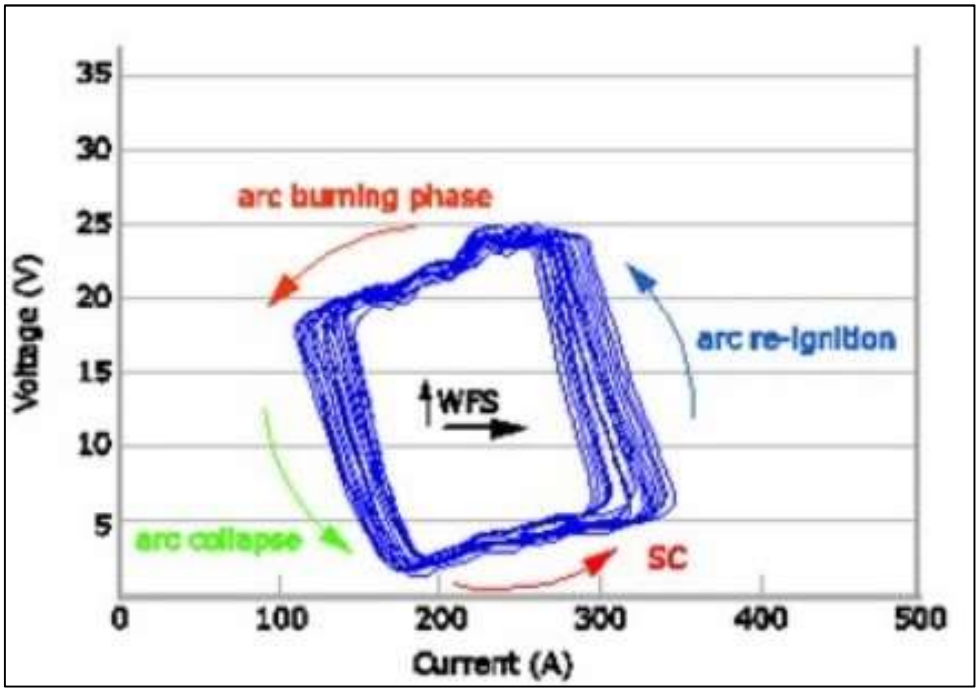

Figure 2.11 Cyclogram of voltage versus current depicting conventional dip metal transfer mode in GMAW [94].

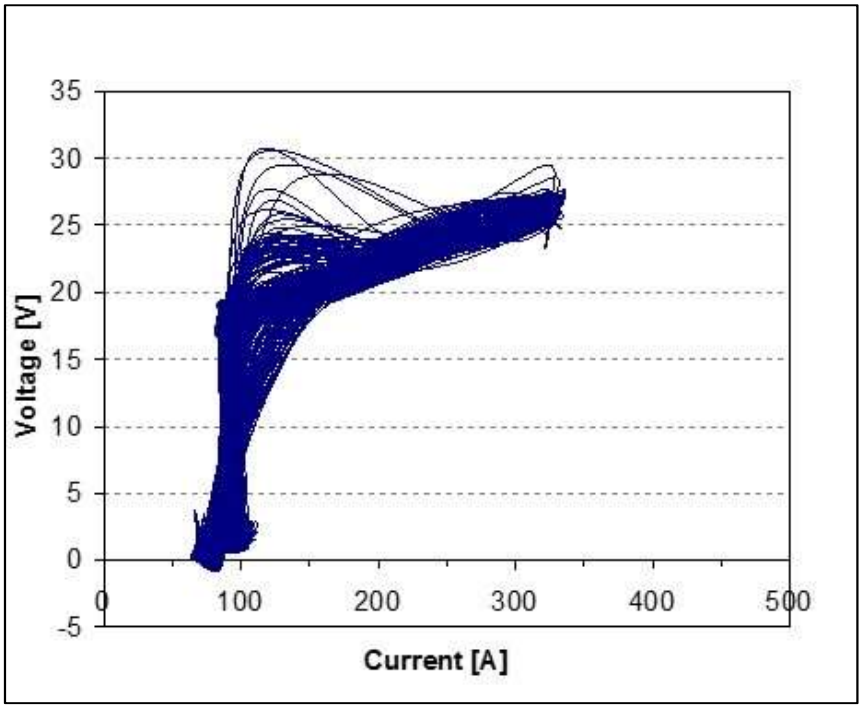

Figure 2.12 Cyclogram of voltage versus current depicting CMT transfer mode (adopted from [3]*).*

Table 2.2 Operational comparison of dip metal transfer mode of GMAW and CMT (adopted from [3]*).*

Stage	**Dip metal transfer in GMAW**			**CMT**		
	Current	Voltage	Wire feed	Current	Voltage	Wire feed
Arc burning	LD	SD	Feed	LI	SI	Feed
Arc collapse	SI	LD	Feed	LD	SD	Feed
Short circuiting	LI	SI	Feed	SI	LD	Feed
Arc re-ignition	SD	LI	Feed	LI	LI	Retract

*Note - LI - Large increase, LD - Large decrease, SI - Small increase, SD – Small decrease

2.3.1.2 Heat input calculation

The traditional formula (Equation Eq. (1)) for heat input calculation considers average heat input which does not accurately applies to newly developing welding techniques with pulsing involved. Therefore, it is advisable to consider instantaneous current and voltage values can provide precise heat input value as mentioned in Equation Eq .(2) [79,90]. It was observed that heat input calculated from Equation Eq. (1) can show an error up to -14.6, 16.6 and 9.1% for MIG/MAG Pulse (RapidArc) Transfer (DC) processes, MIG/MAG Pulse Transfer (DC) and MIG/MAG Short Arc Transfer (DC) respectively [95,96].

$$\text{Heat input (HE)} = \frac{\text{Voltage x current}}{\text{TS}} \quad \text{Eq. (1)}$$

$$Heat\ input\ (HE) = \frac{\eta \sum_{i=1}^{z} \frac{Ii * \text{V}i}{z}}{\text{TS}} \quad \text{Eq .(2)}$$

where Vi and Ii are instantaneous voltage and current values, TS is torch travel speed, z indicates the number of values considered and η is efficiency of the process. Following the later equation, researchers published heat input of four variants of CMT. Heat input varied as lowest for CMT-PADV process and highest for CMT which were 135.4 and 366.8 J/mm respectively. For CMT-P and CMT-ADV processes the values were 331.6 and 273.4 J/mm respectively [92] for identical wire diameter, torch travel speed and wire feed rate. The calculations suggest that as pulsing was increased, actual heat input decreased. Thus, actual heat inputs of CMT-PADV, CMT-ADV and CMT-P were 0.36, 0.74 and 0.9 times that of CMT respectively. With conventional dip metal transfer process, heat input normally remains above 400 J/mm; however, globular and spray transfer mode, heat input crosses 1000 J/mm (for wire diameter 1.2 mm). This explains the importance low heat input CMT process and the fact significantly impacts material properties in additive manufacturing.

2.3.1.3 Applications of cold metal transfer (CMT)

Owing to all these advantages of the process, CMT finds applications in numerous sectors. Due to low heat input, the process is satisfactorily applied for welding of aluminium sheets [97] considering minimal chances of burn through and warpage as well as for cladding of aluminium and Ni-based alloy [98–100] with low dilution rates. Improved mechanical properties by CMT application compared to GTAW and GMAW were reported by Elrefaey [101] for 7xxx aluminium alloys. Also, higher yield strength was reported by Gungor et al. [102] for 5xxx and 6xxx aluminium alloys welded with CMT than to any other welding process earlier studied. The new technique has claimed the ability to produce low volume of intermetallic compounds during dissimilar metal welding that has triggered dissimilar metallic weldings such as Mg-Al [103] and Al-Ni [104]. Expanding applications of CMT to thicker sections, Pickin and Young [97] quoted that the CMT-P produces a good quality weld with thin and thick sections. With proper adjustment of characteristic parameters metal transfer behaviour can be optimised for improved weld properties that can suitably be applied for additive manufacturing of aluminium, Wang et al. [93] deduced from the experimentation.

2.3.2 Forming appearance

To understand the characteristics of metal deposition in a layer deposition format and to avoid unwanted imperfections parametric study is of prime importance. This involves the study of effect of the change of process (welding) parameters on bead/layer geometry at different layer heights during part building and at bead/layer overlapping (in multi-layer multi-bead) as well as controlling of process (welding) parameters the start and end of layer deposition. The formation of heat sinks at the start counts for wrinkle formation and unrestrained flow of weld metal [44,82]. To tackle heat sink effect and to obtain a smooth part profile, insistence was given on developing layer start and end strategies. Increased torch travel speed and arc voltage compared to mean process parameters with same current at the arc striking and decreased torch travel speed at the arc stop has emerged an acceptable layer appearance technique

for the creation of open and closed loop WAAM objects as per Xiong et al. [85]. Also the authors reported that the technique supported in elimination of bulge at layer start and scallop at layer stop (refer Figure 2.13 and Figure 2.14). In one of the studies by Geng et al. [84] reported the minimum angle and curvature of radius viable with WAAM is 20º and 10mm respectively. Though the study highlights an important limitation, the minima are subjected to vary with different bead dimensions and filler metal alloy chemistries as the particular study was with bead width of 7.2mm.

Figure 2.13 Single-bead, multi-layer WAAM part without start and end control (adopted from [3]*).*

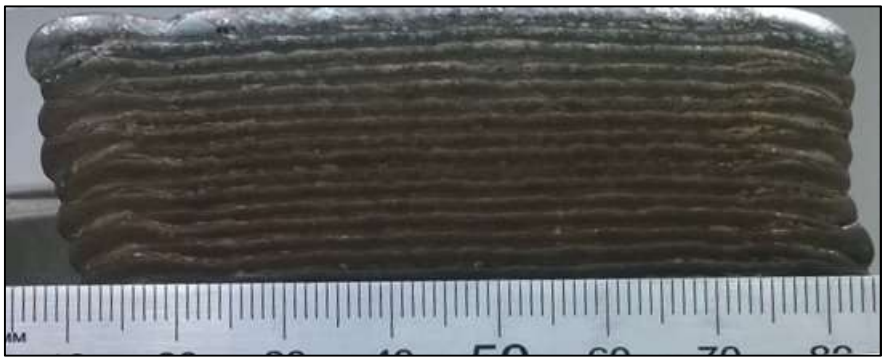

Figure 2.14 Single-bead, multi-layer WAAM part with controlled (adopted from [3]*).*

Ding et al. [83] studied multi-layer overlapping for determining the ideal distance between the two adjacent layers. The study concluded that the critical distance between the adjacent layers should be 0.738 times the bead width (w). The value is different from the historical value of 0.667w which suggests overlapping of one third of bead area. As this experimentation involves study of only one steel alloy, the results cannot assure its applicability to all metallic alloys because each alloy possesses unique material characteristics varying from wettability, viscosity, molten metal flowability and surface tension. Aluminium 4xxx series alloys reveal greater flowability than 5xxx series alloys. While considering the formed component's overall structural integrity penetration, lack of fusion and dilution need to be accounted before conclusion.

As stated by Adebayo et al. [105] the travel speed of welding torch should be restricted to 0.6 m/min to avoid the defect of humping which can affect WAAM productivity. Defect formation in WAAM can be well understood my practical studies, however, systematic statistical analysis of defects following Wei [106], Pradtl and Marangoni [107] numbers and Rayleigh's theory [108] could enhance the understanding. To avoid humping in WAAM the understanding of correlation between effect of volatile elements, surface tension, pitch formation, power density with power distribution and amplitude of humping is necessary. Reduction of backwards metallic flow during deposition using reactive shielding gases and suitable torch angle as described by Nguyen et al. [109] could be valued in WAAM development.

2.3.3 Interlayer rolling

A peculiar problem of formation of highly directional columnar β grains (as long as centimetre scale) along the build direction in Ti-6Al-4V alloy, particularly in directed energy deposition AM technique such as WAAM was reported by many investigators [38,39,70]; however, Szost et al. [70] notified that the epitaxially grown β grains in an opposite direction of heat flow from a partially melted substrate occurs with the absence of nucleation barrier and without undercooling with specific conditions such as presence of strong thermal gradient, matching chemistry of feed stock and substrate and the presence of completely liquefied filler metal. The phenomena is completely different opposed to that usually found in wrought products and affects directional strength [39].

The application of rollers with specific load conditions introducing strain at each layer was experimented as one of the solutions of this peculiar problem [20,21,38]. The instigation of dislocations through the rolling process at the wall surface was impressively successful in disturbing the epitaxial grain growth and produced grains with size down to 100 microns [20]. These newly formed small grains interrupt the grain growth in specific <001> direction by acting as a substrate for the successive depositing layer. Also, the recrystallisation temperature of β phase gets reduced due to instigation of plastic strain. Recrystallisation is a function of temperature; however, Martina et al. [21] claimed that the strain remained a primary affecting parameter instead temperature in this case. Therefore, recrystallisation can be accelerated by the introduction of higher dislocations through increased strain thus, loading pressure by roller forming smaller prior β grains. Additionally, compared to profiled and compound rollers, flat rollers found to provide better microstructural properties in WAAM part by the strain effect. Considering final shape and size of a WAAM product having different thicknesses, it is important to know the actual amount strain value that should be introduced at each layer. Researchers failed in reporting the actual amount of strain that was produced at the top of each rolled layer that helped in producing randomly oriented grains. Application of load not only improved the microstructure but also reduced the residual stresses in the forming component. A section 2.3.4 details the investigations carried out on the effects of application of rolling on residual stress reduction and redistribution in WAAM. An effect of interlayer rolling on WAAM of aluminium is detailed in section 2.5.

2.3.4 Residual stress

Residual stresses arises due to contraction of molten metal during solidification when deposited on a substrate. Contraction of liquid metal creates tensile stresses in a deposit and thus equivalent compressive stresses in the substrate [65]. The effect is remarkable in additive manufacturing in which the deposition part successively adds up tensile stresses and invariably balances compressive stresses. A deposition of metal in a multi-layer format forces previously deposited metal to undergo stress accumulation and relaxation cycles.

While considering the WAAM system, statistical, analytical and computational study of residual stress distribution in formed WAAM part and substrate is necessary. A large thermal stresses are developed in a WAAM deposit and balancing in substrate due to periodical contraction and expansion of deposited metal as the result of addition of noticeable amount of heat during new metal deposition in a layer format. To understand the residual stress distribution and to reduce its magnitude in a WAAM part, the

generation of optimum tool path and build strategy through computer simulation has been exercised [32,62–66,68,71,75,110–113].

Alimardani et al. [112] studied the importance of preheating that not only supported in reducing the overall thermal stresses but also the formation of steady-state molten metal pool. In the modelling of AM part formation by Ti-6Al-4V powder and electron beam, Vostola et al. [71] described an ineffectiveness of change of base parameters such as electron beam size, beam power and scanning speed on the residual stress reduction; however, authors found that every increase of 50°C in preheating temperature of a powder bed reduces residual stresses by around 20%. Mughal et al. [63] highlighted the fact that during continuous metal deposition, preheat supported in reducing the distortion. Further, authors reported the prominence of interpass cooling as during continuous metal deposition substrate temperature increases which reduces the process efficiency as well as imparts dimensional losses and poor surface finish to the forming part. According to their study, different deposition sequences have limited effect on deflection, however, it alters residual stress distribution. Further, authors mentioned that heat sink and interpass time are the main variables in related to the deformation of AM part.

Lei et al. [113] studied the effect of different interlayer dwell times on temperature variation. In multilayer metal deposition in round shape, interlayer dwell time became invariant with respect to the maximum temperature gradient after fourth layer, however, in continuous deposition mode gradient decreases steadily. In one of the studies on residual stress formation and distribution, Zhao et al. [65] noted that for the first layer deposition on the substrate, at the deposit region tensile stresses developed due to liquid metal solidification shrinkage and corresponding balancing compressive stresses appeared at the substrate away from the deposit. In multilayer approach, it was found that the heat treating effect of rear layer deposition on fore layer released tensile stresses and overall stress found reducing with increasing number of layers. Simultaneously, increase in substrate temperature also reduced tensile stresses; however, authors noticed that overall and peak residual stress increased by increasing interlayer idle time as it allowed more time for deposit and substrate to cool increasing contraction and expansion cycles for deposit and substrate. Highest stress was found at the top layer which did not undergo the heat treating effect and also peak stress dependent upon the interlayer idle time, hence interlayer temperature. Li et al. [75] studied stress distribution in circular WAAM part in which they restated the stress release effect of rear layer on fore layers along with decrease of overall stresses with increase of number of layers. Describing the nature of the stresses, further authors found dominance of tensile longitudinal stresses compared to transverse and axial stresses. High stress fluctuations were reported at the arc start and arc end points, however, stress fluctuations were smaller at midpoints. In multilayer single pass modelling approach, Zhao et al. [111] confirmed the effects of stress relaxation by deposition of next layer. Maximum stress at the point found to be decreasing as the number of layers were increasing. Authors reported the central part of deposition had relatively stable stress condition compared to arc start and end parts and last layer found dominating effect on deposit's overall stress condition. Importantly, metal deposition in same direction showed increased stress and plastic strain than reversed metal deposition, hence, parameters optimisation found to have control on residual stress and plastic strain.

On the contrary, Ding et al. [64] reported uniform stress distribution with a minute effect of preceding layer on following layers. Acting bending moment and bending distortion after unclamping had

appreciable influence on the stress redistribution at the interface than at the top of the wall. In another study using neutron diffraction, residual stresses as high as close to yield stress of a material were found to Ghasri-Khouzani et al. [74]. Also researchers reported the importance of part height where maximum stress fluctuation was observed in 5mm thick samples than 10 mm. Brown et al. [72] also confirmed the presence of high tensile residual stresses in longitudinal direction greater than the yield point of the materials. In experimental study Colegrove et al. [38] highlighted the occurrence highest tensile residual stress value around 500MPa at the interface region for Ti-6Al-4V alloy. Further, authors reported the stress relaxation and redistribution after unclamping. Compressive plastic strain in the deposit was held responsible for upward bending that relaxed tensile stresses at the top of the deposit, however, increased stress was reported at the bottom of the substrate. Somashekara et al. [68] studied the effect of different deposition patterns on residual stress evolution by finite elemental method. Authors disclosed the critical role of temperature distribution in residual stress evolution for different patterns studied. During deposition tensile residual stresses at the top of the substrate were found much lower than bottom side. Conversely, after deposition major changeover was observed.

To eliminate distortion and to balance residual stresses, creation of two WAAM objects on both sides of a substrate is the back-to-back building strategy proposed by Williams et al. [45]. Also, to equally distribute arc heat on both sides of predefined plane of the substrate, symmetrical building can be an approach. Certainly, for the applicability of these approaches validation through practical results and computer simulation is highly recommended. Researcher [45,47,50] proposed simplified operation of metal deposition sequence such as corners, junctions and cross-overs that can be produced by WAAM part with minimum tool movement, defects and reduced residual stresses saving overall operation time. Kazanas et al. [46] demonstrated the possibility of formation of horizontal WAAM walls by varying torch angels from vertical to horizontal. Thus, if suitable torch angle and metal deposition parameters are maintained then using WAAM, closed hollow 3D shapes can be manufactured.

Researchers applied interlayer rolling for residual stress reduction because deposits revealed majority of tensile stresses and counter compressive stresses could be imposed by rolling. The formed high tensile stresses the longitudinal direction and implied distortion were appreciably reduced by this process. Different types of rolling methods were investigated such as application of various loads varying as 25kN, 50kN and 75kN, rolling after each layer deposition and rolling after every 4 layers and use of different profiled rollers such as slotted and profiled roller and so on [66,69]. Martina et al. [73] performed contour and neutron diffraction experimentation on Ti-6Al-4V. It was observed that maximum stress of around 500 MPa at the interface region were reduced drastically up to 200 MPa after rolling with 75kN load. The top layer of the deposit showed compressive stresses of the order of 250 MPa in unrolled sample and stress value rose up to 400MPa after rolling with 75kN load. Authors further reported that application of rolling appreciably reduced the distortion and alternation in part geometry after rolling process. Colegrove et al. [66] reported that the slotted rollers provided better results in reducing lateral deformation and residual stresses compared with profiled rollers. Also, in order to reduce the production time researchers applied rolling after every 4 layers which revealed no appreciable difference in the results when rolling was applied for each deposited layer. Colegrove et al. [69] while working on Ti alloy emphasised that the rolling process which reduces lateral deformation such as slotted rollers and side roller effectively reduces residual stresses.

2.3.5 Process variation

For higher deposition rate, application of two or more feed stock wires for WAAM part formation has been another area of interest for many industries. In the similar line, along with twin-wire GMAW [51] application of GMAW and DE-GMAW was studied [52,54] for the benefit of higher deposition rate. The latter process that is GMAW + GTAW was found to be beneficial with respect to lower heat input, reduced average temperature and smaller dimensions and volume of liquid weld pool without compromising the production rate. As can be predicted from the constitutional supercooling theory, highly directional columnar and cellular grains can be foreseen from relatively less energy input for the same volume of filler metal melting (thus producing forced cooling effect) was the unattended part of the study that could be the topic of interest for materials scientist [114].

The advancement of WAAM can be benefited by the study of mechanical and microstructural properties of DE-GMAW and cold metal transfer (CMT). Before manufacturing and producing operational functionally graded parts studied by many researchers [51,53,57], a deep understanding of filler metal's fundamental behaviour under single electric arc producing widely different compositions is essential. The hybrid manufacturing possesses advantages such as attractive cost and real time reaping during manufacturing that involves the concept of addition of metal by arc and subsequent removal of part of it forming the near-net-shape object with a desired surface finish, however, the concept is still underdeveloped. The inconsistency in shape and size of an intended object is the challenging part tool design and movement in hybrid manufacturing.

2.4 Wire arc additive manufacturing (WAAM) advantages and challenges

2.4.1 Cost consideration

When powder is considered steel and titanium material cost £60-93 and £ 264-685 kg^{-1} respectively whereas wire feed costs £ 2-15 kg^{-1} and £ 97-240 kg^{-1} for the same materials [2]. Thus, the cost difference between the wire and powder feed makes wire based method 2-50 times more economically efficient than powder based technique. Through extensive calculations researches showed that formed Ti-6Al-4V components using WAAM could be 7-69% cheaper than produced by conventional routes [115]; however, when aluminium and steel are considered, low cost metal compared to Ti-6Al-4V, similar cost advantage cannot be guaranteed. When manufactured from feed stock, BTF-ratio of 30 is very common for manufacturing intricate aero-engine parts using conventional methods. For the same material, impressive material saving was observed with BTF ratio as low as 1.2 when the same parts were manufactured using WAAM [67].

2.4.2 Deposition rate

Researchers achieved 10 kg/h deposition rate for steel material in WAAM type deposition [20,67] which is almost 16 times to than powder based methods which possess deposition rate of 600 g/h [116]. Difference in the shape of single bead is the fundamental reason. WAAM process revealed bead height of 1-2 mm [117,118] that can be increased along with the deposition rate whereas powder based process demonstrated bead thickness from few microns to up to maximum 1 mm [119]. It is critical to control a large liquid weld pool, though the higher deposition rate is one of the attractive features of WAAM compared with low deposition rate processes. Solidification incurred in WAAM is not largely different

than solidification observed on conventional casting process where different cooling rates are prominent at core and periphery.

The increase in surface roughness and process instability by uncontrolled deposition of high volume metal can be avoided with optimising wire feed rate which will favour high production rate. To restrict BTF ratio below 1.5, the deposition rate needs to be restricted below 1 kg/h and 4 kg/h for titanium and aluminium alloys & steels respectively as demonstrated by Williams et al. [67]. Thus, it can be inferred that machining is unavoidable for WAAM part produced using deposition rates higher than the mentioned above for respective materials. Hence, in consideration of strict surface roughness, WAAM process cannot be the final operation.

2.4.3 Operation / metal deposition strategy

Deposited metal and substrate experiences multiple thermal cycles due to addition of metal in successive layer deposition. Impose of heat discharge causes partial liquefaction and heat treatment of earlier deposited layers and also enlarges the non-isotherm heat treat effect below four to five layers of the deposit. The process heat input and material thermo-physical properties affect this phenomena. Thermal cycles enforce cyclic expansion and contraction of a deposit and substrate resulting in generation of residual stresses. Withers and Bhadeshia [120,121] addressed the formation of residual stresses, its classification, methods of measurements and effect on performance in a formed component. To understand the effect of interlayer rolling, Colegrove et al. [38] applied one of the residual stress measurement methods, neutron diffraction recommended by Withers and Bhadeshia [120], to an arc based layer type deposition of Ti-6Al-4V alloys.

While the sample was clamped in without rolling condition, the wall formed by WAAM revealed approximately 500 MPa tensile residual stresses which was equilibrated by compressive stresses in substrate. On the contrary, tensile stresses in the WAAM wall was relieved up to certain extend by upward bending of a substrate due to acting compressive plastic strain in a formed wall. Surprisingly, massive reduction in tensile residual stresses (down up to 150 MPa) was observed after interlayer rolling. It was also confirmed from the results that stress generation during the arc deposition was comparatively greater than stress relaxation as the stress was not completely eliminated after rolling. During the production of WAAM part, the upwad distortion produced in base plate, when measured at the edge can extends up to 15 mm (refer Figure 2.15). In the similar line, Colegrove et al. [38] reported the base plate distortion of 7 mm.

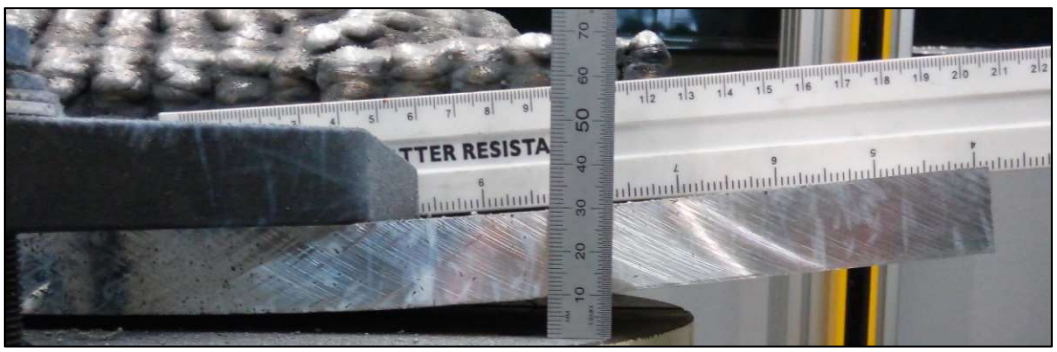

Figure 2.15 Large distortion produced due to multiple thermal cycles during production of the WAAM object (adopted from [3]*).*

The chamber size restricts the overall dimensions of an object in laser and electron based processes while WAAM does not impose any dimensional limits on forming objects. Thus, for the production of medium to large scale parts WAAM is the suitable candidate owing to its capability of theoretically unlimited metal deposition and high deposition rate. On the other hand, increased surface roughness and larger bead volumes compared with powder based processes (25 μm [116]) limit its applications for production of low and medium scaled complex parts. Parts produced by WAAM method, showed lower mechanical properties than the wrought products of similar alloy chemistry as can be observed from Table 2.3. Directional tensile properties are commonly seen WAAM products that commonly depends upon pattern of metal deposition followed. Microstructure and grain orientation found to have great impact in directional mechanical properties making formed part stronger is one direction compared to other.

Table 2.3 Comparison of tensile properties of WAAM parts (in longitudinal direction of build) with comparable wrought/filler wire (adopted from [3]*).*

Alloy	**Wrought product / filler wire**			**WAAM product**			**Reported by**
	Yield strength (MPa)	Ultimate tensile strength (MPa)	Elong-ation (%)	Yield strength (MPa)	Ultimate tensile strength (MPa)	Elong-ation (%)	
Titanium (Ti-6Al-4V)	950	1030	11	870	920	12	[39]
Steel (ER70S)	448	480	22	402 (max)	-	-	[122]
Stainless Steel (316L)	452	520	30	422 (max)	-	-	
Bainitic steel	1230	-	11	1010	-	6	[123]
Stainless steel (304)	552	241	55	235	678	55.6	[124,125]

2.5 State-of-the-art of Wire arc additive manufacturing (WAAM) of aluminium

2.5.1 Application of gas tungsten arc welding (GTAW)

Various studies were followed through developing a background recognised as early need of capability growth with regards WAAM of aluminium. Suitability of varying polarity GTAW was discussed by Wang et al. [126] as one of the first studies on WAAM of 4043 aluminium. As result of microstructural study, researchers reported presence of coarse cellular/columnar grains at the bottom and middle and fine dendritic structure at the top of the formed wall. Hence, increase in hardness at the top was notified compared to bottom through middle section. Afterwards, rarely any study was aimed at the application of GTAW for WAAM part production specifically for aluminium because the advantage of high deposition and other advantages offered by GMAW variant – CMT,

2.5.2 Porosity

In non-heat treatable and heat treatable alloys, porosity formation is closely allied to the presence of allying elements along with primary influencer hydrogen. It was argued that the pore formation in heat treatable alloy is closely linked with the nucleation and dissolution of eutectic phases such as Al_2Cu in 2xxx series during alloy cooling and heating respectively [90]. In heat treatable alloys, formation of large pores was prevented due to detachment and floatation by inter-dendritic spaces, causing formation of small pores varying from 5 to 20 µm. After heat treatment, dissolution of the eutectic phase created vacant sites resulting in a large growth in the numbers of small pores as illustrated in Table 2.4. In non-heat treatable alloy, pore formation was caused due to the effect of alloying elements on metal solidification and the presence of volatile materials Mg.

Table 2.4 Effect of different metal deposition conditions and different loads of inter-layer rolling on porosity in aluminium alloys (adopted from [3]*).*

Filler wire	Condition	Mode of metal transfer	Pore count	Pore diameter	Length/area of consideration for pore count	Reported by
2319	AD	CMT	155	10-50µm	15mm length	[78]
			42	50-100µm		
			25	> 100µm		
		CMTP	21	10-50µm		
			7	50-100µm		
			0	> 100µm		
		CMTADV	17	10-50µm		
			0	> 50 µm		
		CMTPADV	0	> 10µm		
	AD	CMTPADV	614	13.5µm	120mm^2	[89]
	R15		192	12.5µm		
	R30		5	8.8µm		
	HT		2001	15.5µm		
	AD block structure	CMTP	180	15µm	225mm^2	[79]
			40	25µm		
			15	35µm		
	AD wall structure		110	15µm		
			50	25µm		

			100	35µm		
			134	> 35µm		
	AD block structure	CMTADV	60	15µm		
			35	25µm		
			11	35µm		
	AD wall structure		120	15µm		
			90	25µm		
			30	35µm		
			85	> 35µm		
5087	AD	CMTP	454	25.1µm	120mm^2	[90]
	R15		336	33.2µm		
	R30		11	13µm		
	HT		359	9.6µm		

2.5.2.1 Porosity reduction using cold metal transfer (CMT) technique

There has been a close relationship between porosity formation in aluminium with heat input, weld penetration, formed grain's size and shape and dendrite growth of the same [78,92]. The effects of different CMT techniques namely CMT-PADV, CMT-ADV, CMT-P and conventional CMT on porosity formation was compared by Cong et al. [78] (Table 2.4 denotes comparison of pore size distribution). In conventional CMT, the hydrogen escape was prevented due to higher heat input, formed coarse columnar grains and greater penetration [78,92]. CMT mode revealed more pores with size ranging from 10 to >100µm. It was proven that formation of large pores with size >100 µm is due to the fusion of small pores into large pores.

Decrease in escape distance for hydrogen due to less penetration witnessed by CMT-P compared to CMT, supported the evidence of lesser number of pores [92]. Also, the smaller grains size with the CMT-P process was helped in restricting pores size below 100µm. Oxide cleaning effect due to alternating polarities, lower heat input, formed refined equiaxed grains and shallower penetration in CMT-ADV mode significantly supported hydrogen escape and revealed no pore with size >50 µm. An impressive results were shown by CMT-PADV process where no pores found with size greater than 10µm. This techniques combined the effects of CMT-ADV and CMT-P processes forming finest equiaxed grain structure and lowest dilution [78,92].

A block structure revealed lesser number of pores compared to wall structure (refer Table 2.4) when formed from CMT-P and CMT-ADV techniques [79]. Large pores with size >50 µm were present in wall structure while in block structure no large pores were found. In addition, lower heat input CMT-ADV showed lower number of pores than relatively higher heat input CMT-P in a block structure. In

wall structure, heat conduction and extraction is possible only through underlying layers. In the contrary, heat conduction and extraction is possible by the material present adjacent to a layer in the block supports for raising the cooling rate. Hence, reduced porosity is the result of formation of finer microstructure in a block structure when compared to the wall structure.

2.5.2.2 Porosity reduction by interlayer rolling

A pore structure gets affected to a great extent by the application of pressure using rolls onto the WAAM layer. The force is produced by rolling and thus causes formation of number of dislocations and vacancies provide favourable sites for the absorption of atomic hydrogen. Effect of interlayer rolling and heat treatment on porosity formation and distribution in non-heat treatable and heat treatable aluminium alloys was thoroughly studied by Gu et al. [90]. A massive reduction in number of pores was evidenced after application of interlayer rolling with 15, 30 and 45 kN load. Compared to unrolled condition, for heat treatable aluminium alloy, pore numbers were reduced by 68.7% and 99.1% and pore area was found to be reduced by 83.5% and 97.2% after 15 and 30 kN interlayer rolling respectively. For non-heat treatable aluminium alloy, the reduction in numbers was 25.9% and 97.5% and reduction in area was 73.9% and 97% for the similar interlayer rolling conditions (refer Table 2.4).

2.5.3 Grain structure

The interlayer rolling was not only reduced the porosity but also greatly affected grain structure. Effect of loading condition on the grain orientation and grain size is illustrated in graphical format in Figure 2.16. It can be witnessed from Figure 2.16 that the increasing rolling load condition produces small sized grains with low mis-orientation angle [89,91]. For non-heat treatable 5087 alloy, without rolling condition showed only 7% grains with size smaller than 5µm whereas grains larger than 50µm were around 40%. Total fraction of small sized grains (less than 5µm) gradually found to be increased with increasing loading conditions approaching 16%, 34% and 49% for 15, 30 and 45 kN respectively. On the other hand, large sized grains were completely removed after application of 45 kN load. The condition and trend variation was not different for precipitation hardenable Al-Cu alloy. Without rolled samples showed 13% small grains with size less than 5µm that increased to 77% after application of rolling with 45 kN load.

On the similar line, there was increase in the fraction of small grain boundaries as rolling load increased. This confirmed that this increase was at an expense of and splitting of large grains. After application of 45kN rolling load, fraction of small grains were found more than 70% of the considered total volume for 2219 and 5087 alloys which was around 6% and 20% in as deposited condition respectively. Difference between the microstructure of block and wall WAAM structures manufactured using CMT-P and CMT-ADV techniques was studied by Cong et al. [79] pictorially presented in Figure 2.17. Bottom area of the wall structure showed columnar grains that might be attributed to the heat high heat extraction rate encountered near the substrate. As per authors understanding, top and middle part of the wall that experienced reduced heat extraction rate than bottom revealed equiaxed dendritic and equiaxed non-dendritic grains respectively. Cellular grains were reported present between equiaxed and columnar grains for CMT-ADV technique. For CMT-P process, block structure showed microstructural variation within a single layer. Equiaxed non-dendritic structure at centre and columnar grains at outer part was observed due to increased heat extraction. For CMT-ADV, outer part of a layer revealed equiaxed

dendrites. The outcomes of CMT deposition are in coordination with the results from VP-GTAW [126] as discussed in Application of GTAW.

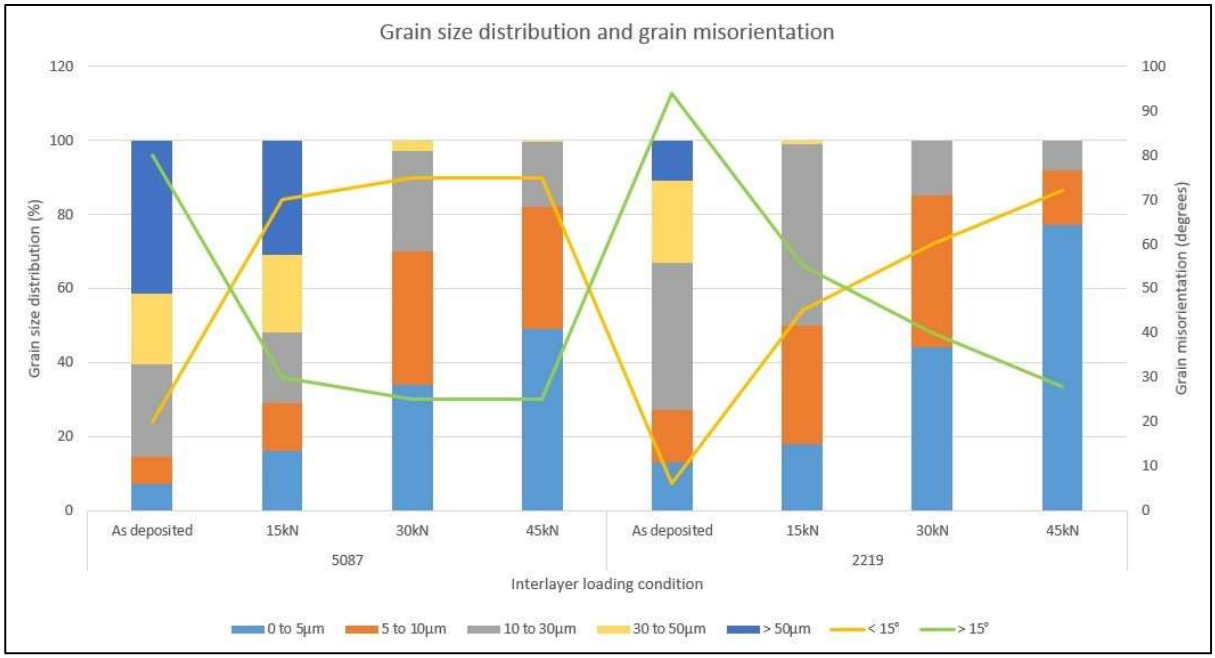

Figure 2.16 Effect of different interlayer rolling conditions on grain size distribution and grain orientation in 5087 and 2219 alloys (adopted from [3]*).*

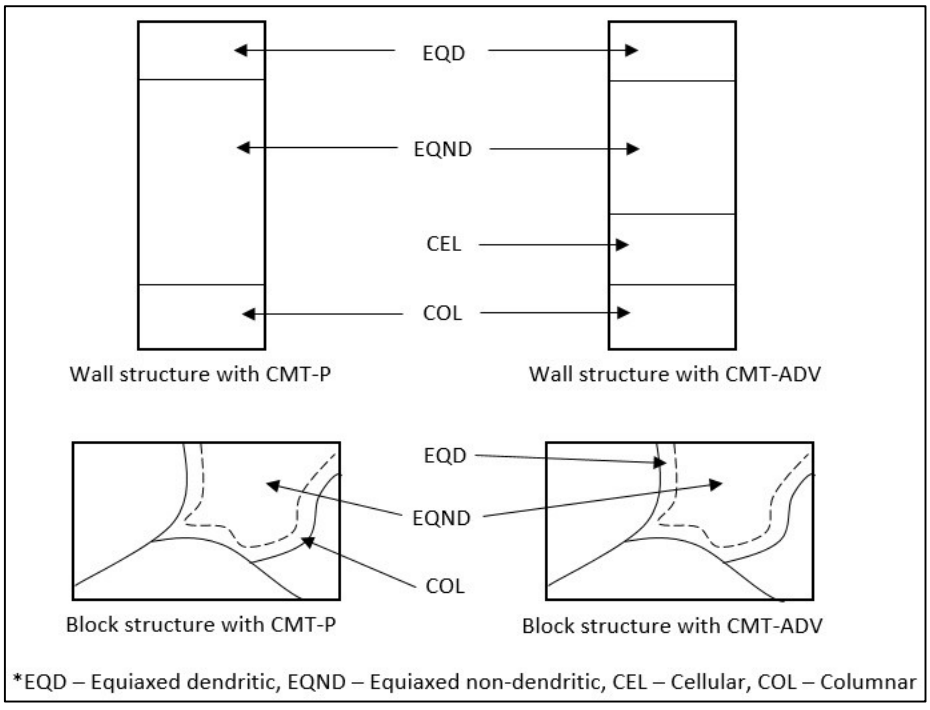

Figure 2.17 Schematic of microstructure variation in wall and block structure using CMT-P and CMT-ADV processes (adopted from [3]*).*

Apart from the CMT technique, Hargar et al. [16] experimented with short pulse mode of metal transfer for depositing AA5183. Authors reported different grain structure between various regions, however, the dominant columnar grains at the fusion line. Reheating effect during deposition of subsequent layers

were held responsible for formation of equiaxed grains. Also authors mentioned the presence of equiaxed grains closer to the central part of individual bead. Interestingly, authors reported presence of intergranular crack supporting the presence of high Mg content.

2.5.4 Tensile properties and micro hardness

Tensile properties of a WAAM part experienced an appreciable enhancement by the application of a rolling process that supported in introduction of large number of dislocations and small sized grains. Dislocations and strains might get released by the recrystallization in a cyclic heating process; however this is not sufficient to neutralize the total effect prompted by rolling and hence accountable density of dislocations can be found in interlayer rolled part [90] favouring increment in the tensile strength. The effect of increment in interlayer rolling load condition on the tensile strengths and elongation of non heat-treatable and heat treatable aluminium alloys is illustrated in Table 2.5. There is a linear relationship can be seen between increase in tensile strength with rolling loads.

Table 2.5 Tensile properties of different aluminium alloys based on different testing conditions (adopted from [3]*).*

Filler wire	**Condition**	**YS (MPa)**	**UTS (MPa)**	**Percentage Elongation**	**Reported by**
5087	As deposited	142	291	22.5	Gu et al. [91]
	Rolled 15kN	169	320	22	
	Rolled 30kN	149	311	21	
	Rolled 45kN	200	344	20	
	Wrought (5083-O)	145	290	22	ASM Vol.2 [127]
2024	As deposited	175	290	12	Fixter et al. [128]
	Rolled 45kN	315	375	8	
	T4	335	465	15	
	T6	415	505	8	
	Rolled 45kN + T6	415	500	11	
	Wrought (2024-T62)	345	440	5	ASM Vol.2 [127]
2319	As deposited	130	260	15	Gu et al. [89]
	Rolled 15kN	140	270	14.5	

	Rolled 30kN	185	285	11	
	Rolled 45kN	245	315	9	
	T6	315	465	13	
	Rolled 45kN + T6	310	460	16	
	Wrought (2219-T62)	220	340	7	ASM Vol.2 [127]
2319	Vertical	106	258	15.5	Gu et al. [129]
	Horizontal	114	263	18.3	
Al-6Mg	CMT	-	320	-	Zhang et al. [80]
	CMTP	-	285	-	
	VP-CMT	-	325	-	
5183	As deposited	145	293	20	Horgar et al. [16]

Eutectic phases were produced in heat treatment alloys due to repeated thermal cycles corresponding to the annealing and aging heat treatment; however, these precipitates, due to their less numbers and increased in size [89], found less active in the strength improvement due to reduced resistance to dislocation movement. Depending upon the applied load during loading, the formed eutectics disintegrated into fragments. Uniform distribution of fragmented eutectics after heat treatment with fined smaller size grains formation [89], greatly enhanced tensile strengths. Interestingly comparable tensile properties were shown by rolled + heat treated and heat treated samples; however the size of grain in rolled specimen was found approximately half of the specimens with no rolling which was attributed to the disintegration of coarse grains into sub-grains due to strain induced by the roller (refer Table 2.5 and section Grain structure). Major strengthening mechanisms in case of non-heat treatable 5087 alloy are sub-grains produced by rolling load (see section 2.5.2), grain refinement and high-density dislocations. An interesting result by Geng et al. [84] described isotropy in tensile strengths/properties when WAAM of aluminium specimens were tested along the perpendicular and parallel directions of deposition. On the contrary, when specimens were tested along perpendicular and parallel directions of the grain orientation, anisotropy was observed. Tensile strength along the parallel direction of grain orientation was lesser than along transverse direction. The important outcome has be taken account for designing a part for real life application.

As presumed for, a linear relationship between rolling load and hardness can be seen irrespective of type of alloy in Figure 2.18. For alloy 5083, experimented by Gu et al. [91], rolling loads 45, 30 and 15 kN increased hardness of WAAM part by 40, 27 and 14.8% respectively compared with as-deposited condition. For the same rolling load criteria, the incremental values were 52.8, 33 and 14.2% while

considering 2319 filler wire [129]. This implies that in the close future there are high chances of replacing conventional wrought products with the WAAM products as it is proven that WAAM parts possess similar or higher mechanical properties than respective wrought products (see Table 2.5) when produced with an appropriate operational techniques.

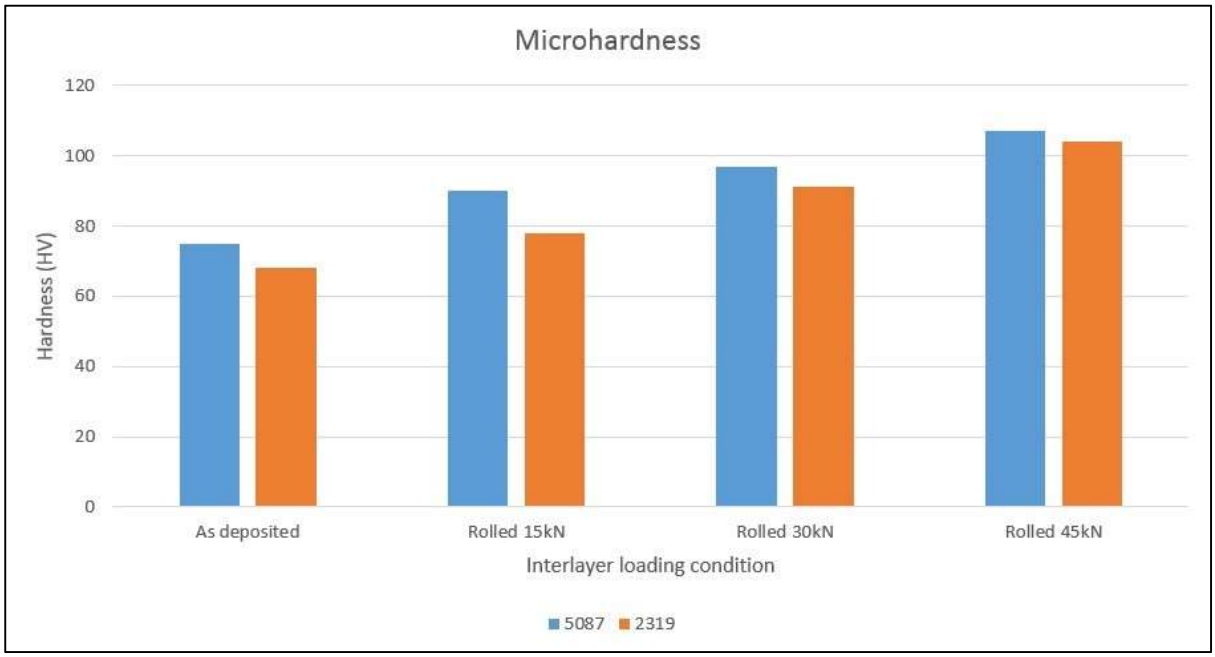

Figure 2.18 Effect of interlayer rolling with different loads on microhardness (adopted from [3]*).*

2.5.5 Chemical composition

Change in composition of a feed stock wire becomes a vital factor to reshape the grain structure in accordance with the new solidification pattern observe in WAAM and to tackle metallurgical challenges. Recently developed corrosion resistant AlMgSc-based Scalmalloy [130] is one of the examples that eliminates the issues linked with the presence of Mg. It reduces elemental loss that is vaporisation of Mg, wettability and spinel formation (MgAl2O4). Moreover, compared to titanium, Scalmalloy shows appreciably good mechanical properties such as specific strength and high ductility.

Fixter et al. [128] studied Mg dependent crack susceptibility for 2xxx series of aluminium alloy for WAAM. Astonishingly, authors revealed that unweldable composition of 2024 wire was suitable for WAAM. From Table 2.5 it is clear that for alloys composition 2024 tensile properties were comparable with wrought products. This emphasises the fact that while choosing a feed stock wire weldability cannot be the guiding criteria. For applicability of other metallic alloys for WAAM, future experimental studies are recommended.

2.5.6 Single-step forming

Though the interlayer-rolling has positive influence on WAAM of aluminium, the process reflects downsides such as tough to apply to a block structure and the process is very slow as metal deposition stops during rolling operation. To overcome the challenges, an idea of single-step forming such as forging and bending [131] were experimented. The researchers supplied supportive outcomes for the application of single step forming operation eliminating porosity and required strain hardening effect

through computer simulation. Likewise mentioned earlier, it is important to study its practical applicability of post processing to the WAAM part.

2.6 Knowledge gap

WAAM process can be considered as a next-generation economical alternative for aluminium products used in aerospace and automobile sectors produced through conventional techniques. A variant of conventional GMAW process called cold metal transfer (CMT), has been currently applied suitably for production of WAAM part made of aluminium. A prominent issue of porosity formation during aluminium deposition during WAAM part production was appreciably addressed and tackled with the application of pulsed advanced CMT and interlayer rolling. Metallurgical phase formation and other change consideration during heat and non-heat treatable aluminium alloys solidification during thin and thick wall formation through WAAM is an important part of WAAM development. A good WAAMability of unweldable aluminium alloy proved the fact that metallurgical study is highly recommended. There is still a wide knowledge gap regarding the understanding of formation and behaviour of residual stresses and distortion and uneven shrinkage in WAAM. Also, residual stresses in closed loop structures such as circular shape and open structures such as a straight or curved wall could be different and imperative to study if WAAM part of different shapes need to be produced. Better understanding of effects of heat maintenance techniques including heat input, interlayer-temperature, interlayer dwell time, preheating, post heating on porosity formation and its correlation with hydrogen dissolution, microstructure, and mechanical properties are some of the prime areas of industry interest. Interlayer-rolling remains a time consuming process, thus an alternative to such as single step forming for aluminium WAAM could be an important point with respect to the productivity. Therefore, overall control on deposition parameters and post deposition operations for controlling microstructure, mechanical properties defines the overall integrity of WAAM aluminium component. Comparable mechanical properties to wrought products, economical advantages, less restrictions on forming part size and shape, necessity of relatively less complex and expensive instrument and simple operation are the benefits of WAAM that can be defining the future of industry.

2.7 Welding terminologies and Wire arc additive manufacturing (WAAM)

Over recent years there seems to be a constant difference amongst researchers and specification terminology about the semantics and meaning associated with the application of some of those terminologies which are being commonly used within the welding area, these being mainly associated with fusion welding and bonding terms, in addition to the meaning of cladding, buttering, build-up and hard facing. The reason behind this misconception has arisen from the manufacturing processes that have been used in the welding field for many, now emerging and finding their way into this newly defined process known as WAAM. The inventors and users of the WAAM technique are trying to apply the same well known welding processes for different functions in a distinct fashion that can give rise to the cause of common disagreement amongst researchers. One of the perceived reasons for this discord could be the unavailability of standards and guidelines pertaining to the immaturity and application of the WAAM process compared with the established and well known welding sector. Thus there is need of establishing standards and guidelines on common ground for investors for intended research in WAAM incorporating all the aspects of WAAM.

Identifying the need for standardisation within the ever developing AM landscape, the ASTM committee has been assigned an edict for the development of AM guidelines encompassing several key strands of AM, and through congregating research work worldwide establish a common language and terminology. Based on research completed by the ASTM F42 committee in assessing those generic and indigenous terms, they have established some guidelines and currently many others are under development. The committee has defined AM, by focusing on its basics as *'process of joining materials to make parts from 3D model data, usually layer upon layer as opposed to subtractive manufacturing and formative manufacturing methodologies'*[1]. The definition is applicable to all the process that are categorised under AM. Therefore the same definition is applicable to WAAM which is identified as sub-process of AM under the DED category.

There are many available standard guidelines that have defined the welding operation in their own perspectives. AWS standard defines the welding operation as *'a joining process producing coalescence of materials by heating them to the welding temperature with or without the application of pressure or by the application of pressure alone and with or without the use of filler metal'*[132]. Comparing both the definitions of AM and welding it can be concluded that all the welding processes cannot befallen under AM unless modified for illustration firstly an autogenous welding process. A classic example is an autogenous TIG welding process. The definition of AM describes a process of formation of components by successive deposition of material but that cannot be the case of autogenous welding which does not use any filler material to form a defined shape. Secondly manual welding process such as SMAW that does not include any computerised data to guide welding electrode for specific weld deposition pattern that finally forms an object.

AWS [132] clarifies cladding as a process of surfacing performed to achieve required corrosion or heat resistance. ASME [133] defines the same function with different terminology as corrosion resistant overlay that may have one or more layers of weld deposition. Initially both the renowned bodies clearly notifies cladding and overlay as a welding process that is only restricted to the surface of an object. Later one and other elucidates the purpose of the surface phenomena that is only restricted to the corrosion or heat resistance enhancement. Along with this, ASME also describes corrosion resistant overlay as non-structural part of the object that can be deposited over and above the minimum thickness of the base material thus the thickness of overlay is not considered in the final thickness measurement. This distinctly contradicts to the definition of AM put forth by ASTM that mandates the formation of complete object by material deposition which can never be restrained to only a surface.

Further as per AWS interpretation [132], a weld build-up is a surfacing operation performed to achieve required dimensions. ASME [133] formulates weld build-up as a process of deposition of weld metal of compatible chemistry to restore the design thickness or structural integrity. The objective of weld build-up is rather exclusively associated with the achievement of required product dimensions which relates to the surface operation than any property enhancement of a product. The other angle to the understanding of this specific term can be deposition of weld metal over an object in order to complete the required shape in case of damage caused by any means such as gouging done on base metal near a welding seam to remove spatter that has initiated a reduced thickness area in the base metal. Thus as per ASME any repairing operation either on parent metal or already deposited weld metal falls under the category of weld build-up where in addition ASM restrict the same operation only at the surface.

Thus from understanding of the definitions recognised by acclaimed bodies weld metal build-up is deposition as weld metal to carry out repair cannot be treated as AM process.

Another welding operation that frequently being practiced during production is buttering. AWS [132] acknowledged buttering term in the form of surfacing variation of welding operation that is performed in order to achieve metallurgical compatibility. Metallurgical compatibility term highlights the fact that buttering operation is more inclined to achieve same composition or a composition that is suitable for producing metallurgically sound joint. ASME [133] describes buttering as a weld deposition process on joining parts that is being carried out before preparation of weld joints. The purpose of buttering is to provide suitable metallurgical transition of weld deposit that assists further weld deposition. In illustration for joining steel to stainless steel, it is recommended that a layer of stainless steel consumable compatible to stainless steel part to be joined should be applied on the joining face of the steel before performing final welding operation by stainless steel consumable. This operation focusses on the metallurgical compatibility of the final joint with smooth transmission of composition throughout the weld. Though ASTM definition of AM does not explicitly discuss about material bonding characteristics and multi material use but varied material combination in single object has been widely accepted as one the major advantages of the AM process. Surprisingly this fact is also applicable to WAAM technique where weld metal deposition to form an object of different composition is possible. The possibility of use of diversified materials inevitably makes AM and buttering complementary techniques however AM possesses capability of formation of single object while buttering is confined only to the surface operation to assist a joining process.

Hard facing is a process of surfacing in which wear resistance of a component is raised by deposition of hard material only at a surface by welding, portrayed by AWS [132] and ASME [133]. Hard facing could be thought as cladding operation or an overlay, as discussed above, with only disparity of purpose of surfacing. Similarly as argued previously hard facing along with corrosion resistant overlay is excluded from the thickness measurement. AM is all about formation of entire product instead of focusing on enhancement of any particular property such as wear and corrosion resistance. Every layer deposited in AM conclusively considered in the dimensional measurement of the formed object.

Definitively, though WAAM technique uses traditionally used welding processes such as GMAW, GTAW and others, the WAAM technique is noticeably different (except basics of welding operation) from familiar welding operations in terms of application. Apparently AM is something that stands for beyond the material property enhancement and dimensional control by welding. In addition AM needs 3D model data that is most likely absent while performing any of the above discussed operations. From the discussion conclusion can be drawn out that along with evolution of WAAM technique and its maturation there is enforcement of redefining the welding definition incorporating wide varied welding application and process variations in order to avoid misconceptions and wrong use of welding related terminologies.

Chapter 3: Experimental Methodologies

3.1 Introduction

Introduction chapter explains the deficiencies in WAAM of aluminium and further the project concept. Main research was directed towards the current identified deficiencies in WAAM of aluminium. As explained earlier, there are three major pillars of this study namely porosity and hydrogen dissolution, microstructure and residual stresses associated with WAAM of aluminium. A separate attention is provided to a concept of interlayer-temperature and its effects on porosity, microstructure and residual stresses. On a broader scale, this chapter explains the methods, experimental planning and procedure followed for the study. Materials, consumables and experiments are included in a sequence that was followed during the study.

3.1.1 Concept of interlayer-temperature

A new concept of interlayer-temperature was introduced in this project for WAAM manufacturing. The concept is based in the interpass temperature idea commonly applied for welding operation. Boiler and pressure vessel code section IX from ASME has defined interpass temperature as '*the highest temperature in the weld joint immediately prior to welding, or in the case of multiple pass welds, the highest temperature in the section of the previously deposited weld metal, immediately before the next pass is started'*[133]. The importance of maintaining interpass temperature is to control the metal solidification rate ultimately controlling microstructure, mechanical properties and residual stresses. The similar concept was introduced in WAAM technique to check the effect of specific interlayer-temperature in porosity, microstructure and residual stress.

Throughout the study, 50 and 100°C, two different interlayer temperatures were considered. Here, temperature maintenance implies to controlling of the temperature of the top layer at chosen interlayer temperature value that is 50 and 100°C. For example, in manufacturing of 15 layered WAAM structure with 50°C interlayer temperature, the temperature of substrate as well as temperature of each depositing layer number starting from 1 to 14 was maintained around 50°C before deposition of layer number 2 to 15 respectively.

3.1.2 Defining interlayer-temperature

The chosen material for this work is 5xxx series aluminium alloy that is Al-Mg alloy. The 5xxx series aluminium alloys obtain their strengths by solution strengthening from alloying addition mainly magnesium (Mg) [134,135]. British welding standard BS EN 1011-4:2000 provided guideline for welding of these alloys in which suggested maximum interpass temperature is 120°C. The fact correlates to the loss of alloying elements at higher temperature that ultimately reduces weld strength.

In view of this, for the current study two interlayer-temperatures were decided below the recommended interpass temperature. Thus, for the project work 50°C and 100°C interlayer temperatures were selected.

3.2 Porosity

3.2.1 Introduction

Literature review confirmed that the use of CMT process reduces porosity in aluminium; however, the effect of parameter change on porosity formation, its distribution and hydrogen dissolution is not discussed in the open literature. Porosity formation is also one of the important problems in aluminium casting. In view of this, it was decided to study and compare hydrogen dissolution and porosity formation in pulsed-MIG and CMT based samples. Although, it was well known that pulsed-MIG process produces increased pores compared to CMT, it was important to study the metal behaviour and its response to the parametric changes. The concept followed during porosity study is depicted in Figure 3.1.

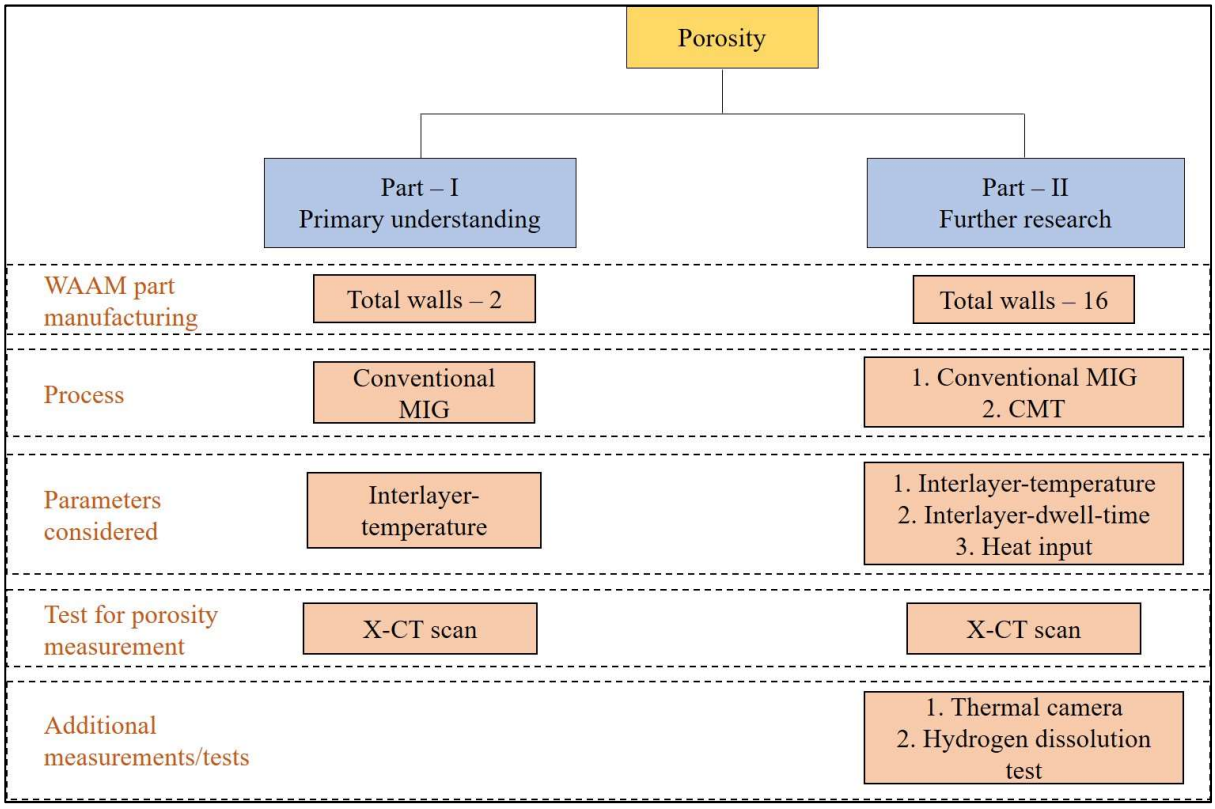

Figure 3.1 Concept for porosity study.

3.2.2 Part – I Understanding the effect of interlayer-temperature

To find out any possible effect of change of interlayer-temperature on porosity content and its distribution in WAAM part of aluminium, primary experiments were conducted. Initially two walls, Wall 1 and 2, were manufactured maintaining two different interlayer-temperatures as shown in Figure 3.1 and were tested for porosity content by X-ray computed tomography technique (X-CT scan). Conventional pulsed-MIG technique was employed for part production and 50 and 100°C interlayer-temperatures were used. Details of part manufacturing are given below.

3.2.2.1 Material and consumables

3.2.2.1.1 Feed stock wire

For this initial experiment, the feed stock wire chosen was commercially available aluminium ER5356 (AWS: A5.10 ER5356) solid wire. A wire diameter was 1.2 mm for this study and kept constant for all the experiments performed. Chemical composition of a feed stock wire is tabulated in Table 3.1.

Table 3.1 Chemical composition (wt%) of feed stock wire ER5356.

Si	Mn	Cr	Cu	Ti	Fe	Mg	Zn	Al
< 0.25	0.15	0.13	< 0.05	0.11	< 0.4	5	< 0.1	Balance

3.2.2.1.2 Substrate

For the deposition of chosen aluminium wire, a substrate of comparable chemistry was chosen. A rolled plate of commercially available grade of 5083 was employed throughout the study. The chemical composition of the plate with thickness 25 mm is provided in Table 3.2.

Table 3.2 Chemical composition (wt%) of substrate plate 5083.

Si	Mn	Cr	Cu	Ti	Fe	Mg	Zn	Ni	Al
0.11	0.66	0.06	0.05	0.05	0.25	4.74	0.05	< 0.1	Balance

3.2.2.1.3 Shielding gas

Throughout the study, the parameter of shielding gas was kept constant. Depositing liquid metal was shielded by commercially available Argon gas with 99.998% purity. The gas flow rate during metal deposition was kept constant at 20 l/min. A product supplied by Air Products and Chemical Inc. under the trade name of Argon Technical was used.

3.2.2.2 Process and welding robot

For the study, a complete setup of OTC modelled recently developed Synchrofeed system was used that integrates robot controller, power source and welding torch as can be seen in Figure 3.2. The system is designed for welding applications that has capability of performing welding using specially designed pulsing current formats. Frequency and amplitude of the pulsing current and voltage can be adjusted through the system. The system uses OTC Welbee P500L power source that operates on the synergic line to control wire feeding speed according to the chosen set of current and voltage values. More details about the machine operation can be found in respective manuals.

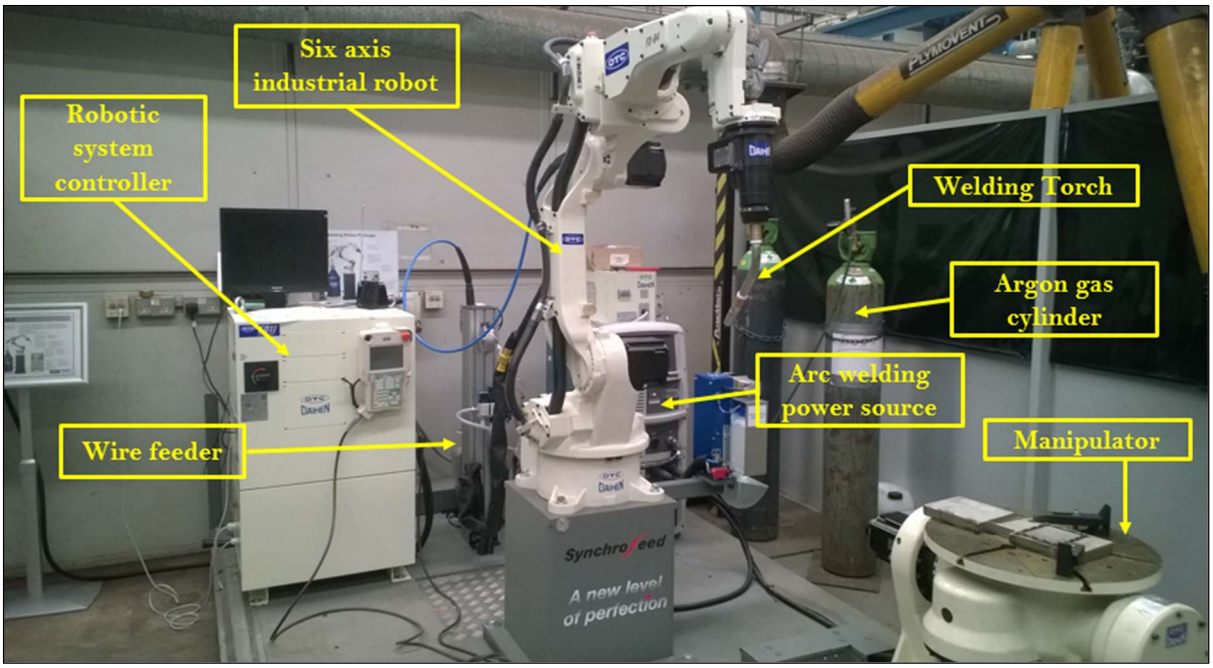

Figure 3.2 OTC equipment and overall set up.

3.2.2.3 Deposition parameters

For the manufacturing of two aforementioned walls, following parameters were selected (refer Table 3.3). Current, voltage and heat input variation is illustrated in graphical format in Figure 3.3.

Table 3.3 Pulse-MIG parameters used for manufacturing of walls in Part – I.

Parameters	**Values**
Average current (A)	130
Average voltage (V)	18.8
Linear torch travel speed (m/min)	0.6
Average Heat input (J/mm)	220
Wire feed speed (m/min)	7.5
Frequency of torch oscillation (Hz)	0.3
Mode of torch oscillation	Linear
Amplitude of torch oscillation (mm)	40
Dwell time for torch oscillation (seconds)	0.1 at ¼ & ¾ distance and 0 at ½

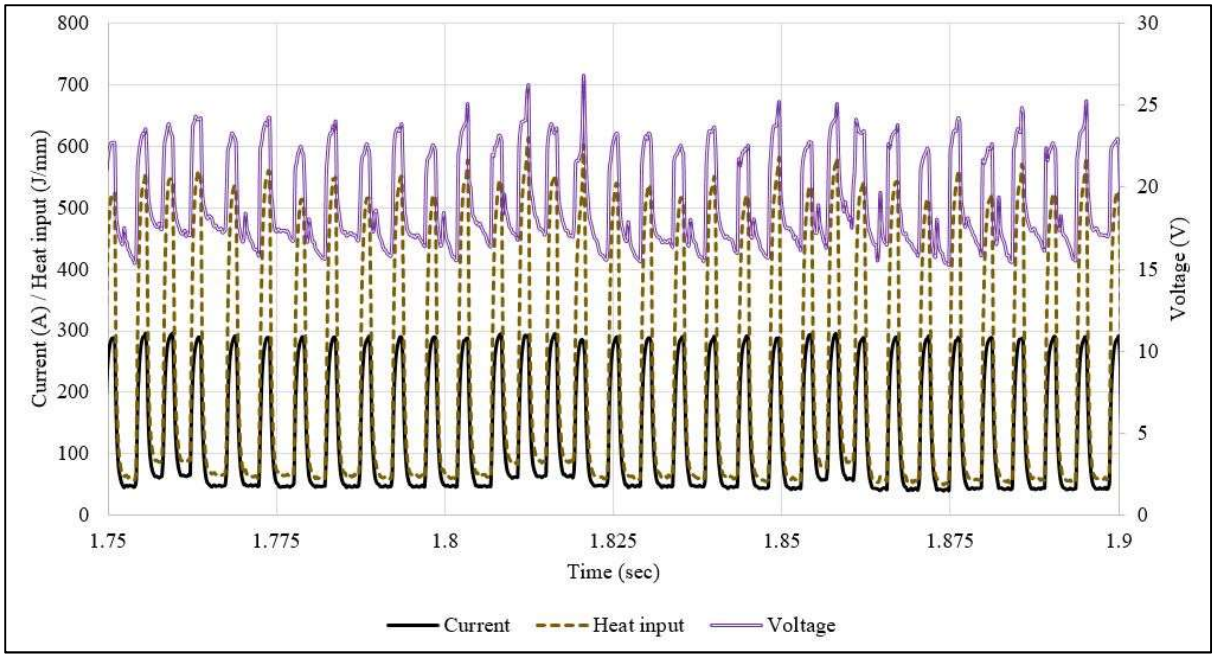

Figure 3.3 Current, voltage and heat input variation for pulsed-MIG in Part – I.

3.2.2.4 Electrical data recording and calculations

The study included deposition of metal using pulsed current and voltage format. Actual current and voltage variation over the time was recorded using transient electrical data acquisition system AMV (refer Figure 3.4). Current and voltage variation using OTC and CMT systems was recorded. The data acquisition system records data after every 0.0002 secs, thus, 5000 entries at every second. The data was helpful in plotting the graphs of current, voltage and heat input versus time. Importantly, the recording aided the calculation of instantaneous power (IP) and further the calculation of heat input (HI). Equation 3 to 5 show the formulae for calculations of instantaneous power and heat input.

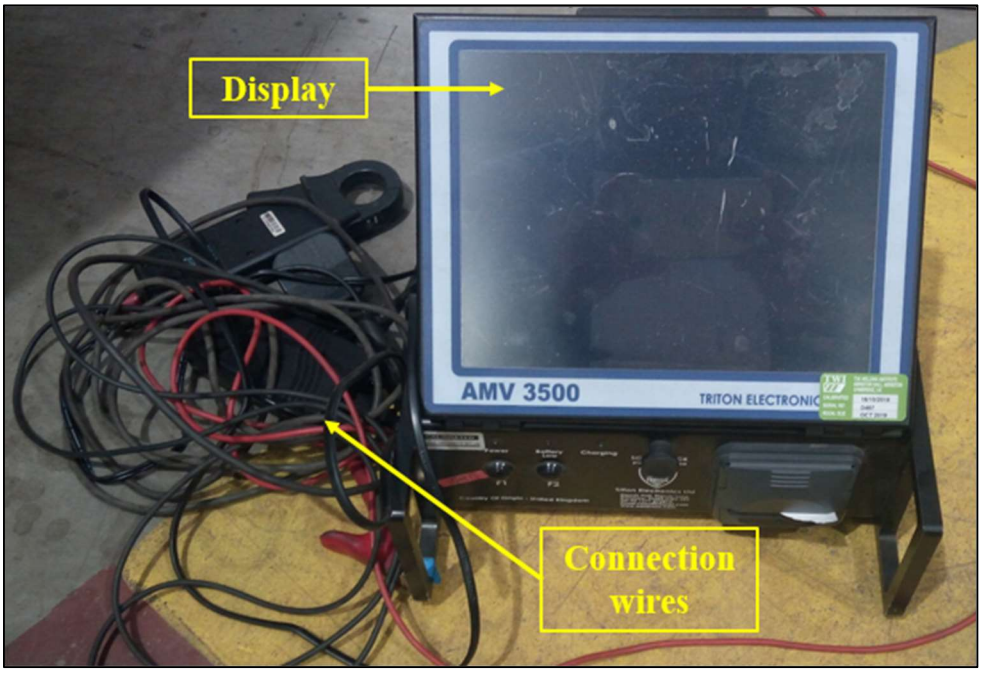

Figure 3.4 Electrical data recoding unit.

$$IP\ (W) = \sum_{i=1}^{z} \frac{\mathrm{Ii}\ .\ \mathrm{Vi}}{z} \qquad \text{Eq. (3)}$$

$$Heat\ input = \eta\ \frac{Average\ voltage\ x\ Average\ current}{\text{Travel speed}} \qquad \text{Eq. (4)}$$

$$Heat\ input = \frac{\eta \sum_{i=1}^{z} \frac{Ii * Vi}{z}}{TS} \qquad \text{Eq. (5)}$$

where Ii and Vi are the instantaneous values of current (A) and voltage (V) respectively, η is process efficiency, z indicates the number of values considered and TS represents the travel speed in m/min. Thus, the mentioned Eq. 3 provides an average power of the arc for the specific time consideration. Heat input was calculated as average IP from Eq. 3 over the travel speed as can be seen in Eq. 4 and 5.

3.2.2.5 Manufacturing of wall 1 and 2

A particular pattern followed for metal deposition in fabrication of wall 1 and 2 is displayed in Figure 3.5. Torch oscillation deployed for wall manufacturing are displayed in Table 3.3. Interlayer-temperature 50 and 100°C was maintained for Wall 1 and Wall 2 respectively. The same interlayer-temperature was maintained at respective substrates. Temperature measurement is explained in next subsection. At this point it is important to mention that although the temperature of a top layer was either 50 or 100°C, other wall surfaces and substrate showed different temperature values. Two walls with approximately 190 X 135 X 45 mm^3 were manufactured having 45 layers. Substrate was clamped firmly to the manipulator of a welding robot to avoid possible distortion. Figure 3.6 shows image of Wall 1.

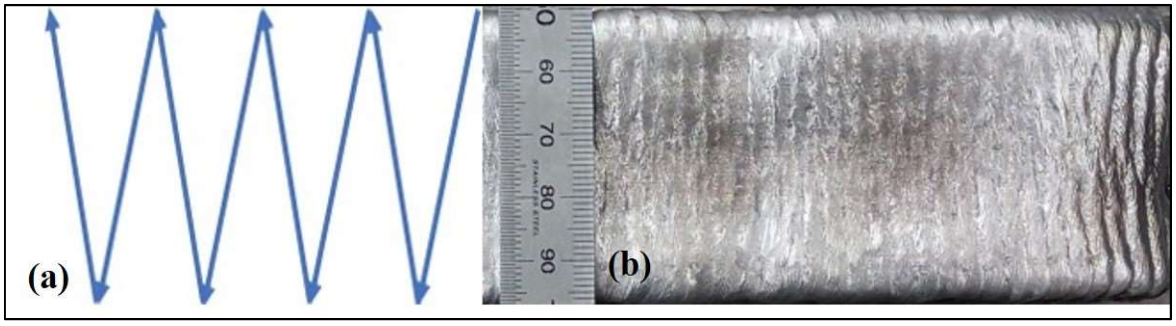

Figure 3.5 Torch oscillation and movement pattern followed for wall manufacturing (a) and top view of manufacture wall (b)

3.2.2.6 Temperature measurement

The temperature measurement of top layer was performed using RS Pro RS52 digital K-type contact type thermometer. Thermometer was selected based on guidance provided in ASTM E2877. It should be marked that temperature of the only top layer was measured and was considered as an interlayer-temperature throughout the study. Temperature of the rest wall surfaces and substrate was not

considered due to expected large variations as discussed by Xiong et al.[110]. It was highly challenging to maintain temperature of whole wall within a short band without external resources. Temperature of the top layer was measured at three locations approximately 50 mm from each wall end and at central location. Next layer was not initiated until desired temperature was not reached by natural cooling..

Figure 3.6 Side view of Wall 1.

3.2.2.7 X-ray computed tomography (X-CT) scan

X-ray computed tomography (XCT) is a radiographic based imaging method that produces 2D cross-sectional and 3D volume images of the object under inspection. Characteristics of the internal structure of an object, such as dimensions, shape, internal defects, and density, are readily available from XCT images. Figure 3.7 illustrates the concept of a simple XCT scanner. Here, an X-ray source generates an X-ray beam that propagates through the object under inspection. The resulting intensity of the X-ray beam is measured using an X-ray detector. This process is repeated at many angles to obtain a stack of 2D X-ray projections. HMX 225 system was used for XCT scanning. Data recording and overall operation was managed by X-Tek InspectX software while visualisation was performed by VGStudioMax software. X-CT scan was performed on two manufactured walls at an area away from wall end which represents stable metal deposition condition.

As an output of the scanning process, software created a spreadsheet containing an information related to the exact location of a probable defect, a pore in this case. The information contains exact location of a pore in 3 dimensional space with a fixed reference point for all the pores detected over the minimum detectable pore size. Pore size and pore shape (sphericity) was also obtained. Therefore, it was not only possible to categorise pores with respect to size and pore diameter but also to measure distance between intended pores.

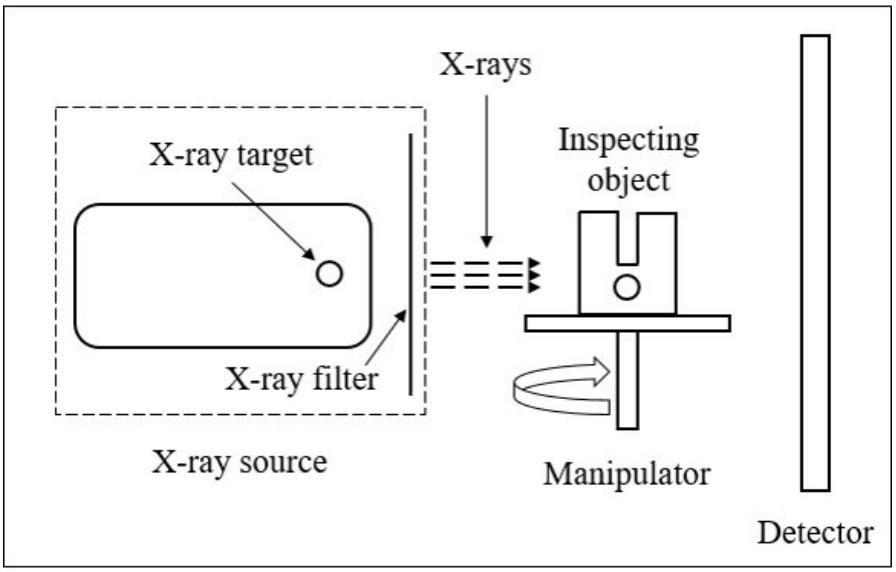

Figure 3.7 Concept and schematic of XCT.

3.2.2.8 Tensile testing

Later, walls were cut from 70 mm from one end using a band saw cutting machine and specimens for tensile test and macro examination were extracted following routine lathe machines operations. Cut sample locations are schematically shown in Figure 3.8. Total six specimens from each wall were taken out such that three were horizontal and three vertical specimens. Tensile test was performed following BS EN ISO 6892-1:2016 for determination of ultimate tensile and yield strength of the deposited walls.

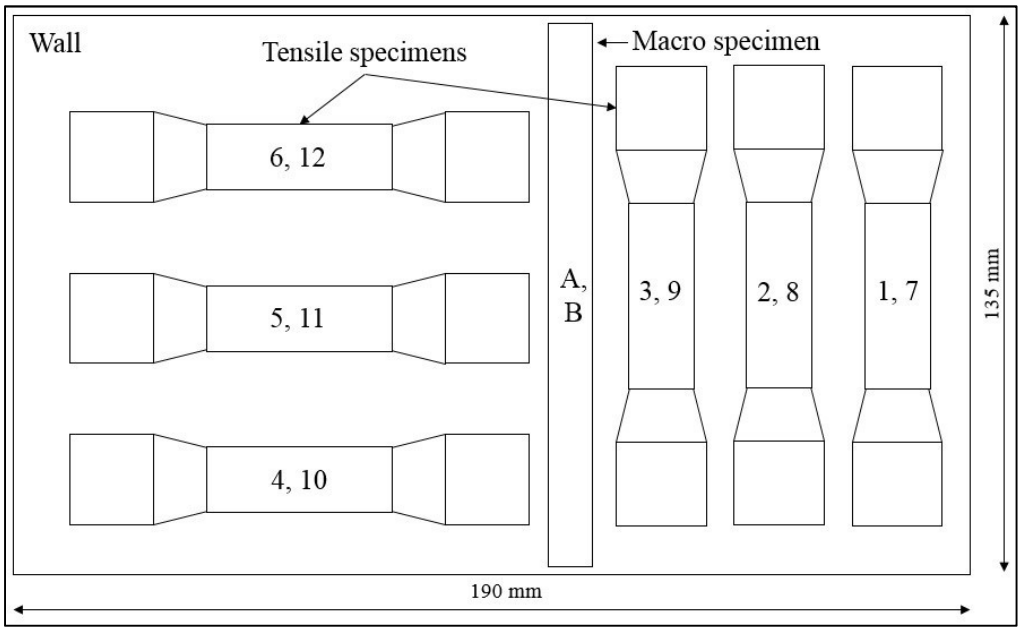

Figure 3.8 Location of tensile test and macro specimens in manufactured wall. Specimen number 1 to 6 are from Wall 1 while specimen number 7 to 12 for Wall 2.

3.2.3 Part – II Investigations into porosity and hydrogen dissolution in pulsed-MIG and cold metal transfer (CMT)

After gaining the primary results regarding the effect of interlayer-temperature on porosity and its distribution, in depth study was undertaken. Along with an interlayer-temperature, metal deposition technique, heat input and interlayer-dwell-time were varied for manufacturing of total 16 samples. Details regarding the same are as follows.

3.2.3.1 Material and consumables

3.2.3.1.1 Feed stock wire

For the study, the Feed stock wire chosen was commercially available ER5183 (AWS: A5.10 ER5183) aluminium solid wire which is commonly used in MIG/MAG welding operation. The study does not include an effect of variation of wire diameter on the deposit properties. Hence, for convenience 1.2 mm wire diameter was selected for entire experiments involved in this thesis. The chemical composition of the Feed stock wire is detailed in Table 3.4.

Table 3.4 Chemical composition (wt%) of feed stock wire ER5183.

Si	**Mn**	**Cr**	**Cu**	**Ti**	**Fe**	**Mg**	**Zn**	**Al**
0.06	0.65	0.07	0.01	0.07	0.14	4.91	< 0.01	Balance

3.2.3.1.2 Substrate

For the deposition of chosen aluminium wire, a substrate of comparable chemistry was chosen. A rolled plate of dimensions 200 X 125 X 20 mm^3 commercially available grade of 5083 was employed. The chemical composition of 20 mm thick plate is provided in Table 3.5.

Table 3.5 Chemical composition (wt%) of substrate plate 5083 (in percentage).

Si	Mn	Cr	Cu	Ti	Fe	Mg	Zn	Al
0.11	0.66	0.06	0.05	0.05	0.25	4.74	0.05	Balance

3.2.3.1.3 Shielding gas

Details are same as discussed earlier in subsection 3.2.2.1.3.

3.2.3.2 Process and welding robot

For this extended study, two types of metal deposition techniques were used namely pulsed-MIG and CMT. Pulsed-MIG technique and robotic detailed are discussed in previous section 3.2.2.2 and Figure 3.2. Fronius designed TPS400i CMT-advanced power source was used. A set up of CMT power source integrated with Fanuc welding robotic arm used for wall preparation is shown Figure 3.9. A separate metal deposition programmes were generated in order to deposit metal in required format.

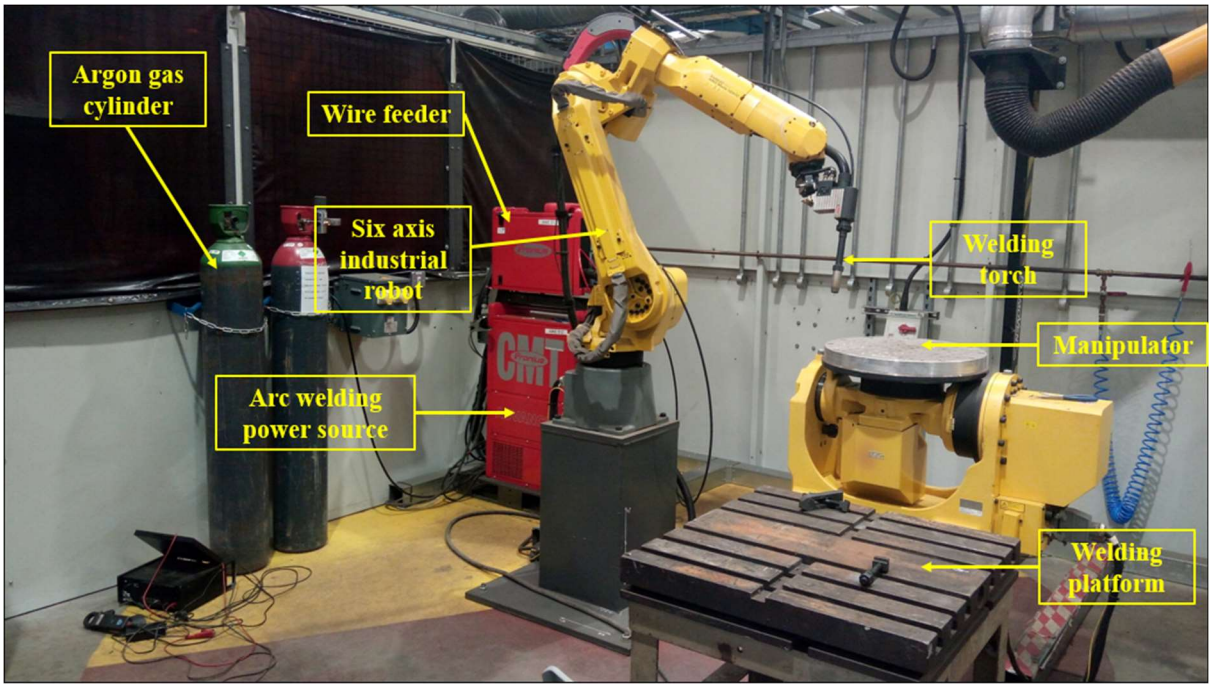

Figure 3.9 CMT-Fanuc welding robot and overall set up.

3.2.3.3 Deposition parameters

Metal deposition parameter deployed for manufacturing of samples are tabulated in Table 3.6. Based on previous experimentations heat input values were chosen. Average values were calculated form the electrical data recorded as described in earlier section. Approximately 25000 values were considered for a calculation of the average values. Also, the heat input was calculated using Eq. 5. General graphical representations of current, voltage and heat input are given in Figure 3.10 to Figure 3.13.

Table 3.6 Metal deposition parameters used for Pulsed-MIG and CMT samples for manufacturing of 16 samples in Part – II.

Parameter	**Pulsed-MIG**		**CMT**	
	Low heat input (LH)	High heat input (HH)	Low heat input (LH)	High heat input (HH)
Average current (A)	73	152	73	152
Average voltage (V)	18.3	18.7	18.2	19.2
Linear torch travel speed (m/min)	0.6	0.6	0.6	0.6
Heat input (J/mm)	120	280	120	280
Wire feed speed (m/mim)	4.85	8.65	4.9	8.6
Wire feed speed / travel speed (WFS/TS)	8.1	14.4	8.1	14.3

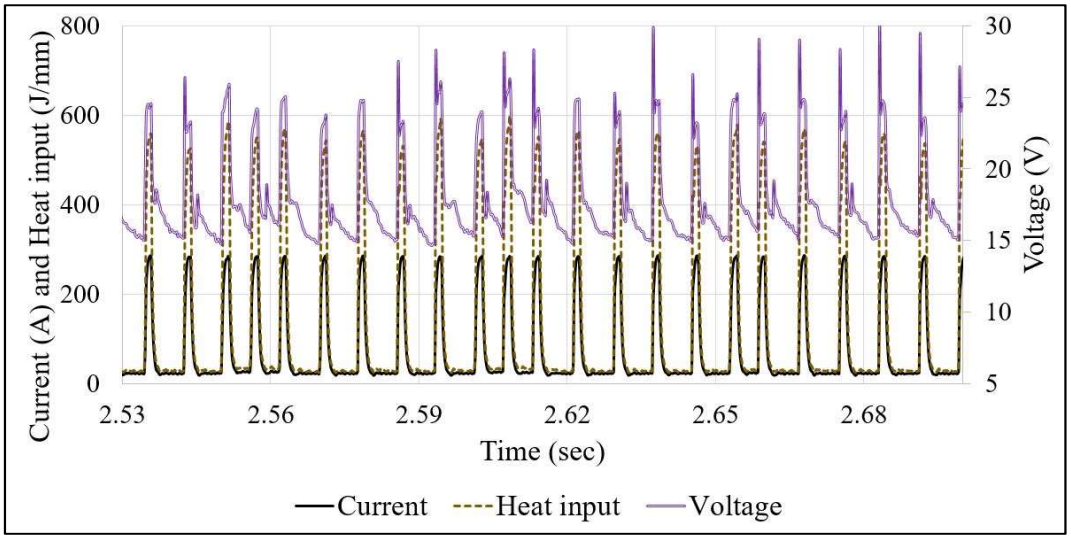

Figure 3.10 Current, voltage and heat input variation for pulse-MIG low heat input method.

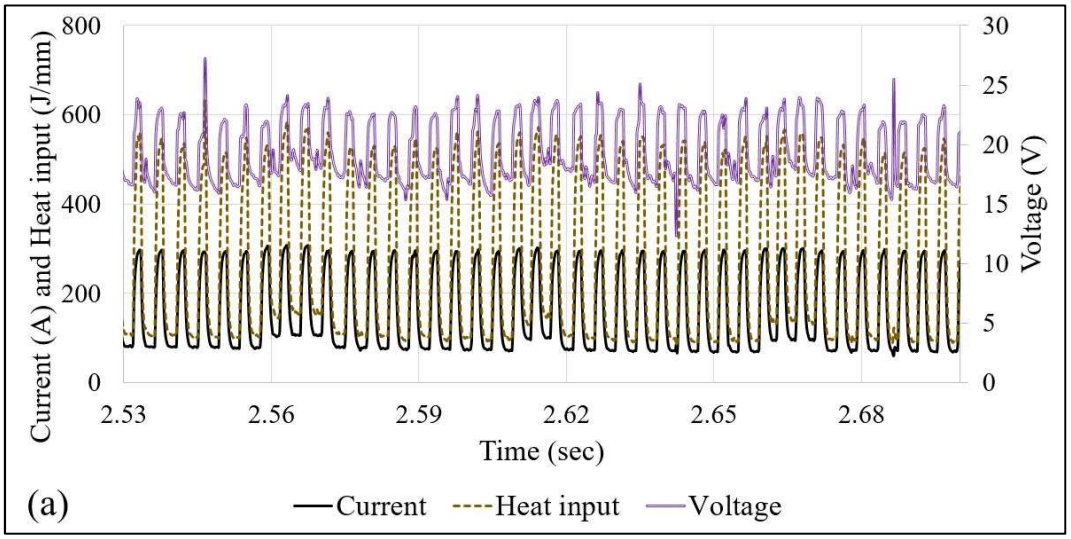

Figure 3.11 Current, voltage and heat input variation for pulse-MIG high heat input method.

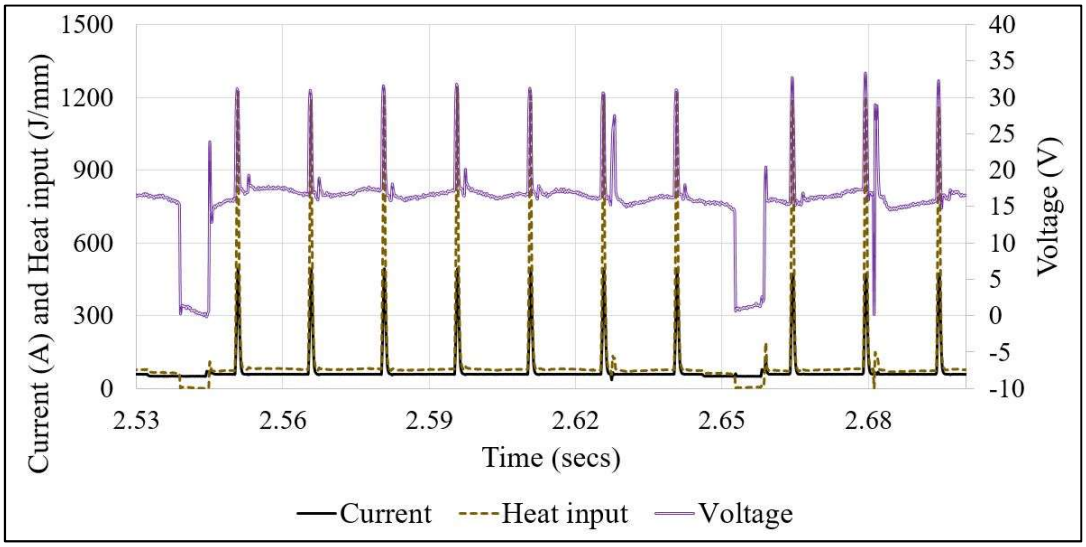

Figure 3.12 Current, voltage and heat input variation for CMT low heat input method.

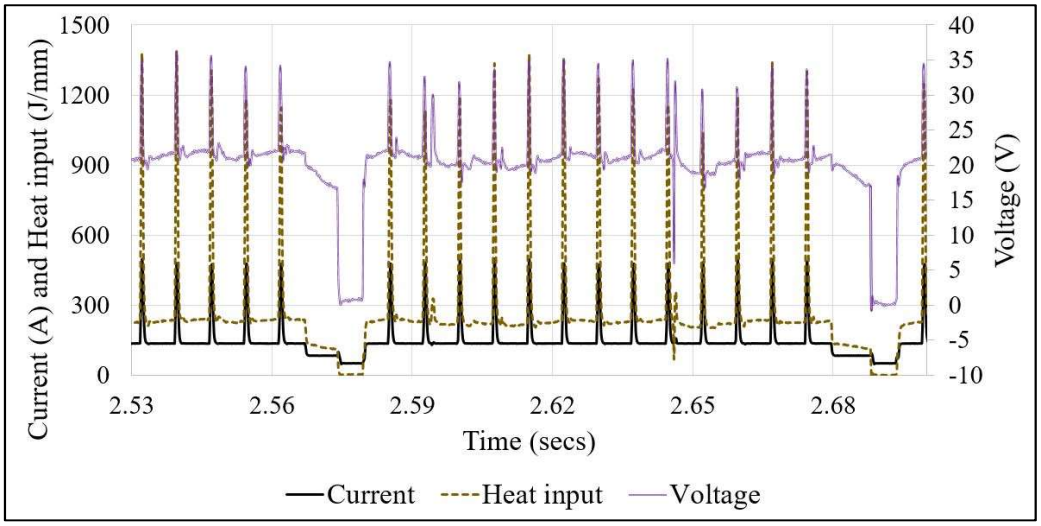

Figure 3.13 Current, voltage and heat input variation for CMT high heat input method.

3.2.3.4 Manufacturing of 16 wire arc additively manufactured (WAAM) samples

The extended study incorporated manufacturing of eight samples using pulsed-MIG and CMT technique each. Sequence of metal deposition and overall operation followed during samples manufacturing is shown in Figure 3.14. Each sample was manufactured with total of 15 layers and possesses 100 mm length. Each sample was manufactured with linear torch travel, hence, all samples were single-bead multilayer deposition. As discussed earlier, K-Type contact digital thermometer was used for temperature measurement. Temperature was measured at every layer at three defined locations that is 25 mm from each end and central area of 100 mm layer length.

For interlayer-temperature based samples, successive layer was not instigated until top layer temperature reached at desired temperature (either 50 or 100°C) by natural cooling. For interlayer-dwell-time method, interlayer-temperature was not accounted and metal deposition with robotic programming was performed based on time scale only. Two interlayer-dwell-times, 30 and 120 seconds were considered in this study. Apart from temperature and time variations, heat input and metal deposition technique were the variations.

Sample manufacturing was recorded using calibrated Flir made A320 infrared thermal camera. The purpose of the thermal camera used in this study was to highlight the temperature variation throughout WAAM structure while depositing layers. All temperature variations during and after layer deposition at the wall deposits were recorded for layer numbers 1 to 15 for pulsed-MIG and CMT samples. For processing of recordings, a ThermaCAM Researcher pro 2.9 software was used. For the study, a temperature range selected was 0 to 530°C. Higher temperature range of 530 to 2000°C was neglected from the study because a focus was the temperature of deposited solid part instead an arc or molten depositing metal. Emissivity value was 3.5 in this study. The chosen emissivity was based on real time confirmation using K-type contact type thermometer during and immediately after metal deposition on top layer and side wall forming wall structure. Refer Figure 3.15 for overall arrangement of WAAM part manufacturing and position of thermal camera for thermal variation recording.

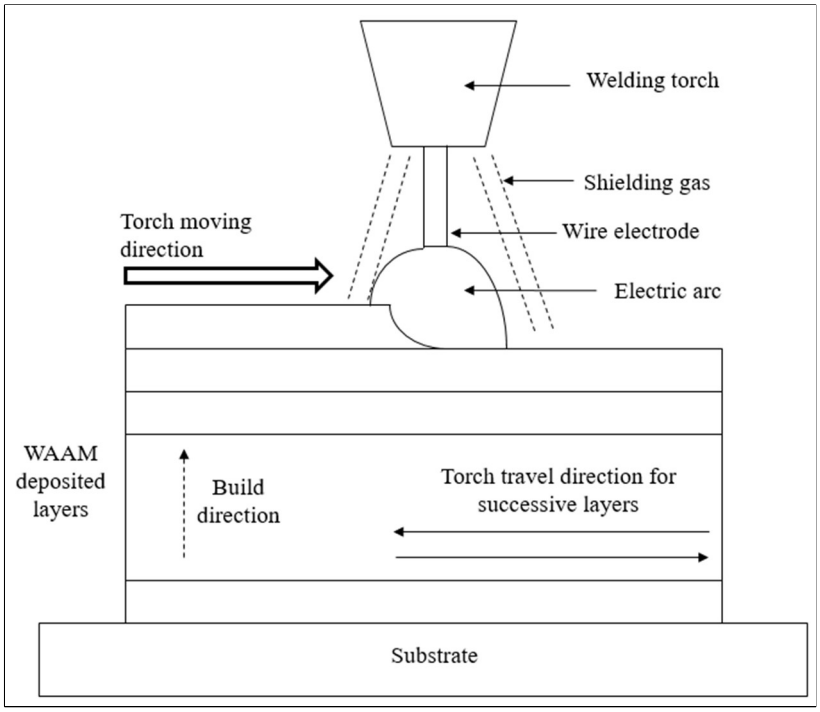

Figure 3.14 Schematic of sequence of metal deposition and overall operation using gas metal arc technique. Schematic showed front view of WAAM deposit.

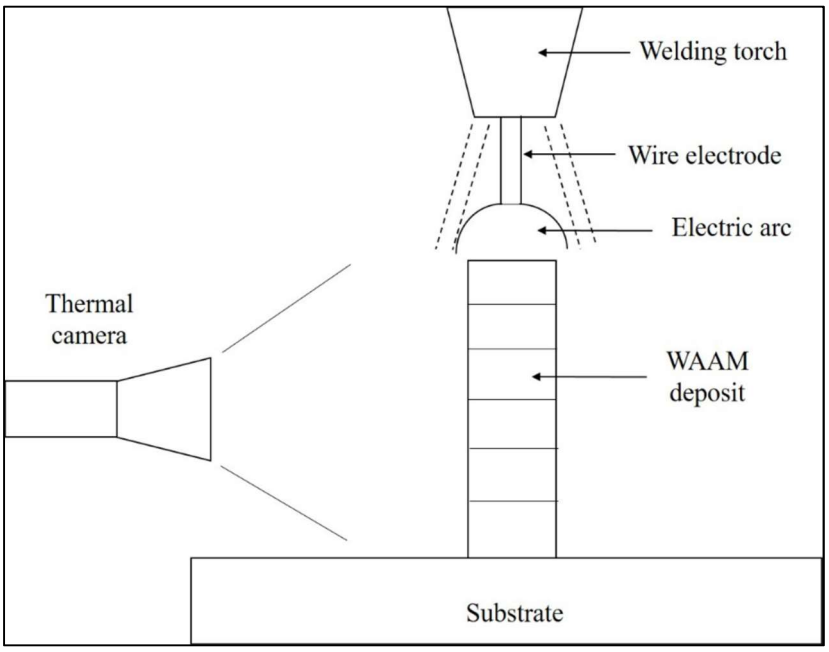

Figure 3.15 Schematic of arrangement of WAAM deposition and thermal camera. Schematic showed side view of WAAM deposit.

3.2.3.5 Samples identification

With proper combinations of the variables, total 16 samples were categorised into four sets as shown in Table 3.7. Each sample was given a specific identification describing all the deposition conditions for that sample. Sample processed with pulsed-MIG and CMT possessed 'P' and 'C' in their identifications respectively. High and low heat inputs were denoted by 'HH' and 'LH' respectively. Interlayer-

temperature based samples were identified by 'T' while interlayer-dwell-time samples showed 't'. Further, high heat input referred heat input close to 350 J/mm and for low heat input it was approximately 150 J/mm. Interlayer-temperatures, 'T1' and 'T2' understood 50 and 100°C temperature values respectively. On the other hand, interlayer-dwell-time, 't1' and 't2'specified 30 and 120 seconds of time span. Thus, for example, sample identification P-LH-t2 revels sample was manufactured with pulsed-MIG process, low heat input and 120 seconds (longer) interlayer-dwell-time; another sample C-HH-T2 denotes sample manufacturing with CMT technique, high heat input and high interlayer-temperature (100°C).

Table 3.7 Set identification and sample nomenclature.

Set number	**Metal deposition technique**	**Heat input**	**Interlayer-temperature / Interlayer-dwell-time**	**Samples IDs**
1	Pulsed-MIG (P)	High (HH)	50°C (T1)	P-HH-T1, P-HH-T2
		Low (LH)	100°C (T2)	P-LH-T1, P-LH-T2
2	CMT (C)	High (HH)	50°C (T1)	C-HH-T1, C-HH-T2
		Low (LH)	100°C (T2)	C-LH-T1, C-LH-T2
3	Pulsed-MIG (P)	High (HH)	30 seconds (t1)	P-HH-t1, P-HH-t2
		Low (LH)	120 seconds (t2)	P-LH-t1, P-LH-t2
4	CMT (C)	High (HH)	30 seconds (t1)	C-HH-t1, C-HH-t2
		Low (LH)	120 seconds (t2)	C-LH-t1, C-LH-t2

3.2.3.6 Scanning with XCT

Details regarding instrument used for scanning is descried in 3.2.2.7. For the deposited samples of 100 mm length, approximately 35 mm deposit representing stable metal deposition condition was cut and scanned from each sample. Scanned volume remained approximately 7200 mm^3 for each sample.

3.2.3.7 Dissolved hydrogen test

From the results obtained after XCT scan, total four samples, two from similar conditioned pulse-MIG and CMT each, were chosen for the dissolved hydrogen test. These samples were extracted from the samples used in XCT scan because these represented stable metal deposition and total pore volume was already known. Dissolved hydrogen test was performed using Leco RH402 instrument. The detected hydrogen represented hydrogen in states present in the samples that is entrapped and dissolved states.

3.3 Microstructure

3.3.1 Introduction

Literature review asserted that the CMT process produces finer and equiaxed grains in WAAM of aluminium; however, the effect of parameter change on microstructure and mechanical properties is not widely reported in the open literature. In view of this, it was decided to study and compare the microstructure from pulsed-MIG and CMT processed samples. Although, it was agreed that CMT produces smaller grains supporting in enhancing overall mechanical properties compared to pulsed-MIG process, it was important to study the metal behaviour and its response to the parametric changes, particularly under WAAM format. The concept followed during microstructure study is manifested in Figure 3.16.

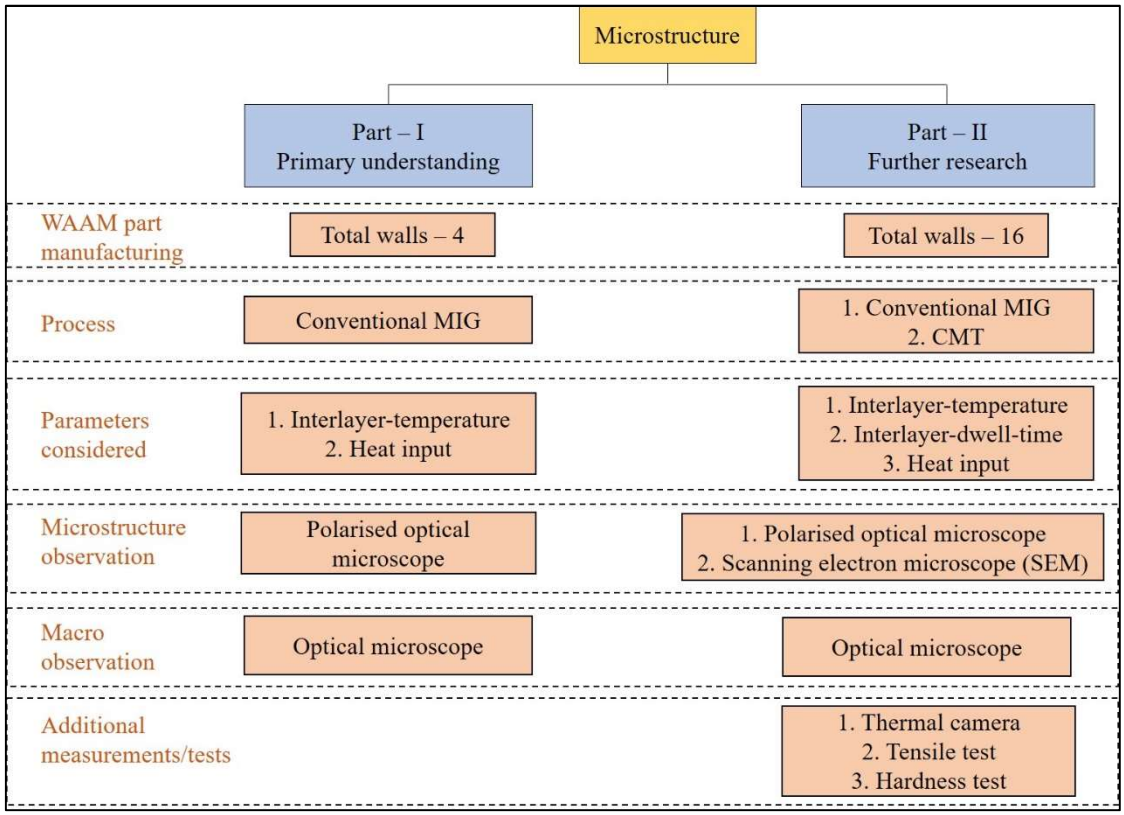

Figure 3.16 Concept followed for microstructural study.

3.3.2 Part – I Understanding the effect of interlayer-temperature and heat input

To find out any possible effect of change of heat input and interlayer-temperature on geometrical features and microstructure in WAAM part of aluminium, primary experiments were performed. Initially, four wall structures were manufactured with two different heat inputs and interlayer-temperatures. Conventional pulsed-MIG technique was employed for part production. More details of part manufacturing are given below. A block diagram representing the concept followed is shown in Figure 3.17.

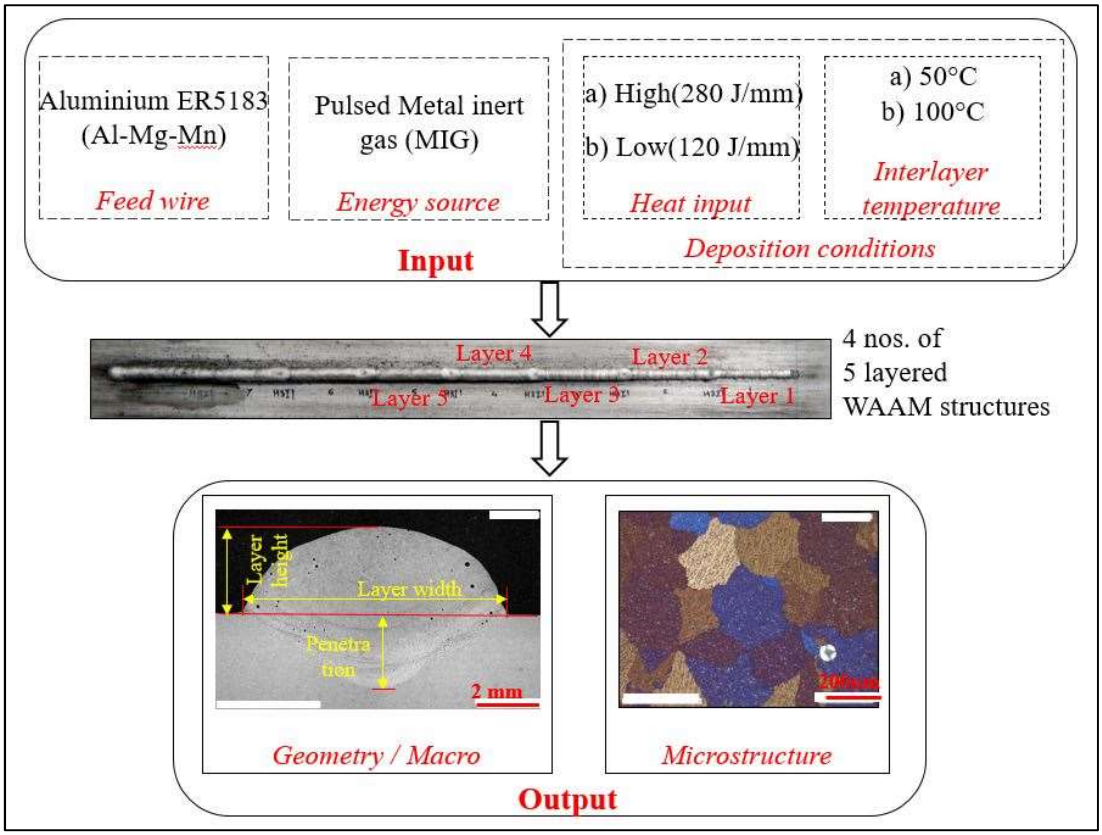

Figure 3.17 Block diagram representing concept followed during initial microstructural related study.

3.3.2.1 Material and consumables

3.3.2.1.1 Feed stock wire

Details of feed stock wire 5183 are same as discussed earlier in 3.2.3.1.1 section. Refer Table 3.4 for chemical composition.

3.3.2.1.2 Substrate

For the production of four unique wall structure, a substrate material used was 5083 with dimensions 500 X 250 X 20 mm3. Chemical composition is given in Table 3.5.

3.3.2.1.3 Shielding gas

Details are same as discussed earlier in 3.2.2.1.3 section.

3.3.2.2 Process and welding robot

Pulsed-MIG technique was considered for primary investigation. All details regarding pulsed-MIG and robot are discussed in previous section of 3.2.2.2 and Figure 3.2.

3.3.2.3 Deposition parameters

For manufacturing of total four walls, two heat inputs were used. Refer Table 3.6 for deposition parameters of pulsed-MIG technique and Figure 3.10 and Figure 3.11 for graphical presentation of current, voltage and heat input variations.

3.3.2.4 Manufacturing of samples

A component with staggered layer deposition of five layers was manufactured such that samples for macro and micro examination can be extracted from each layer of each structure separately. Illustration of component can be found in Figure 3.18. Two components with staggered layers were built by using high heat input and two interlayer temperatures, 50°C and 100°C. Alternatively, the procedure was replicated for low heat input. Thus, overall four staggered layers components were manufactured. Similar interlayer-temperature was maintained at the substrate for respective components. As discussed in 3.2.2.6 section, a K-type contact thermometer was practiced for the measurement of interlayer-temperature at each layer before deposition of next layer.

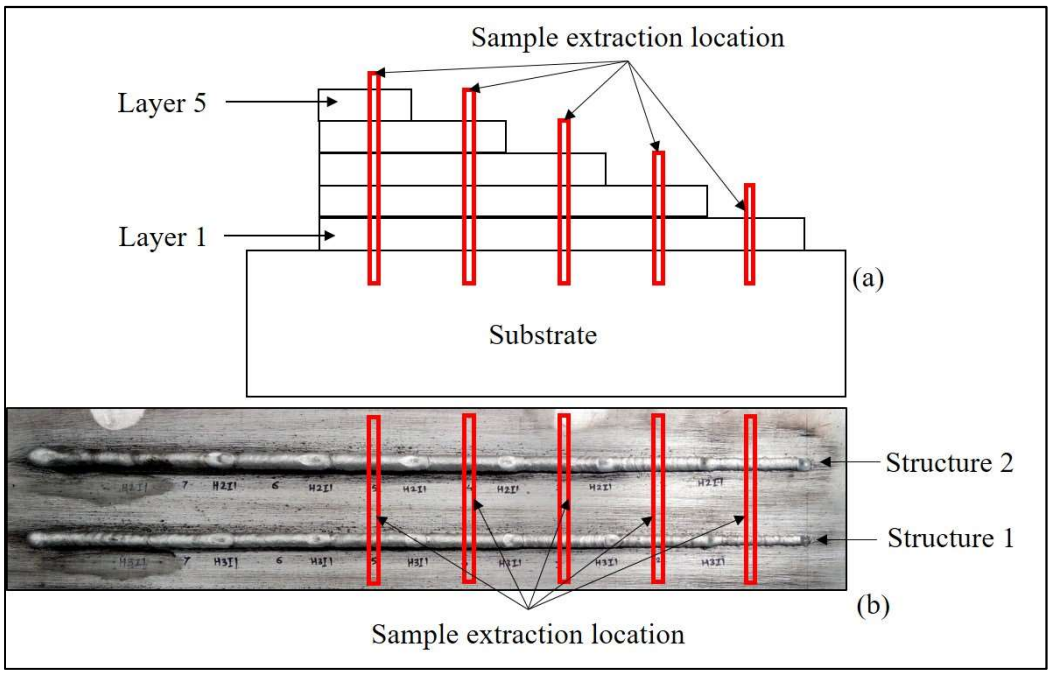

Figure 3.18 Schematic showing a side view of staggered layered component (a) and image showing a top view with location of sample extraction for macro and micro examination (b).

3.3.2.5 Sample nomenclature

Macro and micro structure of each layer of each deposited component was examined and therefore, an identification was given to each test sample extracted from staggered component. For two variables of heat input, 'H' and 'L' letters were used for high and low heat input respectively followed by '50' and '100' representing two interlayer-temperatures 50 and 100°C respectively. Numbers 1 to 5 were allocated for similar layered component from staggered section. For example 1H50 represented single layered component with high heat input and 50°C interlayer-temperature while 5L100 indicated 5 layered sample manufactured with low heat input and 100°C interlayer-temperature.

3.3.2.6 Macro and microstructural examination

From the locations shown in Figure 3.18, which represents central and stable part of deposition for that respective layer, suitable shaped 20 samples were extracted for macro and micro analysis. A standard cold mounting procedure was followed using Quick-set cold mounting kit made by MetPrep. Later, samples were polished using standard polishing papers having grades from 120, 320, 600, 1200 and

2500 sequentially. Sample polishing on paper was performed under a steadily flowing water. After completion of paper polishing, samples were polished on a lap wheel with lubricating agent having suspended diamond particles of a size varying from 3 µm, 1 µm and ¼ µm sequentially.

Macro analysis was carried out to determine geometrical variations with respect to height and width of each prepared sample. Optical microscope with Leica – LAS v4.4 software package was used for the same. Schematic representation of geometrical terms applied during macro analysis are shown in Figure 3.19. Further, microstructural analysis involved careful electrolytic etching (anodising) of samples with Barker's reagent, 6% Fluoroboric acid (HBF_4) in water for 90 seconds. Current and voltage during the anodising was maintained approximately 0.5A and 30V respectively. Polarised microscope was used for microstructure observations with Leica software. Grain size measurement was performed following the standard line intercept method defined under ASTM 112-13.

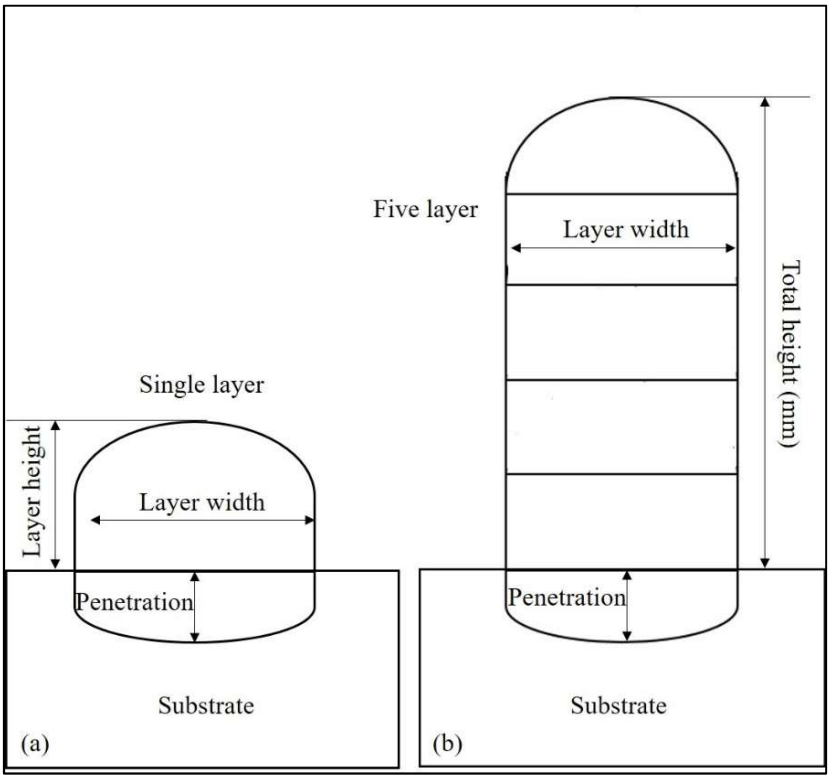

Figure 3.19 Schematic representation of geometrical terms applied during macro analysis.

3.3.3 Part – II Comparative investigation of pulsed-MIG and cold metal transfer (CMT)

After obtaining initial results regarding the effect of heat input and interlayer-temperature macro and micro features, in depth study was undertaken. Along with the heat input and interlayer-temperature, metal deposition technique and interlayer-dwell-time were also considered (refer Figure 3.16). Total 16 samples were manufactured.

Procedure followed for manufacturing of total 16 samples with unique nomenclature was identical to the procedure described in 3.2.3.5. Refer 3.2.3.1, 3.2.3.2, 3.2.3.3, 3.2.3.4, 3.2.3.5, from 3.2.3 for materials, processes, metal deposition parameter, deposition technique and sample nomenclature details respectively. Microstructural examination was performed following the similar procedure detailed in 3.3.2.6 subsection. Also, refer Figure 3.15 for the use and arrangement of thermal camera. Thus, similar

processing conditions were followed while manufacturing 16 samples for porosity and microstructural study.

3.3.3.1 Micro examination with electron backscattered diffraction (EBSD)

Chosen samples from CMT process were scanned under Zeiss made scanning electron microscope with electron back scattered diffraction (EBSD) mode for microstructural investigations. An area of 1 mm × 1 mm map size was selected with 6 µm step size for the study. Before processing samples under EBSD, samples were polished with polishing paper grades starting from 120, 320, 600, 1200 and 2500 sequentially with steady water flow. Later, samples were lap polished with rotating lapping wheel having lubricating agent with suspended diamond particle of size 3 µm, 1 µm and ¼ µm consecutively. The polished surface was them scanned for EBSD without any further treatment.

3.3.3.2 Mechanical testing

3.3.3.2.1 Tensile

From the processed samples, eight pulsed-MIG samples were tested for tensile properties following ASTM E8/E8M-16a Method C. Two sub-sized tensile test specimens in horizontal direction were extracted from bottom and top portion of deposited walls as shown in Figure 3.20.

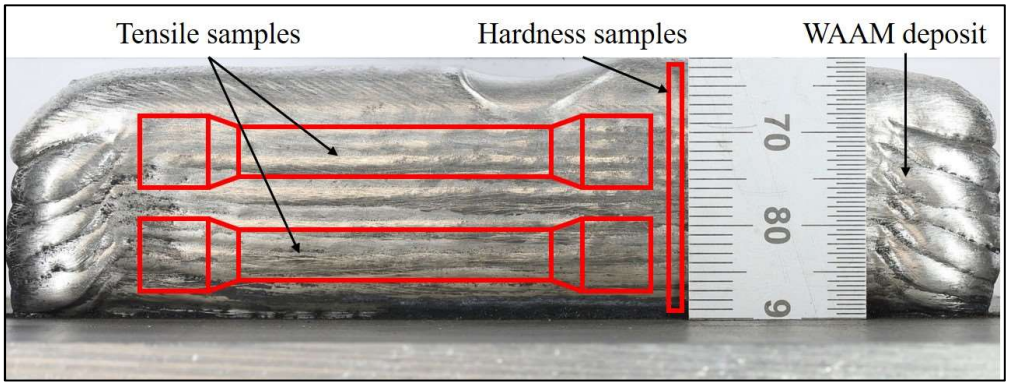

Figure 3.20 Approximate locations of tensile and hardness specimens.

3.3.3.2.2 Hardness

Further, hardness testing was carried out on all 16 samples. Refer Figure 3.20 for approximate location hardness sample. Vickers hardness number was obtained by applying 200 g load at every 0.5 mm distance starting from top of the deposit up to substrate as shown in Figure 3.21. All the testing was carried out following the guidelines as per BS EN ISO 6507-1:2005.

3.3.3.3 Alternative wire arc additive manufactured (WAAM) structure

A parallel study was conducted for determining the effect of orientation of tensile specimens with respect to deposited layers. Two multibead-multilayer WAAM structures were manufactured with pulsed-MIG low heat input conditions (refer Table 3.6 for parameters) following a layer deposition sequence as shown in Figure 3.22. Odd number of layers were deposited using layer pattern depicted in Figure 3.22a while all even layers were deposited using patter in Figure 3.22b. Two structures represented two different interlayer-temperatures that is 50 and 100 °C. A wall structure was approximately 250 mm long, 165 mm high and 15 mm thick.

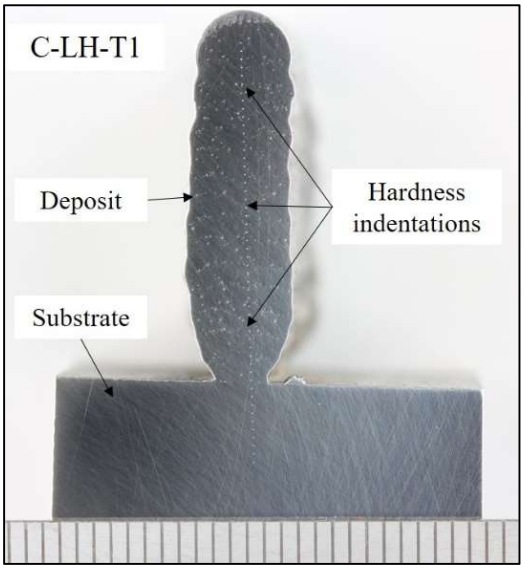

Figure 3.21 Hardness specimen C-LH-T1 with hardness indentation marks.

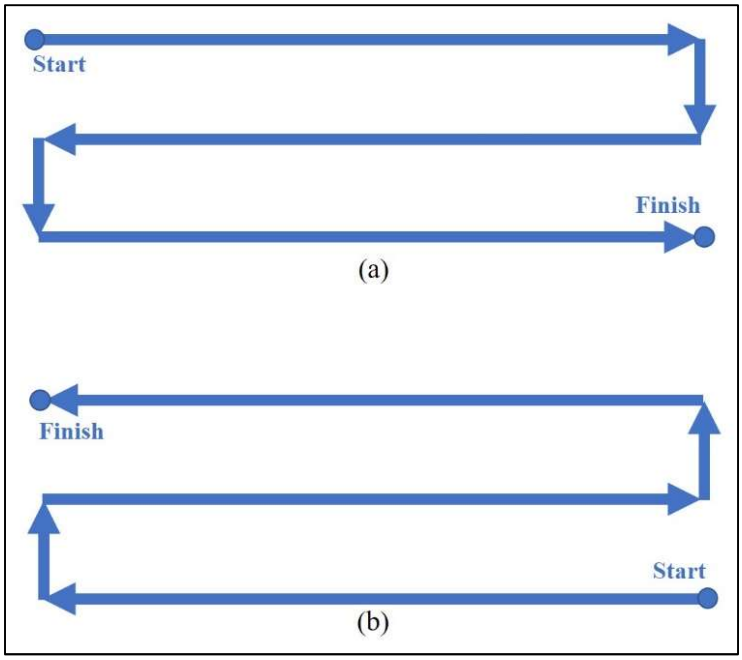

Figure 3.22 A layer deposition sequence followed in multibead-multilayer deposition. All odd numbered layers deposited using pattern in (a) while even number of layers were deposited using pattern in (b).

Later, total six tensile specimens were extracted from each wall structure such that three specimens were horizontal and three were vertical. All samples were tested following BS EN ISO 6892-1:2016 standard guidelines. A separate nomenclatures was initiated for identification of each tensile specimen. For example, specimen identification 1-T1-A-H denoted a wall structure number 1 manufactured with 50°C interlayer-temperature at a position 'A' in horizontal direction. Similarly, 2-T2-C-V represented wall structure number 2 with 100°C interlayer-temperature from location 'C' and had vertical orientation. Refer Figure 3.23 for more details.

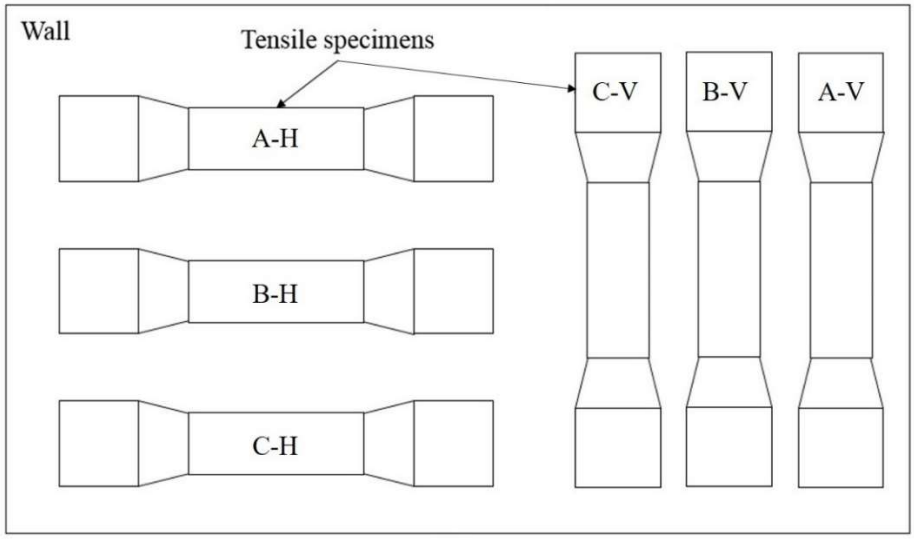

Figure 3.23 Location of tensile samples for multibead-multilayer WAAM structures.

3.4 Residual stress

3.4.1 Introduction

From literature review it was asserted that residual stress in WAAM component is one of the major concerns and needs in depth investigation. Further, particularly with WAAM, high strength alloys such as Ti-6Al-4V and Ni-based alloys have been studied for residual stress, however, aluminium is less attended. Also, the effect of parameter change on residual stress and its distribution is not widely reported in the open literature. In view of this, study was directed towards the effects of change of processing parameters on residual stresses in WAAM of aluminium. Interlayer-temperature, substrate thickness, heat input, number of layers and total deposit height were the main variables. The concept followed during residual stress study is manifested in Figure 3.24.

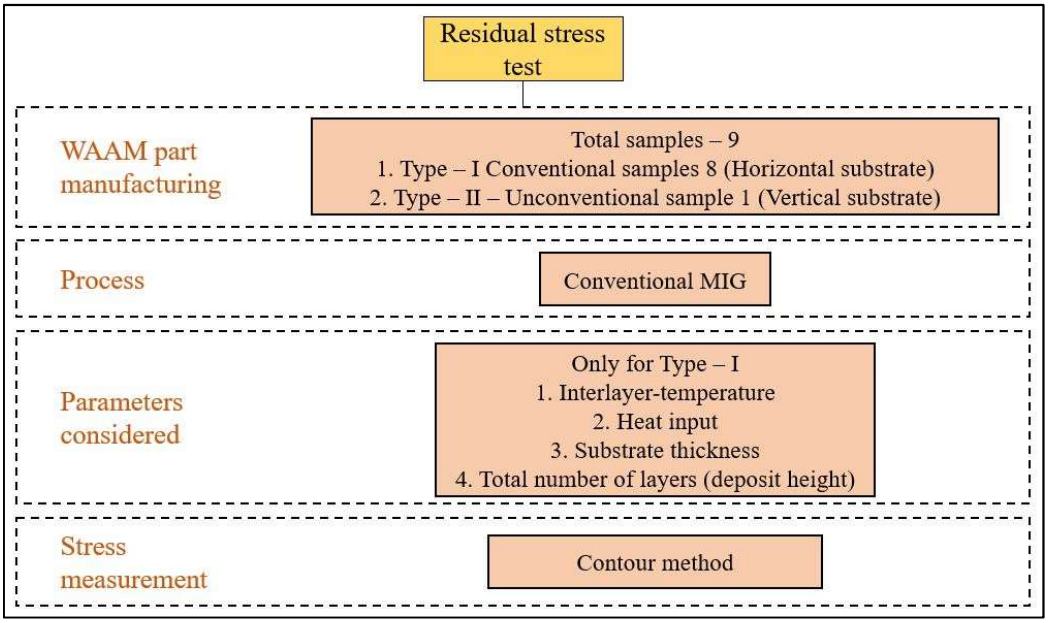

Figure 3.24 Concept followed for residual stress study.

3.4.2 Material and consumables

3.4.2.1 Feed stock wire

Details of feed stock wire 5183 are same as discussed earlier in 3.2.3.1 section. Refer Table 3.4 for chemical composition.

3.4.2.2 Substrate

For the production of eight wall structures, a substrate material used was 5083 with dimensions of 150 mm length and 125 mm width. For Type 1 samples, 6 and 20 mm thick substrates were used. For Type 2 sample, substrate plate with dimensions 150 × 60 × 6 mm^3 was used. Chemical composition of a substrate plates is given in Table 3.8.

Table 3.8 Chemical composition of substrate plate 5083 in wt% for 6 and 20 mm thick substrate.

Plate thickness	Si	Mn	Cr	Cu	Ti	Fe	Mg	Zn	Al
6 mm	0.07	0.48	0.07	0.04	0.02	0.32	4.61	0.01	Balance
20 mm	0.11	0.66	0.06	0.05	0.05	0.25	4.74	0.05	Balance

3.4.2.3 Shielding gas

Details are same as discussed earlier in 3.2.2.1.3 section.

3.4.3 Process and welding robot

Only pulsed-MIG technique was considered for residual stress study. All details regarding pulsed-MIG and robot are discussed in 3.2.2.2 section and Figure 3.2.

3.4.4 Manufacturing of samples

Total nine samples for residual stress measurement were categorised onto 2 types based on the substrate dimensions. Total eight samples in Type 1 were manufactured with conventional approach where substrate was horizontal. Out of eight, six samples had 20 mm thickness while rest two possessed 6 mm thick substrate. The single bead multilayer WAAM parts, similar to 16 samples manufactured for porosity and microstructural study, of a length 100 mm were deposited on a plane with 150 × 125 mm^2 dimensions. As described in Figure 3.24, heat input, interlayer-temperature, substrate thickness and total number of layers that is height of deposit was varied. A proper clamping arrangement was made such that substrate should not bend/warp during metal deposition. All the details about deposition conditions are tabulated in Table 3.9. Detailed illustration of metal deposition for Type 1 samples can be found in Figure 3.25.

Table 3.9 Parameters used for manufacturing of nine samples.

Sample type	Sample number	Substrate thickness (mm)	Number of layers	Deposit height (mm)	Heat input (J/mm)	Interlayer-temperature (°C)
Type 1	1	20	20	35	280	50
	2	20	10	18	280	50
	3	20	26	35	120	50
	4	20	20	35	280	100
	5	20	10	18	280	100
	6	20	26	35	120	100
	7	6	10	18	280	50
	8	6	10	18	280	100
Type 2	9	6	15	19	120	-

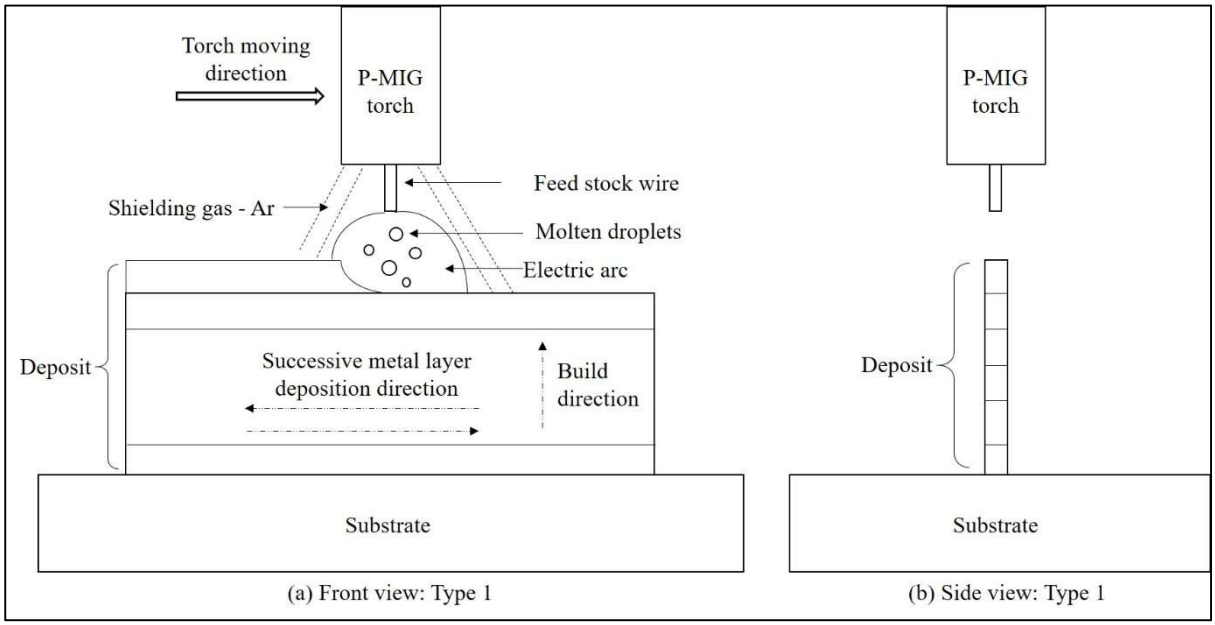

Figure 3.25 Schematic of WAAM process for manufacturing of Type 1 samples. Front view (a) and side view (b).

The last, sample 9, was manufactured with vertical substrate. Thus, smaller plane of a substrate, 150 × 6 mm^2 was used for layer deposition. Total layer length for Type 2 sample was 150 mm in contrast to 100 mm for type 1. Therefore, substrate height for sample 9 was 60 mm while length was 150 mm. Details about metal depositing parameters are given in Table 3.9. Details about manufacturing are depicted in Figure 3.26.

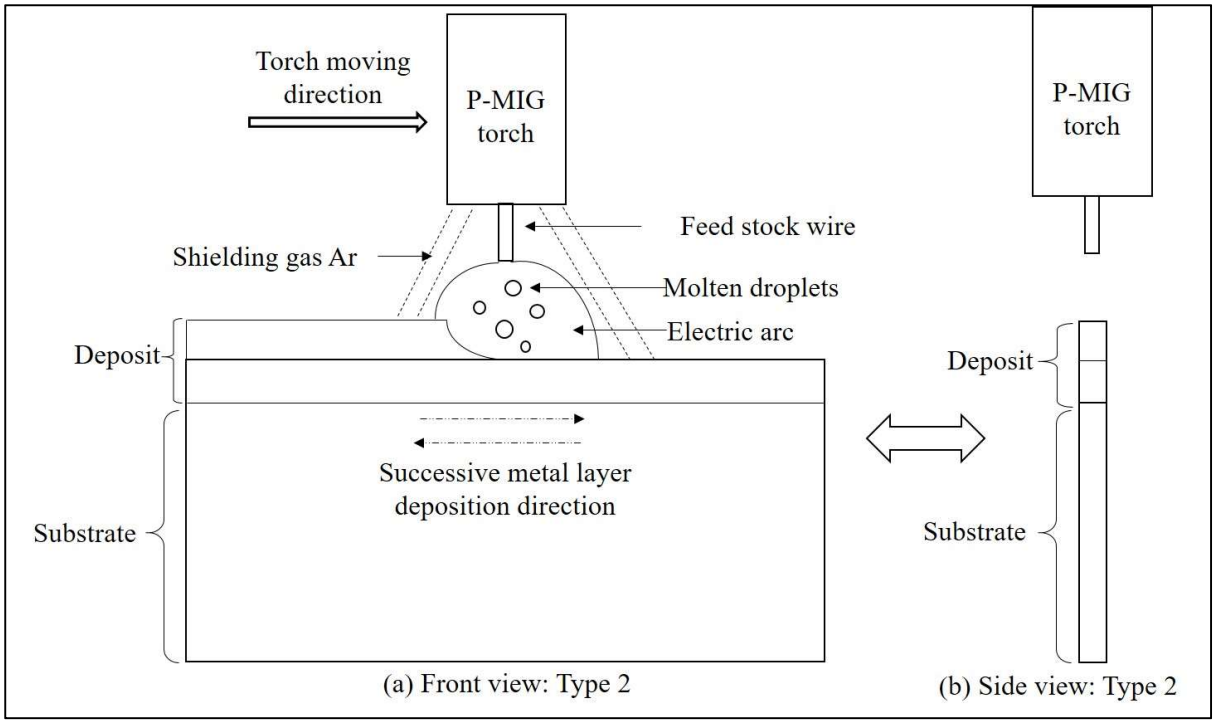

Figure 3.26 Schematic of WAAM process for manufacturing of Type 2 samples. Front view (a) and side view (b).

3.4.5 Contour method for residual stress measurement

3.4.5.1 Concept

Contour method is a destructive residual stress measurement technique that is based on the stress relaxation. In contour method, a part is cut into two halves, and the stress component being measured is normal to the cut surface. A wire electro-discharge machining (WEDM) is used to cut the component/part in which stress state is to be determined. It is assumed for the cutting stage that the cut surface is flat and no new stresses are incorporated. Followed by cutting stage, both the cut surfaces/halves are measured with a coordinate measuring machine (CMM) to get the displacement profile. Then data analysis is carried out to average, clean and smooth the measured surface displacement data. Finally a 3D FE model of one of the cut surfaces is built and the reverse of the measured contour is applied as the displacement boundary condition. The constraints are applied to model to avoid rigid body motion. A linear elastic FE analysis is finally used to calculate the residual stress in the sample. A schematic of contour process and steps followed are given in Figure 3.27.

3.4.5.2 Experimental setup and procedure

After required layers of metal deposition, samples were unclamped from the work station for further testing. In order to determine the residual stresses in longitudinal direction of torch travel, samples were cut in transverse direction of wall length. A central cut was made using wire electric discharge machine Robocut α-C600i made by Fanuc. A brass wire with diameter 250 µm was used. All samples were cut in a similar fashion as cut started at substrate, then through substrate and deposit simultaneously and finally through remaining substrate. The cutting speed maintained was less than 1mm/min. WAAM sample before and after cut is shown in Figure 3.28.

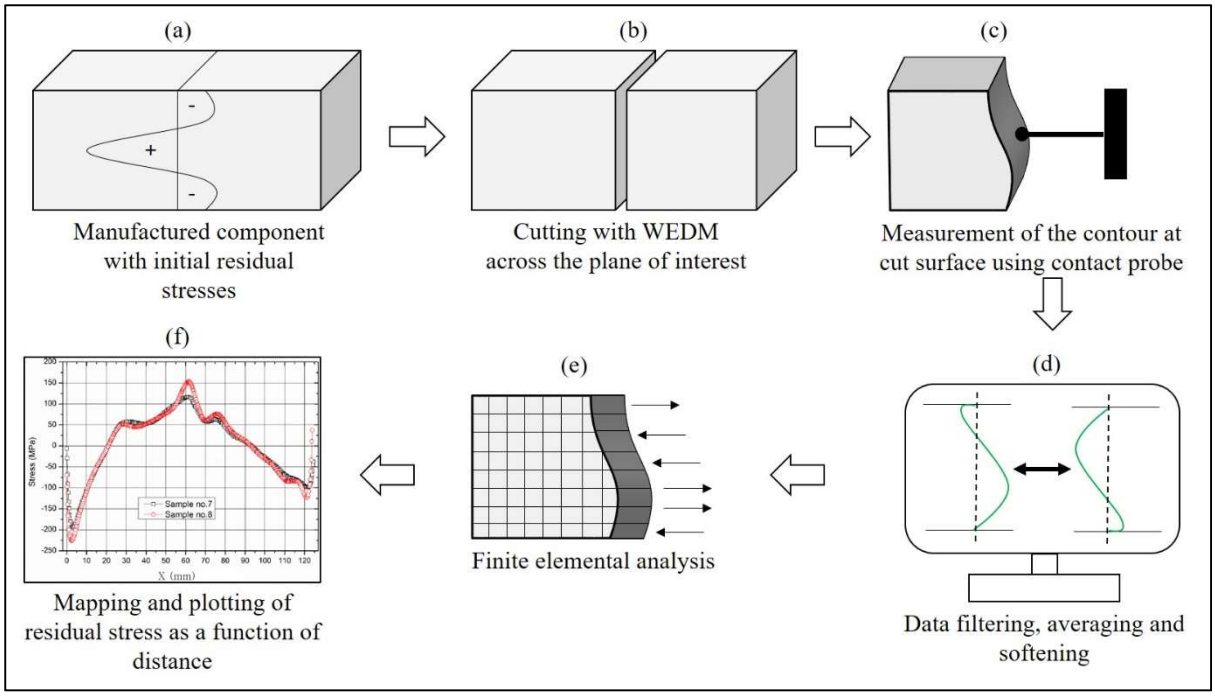

Figure 3.27 Schematic of procedure and steps followed in contour method. Manufactured part (a), after cutting a part at desired location with WEDM (b), contour measurement using coordinate measurement machine (c), data analysis and filtering (d), finite elemental analysis and data fixing (e) and plotting of graph stress versus distance (f).

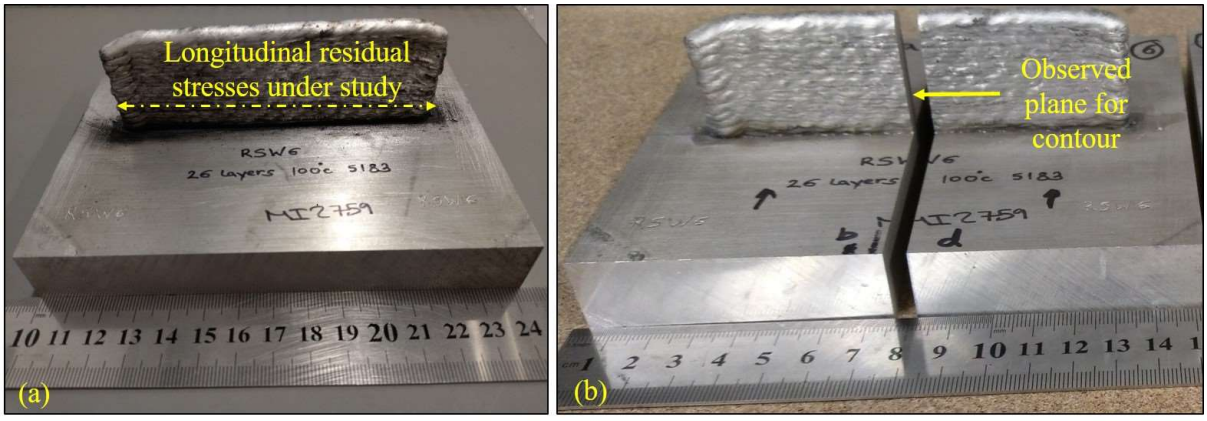

Figure 3.28 Images of WAAM sample (a) and WAAM sample after WEDM cut (b).

A cut surface contour that is displacement profile was measured using a Contura g2 coordinate measurement machine (CMM) manufactured by Zeiss. A 3 mm diameter probe was used. The distance from perimeter and between the individual measurement points in both directions of the sample surface was set as 0.4 mm. Later, MatLab was used for post processing of the recorded data for aligning, cleaning and smoothing. A cubic spine knot spacing of 10 and 7 mm was used along X and Y directions for data smoothing for sample 1 to 6 and 7 to 8 respectively. Further, a finite elemental model was developed for one of the cut surfaces. A 8-node brick element (C3D8R) of Abaqus software was employed. Non-uniform mesh size (that is distance between adjacent FE nodes) was used on the cut surface, and this distance was in the range of 0.5 - 1 mm for all samples. Material properties Young's modulus i.e. modulus of elasticity (E) and Poisson's ratio (υ) were 70.3 GPa and 0.33 respectively.

Chapter 4: Correlation between Porosity and Hydrogen Dissolution

4.1 Introduction

Broad applications of low cost aluminium alloys in the aerospace and automotive sectors attracted many researchers. During aluminium fabrication, inter-granular cracking [16] and porosity formation as a result of hydrogen pick up [78,90] are the widely discussed issues. Difference in the limit of solubility of hydrogen in liquid and solid state aluminium drives pore formation. The solubility of hydrogen in liquid state of aluminium is 17.5 times higher than solid state (0.4 ml/kg in solid while 7 ml/kg in liquid) [15]. Primary sources of hydrogen during welding and WAAM fabrication are hydrocarbons in the form of grease carried from wire fabrication/drawing process and a moisture on the filler wire [14,90,136]. Secondary sources are tubes, hoses, contaminations and moisture in shielding gas and moisture from substrate plate. In addition, dissolved hydrogen in feed wire and substrate can add up to the total hydrogen value. Liquid aluminium readily absorbs atomic hydrogen formed from hydrogen present in the contaminants during fabrication process [136].

As discussed in literature review chapter, dip metal deposition mode of CMT has profoundly reduced the overall porosity thanks to low heat input and unique mode of metal deposition method [3,78,90] than traditional metal inert gas (GMAW) method. In additive manufacturing of aluminium, metal deposition in a layer format imposes repeated reheating of earlier deposited layers that not only affects microstructure and mechanical properties but also porosity and residual stresses [3,67,89,129]. Therefore, it is imperative to control the heat input and manage the heat distribution intuitively for betterment of material properties in robotic metal operation. More commonly in robot controlled metal deposition, time lag between two depositing layers is managed [89,90]; however, the dwell-time does not account and control the heat distribution evenly throughout the forming part that entirely depends upon its size and shape. Actual temperature of the top layer, interlayer-temperature, could be one of the reasonable aspects. In a similar approach Geng et al. [137] reported the improved layer appearance by controlling initial layer temperature upto 120°C. A welding standard BS EN 1011-4:2000 recommends application of interpass temperature of 120°C for welding of 5xxx series aluminium alloys.

The effects of varying heat input, inter-layer temperature and interlayer dwell time on porosity formation, distribution and overall hydrogen dissolution are studied in this chapter. Thus, samples produced from conventional pulsed MIG and CMT are compared for metal deposition methods, hydrogen dissolution and porosity formation.

This chapter focuses on the effects of different metal deposition conditions on porosity formation, porosity distribution and hydrogen dissolution in wire arc additively manufactured (WAAM)

aluminium (refer section 3.2 for related experimental details). The chapter is divided into two parts where part 1 discusses initial study focused on effect of interlayer-temperature on porosity formation and distribution in thick walled (~ 45 mm) WAAM part. Related experiments are described in section 3.2.2 of chapter 3. The second part of the chapter incorporates detailed understanding of effect of metal deposition techniques that is pulsed MIG and CMT, heat inputs, interlayer-temperatures and interlayer-dwell-times on porosity formation, distribution and hydrogen dissolution in thin (~ 8-9 mm) WAAM parts. The experiments related to this part are described under section 3.2.3 of chapter 3.

4.2 Part – I Understanding the effect of interlayer-temperature

This section is focused on the results and related discussion referring to the experiments described in section 3.2.2 i.e. manufacturing of two thick WAAM walls with interlayer temperature 50 and 100°C manufactured using pulsed MIG and were X-CT scanned for porosity measurement. Also, tensile and macro examination was carried out in order to determine the effect of interlayer temperature on porosity formation and distribution.

4.2.1 Pore size, volume and distribution

Optical microscopy can be used for porosity measurement, however, the method is restricted to the observing surfaces and two dimensional planes. These results cannot guaranty its replication in three dimensions, hence, surface observations cannot be implied in volumetric scale because it depends upon the selection of an observation surface. Thus, the results are often subjected to errors if such a replication is assumed. The CT radiography reveals volumetric defects that not only increases the accuracy level of the defect identification but also it offers insight into material characterisation.

Two walls manufactured with 50 and 100°C interlayer temperature are shown in Figure 4.1a and b respectively. Wall-1 and Wall-2 showed overall 0.008624% and 0.007204% porosity by volume respectively in the considered stable metal deposition area having volume 149625 mm^3. It is important to mention that all the pores with volume greater than 0.01 mm^3 or diameter higher than 0.13 mm were considered in the study. The reason being the limitation on the resolution of CT scanning in detecting pores smaller than 0.01 mm^3 in WAAM wall of 550000 mm^3 (approx.) volume.

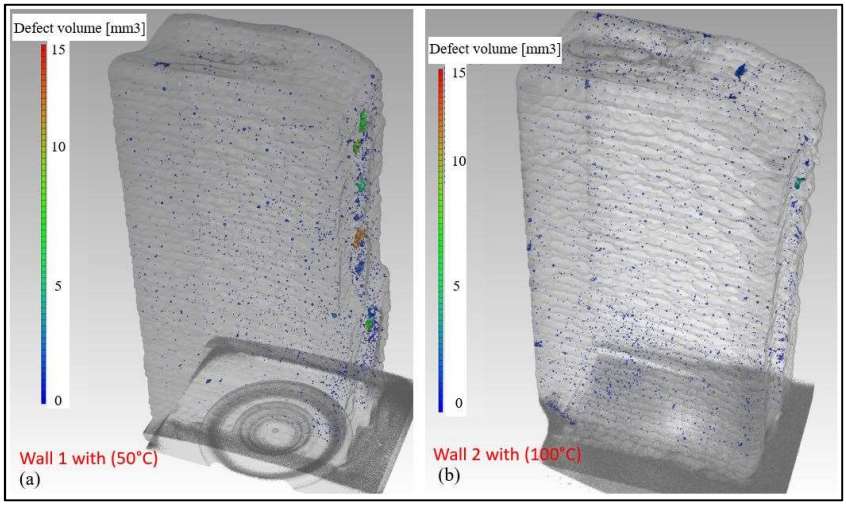

Figure 4.1 CT radiography image of Wall 1 (a) and Wall 2 (b) having 50 and 100°C interlayer temperature respectively

It was clear from Table 4.1 that 50°C and 100°C interlayer temperature samples possessed 12.905 and 10.78 mm^3 pores respectively that is low interlayer temperature sample showed 19.71 % more porosity than high interlayer temperature sample. Pores with volume range between 0.01 and 0.05 mm^3 occupied around 60% of the total pore volume in both the walls. Pore size between 0.05 and 0.2 mm^3 were 3.615 mm^3 (27.41% of pore total volume) and 4.332 mm^3 (50.19% of total volume) in Wall-1 and Wall-2 respectively. Interestingly, high interlayer temperature sample showed no pore with volume greater than 0.2 mm^3, however, low interlayer sample contained 1.601 mm^3 of pores contributing 12.4% of total pore volume.

Table 4.1 Comparison of pore volume fraction and pore count based on individual pore volume.

Pore volume (mm^3)	**Wall 1 (50°C interlayer temperature)**				**Wall 2 (100°C interlayer temperature)**			
	Volume (mm^3)	Volume fraction %	Total pore Count	Count %	Volume (mm^3)	Volume fraction %	Total pore Count	Count %
0.01 – 0.05	7.689	59.59	401	89.11	6.448	59.81	316	85.87
0.05 – 0.1	2.288	17.13	35	7.78	2.625	34.36	39	10.59
0.1 – 0.15	0.851	6.59	7	1.56	1.061	9.84	9	2.45
0.15 – 0.2	0.476	3.69	3	0.67	0.646	5.99	4	1.09
0.2 – 0.3	0	0	0	0	0	0	0	0
0.3 – 0.4	0.723	5.6	2	0.44	0	0	0	0
> 0.4	0.878	6.8	2	0.44	0	0	0	0
Total	12.905	100	450	100	10.78	100	368	100

Total number of pores were more in 50°C interlayer sample which was 450 compared to 100°C interlayer samples that showed 368. Number of pores with size ranging from 0.01 to 0.05 mm^3 were more than 85% in both the walls. The contribution of pores varying from 0.05 to 0.2 mm^3 was 10% and 14% in Wall-1 and Wall-2 respectively. Pores with size greater than 0.2 mm^3 showed less than 1% contribution in low interlayer temperature case and no pore of similar size was present in high interlayer temperature sample.

Further, for simplicity, pores were categorised into three ranges based on diameters. Pore dimeter was calculated from available pore volume assuming pores were perfect sphere. Pores with diameter from 0.13 to 0.2 mm (small pores) occupied more than 45% of total pore volume fraction in both the walls (refer Table 4.2). Medium size pores were 29.82% in Wall-1, however, it was 44.25% in Wall-2. Lastly, volume fraction of large pores was found higher in Wall-1 than Wall-2. Interlayer temperature showed impact on porosity distribution. Considering the number of pores present in the walls, small pores dominated the pore distribution contributing more than 75% in both the walls. Further, similar trends as that of volume fraction percentage were observed in pore numbers.

Table 4.2 Comparison of pore volume fraction and pore count based on individual pore diameter.

Size range	Average pore diameter range (mm)	Wall-1 (50°C interlayer temperature)				Wall-2(50°C interlayer temperature)			
		Volume (mm^3)	Volume fraction %	Count	Count %	Volume (mm^3)	Volume fraction %	Count	Count %
Small	0.13-0.2	6.440	49.90	372	82.67	4.949	45.90	281	76.36
Medium	0.2-0.3	3.849	29.82	67	14.89	4.770	44.25	80	21.73
Large	> 0.3	2.616	20.28	11	2.44	1.061	9.85	7	1.91
Total		12.905	100	450	100	70.78	100	368	100

Comparison is made amongst normalised distances of pores from the centroid of all pores as a function of interlayer temperature and pore sizes (large pores are not considered due to less numbers). Referring to Figure 4.2, the average normalised distance from centroid of all pores was smaller for medium sized pores in high interlayer condition than rest of the cases. Additionally, the distribution of small pores on the normal distribution curves was comparatively wider for high interlayer temperature suggesting that the variance in the normalised distance of the pores was larger that is non uniform distribution of pores in the high interlayer temperature sample. Least variance was recorded for medium sized pores with low interlayer temperature. Curves of small and medium sized pores of low interlayer temperature were in conjunction with each other, however, variation in average normalised distance was present in high interlayer samples.

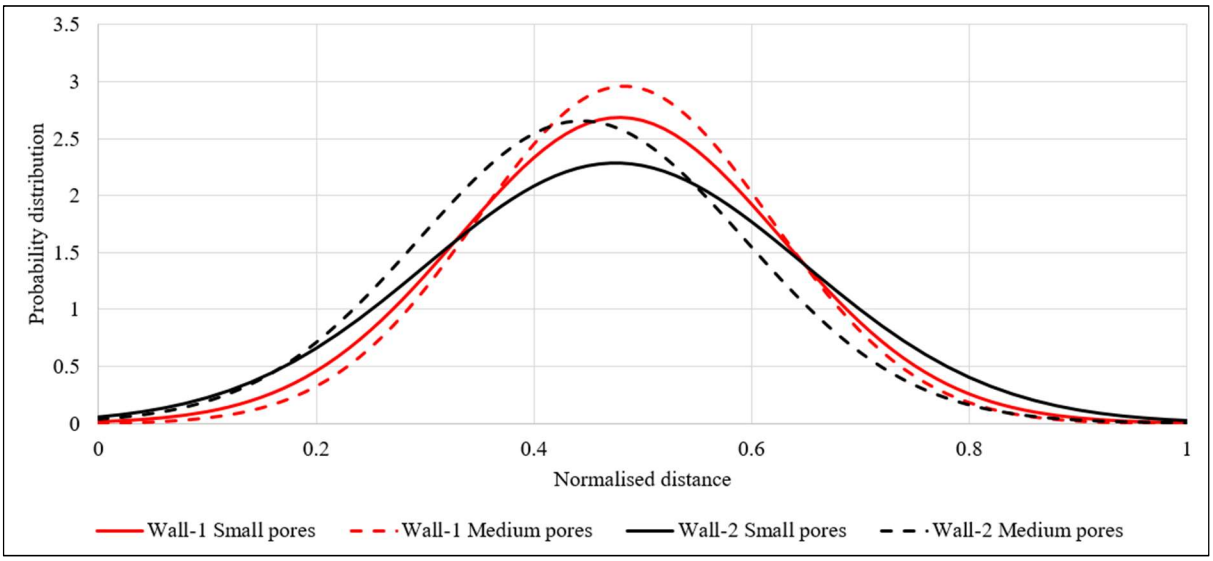

Figure 4.2 Effect of interlayer temperature on normal distribution of pore normalised distances from centroid of all pores in thick wall samples.

Effect of interlayer temperature on pore sizes can be displayed with respect to the probability distribution graph as shown in Figure 4.3. Both the curves reach peak value at approximately the same

pore diameter which is just below 0.2 mm (approximately 0.18 mm) indicating that average pore dimeter is roughly similar irrespective of the interlayer temperature considered; however, high interlayer temperature showed higher peak indicating higher probability for average sized pores along with high variance.

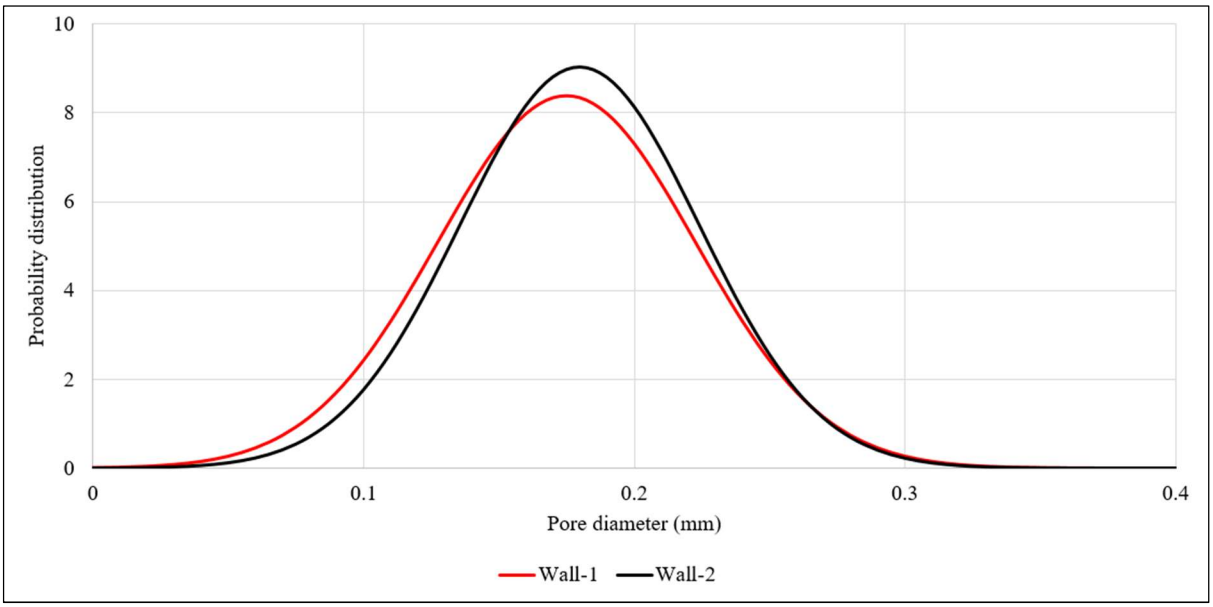

Figure 4.3 Effect of interlayer temperature on normal distribution of pore sizes in thick wall samples.

4.2.2 Heat effects

Two manufactured walls revealed increased porosity at the central part of one surface as can be seen in Figure 4.1. This area was identified as a set of points of start and end of layers where metal deposition was unstable. Therefore, this part of the wall was omitted from the study. An area highlighted the need of optimisation of metal deposition parameters to avoid defect formation at the start and end of the deposited part. The importance of uniform height and shape of the deposited layer that serves as base for successive layer has been highlighted by Xiong et al. [85] and Xiong et al.[82]. A minor increase or decrease in height at the start and/or end of a layer adds-up to a significant value after 5 to 7 layers which can be evidenced from Figure 4.4. Thus, the unequal surface at the start and end of a layer increases possibility of forging weld defects. Therefore, the WAAM part with stable metal deposition was considered during the study. Apart from the defect accumulated area, other part showed random distribution of pores.

Figure 4.4 Effect bead height variation and its cumulative effect on overall shape of WAAM part.

During the solidification of the molten weld pool, dissolved atomic hydrogen in solid metal is rejected into the liquid metal depending upon the temperature and the difference in solubility limit of hydrogen

in liquid and solid aluminium. The quickly formed oxide layer also absorbs hydrogen from moisture in the air. The continuously increasing hydrogen in liquid reaches to solubility limit and finally forms a pore at the grain boundary of the solidified metal. Depending upon the pore size and buoyancy force, pores are usually entrapped at the top of the fusion line [138]. A macro of the wall samples reveals increased porosity at the fusion lines (refer Figure 4.5).

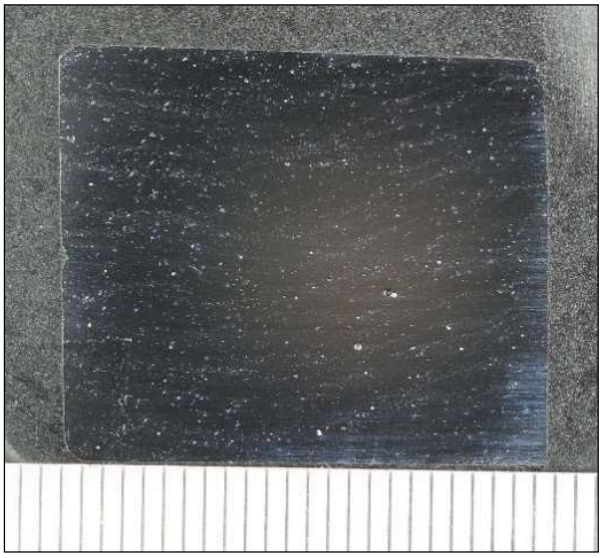

Figure 4.5 Macro test specimen revealing fusion lines.

The possibility of increased pores at the top layer could be floatation of pores layer by layer. While depositing successive layer, pores at the surface of the previous layer were taken to next layer by partial re-melting and addition of new liquid metal by welding arc. The entrapped pores at the bottom of the previous layer cannot reach to the top. Also, arc forces while depositing next layer possess limited penetration where liquid metal cannot form, the entrapped porosity remains untouched that can be witnessed as increased porosity near the fusion line. The inter layer waiting time for Wall-2 was less than Wall-1. During the solidification of metal while depositing a layer, comparatively faster solidification is expected at Wall-1 than Wall-2 due to lower and higher interpass temperatures respectively. Thus, liquid metal is exposed to the air for a longer time in Wall-2 than Wall-1. Also, the solidified metal at top surface is readily exposed to the air for longer time period compared to the rest part of wall and thus, comparatively higher cooling effect is expected at the top surface. Thus, it can be inferred that the time was insufficient for coalescence and growth of the micro pores at the top layer. This could explain the presence of majority of the small sized pores at the top surface. The effect greatly increases along with wall height.

The presence of large sized pores in Wall 1 can be attributed to the classical Ostwald Ripening effect [90]. The inter-pores coalescence is expected from the micro-pores as well as hydrogen entrapment site such as grain boundaries or lattice imperfections. As explained previously, the entrapped untouched pores at the fusion line are cyclically exposed to higher and lower temperatures by successive deposition of weld layers. A time factor greatly influences the hydrogen diffusion and coarsening of pores. Pores of Wall-1 were exposed to higher temperature for longer time due to the increased inter-layer waiting time compared to Wall-2 that could have allowed hydrogen diffusion and pore coarsening. This could be the reason for the presence of large sized pores in Wall-1 which were virtually absent in Wall-2. In

previous studies on pore coarsening [90,138] a single bead wall structure was considered (wall width around 6 to 7 mm) where heat extraction is comparatively faster compared with higher width wall structures such as 45mm studied in this study. As discussed in Section 2.2, only temperature of the top layer was the criteria for deposition of next layer, the temperature of the wall samples below 3 to 4 layers was certainly much higher than measured at the top due to heat sink effect. From the experimental results it can be deduced that the mechanism of formation of large pore is not only a function of solubility limit and temperature alone but also a rate of heat extraction and time that facilitates the movement of entrapped dissolved hydrogen through pipes such as dislocations.

In overall comparison, Wall-2 displayed reduced porosity over Wall-1. It can be said that the porosities that passed upwards through the solidifying melt to the top of the layer were disturbed by the deposition of next layer. The overall hydrogen content was more than the solubility limit so that most of the hydrogen gas was released to the air reducing overall hydrogen content in the wall sample.

4.2.3 Tensile properties

Wall 1 and 2 with 50 and 100°C interlayer temperatures respectively manufactured as per descried in section 3.2.2.5 were tested for tensile properties. Tensile testing was carried out following BS EN ISO 6892-1:2016 as described in section 3.2.2.8. Total six samples, three in horizontal and three in vertical direction, were exacted as shown in Figure 3.8 of chapter 3. The weld consumable is expected to give typical tensile strength, yield strength and % elongation of 265MPa, 120 MPa and 26% respectively, based on data provided by the consumable manufacturer; however, based on the specimen locations in the WAAM walls, not all specimens showed expected properties. A comparable compositional wrought products, 5083 and 5086 reveal 290 and 260 MPa tensile strength, 145 and 115 MPa yield strength and 22 % elongation respectively [127]. Figure 4.6 compares the ultimate tensile strengths of Wall-1 and Wall-2 in horizontal and vertical directions. From Figure 4.6, all the specimens from Wall-2 revealed tensile strength higher than the recommended by manufacturer, except for one specimen (specimen no. 9) that witnessed pores at the fracture surface; however, total three specimens from Wall-1 showed less strength than recommended. Horizontal specimens showed higher tensile properties than vertical specimens in both the wall samples. The average tensile strength of the horizontal specimens was 3.6 and 3.9 % more than vertical specimens for Wall-1 and Wall-2 respectively.

Vertical specimens contained more fusion lines and thus increased entrapped pores, as disused earlier, than the horizontal specimens. The multiple existence of fusion lines and increased pore numbers could be the possible reason for reduced strength for the samples in vertical direction. In case of horizontal specimens, such multiple fusion lines were absent due to its parallel orientation with the direction of layer deposition (torch progression). Comparing the overall strength of the two walls, Wall-2 with higher interpass temperature showed more strength than Wall-1 with marginal difference of 4 MPa.

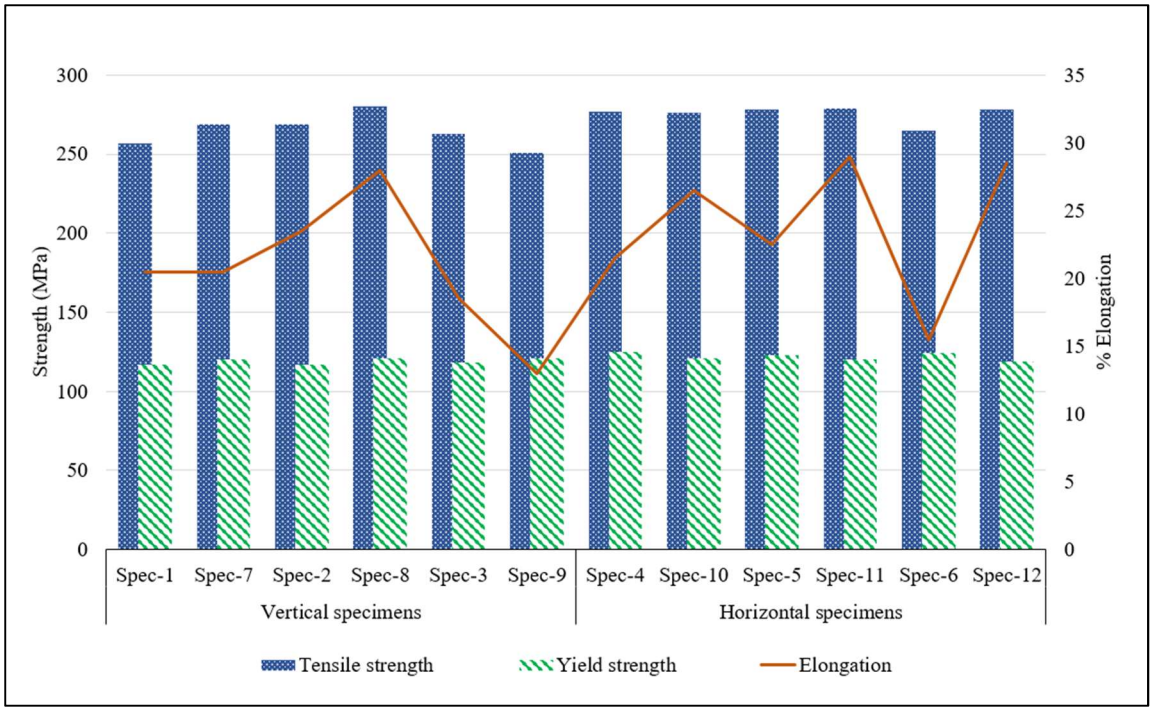

Figure 4.6 Comparison of tensile strengths of specimens extracted from Wall-1 (specimens 1 to 6) and Wall-2 (specimens 7 to 12).

4.3 Part – II Investigations into porosity and hydrogen dissolution in pulsed-MIG and cold metal transfer (CMT)

This section of the chapter is focused on results and related discussion referring to the experiments described in section 3.2.3 i.e. manufacturing of sixteen WAAM walls with combination of interlayer temperature (50 and 100°C), heat input (~ 280 and 120 J/mm), metal deposition technique of MIG variants (pulsed MIG and CMT) and interlayer dwell time (30 seconds and 2 minutes). Further these walls were X-CT scanned for porosity measurement. Hydrogen dissolution study was carried out in order to investigate interrelation and effect of mentioned variables on porosity formation.

4.3.1 Volume consideration

Figure 4.7a and b show XCT scan images of C-HH-T2 and P-HH-T2 samples respectively. Similar porosity distribution data and images were obtained for all 16 samples. From Figure 4.7a and b it was clear that porosity population increased at arc start and stop areas. In general, these areas are machined off from the final part, therefore, they are omitted from the analysis. A stable metal deposition area, roughly more than 15 mm away from arc start and stop and more than 6 mm above the substrate, was considered for detailed analysis. Porosity observable at the YZ plane from the representative micrographs of C-HH-T2 and P-HH-T2 samples can be seen in Figure 4.7c and d.

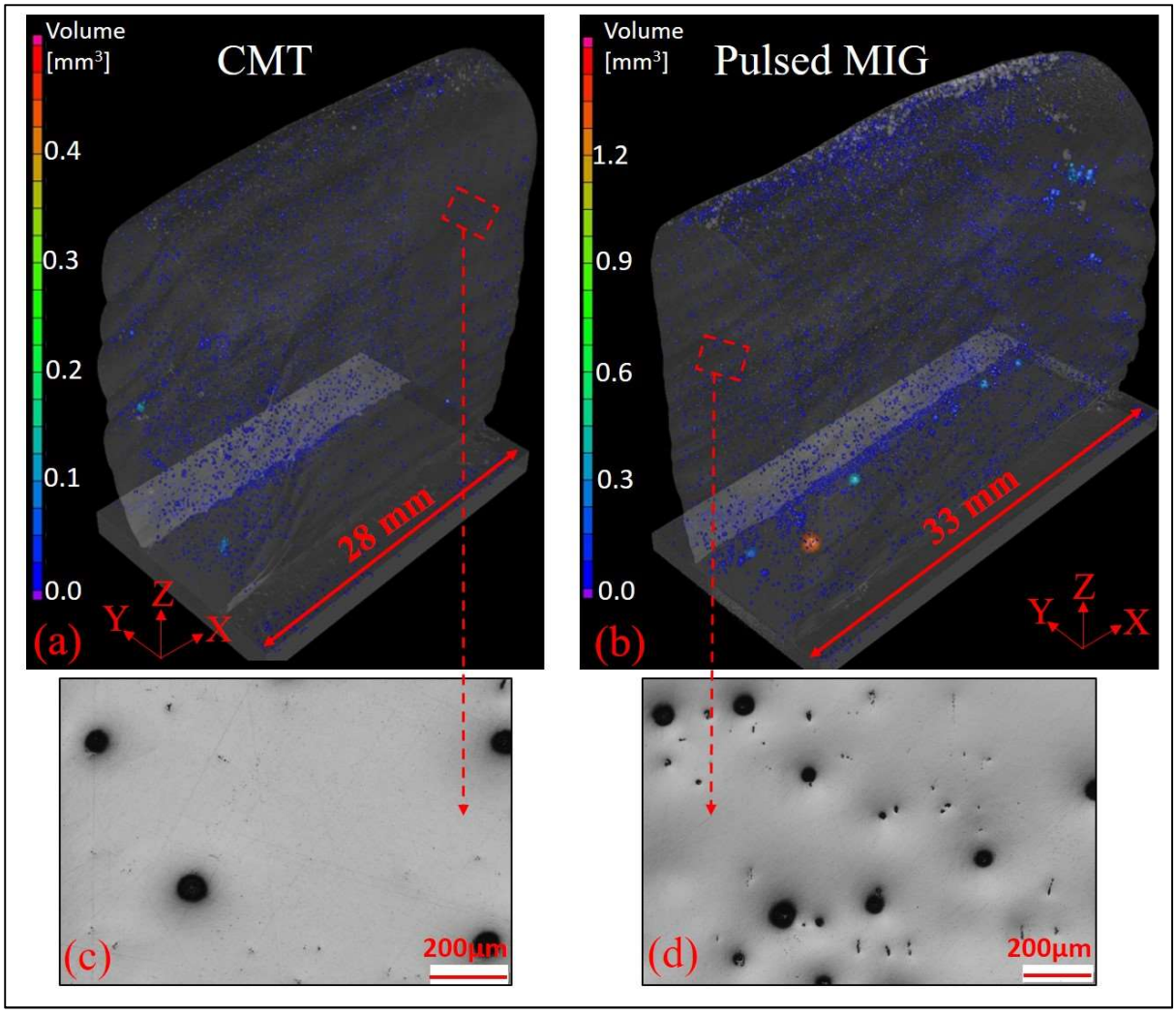

Figure 4.7 XCT image of Samples (a) C-HH-T2 and (b) P-HH-T2. Porosity morphology in the same samples (c) C-HH-T2 and (d) P-HH-T2.

4.3.2 Porosity content comparison

4.3.2.1 Effect of metal deposition techniques (Pulsed MIG versus cold metal transfer (CMT))

Processing techniques showed significant effect on the pore content. Pulsed MIG samples displayed higher overall pore volume compared with samples manufactured using CMT technique. Table 4.3 compares respective overall pore volume of samples manufactured with different conditions such as interlayer-temperature, interlayer-dwell-time and heat input. Dip metal transfer mechanism, oscillating wire with high frequency and low heat input offered by CMT developed less porosity [78,92] compared to pulsed MIG samples. As an exception, pulsed MIG sample processed with 30 seconds interlayer-dwell-time and high heat input (P-HH-t1) revealed reduced porosity compared to an equivalent CMT sample (C-HH-t1) by 6%. Samples prepared using CMT and pulsed MIG with 100°C interlayer-temperature and high heat input (C-HH-T2 and P-HH-T2) disclosed least that is 10% difference in the porosity content. Conversely, 50°C interlayer-temperature and low heat input processed samples, C-LH-T1 and P-LH-T1, exhibited highest difference of 390% in porosity content. On similar note, 120 seconds interlayer-dwell-time and low heat input samples from CMT and pulsed MIG (C-LH-t2 and P-LH-t2) also showed significant 360% difference in porosity content.

Table 4.3 Overall Pore volume percentage of samples manufactured using different interlayer-temperatures (sets 1 and 2) and interlayer-dwell-times (Sets 3 and 4).

Process	Heat input	Sample ID	Overall pore volume % with respect to sample volume
Pulsed MIG (Set 1)	High	P-HH-T1	0.106
		P-HH-T2	0.063
	Low	P-LH-T1	0.152
		P-LH-T2	0.122
CMT (Set 2)	High	C-HH-T1	0.05
		C-HH-T2	0.057
	Low	C-LH-T1	0.031
		C-LH-T2	0.041
Pulsed-MIG (Set 3)	High	P-HH-t1	0.066
		P-HH-t2	0.127
	Low	P-LH-t1	0.077
		P-LH-t2	0.175
CMT (Set 4)	High	C-HH-t1	0.07
		C-HH-t2	0.061
	Low	C-LH-t1	0.049
		C-LH-t2	0.038

4.3.2.2 Effect of heat input

Similar processed CMT and pulsed MIG samples witnessed opposite effect of heat input on overall porosity content. Irrespective of the control methods such as interlayer-dwell-time or interlayer-temperature, all CMT samples manufactured with low heat input showed reduced overall pore volume than high heat input samples (refer Table 4.3). Largest difference of 61.2% in the porosity volume for CMT samples was noticed between high and low heat input samples (C-HH-T1 and C-LH-T1 having 0.05% and 0.031% overall pore volume respectively) produced using 50°C interlayer-temperature while smallest difference of 39% was witnessed between sample produced with 100°C interlayer-temperature.

On the contrary, in case of pulsed MIG processed samples, high heat input samples disclosed less pore by total volume than low heat samples as can be seen from Table 4.3. Highest difference, 93.6%, was present between pulsed MIG samples manufactured with 100°C interlayer-temperature (P-LH-T2 and P-HH-T2 with 0.122% and 0.063% overall pore volume respectively). Samples with 30 seconds interlayer-dwell-time (P-LH-t1 and P-LH-t2) showed least difference of 16.6%.

4.3.2.3 Effect of an interlayer-temperature and dwell time

One of the important parameters in the study, interlayer-temperature, affected the pore content. Pulsed MIG processed high interlayer-temperature samples showed reduced overall pore content compared low interlayer-temperature samples for similar heat input cases. For high heat input case, the difference was observed around 68% for P-HH-T1 and P-HH-T2 samples and it was reduced to 24.5% for (P-LH-T1 and P-LH-T2) low heat input samples (Table 4.3); however, reversed trend was observed for CMT samples. More porosity was revealed by high interlayer-temperature samples compared to low interlayer-temperature that can be seen by comparing C-HH-T2 with C-HH-T1 and C-LH-T2 with C-LH-T1.

Interlayer-dwell-time also found to have an influence on porosity. Results from 30 and 120 seconds interlayer-dwell-time could be compared with 100°C and 50°C interlayer-temperature. Considering pulsed MIG process, the 30 seconds interlayer-dwell-time samples showed lower porosity than 120 seconds irrespective of the heat input. The difference as high as 92% and 127% was reported for high and low heat input samples respectively. CMT samples showed increased porosity content for 30 seconds interlayer-dwell-time compared to 120 seconds samples. The difference of 29% and 15% for low and high heat input samples was observed.

4.3.3 Pore size

Pore distribution and size within each sample was measured by XCT scans and relative percentage population was identified by processing software. Pore size smaller than 0.1 mm that is 100 µm was not considered in the study due to machine restrictions and its negligible effect on fatigue life [139]. All the identified pores were categorised into 3 sections depending upon the size; small pores ranging from 0.11 mm to 0.2 mm, medium from 0.21 mm to 0.3 mm and large with size more than 0.31 mm. Pore count fraction for each size range is provided in Table 4.4.

Table 4.4 Pore size wise pore count fraction comparison for pulsed MIG and CMT processed samples.

Pore diameter range (mm)	**Pore count fraction (%)**	
	Pulsed MIG	CMT
Small (0.11 – 0.20)	52.79 – 62.9	60.69 – 77.47
Medium (0.21 – 0.30)	32.34 – 42.36	20.0 – 35.59
Large (≥ 0.31)	3.3 – 5.78	1.15 – 4.63

From Table 4.4 it can be deduced that medium and large sized pores were dominant in pulsed MIG samples, however, small pores were largely found in CMT processed samples. Despite some small differences, the pattern was replicated in both interlayer-temperature and interlayer-dwell-time controls as can be seen from Figure 4.8 a and b. For all the considered 16 samples, it was evident that small pores were predominant with total pore count of more than 50%. Further, it can be said that significant amount of medium sized pores were present. Amongst all the CMT samples, small pores were counting from 60.67% to 77.47% of total pores in respective samples. The count percentage of small pores was relatively less for pulsed MIG samples which was varying from 52.79% to 62.9%. In case of medium size pores, relatively higher count was observed in pulsed MIG samples which was varying from 32.2%

to 42.3% while CMT samples showed lower range from 20% to 35.5%. Similar to medium sized pores, large pores were around 3.3% to 5.8% in pulsed MIG processed samples and much less in CMT samples (1.15% to 4.63%).

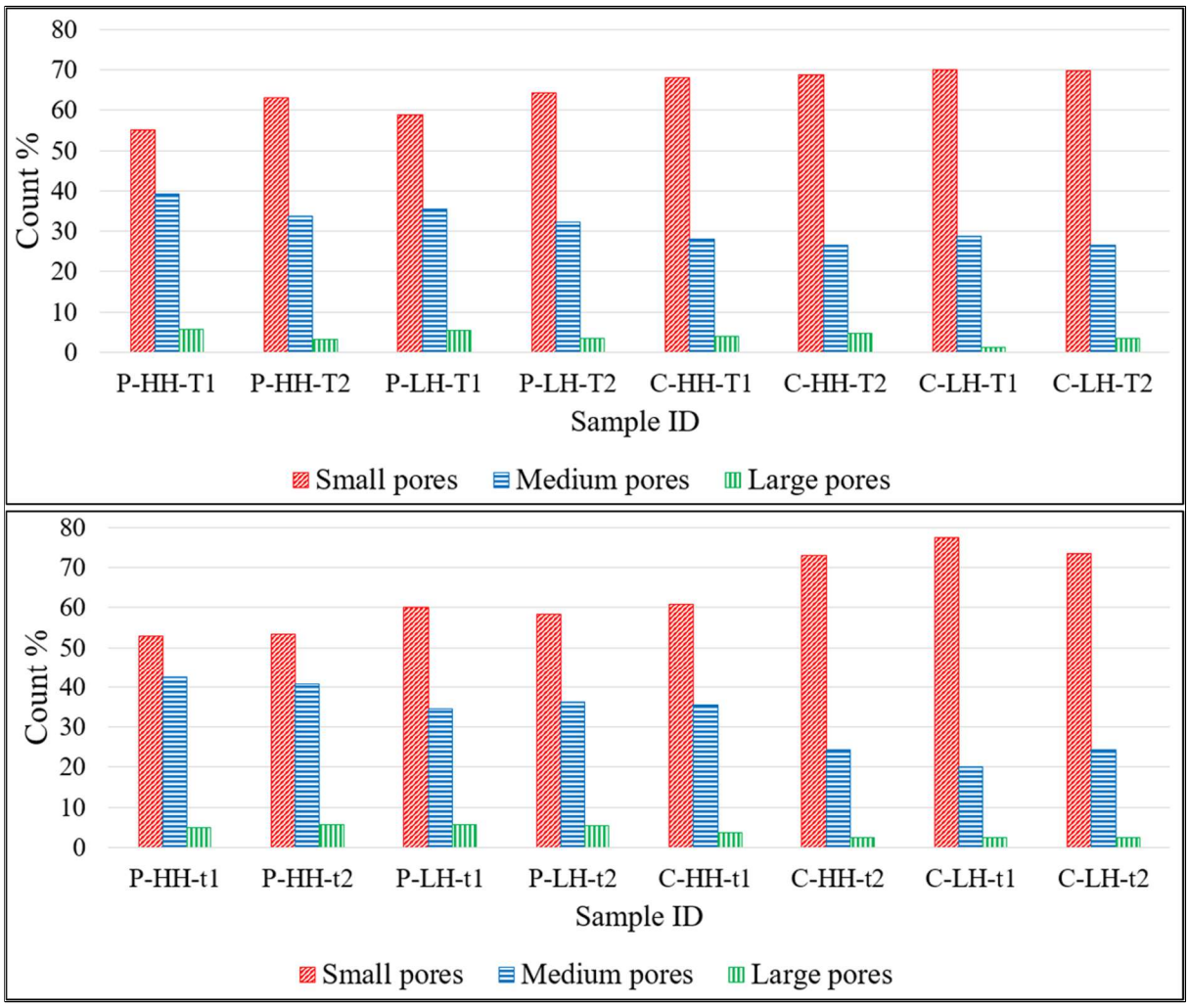

Figure 4.8 Count percentage of small, medium and large sized porosity ranges in the samples manufactured with (a) interlayer-temperature control and (b) interlayer-dwell-time control.

4.3.4 Pore size distribution

XCT scans results of pore size distribution are shown in Figure 4.9 to Figure 4.12. Probability distribution of pores with respect to pore size, interlayer-temperature and high and low heat inputs on CMT processed samples is illustrated in Figure 4.9. From the probability curves, average pore size, hence, the peak of curves was same in all four cases that is 0.2 mm, in split of minor increment in the average for high heat input samples. High heat input samples showed wider pore size distribution than low heat input. Despite the heat input, high-interlayer-temperature samples revealed greater variation in porosity diameter distribution than low interlayer-temperature. Hence, samples prepared with high interlayer-temperature and high heat input had increased irregularities in pore sizes.

Similar conditions were applied to pulsed MIG samples and surprisingly, the trend was found to be reversed for interlayer-temperature controlled samples as shown in Figure 4.10. Samples from lower interlayer-temperature showed relatively higher variance and increased average pore size inferring that

low interlayer-temperature and low heat input imparted more irregularities. On different note, average pore size was not different than obtained for CMT samples (0.2 mm) with slight variation between low and high interlayer-temperature samples.

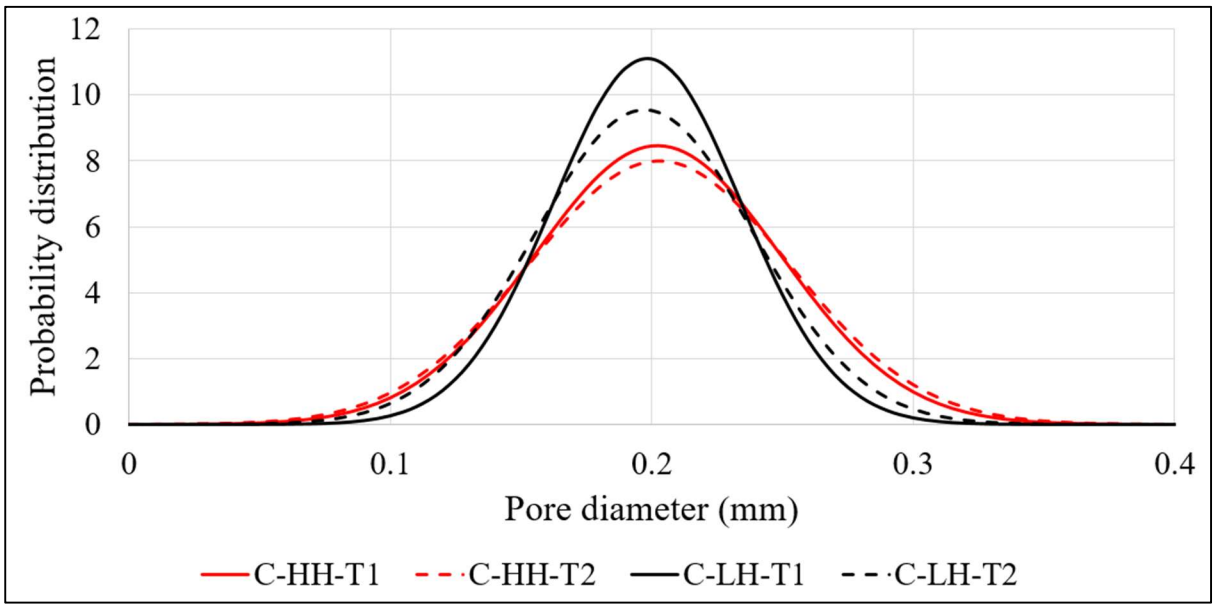

Figure 4.9 Effect of interlayer-temperature and heat input on normal distribution of pore size in CMT samples (Set 2).

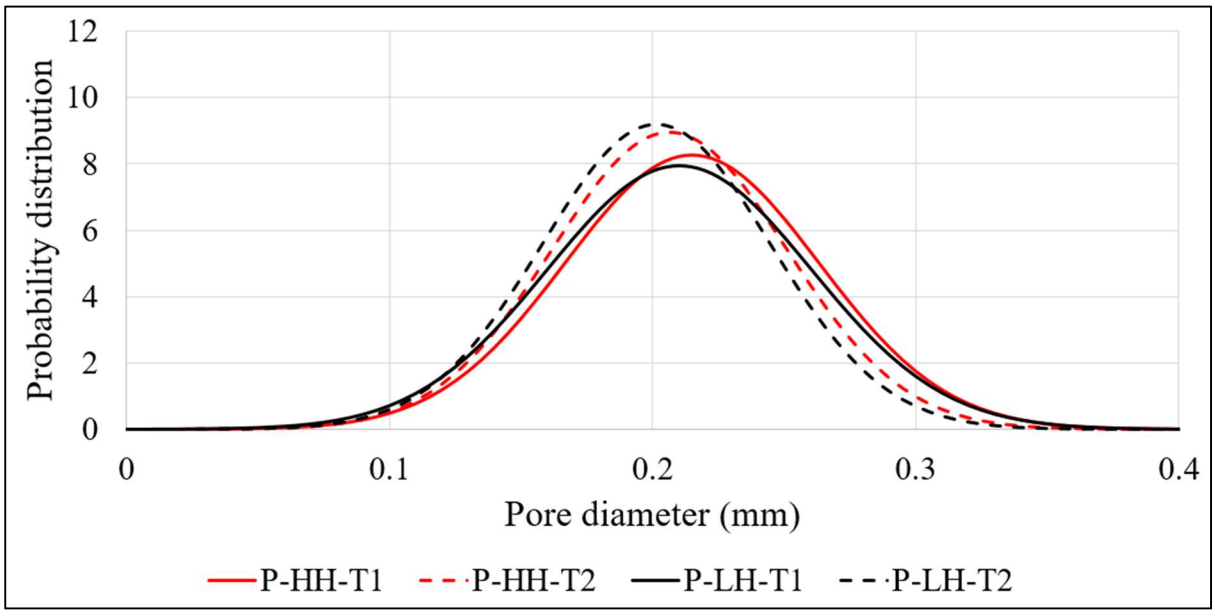

Figure 4.10 Effect of interlayer-temperature and heat input on normal distribution of pore sizes in pulsed MIG samples (Set 1).

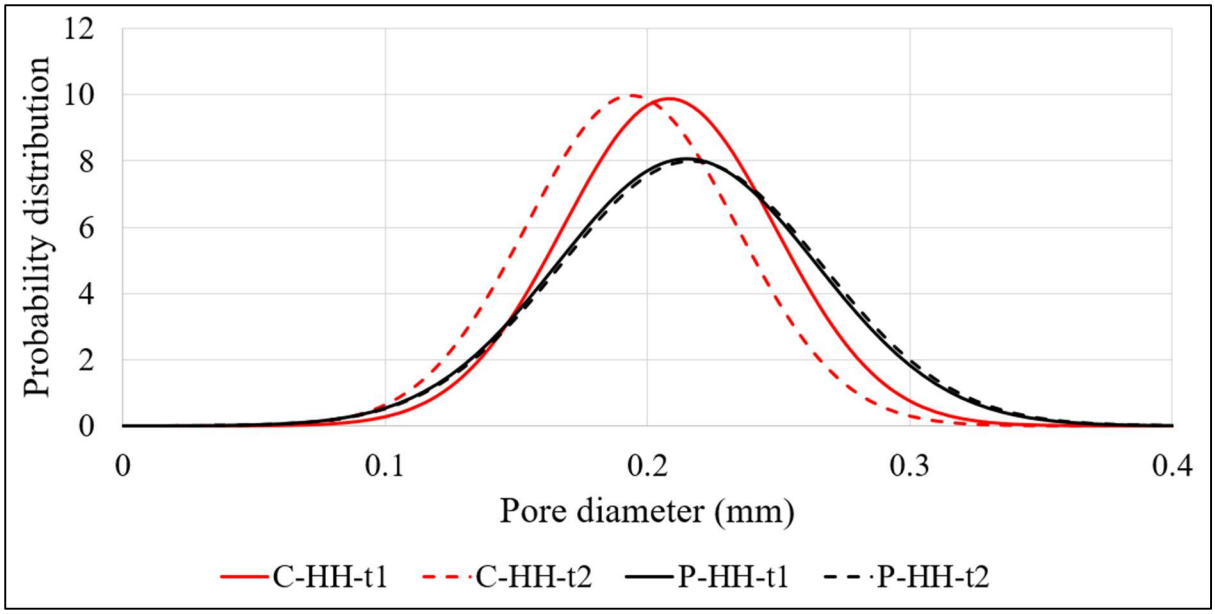

Figure 4.11 Effect of interlayer-dwell-time and metal deposition technique (CMT and pulsed MIG) on normal distribution of pore size for high heat input condition.

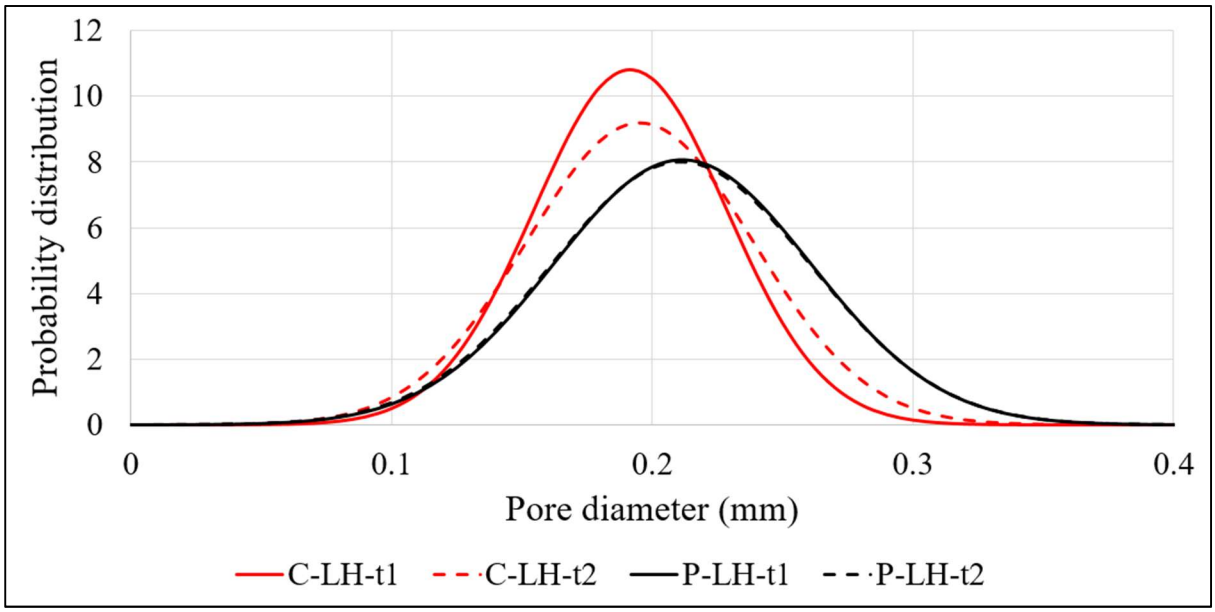

Figure 4.12 Effect of interlayer-dwell-time and metal deposition techniques (CMT and pulsed MIG) on normal distribution of pore size for low heat input condition.

The overlapping curves of pulsed MIG samples in Figure 4.11 and Figure 4.12 it can be said that interlayer-dwell-time control showed no observable influence for pulsed MIG processed samples for both low and high heat inputs. For both high and low heat input samples, when CMT and pulsed MIG samples were compared, pulsed MIG displayed increased variance than CMT samples. This implies that CMT samples had narrower pore size distribution and smaller pores than pulsed MIG. In addition, CMT showed smaller average pore size than pulsed MIG.

4.3.5 Physical pore distribution and average pore location

Figure 4.13 to Figure 4.16 represent the comparison of the effect of interlayer-dwell-time, interlayer-temperature, pore diameter and deposition process on distribution of small and medium sized pores as a function of normalised pore distance from centroid of all pores in a given sample. From Figure 4.13, it can said that the pulsed MIG samples had higher average normalised distance from centroid of all pores than CMT samples. The fact indicated the close occurrence pores in CMT samples than pulsed MIG. In addition, a bell curve of CMT small pores was broader than pulsed suggesting that higher variance. This indicates that pores distribution in pulsed MIG sample was more uniform than CMT sample. Wider distribution of medium sized pores was evident indicating lower predictability for number of pores in the selected area for analysis. Regardless of pore size, CMT sample showed shorter normalised distance from the centroid of all pores than pulsed MIG.

CMT samples were considered in Figure 4.14 for comparison of effect of interlayer-temperature on normal distribution of normalised distances from centroid of all pores. Disregarding the pore size, samples from high interlayer-temperature illustrated larger average normalised distance between the centroid of all pores than low interlayer-temperature samples which indicates pores were widely distributed in the high interlayer-temperature sample. Further, the 100°C interlayer-temperature samples revealed increased variance suggesting pores were widely distributed than 50°C interlayer-temperature samples. Small sized pores had lower variance and reduced average normalised distance between centroids indicating small pores had uniform distribution.

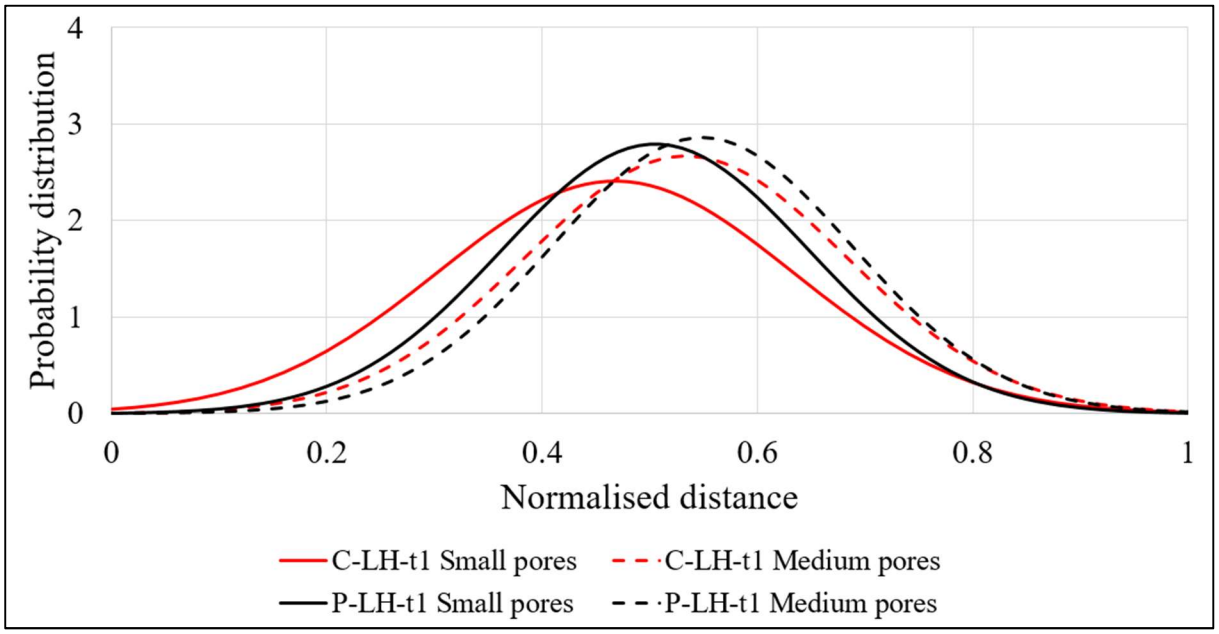

Figure 4.13 Effect of CMT and pulsed MIG technique on normal distribution of pore normalised distance between centroids of all pores for small and medium sized pores.

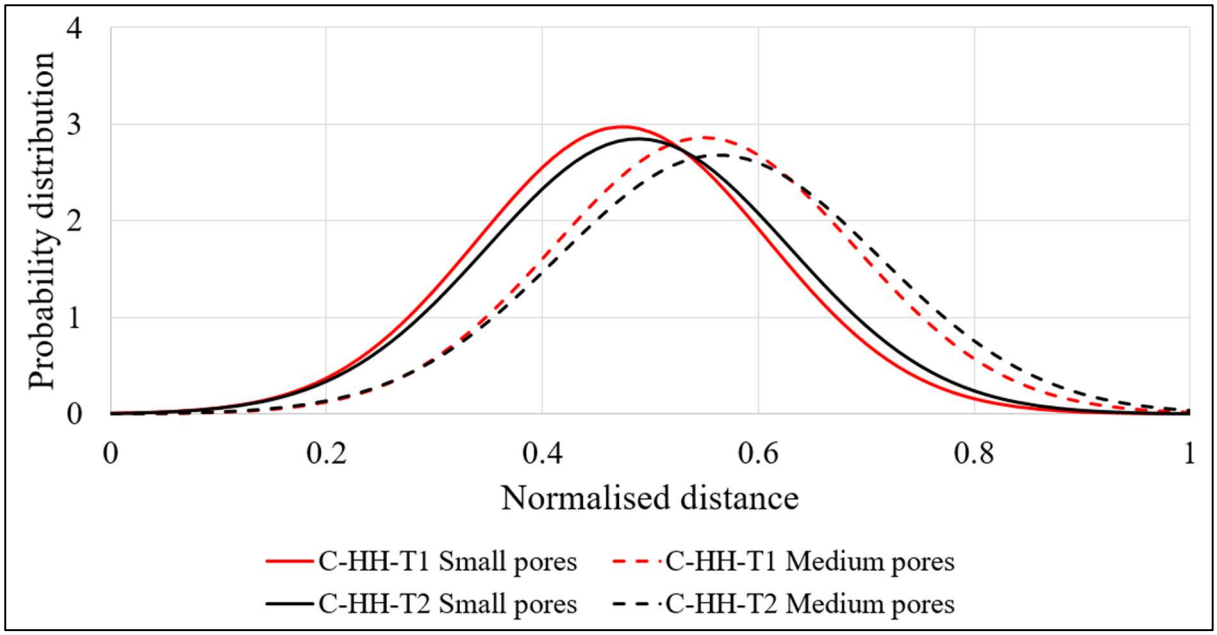

Figure 4.14 Effect of interlayer-temperature and metal deposition techniques (CMT and pulsed MIG) on normal distribution of pore normalised distances from centroid of all pores for small and medium pores.

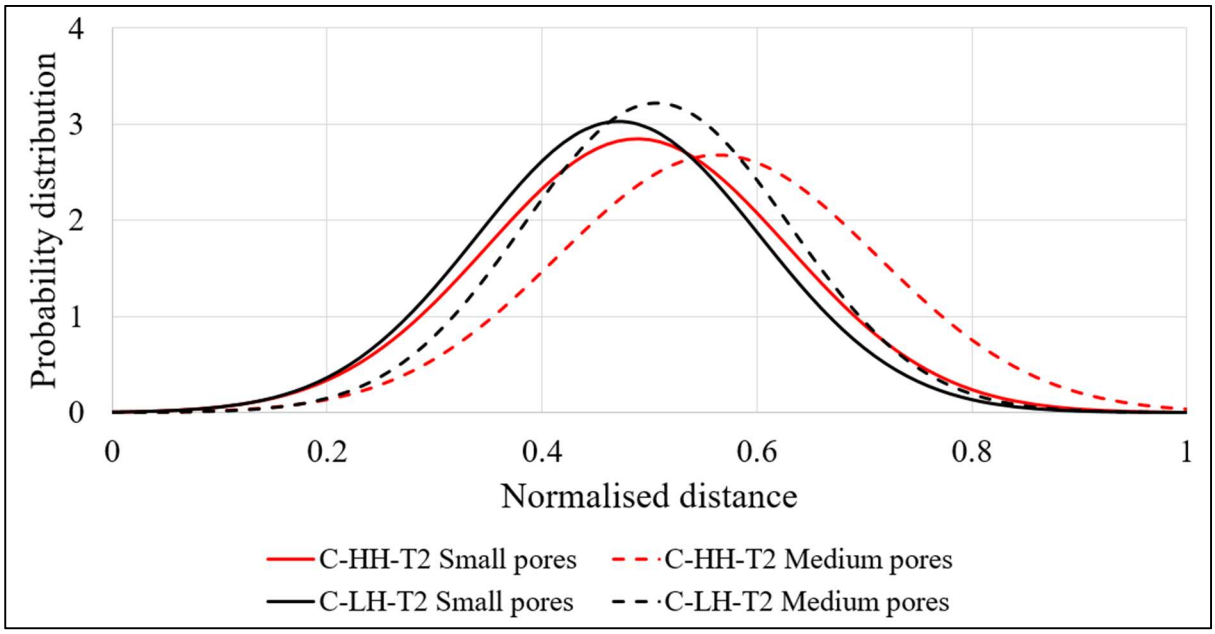

Figure 4.15 Effect of heat input on normal distribution of pore normalised distances from centroid of all pores for small and medium pores.

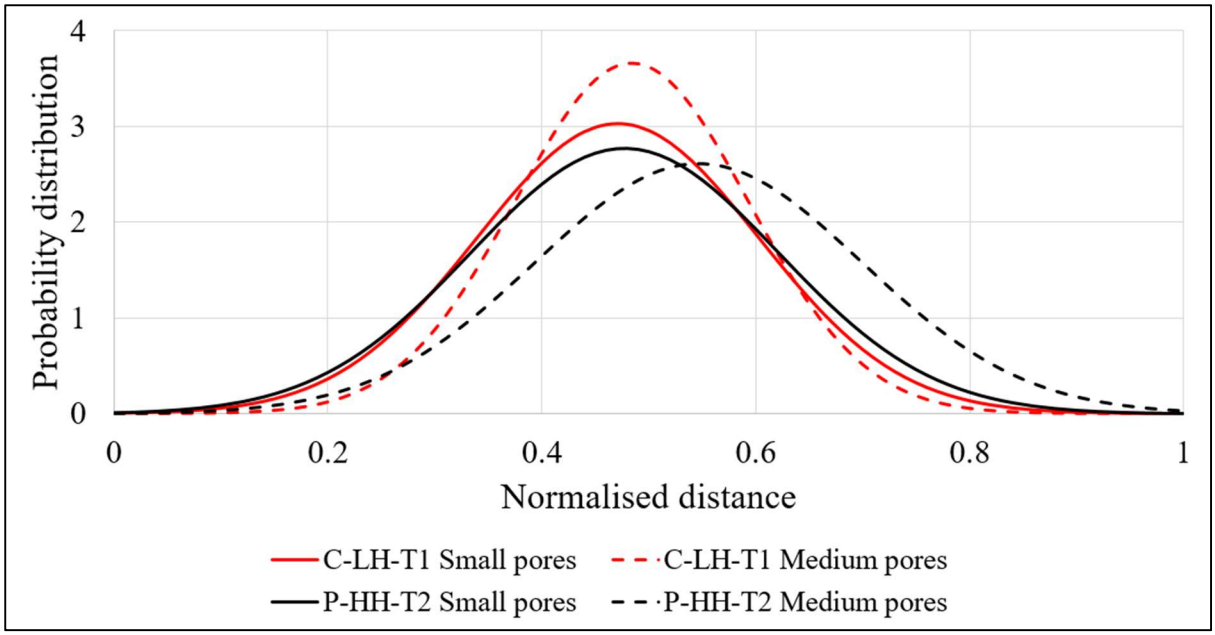

Figure 4.16 Comparison of normal distribution of pore normalised distances from centroid of all pores for small and medium pore for high and low heat content condition.

Effect of heat input in normalised distances are shown in Figure 4.15. The low heat input samples showed shorter difference in the average normalised distance compared to high heat input samples. For medium pores, the difference in normalised was appreciable, however, it was negligible for small sized pores. Larger pores showed less variance than the small pores. Also, medium pores revealed relatively wider distribution than smaller pores.

High and low heat content conditions of metal deposition are compared for small and medium sized pores in Figure 4.16. Similar results were obtained following shorter normal distance and more uniform distribution for CMT samples than pulsed MIG processed samples for both pore types. Appreciable difference in average normal distance was recorded for small and medium sized pores from pulsed MIG samples.

4.3.6 Pore volume

The discussed pore distribution and pore size directly reflect into the overall pore volume. Small pores found to be predominating in CMT samples as can be seen from Figure 4.17a and b where small pores showed higher pore volume fraction (>50%) than medium and large sized pores. Only one CMT sample, C-HH-t1, witnessed small pore volume fraction less than 50%. For medium sized pores, pore volume fraction varied from 31.5% to 44.7% of overall pore volume in respective samples. Pore volume fraction difference between small and medium pores was minimum for C-HH-t1 sample (2.55%) and maximum for (C-HH-t2) sample. Large sized pores occupied only 2.72% to 9.76% of overall pore volume.

However, distinctly different results were obtained in case pulsed MIG samples (refer Figure 4.17a and b). Although the small pores were higher in numbers than medium and large pores, medium sized pores showed higher pore volume fraction than small and large pores; the exception being P-HH-T2 and P-LH-T2. It can be argued here that, six samples out of eight displayed higher pore volume fraction for medium sized pores than volume fraction for small and large sized pores. Medium and small sized pores

did not show large difference in the pore volume fraction. The difference was minimum 0.91% for sample P-LH-t1 and maximum for P-HH-t1 (9.71%). Large pores from pulsed MIG samples showed increase pore volume fraction than CMT sample. The average pore volume fraction of all the large sized pores from CMT was 6.1% while it was 10.8% for pulsed MIG.

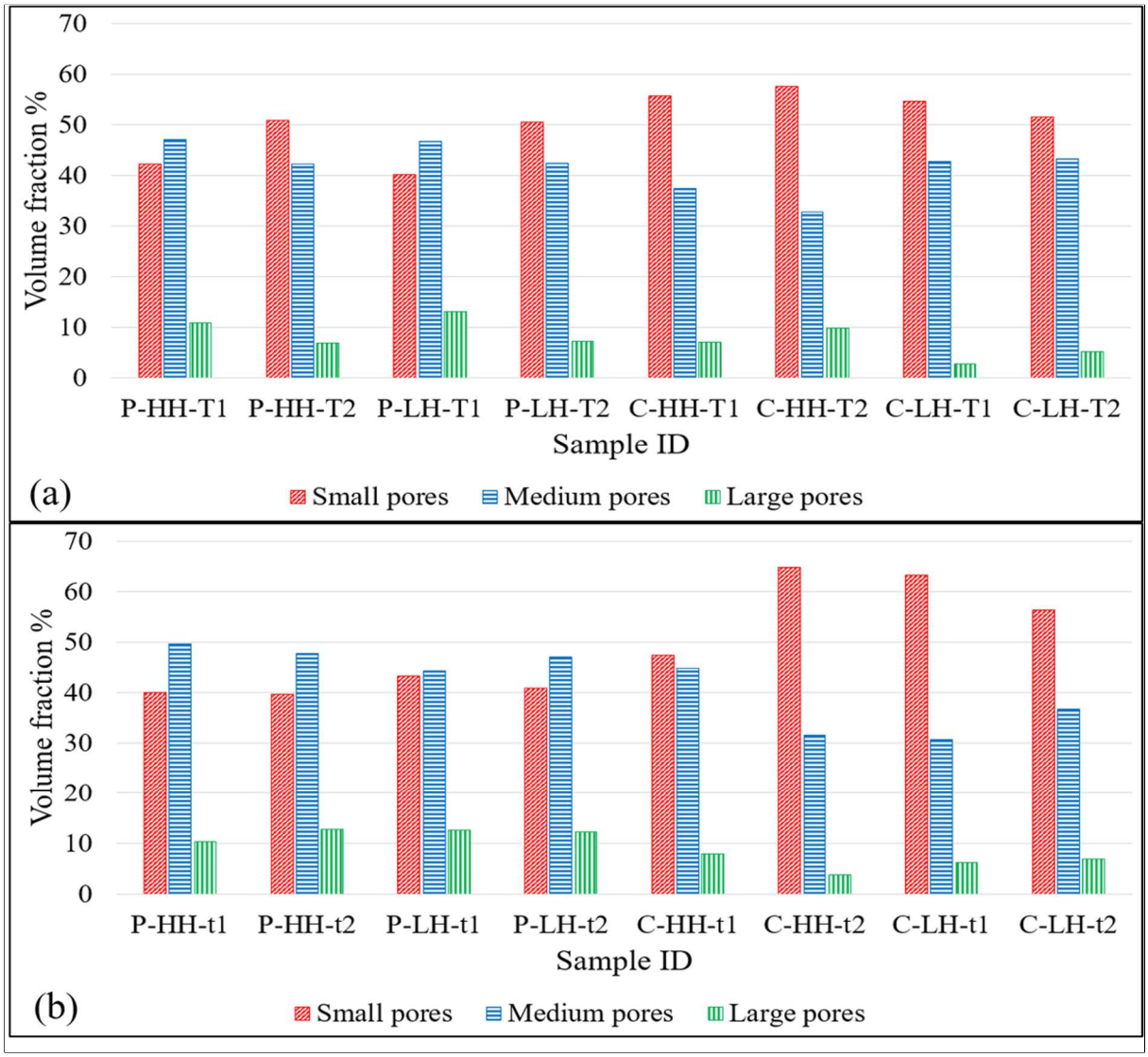

Figure 4.17 Comparison of pore volume fraction of small, medium and large sized pores in 16 samples manufactured with interlayer-temperature control (a) and interlayer-dwell-time control (b) methods.

4.3.7 Dissolved hydrogen

For maximum clarity of results, two sets of samples, DH1 and DH2, were carefully chosen. A set had total two samples, one from CMT and one from pulsed MIG. The set was selected such a way that CMT and pulsed MIG samples had the largest difference in porosity content (refer Table 4.5). The dissolved hydrogen test does not only detect the atomic dissolved hydrogen coming out solid solution of aluminium but also hydrogen released from present pores. Thus, detected hydrogen is a sum of atomic hydrogen from solid solution (becomes diatomic) and hydrogen molecules from pores. Dissolved hydrogen term will be used in further discussion referring to the atomic hydrogen dissolved in solid

solution of aluminium. From this it is clear that absorbed hydrogen forms pores or dissolves in solid solution of aluminium.

Table 4.5 Results of dissolved hydrogen test for CMT and pulsed MIG samples.

Set ID	Process / technique	Sample ID	Pore volume fraction (%)	Detected hydrogen content (ppm)	Hydrogen content (ppm) / pore volume fraction (%) (ppm/volume fraction %)
DH1	CMT	C-LH-T1	0.031	0.834	26.900
	Pulsed MIG	P-LH-T1	0.152	0.993	6.530
DH2	CMT	C-LH-t2	0.038	1.020	26.840
	Pulsed MIG	P-LH-t2	0.175	1.250	7.140

CMT and pulsed MIG methods influenced the total hydrogen content detected in solid aluminium as can be evidenced from Table 4.5. Interestingly, it was noticed that both the sets of samples witnessed comparable hydrogen, however, after considering the difference between pore count and pore volume, it can be deduced that there could be difference in the amount of dissolved hydrogen. It is reflected in Table 4.5 as total hydrogen available per pore volume. Lesser pore volume of CMT samples had around hydrogen to pore volume ratio around 27 ppm/volume fraction while it was around 7 ppm/volume fraction for pulsed MIG. It is clear at the point that the formation of pores has a great effect on hydrogen dissolution in aluminium.

It is worthwhile mentioning here that the feed stock wire had around 7.5ppm/100gm of detected hydrogen which was impressively higher than the detected hydrogen in deposits. The possible reasons for the differences in hydrogen content of feed stock and build deposit have been focused and elaborated in following section.

From Table 4.5, pore volume fraction when compared for pulsed MIG and CMT, it can be said that it was much higher in pulsed MIG. For both the Sets DH1 and DH2, pulsed MIG showed pore volume fraction approximately five times higher than CMT. Surprisingly, hydrogen content in both the sets was found comparable. A ratio of detected hydrogen to total pore volume in respective sample was calculated. Hence, total hydrogen available per pore volume fraction in CMT sample was around 7 ppm / pore volume fraction whereas the ratio was around 26 ppm / pore volume fraction for pulsed MIG samples. It is clear that much higher hydrogen was available per pore volume fraction for CMT samples than pulsed MIG. The fact indicates that hydrogen can be present in the solid solution as a dissolved hydrogen which is discussed in next section.

4.3.8 Relation between interlayer-temperature and interlayer-dwell-time control

Methodology chapter discussed about the manufacturing of samples based on interlayer-temperature and interlayer-dwell-time control methods which were independent of each other and considered

entirely separate in this study; however, interlayer-dwell-time indirectly controls interlayer-temperature. It can be explained with the support of the research performed by Wu et al. and Xiong et al. [110,140,141]. Researchers discussed the variation in temperature of a forming part with respect to number of layers and substrate effects. Temperature of the part being manufactured found to be increasing with the number of layers being deposit due to heat accumulation. Effect of heat extraction by substrate is prominent for initial layers which diminishes as number of layers increases. Due to the reduced rate of heat extraction, heat accumulates in the forming part raising its temperature after each and every layer deposition. Hence, initial layers cool rapidly encountering drastic temperature reduction when compared to higher number of layers. Thus, to maintain fixed interlayer-temperature that is 50°C or 100°C for initial layers, new layers were deposited with fairly short time gap, hence, short interlayer-dwell-time. Subsequently, this time was increased as number of layers increased due to heat accumulation.

Time required by molten metal to reduce its temperature from freezing temperature to 50°C is more than cooling down to 100°C. Applying similar concept in metal deposition, time taken by deposited metal to cool to 50°C interlayer-temperature is more than time taken to reach 100°C interlayer-temperature which indirectly suggests change in interlayer-dwell-time for maintaining two interlayer-temperatures. Hence, for maintaining interlayer-temperature 50°C requires longer interlayer-dwell-time and 100°C interlayer-temperature requires shorter dwell time. At this point, it can be argued that samples prepared with 100°C interlayer-temperature were hotter all the time than samples manufactured with 50°C interlayer-temperature that possessed increased time to release heat.

On the other hand, fixed time based samples were manufactured irrespective of temperature consideration. Therefore, considering heat accumulation effect discussed previously [141], interlayer-temperature was changing from low to high for initial layers and later number layers respectively. It can be easily notice that shorter interlayer-dwell-time of 30 seconds enforced increased heat accumulation compared to longer 120 seconds interlayer-dwell-time that supported more time for heat dissipation. Hence, samples with 30 seconds interlayer-dwell-time were hotter and possessed increased interlayer-temperature than samples prepared with 120 seconds of interlayer-dwell-time, however, the temperature was not constant. It can be concluded from the above discussion that samples prepared with 100°C interlayer-temperature were comparable with samples manufactured using 30 seconds interlayer-dwell-time and samples from 50°C interlayer-temperature were similar to samples from 120 seconds interlayer-dwell-time, provided other variables being unchanged. Interlayer-temperature variation during fixed time deposition method can be found in microstructure chapter.

4.3.9 Effect of metal deposition methods and penetration

CMT and pulsed MIG processes possess different characteristics of penetration that is depth of remelting of portion of metal from earlier deposited layer while depositing a new layer. CMT technique shows lower penetration than pulsed MIG, as discussed in detail in Literature review chapter. A schematic of penetration effects of pulsed MIG and CMT are compared in Figure 4.18 a and b. Short circuiting mode of metal transfer and lower heat input in CMT are governing factors that controls the penetration. Electronically controlled oscillatory motion of wire as well as arc on and off effects mainly supports in reducing the overall heat input and arc energy [3,78]. In pulsed MIG process, globular and spray transfer metal deposition and relatively higher heat input increases the penetration. Relatively

constant arc length increases overall arc energy that increases penetration. Current values were seen touching zero hence, heat input in CMT, however, this is not apparent in pulsed MIG. The difference in penetration at single layer deposition can be seen in Figure 4.18 c and d.

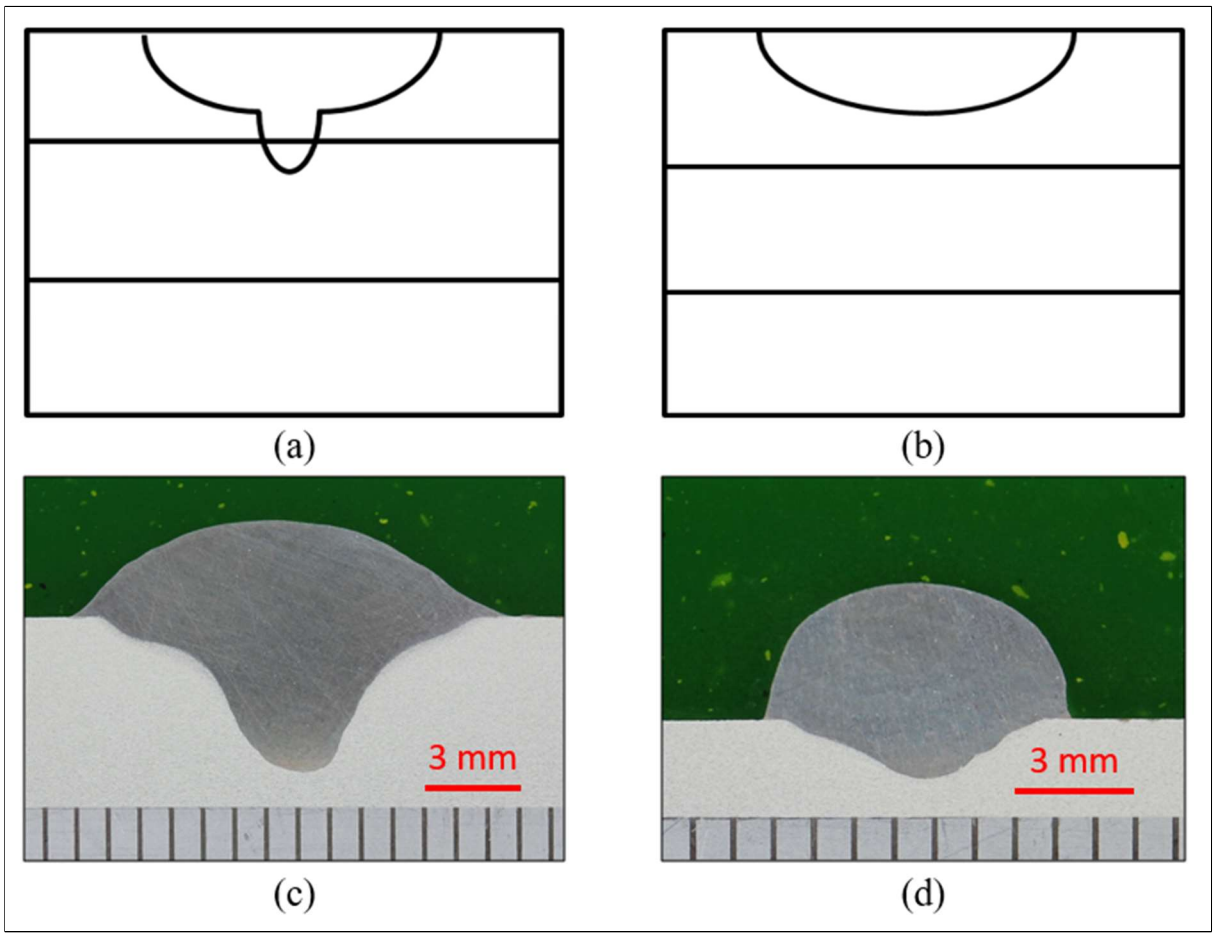

Figure 4.18 Difference in penetration obtained from pulsed MIG and CMT shown in schematic form (a) and (b) and macro-graphs (c) and (d).

From Figure 4.18 it can be asserted that pores at the top region of a layer were entirely removed by deposition of successive metal layer due to arc penetration effect. Pores from the particular portion of the layer were eliminated due to formation of liquid metal. Pores that is hydrogen from the melted region is expected to get carried into newly deposited and re-melted liquid aluminium as a dissolved gas forming new pores and/or releasing to the atmosphere. The phenomena depends upon the local hydrogen concentration and rate of absorption and evolution of hydrogen gas [14]. Following Figure 4.19, multiple pores can be clearly seen at the upper region of top layer in samples of the both processes. While depositing the successive layer, pores from the area that falls under penetration area gets removed. Pores in the region below penetration area that is lower portion of a layer and interlayer-region remains intact (refer Figure 4.19). This is because the arc and heat cannot be reach the entire depth of previous layer, hence, has a limited penetration. Pore banding at interlayer-region is prominent in CMT and pulsed MIG samples that can be seen in lengthwise direction in Figure 4.19. Metal depositing technique and its effect on hydrogen absorption for CMT and pulsed MIG is outlined in Figure 4.20.

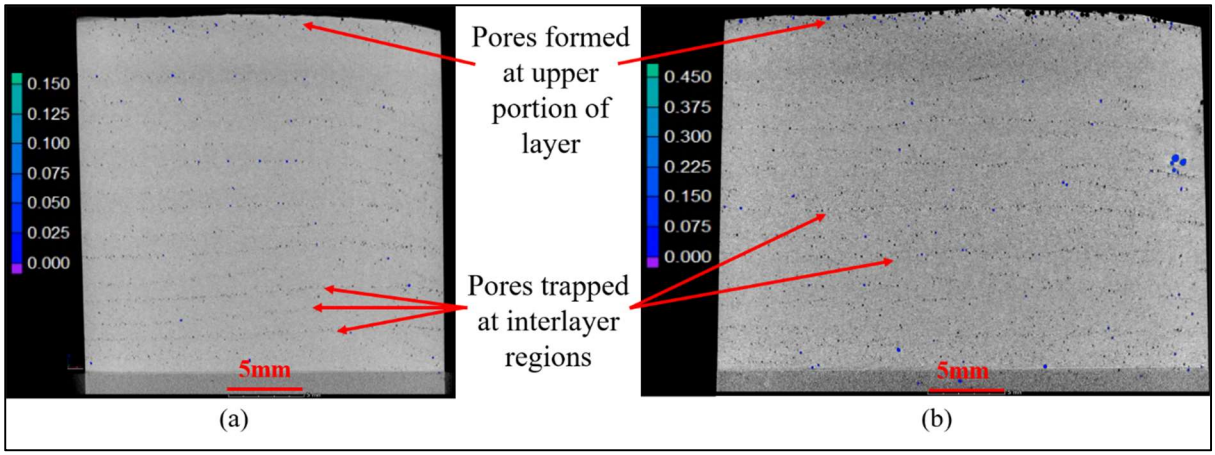

Figure 4.19 XCT image revealing porosity distribution in longitudinal direction of metal deposition by (a) CMT technique and (b) pulsed MIG process.

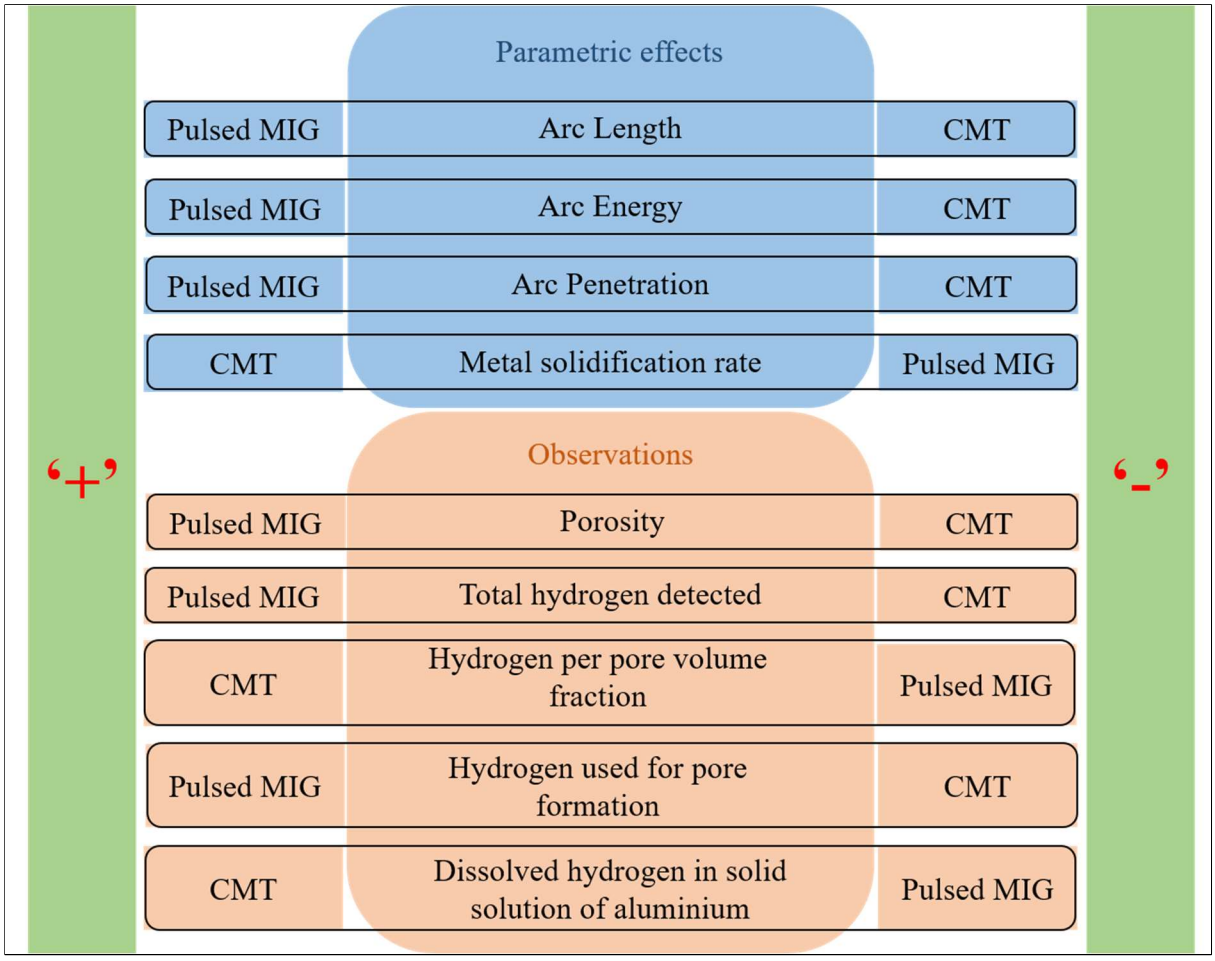

Figure 4.20 Effect of pulsed MIG and CMT metal deposition techniques on hydrogen absorption.

Previous study by Devletian and Wood [136] clearly stated that the pore banding is common phenomena in welding of aluminium particularly by pulsed MIG method which is alike banding of solutes elements in welds. The particular porosity entrapped zone was found as a result of drastic solidification rates encountered at solid-liquid interface while depositing liquid metal on solidified previous layer. In the present study, instead of depositing the layers adjacent to each other as in welding, layers were deposited

in different manner, however, the basic process of pulsed MIG deposition/operation and welding wire were same. It can be proclaimed that the banding observed in additive manufactured samples resembles with that being observed in welding process. Inconstant solidification rates influenced pore banding more than any other factor. Another possibility of formation of increased pores at the interface could be the pore formation in solid state that is secondary porosity. When the temperature of metal raises above or upto the solidus temperature there are chances of formation of secondary porosity due to movement of hydrogen atoms and molecules. Metal deposition in a layer format has seen increase of developing part temperature upto the required temperature.

4.3.10 Absorbed hydrogen

According to Grigorenko [142] pore formation will take place when the hydrogen concentration at the solid-liquid interface reaches threshold value that is maximum solubility of hydrogen in solid aluminium. Liquid aluminium at the hotter central area of an arc from pulsed MIG absorbs hydrogen up to maximum solubility limit and it is then distributed to surrounding liquid metal by convection. Hydrogen globule formation and its shape, size and distribution in solidifying aluminium is determined by total hydrogen pressure, nucleation and growth kinetics, solubility considerations and solidification morphology [136].

As per earlier discussion and from Table 4.5 it can be argued that CMT samples possessed more hydrogen availability for porosity formation than pulsed MIG samples. Pulsed MIG samples from sets DH1 and DH2 had around 5 times higher porosity volume fraction than CMT samples. On the contrary, CMT samples showed higher hydrogen availability per porosity volume fraction than pulsed MIG sample by 4.1 and 3.7 times for DH1 and DH2 set respectively irrespective of similar amount of available hydrogen. The values refers to the fact that there is dissolved hydrogen in solid aluminium. If it is considered that all the pores were formed due to hydrogen and there was no pore formed from solidification shrinkage, it will not be absurd to consider that more hydrogen was remain dissolved in solid aluminium.

After detailed calculations, (refer Appendix – I) Table 4.6 shows detected dissolved hydrogen values against 100 g of solid aluminium samples. For wire with composition of 5183, Devletian and Woods [136] reported hydrogen solid solubility of around 1.2 ml / 100 gm. The results shown in Table 4.6 remains in conformity with the same results. Results are in agreement with presumption that pulsed MIG samples had higher dissolved hydrogen than CMT samples. As the same wire spool was used for deposition, it can be said that same amount of hydrogen was available for pick up during both processes. Hotter liquid metal in pulsed MIG absorbed more hydrogen than relatively colder CMT process from wire and atmosphere. Relatively slower solidification rate and increased dissolved hydrogen in liquid aluminium resulted in increased porosity in pulsed MIG samples. Thus, it can be concluded that pulsed MIG processes support in pore formation and pore coalescence in aluminium [136] compared to CMT. It could be correlated with the larger liquid metal pool availability [14] in pulsed MIG than CMT. This eases atomic hydrogen movement for coalescence forming hydrogen molecule, thus hydrogen gas. From the above discussion, it can be inferred that hydrogen pick up during metal deposition by pulsed MIG method was higher than CMT metal deposition due to the reasons discussed earlier.

Table 4.6 Total hydrogen content and its distribution in the tested samples of CMT and pulsed MIG.

Set ID	Samples ID	Total hydrogen in samples of 100 g (ml)	Percentage of hydrogen forming pores	Percentage of hydrogen in solid solution
DH1	C-LH-T1	0.934	1.220	98.780
	P-LH-T1	1.112	5.060	94.940
DH2	C-LH-t2	1.142	1.250	98.750
	P-LH-t2	1.400	4.480	95.520

Feed stock wire revealed much higher amount of dissolved hydrogen than samples manufactured using both pulsed MIG and CMT. The difference in the detected hydrogen contents could be the result of; a) wrong dissolved hydrogen value obtained in the wire. This could be the result of hydrocarbons remain on the wire due to its surface roughness and irregularities [143,144] carried from wire manufacturing. b) Shielding gas used in the experiments, argon, was 99.998% pure. The impurities could be gaseous oxygen and nitrogen in miniscule amounts (~ 10 to 20 ppm) that can react with hydrogen. c) Following the Ellingham diagram [145], a reaction between hydrogen and surface aluminium oxide is possible forming a metal aluminium and water vapour. As a result hydrogen content in the wire could be higher than the build deposits.

Table 4.6 showed the difference in hydrogen content of solid aluminium deposits. From both set, DH1 and DH2, it is clear that around 95% of hydrogen was present dissolved in solid aluminium while for CMT samples it was 98.75%. The rest of hydrogen was consumed by the pores. As mentioned earlier, no pores were present with vacuum that is formed by solidification shrinkage was not considered, hence, all the available hydrogen was either considered at pores or at lattice imperfections that is atomic hydrogen in dissolved state. From overall discussion, it can be said that pulsed MIG samples absorbed more hydrogen which was consumed to form more pores compared to CMT samples. Therefore, even after absorbing more hydrogen, hydrogen was spent at forming more pores leaving lower fraction hydrogen dissolved in solid aluminium. On the other hand, although the CMT samples absorbed lesser hydrogen it formed less porosity than pulsed MIG leaving behind more amount of dissolved hydrogen in solid aluminium.

4.3.11 Arc length effect

Pulsed MIG and CMT processes possess considerable differences in metal deposition. In CMT process, arc length continuously changes from maximum to zero due to oscillating feed wire. Metal transfer from wire to deposit occurs by touching of liquid metal droplet to the deposit, thus, dip metal transfer. In case of pulsed MIG, it maintains relatively constant arc length and metal transfer from wire to deposit side is by globules or/and droplet in spray from depending upon electric current. Thus, in pulsed MIG liquid droplets is exposed to the surrounding atmosphere and contaminants for relatively longer time span than CMT. The longer time allows liquid metal to absorb more hydrogen from shielding gas and

contaminants, if any [14]. Smaller droplet formed during pulsed MIG transfer must have higher surface area than droplet formed during CMT metal transfer. Higher surface area and longer exposure time to the surrounding atmosphere and contaminants shown by pulsed MIG might have absorbed more hydrogen compared to CMT.

4.3.12 Solidification and cooling rate effects

Hydrogen in solid aluminium is found either at the porosity or in solid solution at lattice imperfections ranging from dislocations, impurities, grain boundaries *etc* [146]. Solubility of hydrogen in aluminium reduces as a function of temperature as discussed in literature review chapter. Therefore, at lower temperature sites such as solid liquid interface aluminium rejects out the excess hydrogen. Hence, pore in general are formed at the solidification front where the hydrogen concentration crosses solubility limit at that temperature. Further, the dissolved hydrogen gas rejection is time dependent process. Slower solidification rate supports pore formation while rapid solidification suppresses pore formation and gas remains dissolved in solid aluminium. As discussed earlier, CMT process allows faster solidification due to typical metal deposition [93] than pulsed MIG. Therefore, it can be argued that CMT processed samples possessed more chances of hydrogen retention in solid aluminium than pulsed MIG manufactured samples. In pulsed MIG samples, slower solidification not only supported in formation of increased pores but also provided longer time that increased exposure time of liquid aluminium to the atmosphere increasing chances of hydrogen pick up [14]. Presence of higher hydrogen in pulsed MIG samples can be correlated with the above explanation.

Pore formation and distribution in highly dependent upon solidification mechanism in MIG welding [136]. The distance between growing dendrites is the preferential site for pore formation, although its shape and size further determines detachment and floatation of the growing pore in to liquid aluminium. Faster cooling rates of liquid aluminium does not provide sufficient time to grow a pore and thus it cannot catch the speed of closely packed forming crystalline structure. Thus, pore cannot grow to required size, cannot detach and remain entrapped between forming lattice cells [147]. With slower cooling rates dendrites are widely spaced providing space as well time to grow which is sufficient for pore formation, growth and detachment. This could be probable reason for the formation of large sized pores in pulsed MIG process.

4.3.13 Secondary heat effects

In arc based additive manufacturing, temperature of a forming part is raised to appreciably high level. The temperature rise at the specific location of the deposit is based on arc energy, thermal conductivity and its distance from the top layer that is heat source. Xiong et al. in their different studies [141] and [110] have discussed the temperature distribution in forming WAAM part. Temperature rise at a layer on which a new layer is deposited is raised up to and above the melting point (it can be confirmed by observing penetration effect showing liquid formation in the specific area). Thus it can be argued that temperature of a layer immediately below can be raised above recrystallisation temperature.

Concentration of vacancies at such a high temperature become significant that influences hydrogen diffusion. The probable reason could be the high bonding energy between vacancy and hydrogen atom [146,148]. Hashimoto and Kino [146] proclaimed that total concentration of vacancies and concentration of hydrogen drives hydrogen diffusion in aluminium. Due to higher arc energy,

temperature, penetration and forced vacancy diffusion, thus, hydrogen diffusion in pulsed MIG could be higher than CMT. Rapid solidification, relatively lower temperature, penetration and arc energy of CMT could have experienced less diffusion of hydrogen than pulsed MIG. Thus, higher diffusion of vacancies associated with hydrogen may have supported in forming hydrogen clusters [15] which grew and formed large sized pores with higher numbers in pulsed MIG samples. This supports results obtained from XCT scan showing more large sized pores and higher volume fraction of pores in pulsed MIG samples that CMT samples (Table 4.3 and Figure 4.7).

While comparing overall porosity content, it was observed that pulsed MIG samples manufactured with low interlayer-temperature and low heat input showed higher pore content than high interlayer-temperature high heat input condition. The results are in agreement with outcomes put forth by Derekar et al. [149]; however, for CMT samples processed high-interlayer temperature and high heat input had more pore volume fraction than samples with low-interlayer temperature and low heat input. The contrasting results highlights the close relationship between total heat content and pore formation and pore coalescence taking place in deposit. A graphical representation of the observed phenomenon is shown in Figure 4.21. From the results it can be inferred that the high heat content case of pulsed MIG samples possessed sufficient heat for pore formation, coalescence and importantly pore escape. On the other side, CMT samples of low heat content could not provide sufficient heat for hydrogen coalescence therefore forming increase small number of pore and less pore escape. Remaining case of the pulsed MIG and CMT that is low heat content pulsed MIG and high heat content CMT showed increase pores. It can be argued that for these cases, heat was sufficient for hydrogen to diffuse, coalescence and grow a pore, however, not high enough to escape pore reducing pore content and total hydrogen in the sample. It is worthwhile mentioning that pulsed MIG is hotter metal deposition technique than CMT irrespective of similar heat input.

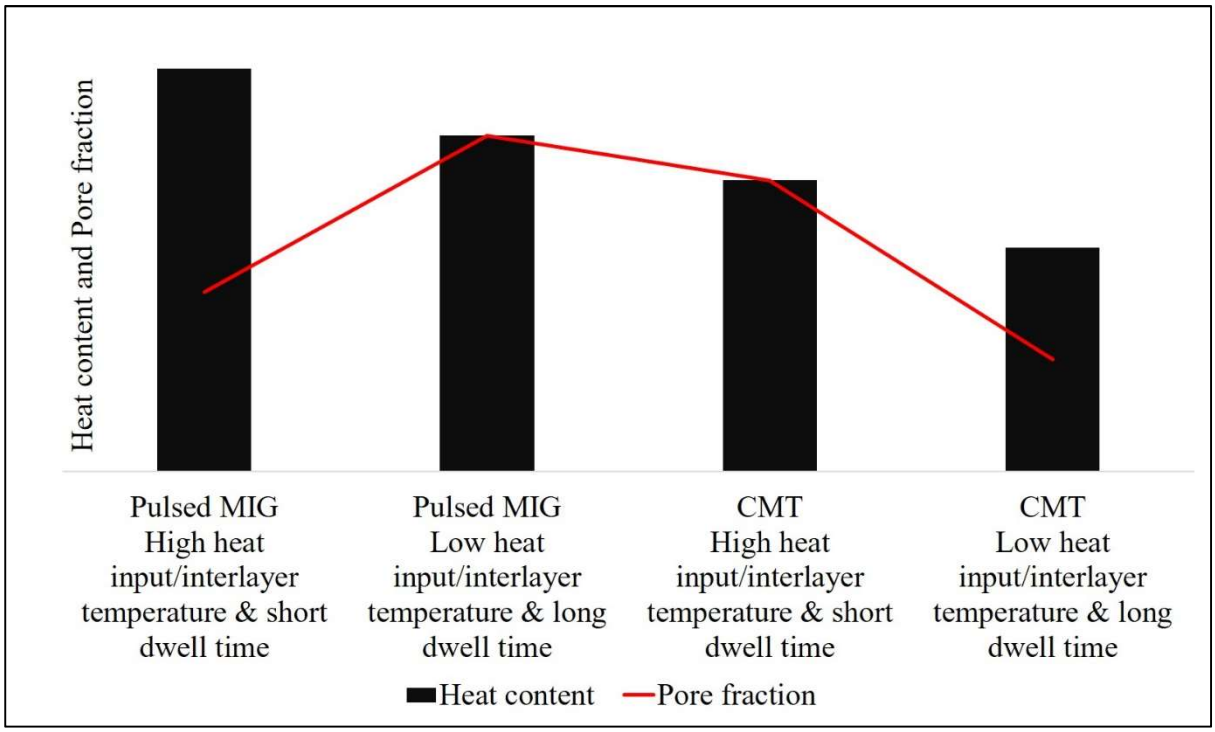

Figure 4.21 Graphical representation of relation between total heat content and pore fraction.

4.3.14 Statistical analysis

Verifying the similarity and differences between all the samples manufactured considering different metal deposition techniques, interlayer-temperatures, interlayer-dwell-times and heat inputs is worthwhile, therefore, the ANOVA, analysis-of-variance, was performed with respect to pore diameters. The analysis was based on the output obtained, p-value, from the analysis. A typical null hypothesis concept was applied that initially assumes no difference between the samples with respect to pore diameters. If the p-value from the analysis is below 0.05 that is less than 5%, it suggests that there is only that much percentage of chance of being considered samples same, hence, for any value below 0.05 the considered comparing samples are different that proves initial consideration of samples being same is false. Here, typical 95% confidence band considered for the analysis. Sample from different conditions are analysed as represented and compared in tabular format from Table 4.7 to Table 4.9.

Table 4.7 Comparison of p-values of pulsed MIG and CMT sample combinations considering interlayer-temperature, interlayer-dwell-time and heat input.

Comparison	**CMT**		**Pulsed MIG**	
	Sample IDs	p-values	Sample IDs	p-values
Interlayer-temperature	C-HH-T1 C-HH-T2	0.3591	P-HH-T1 P-HH-T2	0.552
	C-LH-T1 C-LH-T2	0.1387	P-LH-T1 P-LH-T2	0.7614
Interlayer-dwell-time	C-HH-t1 C-HH-t2	0.359	P-HH-t1 P-HH-t2	0.625
	C-LH-t1 C-LH-t2	0.2247	P-LH-t1 P-LH-t2	0.6318
Heat input	C-HH-T1 C-LH-T1	1.1×10^{-38}	P-HH-T1 P-LH-T1	0.2662
	C-HH-T2 C-LH-T2	4.49×10^{-40}	P-HH-T2 P-LH-T2	0.3865
	C-HH-t1 C-LH-t1	1.37×10^{-75}	P-HH-t1 P-LH-t1	0.6669
	C-HH-t2 C-LH-t2	2.93×10^{-44}	P-HH-t2 P-LH-t2	0.4657

Table 4.8 Comparison of p-values of pulsed MIG and CMT sample combinations based on interlayer-temperature and interlay-dwell-time.

Condition		Sample ID	p-values
High heat input	Interlayer-temperature	C-HH-T1 P-HH-T1	0.3216
		C-HH-T2 P-HH-T2	0.246
	Interlayer-dwell-time	C-HH-t1 P-HH-t1	0.3871
		C-HH-t2 P-HH-t2	0.1172
Low heat input	Interlayer-temperature	C-LH-T1 P-LH-T1	1.23×10^{-37}
		C-LH-T2 P-LH-T2	3.69×10^{-38}
	Interlayer-dwell-time	C-LH-t1 P-LH-t1	4.57×10^{-91}
		C-LH-t2 P-LH-t2	5.11×10^{-86}

Pulsed MIG processed samples showed no statistical difference for the conditions compared in Table 4.7 indicating no major difference in pore diameters; however, the case was different for CMT samples. Heat input found to have major impact on pore diameters in CMT samples, although the interlay-temperature and interlayer-dwell-time revealed no large differences. Low heat input interlayer-temperature case of CMT samples showed higher chances of being null hypothesis wrong which was around 86%. For high heat input the chances reduced down to around 64%. The similar effect was observed in case of interlayer-dwell-time based samples of CMT that supports the discussion from the section Relation between interlayer-temperature and interlayer-dwell-time control methods.

Heat input found to have major impact on pore diameters irrespective of other metal deposition conditions. Following Table 4.8, low heat input conditioned samples showed p-values much lower than 0.05 suggesting that hypothesis was false and samples were not identical. In case of high heat input pores found to reveal not much differences between pulsed and CMT samples. This suggests that high heat input has less influence on pore diameters than low heat input for both pulsed MIG and CMT processes. On a similar note, though it was apparent that high heat input samples were similar with respect to pore diameters, the p-values suggested that confidence of hypothesis was weak.

Table 4.9 p-values obtained for pulsed and CMT sample combinations for different deposition parameters.

Condition		Sample IDs	p-values
Extreme condition of heat content		P-HH-T2 C-LH-T1	1.44×10^{-30}
Comparable condition of heat content		P-LH-T1 C-HH-T2	0.0336
Comparable condition of temperature and time based samples	CMT	C-HH-T1 C-HH-t2	0.1029
		C-HH-T2 C-HH-t1	0.092
		C-LH-T1 C-LH-t2	1.5×10^{-12}
		C-LH-T2 C-LH-t1	6.27×10^{-29}
	Pulsed MIG	P-HH-T1 P-HH-t2	0.2719
		P-HH-T2 P-HH-t1	0.6474
		P-LH-T1 P-LH-t2	0.709
		P-LH-T2 P-LH-t1	0.2708

Analysis was performed for different combinations such as high heat content and low heat content as illustrated in Table 4.9. When compared both samples, the p-value was far below 0.05 indicating that heat content affects pore to a large extent. In another combination, samples from comparable heat contents (P-LH-T1 and C-HH-T2) were compared which showed pores were appreciably different. In accordance with the discussion comparing samples from interlayer-temperature and interlayer-dwell-time, samples prepared with 30 seconds and 120 seconds interlayer-dwell-time were compared with samples manufactured by 100°C and 50°C interlayer-temperature respectively. Significant difference was observed between samples from CMT and low heat input conditions where hypothesis was statistically false. High heat input samples statistically were similar, however, confidence of hypothesis being wrong was around 90%. In case of pulsed MIG samples no such difference was noticed.

Alternatively, a pattern can be observed from results. High heat content samples such as high heat input and high interlayer-temperature and short interlayer-dwell-time showed similar p-values when compared with low heat content samples such as low heat input, low interlayer-temperature and longer interlayer-dwell-time. On the contrary, other conditions of pulsed MIG showed comparative p-values around 0.27. The results are in accordance with the discussion made in different sections of discussion earlier.

Chapter 5: Microstructural Characterisation

5.1 Introduction

No restrictions on size during part manufacturing, appreciable flexibility of operation, high deposition rate and material efficiency are some of the advantages of WAAM technique [3]. Suiting to high deposition rate, part with complexity varying from low to medium and size from medium to large can be efficiently manufactured with WAAM [67].

Widespread application of the aluminium alloy components in the automobile, aerospace and other sectors has triggered the interest in manufacturing and use of WAAM parts [3]; however, there are imperfections such as solidification cracking [16], porosity [90] and reduced strength than the wrought products [150] which can be considered as critical factors limiting the applications of WAAM processes aluminium alloys. In finished WAAM, implementation of Fronius developed cold metal transfer (CMT) which is an example of controlled dip metal transfer method and post processing such as interlayer rolling are reported to reach to reduction and in few cases absolute eradication of porosity [90]. At the instance, it is important to understand the effect of WAAM processing parameters to minimize the need of after processing, development of preferred microstructure and to reduce the formation of defects in WAAM material.

WAAM has been progressed from the traditional arc welding technique. Interpass temperature control has always been considered as one of the important factors in welding. It has been discussed [114] that high interpass temperatures during welding produce unwanted effects on hardness of 7xxx series aluminium alloy plates. In alloy steels, to avoid hydrogen cracking the author also mentioned that interpass temperature can be one of the decisive parameters. Many researchers have discussed the microstructure of the formed object through layer deposition in detail. The effect of alternating polarity CMT on mechanical properties of aluminium alloys and their microstructure was studied by Zhang et al. [80]. In an alternative approach, work piece vibration and its effects on the mechanical and microstructural properties was studied by Zhang et al. [151]; however, the specific temperature maintained for a layer immediately ahead of deposition of following layer, here reported as the interlayer-temperature, and its effect on material properties was not reported in the open literature. The expression interlayer-temperature mentioned here is conceptually identical to the interpass temperature used for welding operation. The interlayer-temperature is nothing but temperature of the top most layer of an additively manufacturing part immediately ahead of the deposition of consecutive layer. As discussed by Ortega et al. [152] and Gu et al. [90], while depositing a WAAM part through robotic programing, the focus is conventionally provided to the interlayer-dwell-time than the temperature of earlier deposited layer immediately before the deposition of consecutive layer. The temperature of a forming object gradually increases due to deposition of a feed stock wire with the defined time interval in an additive manufacture format [140]. This causes raise in an interlayer-temperature along with the

progress of layer deposition. Heat sink effects and heat removal techniques were explored by Wu at al. [153] and Xiong et al. [110] in order to reduce adverse heat buildup effects. In different approach, Geng et al. [137] reported that by raising the interlayer-temperature up to 120°C from 50°C, consistent, improved and smooth layer appearance can be obtained. It was suggested that the layer geometry was impermissible when interlayer-temperature rose above 150°C. The results match the guidelines provided by the arc welding standard, BS EN 1011-4:2000, which restricts the maximum interpass temperature at 120°C for similar feed wire chemistry.

Microstructural features, particularly grain orientation and crystallographic texture denote a large impact on strength of WAAM manufacture aluminium object. Development of grain orientation mostly depends upon the direction of metal deposition. Anisotropy in tensile strengths were reported by Geng et al. [84] for the samples tested in perpendicular and parallel direction of the grain orientation. Moreover, it is expected that microstructure development in WAAM material gets affected by processing parameters including interlayer-temperature and heat input.

The effects of interlayer-temperature on microstructure are relatively unattended area in WAAM of aluminium. In the similar line, the present study explores the effect of interlayer-temperature on the dimensional and microstructural variations in aluminium 5183 alloy chemistry. Thus, the results of experiments detailed in section 3.3 are studied and discussed in this chapter. Two parts of this chapter divides study focussing initially on the layer geometry and microstructure of staggered layered WAAM component. Latter part includes study of sixteen samples with added variables such as metal deposition technique (pulsed MIG and CMT) and interlayer dwell time. This further considers results from infra red camera and temperature variation across the walls.

5.2 Part – 1 Understanding the effect of interlayer-temperature and heat input

The aim of this part was to understand the effect of interlayer temperature and heat input on layer geometry. The results of experiments from section 3.3.2 are discussed in detail in this section. This includes study of staggered layered component manufactured using two interlayer temperatures and heat inputs (refer Figure 3.18) manufactured using pulsed MIG technique. Macro and microstructural study are performed at different layers that revealed effect of mentioned deposition variables on layer shape.

5.2.1 Investigation of layer geometry

Height and width difference between high and low interlayer temperature samples was 0.37 mm and 0.89 mm for high heat input samples (refer Figure 5.1a and b) while for low heat input samples the difference was 0.26 mm and 0.25 mm respectively (refer Figure 5.2a and b). In both high and low heat input cases, samples processed with higher interlayer temperature showed lesser height than samples from lower interlayer temperature, however, reverse was true while considering the layer width. Figure 5.3 describes the measurement method employed for height and width measurement.

Figure 5.4 and Figure 5.5 illustrate the effect of interlayer-temperature on layer geometrical features with consideration of high and low heat input samples. It was shown in Figure 5.4 that for a particular layer, there was minor difference in width and height between two different interlayer-temperature values. For samples 5H100 and 5H50, percentage difference between height and width was around 7

and 9%. The graphs clarified that samples deposited using 100°C interlayer-temperature were wider and shorter when compared with 50°C interlayer-temperature samples. A linear increasing trend of height-to-width ratio (H/W) was seen for all the samples prepared using high heat input despite revealing a small difference in geometrical features. For all samples, it was observed that H/W ratio was higher for 50°C interlayer-temperature samples than 100°C interlayer-temperature samples while comparing for respective layers numbers. It can be concluded that 50°C interlayer-temperature samples evidenced reduced width that was compensated by increased height compared to 100°C interlayer-temperature samples. Thus, samples prepared using 50°C interlayer-temperature were taller and thinner than 100°C interlayer-temperature.

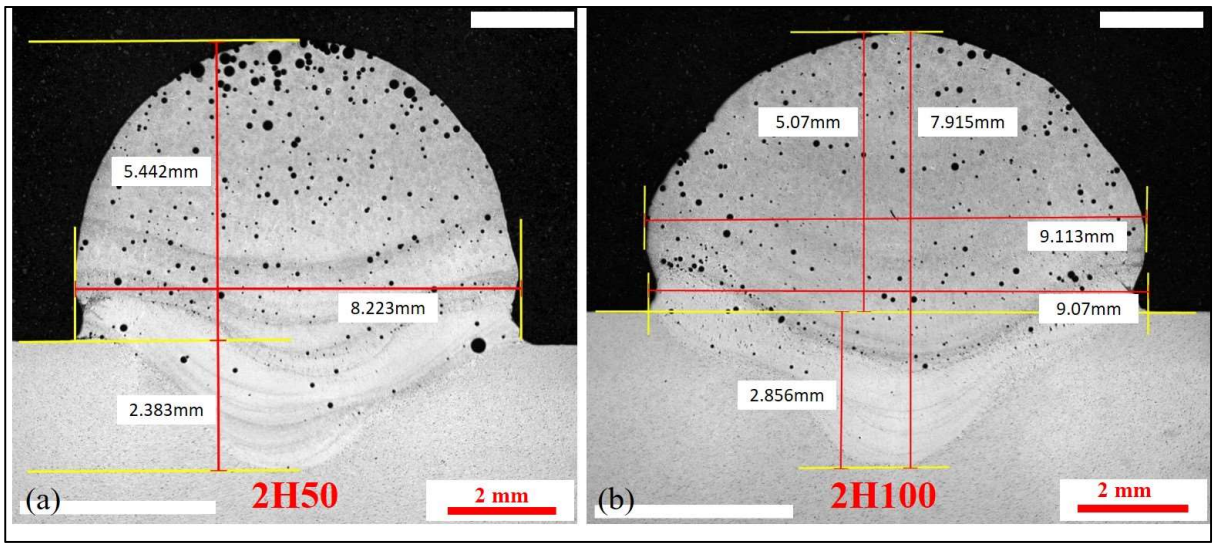

Figure 5.1 Macrostructure graphs revealing geometrical features of Samples 2H50 (a) and 2H100 (b).

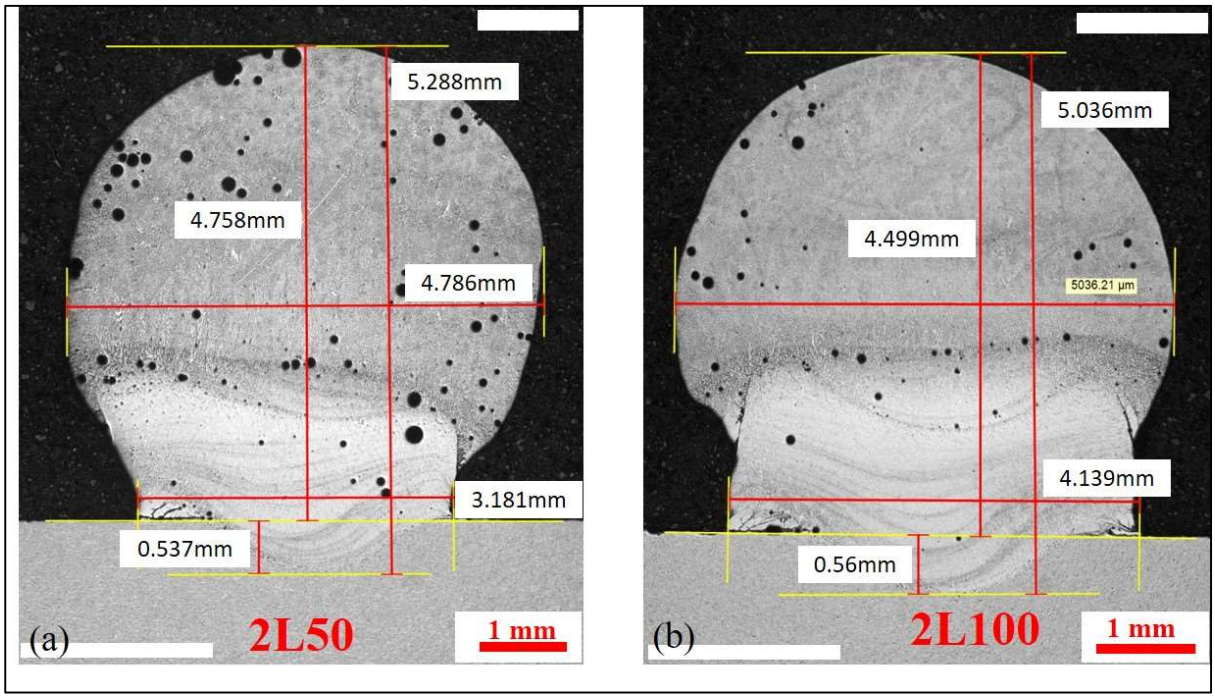

Figure 5.2 Macrostructure graphs revealing geometrical features of Samples 2L50 (a) and 2L100 (b).

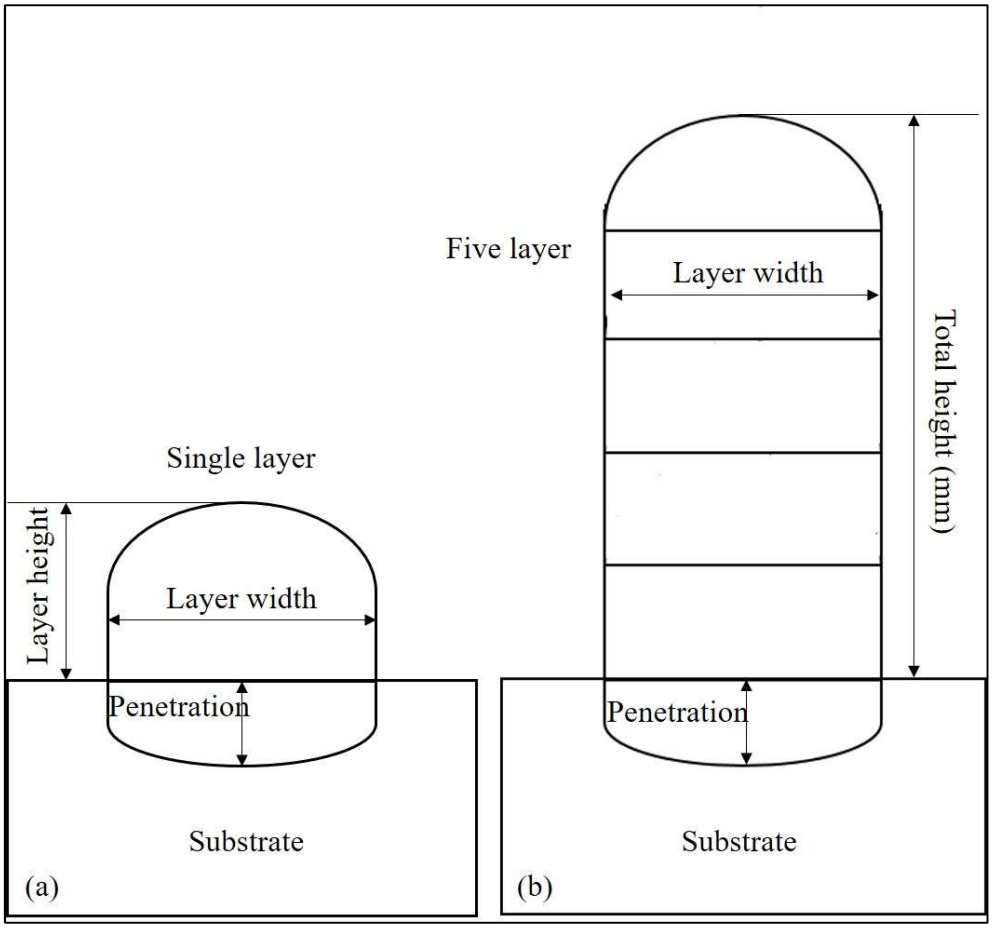

Figure 5.3 Schematic of WAAM wall describing dimensional measurements for single layer (a) and five layered wall (b).

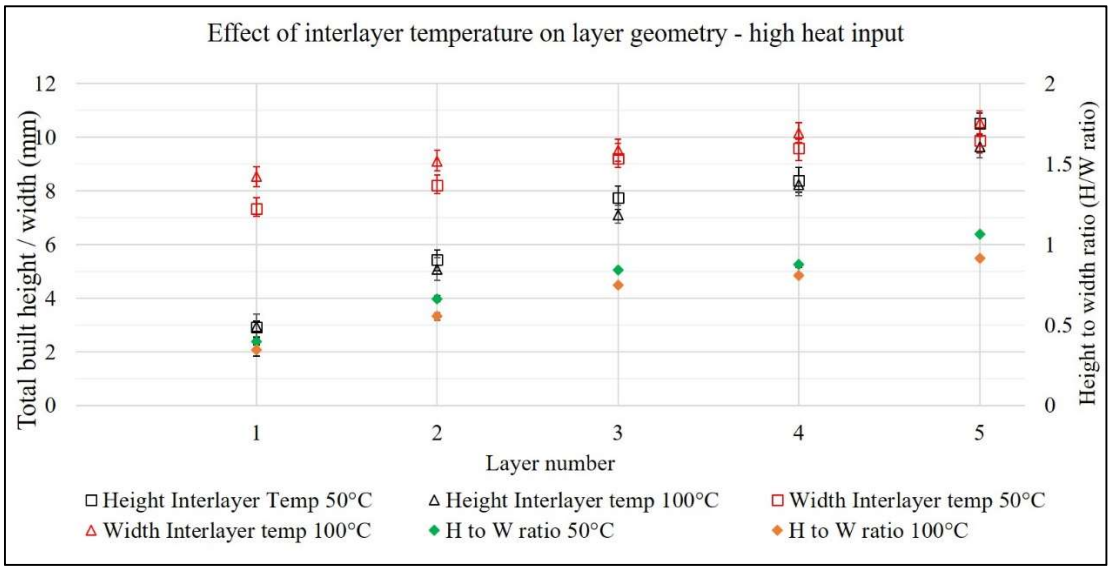

Figure 5.4 Graphical representation of variation in build geometry as an effect of interlayer-temperature for high heat input samples.

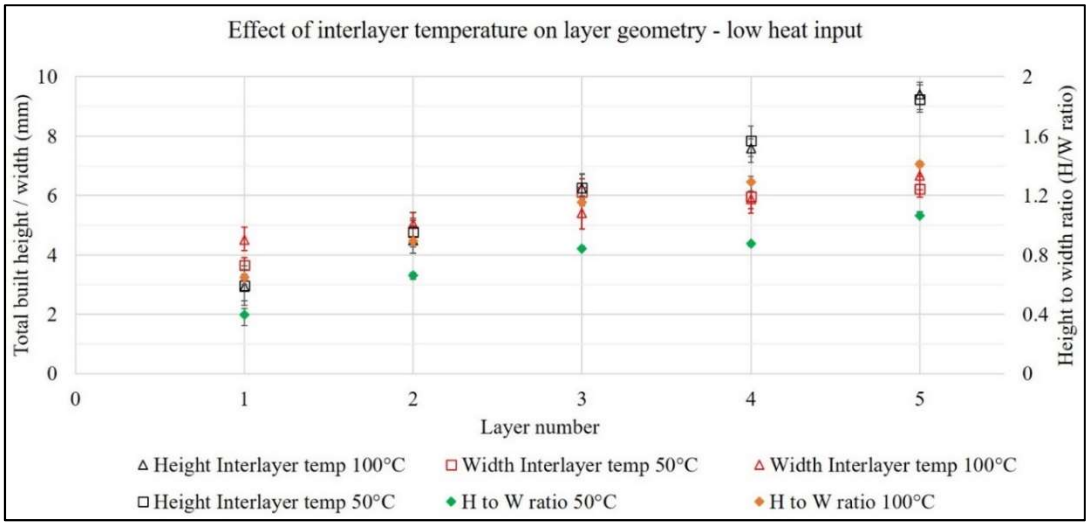

Figure 5.5 Graphical representation of variation in build geometry as an effect of interlayer-temperature for low heat input samples.

Minute difference in sample geometry (width and height) between two interlayer-temperatures were seen in case of low heat input samples (refer Figure 5.5); however, as discussed earlier, the overall tendency of height and width variation with respect to interlayer-temperature was similar to high heat input samples. Two unexpected variation were reported where samples 5L100 was found taller than 5H100 by marginal 0.167 mm while samples 4L50 was wider than sample 5L100 with minor difference of 0.09 mm. Height and width of a deposit was found to be affected by heat input (refer Figure 5.6). Increased width and height was evidenced for high heat input samples compared to low heat input irrespective of layer number. Wire feed speed was roughly doubled while increasing low heat input to high heat input, however, layer width and height did not reveal change in the same proportion.

While comparing four sets of samples based on layer geometry and H/W ratio as shown in Figure 5.6, a particular trend can be observed for each set of samples. Figure 5.6a, high heat content sample that is 100°C interlayer-temperature and high heat input combination had widest layers and low heat content samples that is 50°C interlayer-temperature and low heat input had least wide layers. Also, for all cases considered, high heat input samples denoted comparatively wider and taller layer compared to low heat input samples. There was minute difference in layer heights while comparing low nd hig heat input samples, however, difference in the widths was considerably high. Interlayer-temperature revealed higher impact in high heat input samples than low heat input. This could be ascribed to the increased amount of liquid metal addition in high heat input mode than low heat input. Wider spread and larger expansion of aluminium was evidenced in case of high interlayer-temperature. Figure 5.6b clearly reflected the results from Figure 5.6a that confirmed the widest layer showed lowest H/W ratio. Whereas, least heat content sample, low interlayer temperature and heat input, showed highest H/W ratio affirming deposition of the least wide layer. Interlayer-temperature and heat input significantly affected the penetration as shown in Figure 5.7 that further affected build geometry. Formation of microstructure in the build walls with different conditions is discussed in upcoming sections.

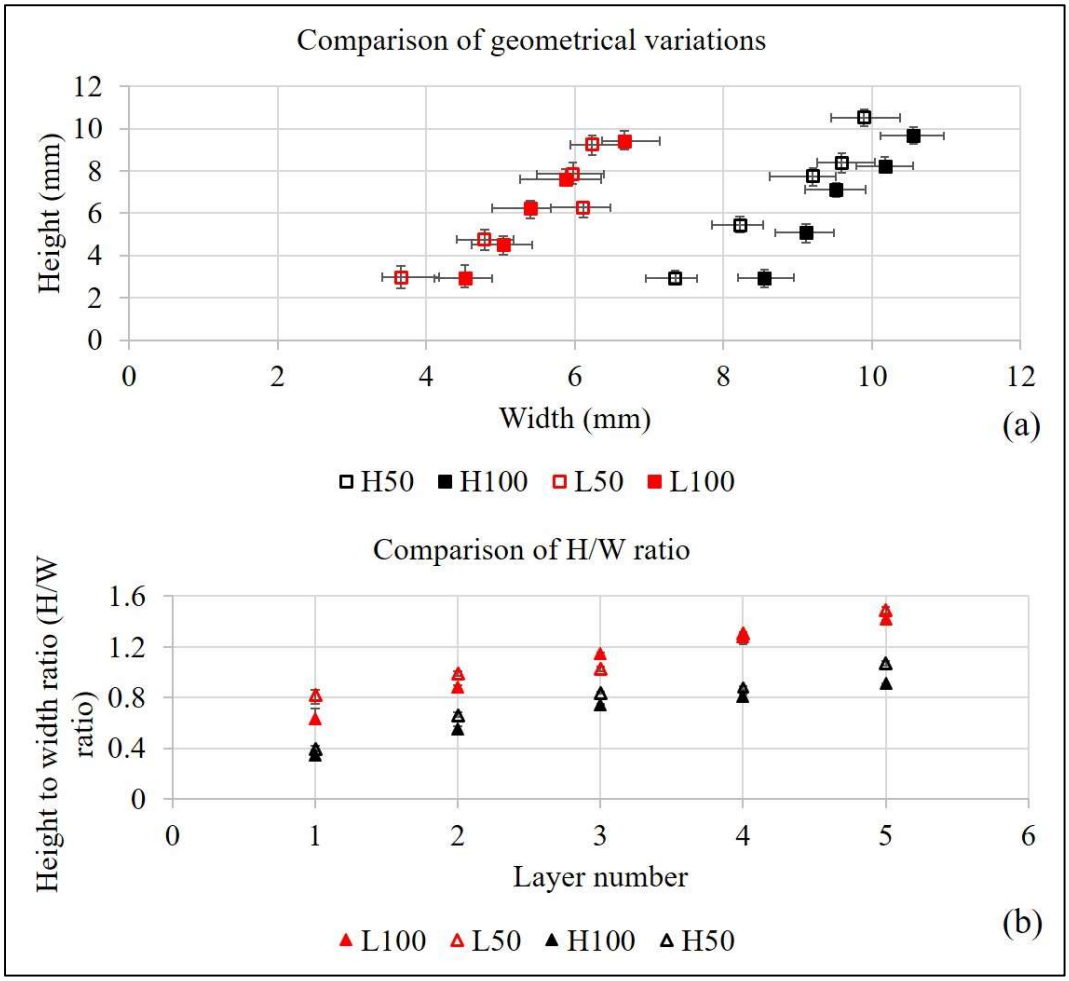

Figure 5.6 Graphical representation of an effect of heat input and interlayer-temperature on layer width and height (a) and height-to-width ratio (H/W ratio) (b).

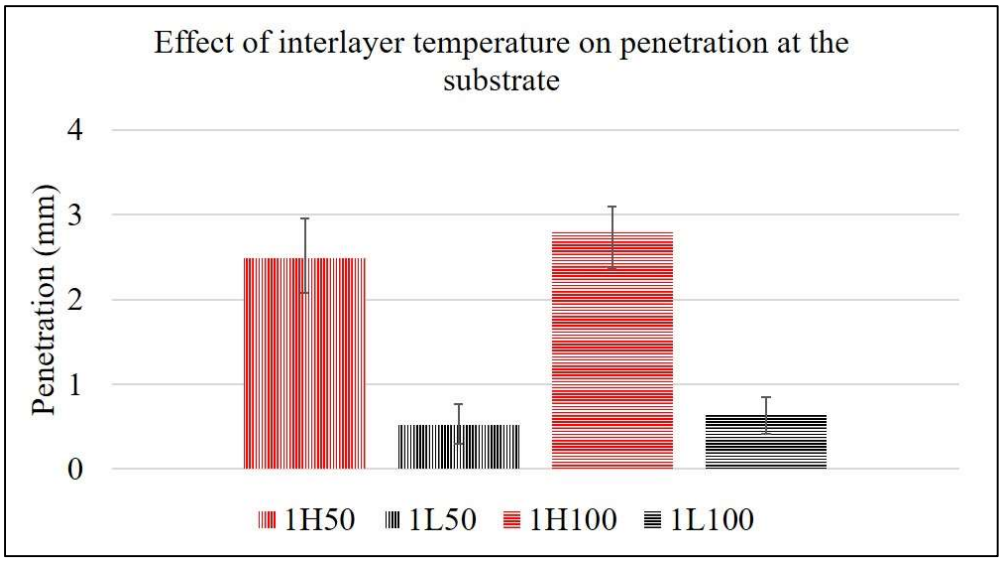

Figure 5.7 Graphical representation of an effect of interlayer temperature and heat input on the penetration at substrate.

5.2.2 Microstructure

5.2.2.1 Microstructure evolution within single layer

Polarised microscope images of single layer showed columnar grains in penetration area that can be seen in Figure 5.8 and Figure 5.9. The columnar grains showed linear relation with the depth of penetration. Longer columnar grains were witnessed in penetration area of the high heat input samples compared to shorter in low heat input samples (refer Figure 5.8 and Figure 5.9). Columnar grain formation, irrespective of interlayer-temperature, could be the result of faster heat dissipation into the substrate that triggered rapid temperature reduction in the penetration area. Effect of heat dissipation and columnar grain formation has been reported earlier [114].

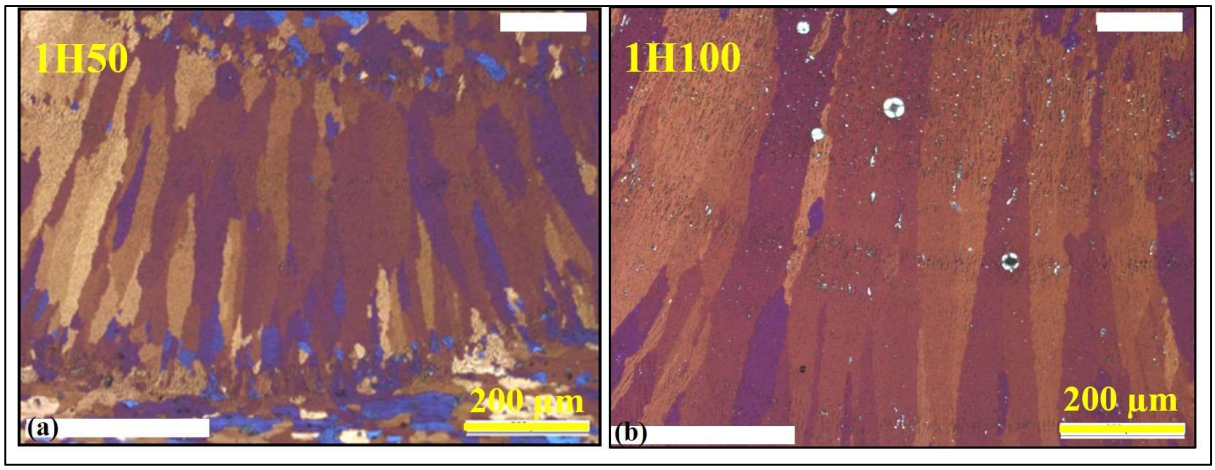

Figure 5.8 Micrographs showing columnar grains at penetration area of Samples 1H50 (a) and 1H100 (b).

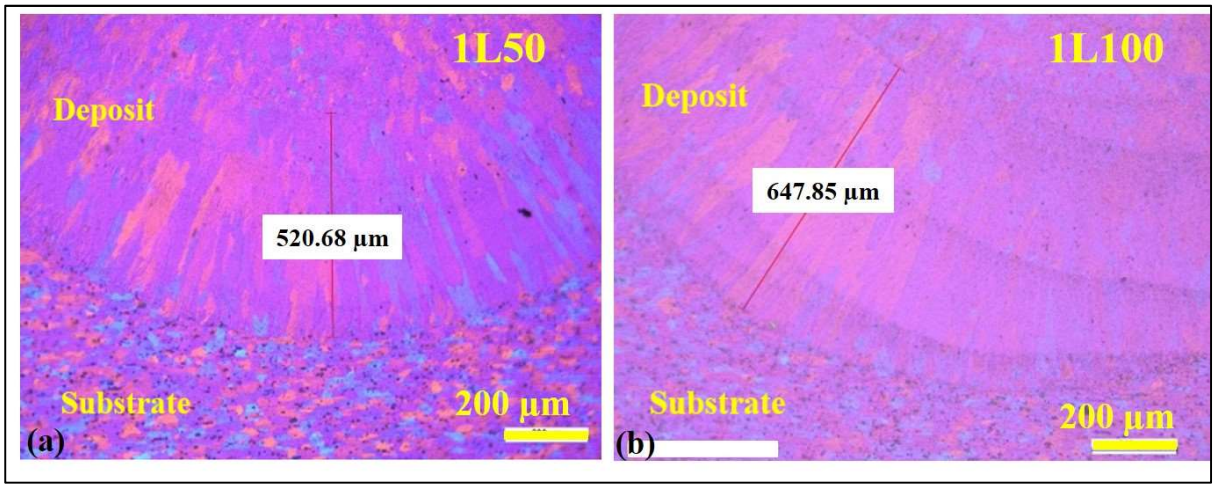

Figure 5.9 Micrographs showing columnar grains at penetration area of Samples 1L50 (a) and 1L100 (b).

Equiaxed grain structure was present in the deposit region above the substrate immediately after columnar grains (refer Figure 5.10). Figure 5.11 and Figure 5.12 represent high and low heat input samples microstructures respectively. Interlayer-temperature found affecting the grain size when Figure 5.11a was compared with Figure 5.11b and Figure 5.12a with Figure 5.12b. A grain size difference of 51.5% (10.3 µm) and 15.7% (2.3 µm) was noticed between high and low interlayer temperature samples

when grain size was measured using following the standard line intercept method defined under ASTM 112-13. Samples from low heat input showed lower grain size compared to high heat input samples. Thus, average grain size in Figure 5.11a was 20 µm and Figure 5.12a had 15.15 µm while grains in Figure 5.11b showed average grain size of 30.3 µm and Figure 5.12b illustrated 17.54 µm. It was clear from the figures that high heat input grains from Figure 5.11a and Figure 5.11b were larger than low heat input grains from Figure 5.12a and Figure 5.12b by around 32% and 72% respectively. The probable reason for the presence of roughly equiaxed grains at the vicinity of columnar grains could be comparatively slower solidification and heat extraction. Metal penetrated into the substrate experienced higher cooling rate, however, a deposit metal above substrate region did not experience similar cooling rates.

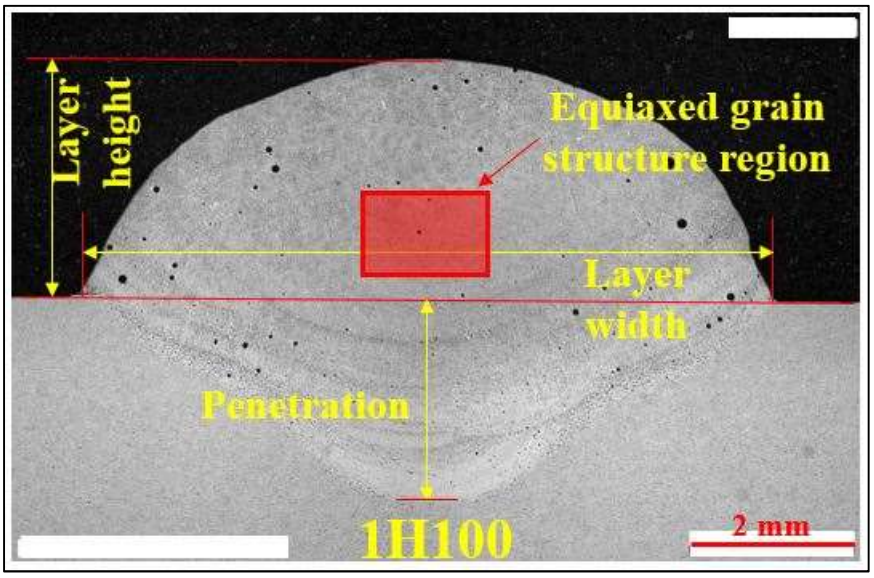

Figure 5.10 Macrograph of a single layer deposit taken by optical microscopy revealing an approximate location of equiaxed grains that are shown in Figure 5.11 and 5.12.

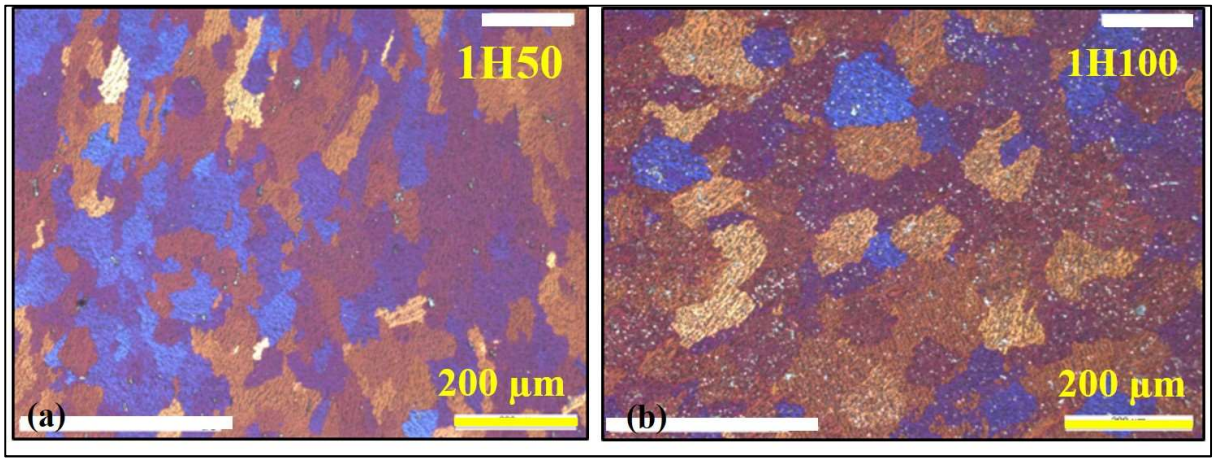

Figure 5.11 Micrographs illustrating equiaxed grains in high heat input single layer sample 1H50 (a) and 1H100 (b) at a location shown in Figure 5.10.

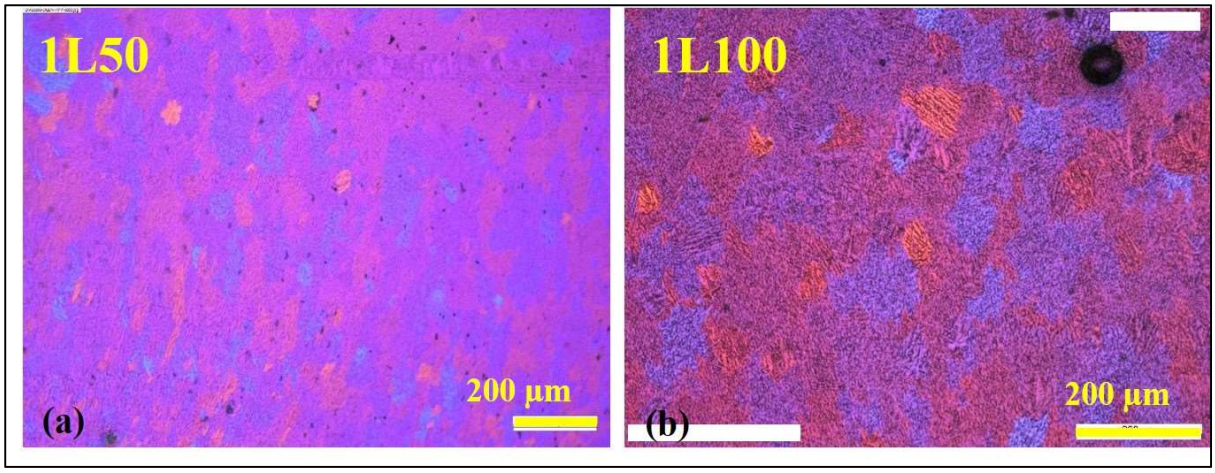

Figure 5.12 Micrographs illustrating equiaxed grains in low heat input single layer sample 1L50 (a) and 1L100 (b) at a location shown in Figure 5.10.

5.2.2.2 Microstructure evolution at five-layered samples

Columnar grains, similar to those observed in penetration area, were found prominently in a multilayer deposition with five layers. Irrespective of heat input and interlayer-temperature, vertical columnar grains shown in Figure 5.13 and Figure 5.14, were evidenced at layer number 3. It can be seen in these figures that columnar grains grew from bottom to top of the layer, however, in every case it should be noticed that growth of these grains was disrupted at the interlayer region (refer Figure 5.13 and Figure 5.14). At interlayer region between three and four, fine grains along with porosity were observed that presumably disturbed columnar grain growth shown between yellow lines in Figure 5.13 and Figure 5.14. The size of these fine grains was appreciably smaller than the undisturbed grains found at the top layer.

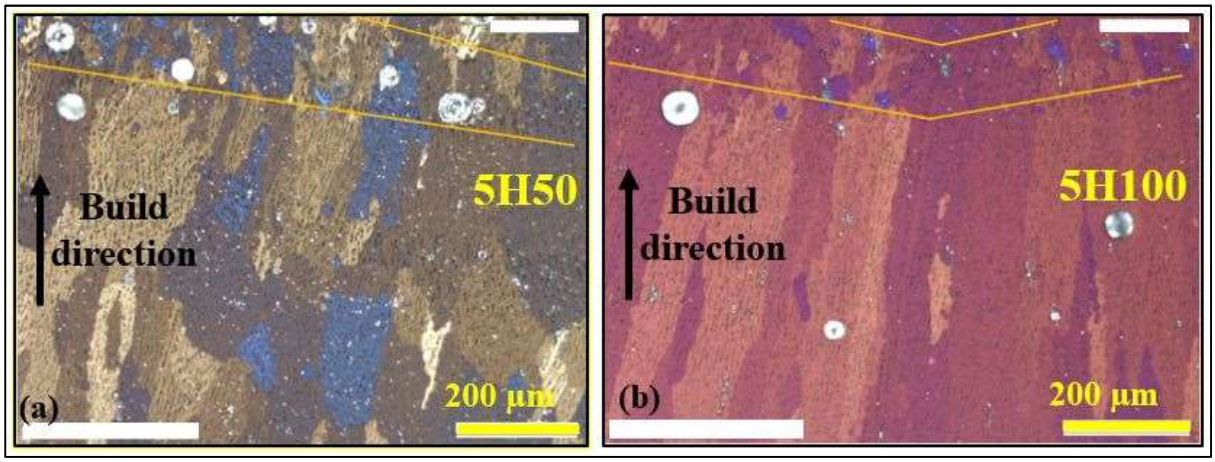

Figure 5.13 Micrographs of high heat input samples 5H50 (a) and 5H100 (b) revealing columnar grains at layer number 3 with presence of porosity and fine grains at the interlayer region.

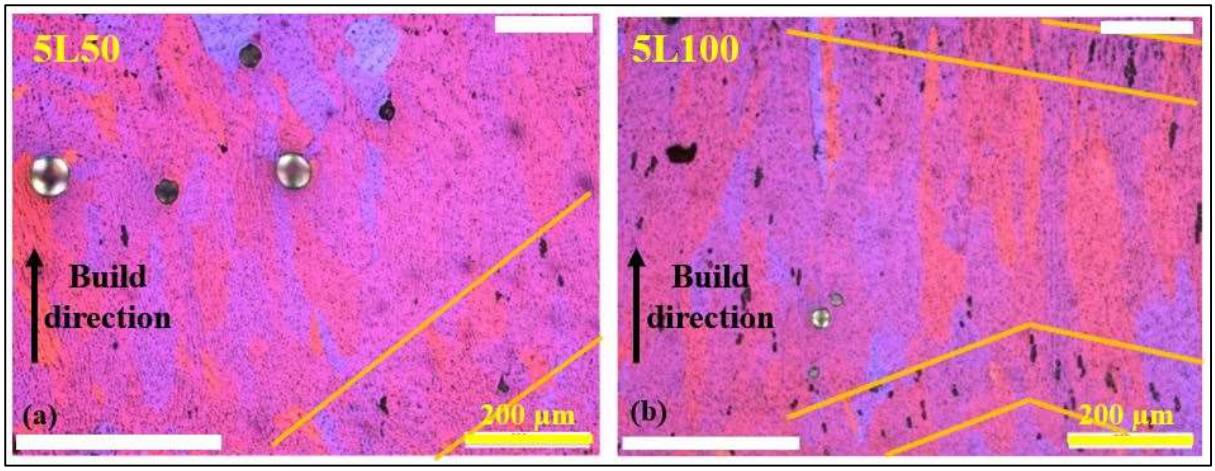

Figure 5.14 Micrographs of high heat input samples 5L50 (a) and 5L100 (b) revealing columnar grains at layer number 3 with presence of porosity and fine grains at the interlayer region.

Columnar grains showed the presence of heat gradient that is flow of heat from top layer to substrate. Interlayer-temperature showed pronounced effect on grains morphology which can be witnessed by comparing Figure 5.13a with Figure 5.13b and Figure 5.14a with Figure 5.14b. Average length of columnar grains in high interlayer-temperature sample was greater than low interlayer-temperature.

Top layer shown in Figure 5.15 and Figure 5.16 exhibited entirely different microstructure compared to rest of the layers. All top layers of four samples had equiaxed randomly oriented grains with dendritic structure. Being a top layer it was clear that this particular layer did not undergo any reheating due to absence of layer deposition above. Therefore, this microstructure was inhomogeneous with the rest of the layers. Similar effect of interlayer-temperature on microstructure was reflected. Low interlayer-temperature samples, 5L50 and 5H50, showed 35.7 µm and 55.55 µm average grain size that was lower than high interlayer-temperature samples, 5L100 and 5H100 that showed around 37.03 µm and 71.42 µm. The difference turned out to be around 3.7% and 28.5% for low and high interlayer temperature respectively. Comparing the grain size variation due to heat input, it was confirmed that high heat input samples greater grain size than low heat input. Thus, samples 5L50 and 5H50 showed a grain size difference of 55.4% while it was 92.8% for 5L100 and 5H100 samples. Alloy composition 5183 shows melting point (liquidus temperature) of around 638°C. Therefore, temperature difference between interlayer-temperature and melting temperature remained 588 and 538°C for 50 and 100°C interlayer-temperature. This temperature difference triggered different cooling rates that ultimately produced different sized grains. For 50°C interlayer-temperature metal becomes more viscous which restricts its spread therefore reduces its width, however, comparing with 100°C interlayer-temperature that possesses less viscous aluminium supports in wide spreading increasing width and reducing layer height.

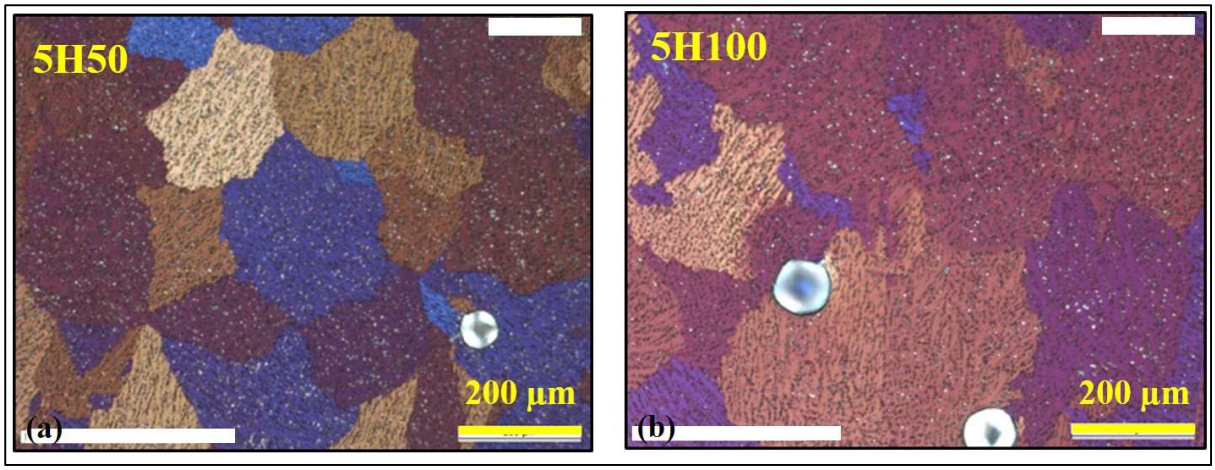

Figure 5.15 Micrographs of high heat input samples 5H50 (a) and Sample 5H100 showing a top layer.

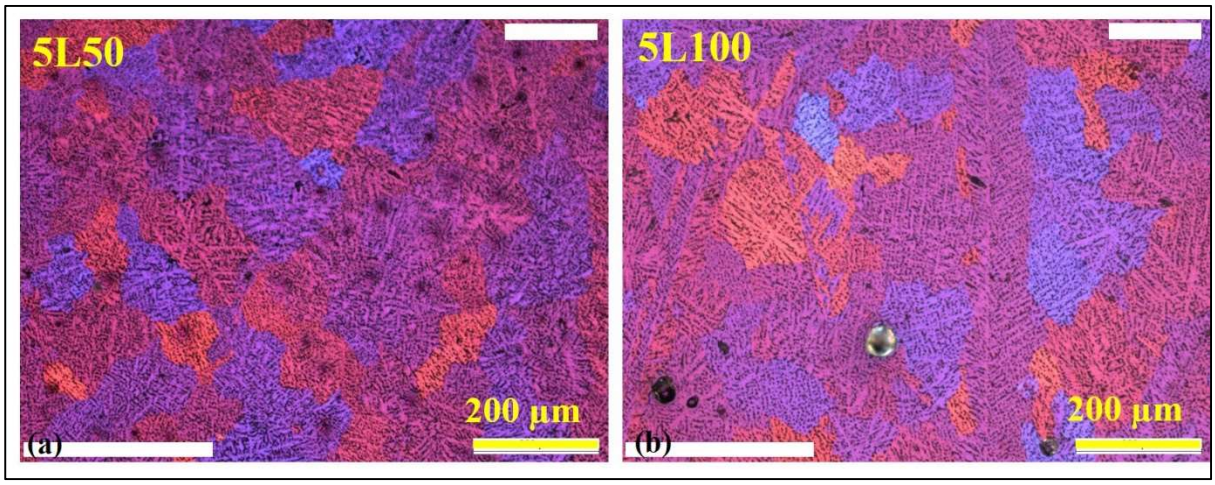

Figure 5.16 Micrographs of low heat input samples 5L50 (a) and Sample 5L100 showing a top layer.

Apart from specific locations such as bottom layer and top layer, it is advisable to study microstructural variations throughout the cross section. Figure 5.17 revealed the microstructure of 5 layered WAAM part at a surface transverse to the direction of torch travel. Microstructural variations with respect to interlayer-temperature and heat input can be compared. Figure 5.17b to Figure 5.17e showed elongated grains in the build direction, however, depending upon heat input and interlayer-temperature variations can be highlighted. Grains from Figure 5.17b revealed lengths from 300 to 400 µm in elongation direction while it was 500 to over 600 µm in Figure 5.17c. Similarly, Figure 5.17d showed comparatively lower grain elongation with 200 to 400 µm while it was around 300 to 400 µm in Figure 5.17e. Firstly, considering the effect of interlayer-temperature it can be argued by comparing Figure 5.17b with Figure 5.17c and also Figure 5.17d with Figure 5.17e that higher interlayer-temperature, thus, higher heat content supported in growing the grains longer in build direction. Likewise, similar effect can be asserted for heat input cases applied for WAAM build up. Figure 5.17b compared with Figure 5.17d and Figure 5.17c with Figure 5.17e showed higher heat input contributed in formation of longer grains. Also, it is worthwhile mentioning that higher heat content also supported in providing increased penetration that ultimately growing the length of formed columnar grains. Further, higher

penetration supported in reducing overall wall height in multilayer deposition which increased wall width.

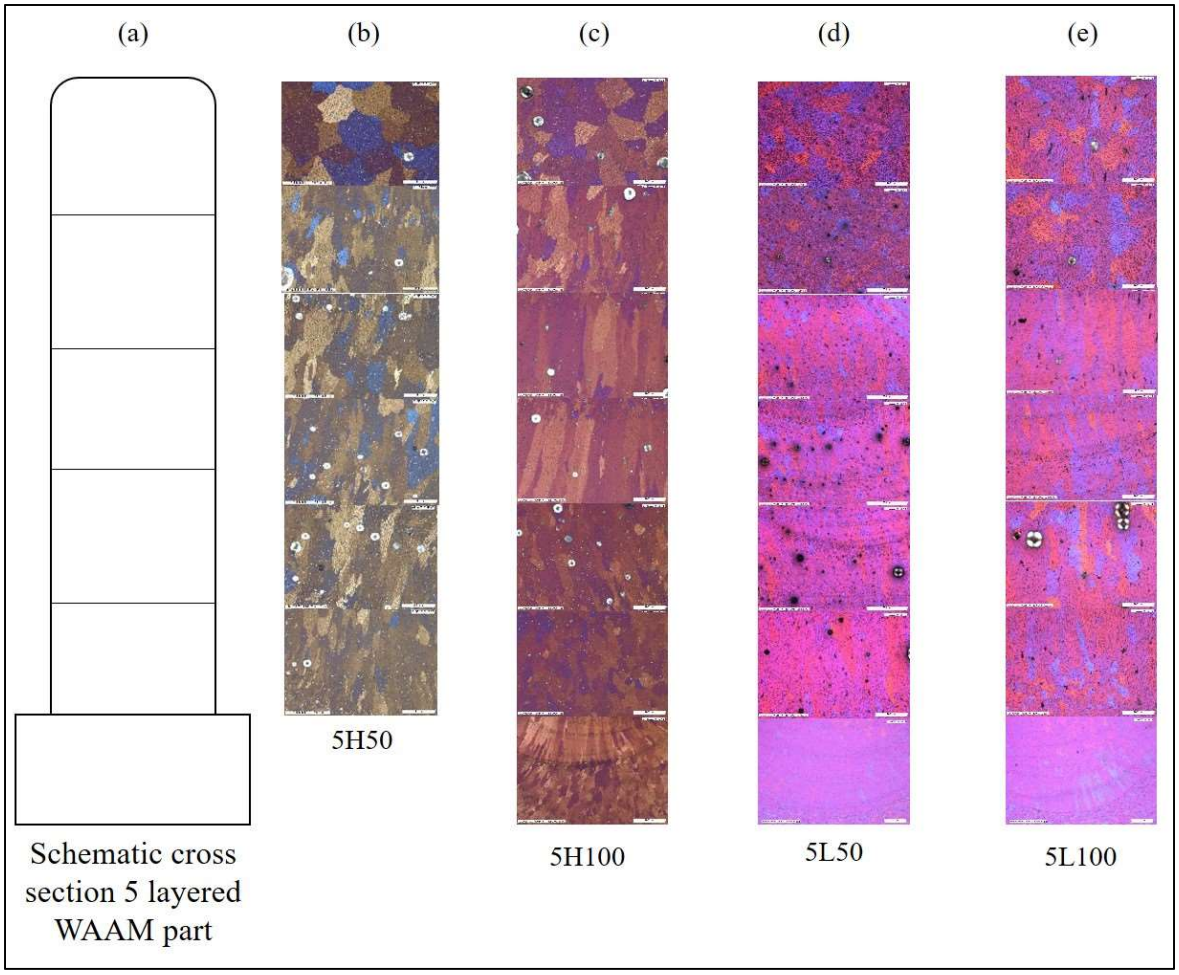

Figure 5.17 Microstructural variations in 5-layered WAAM part throughout the thickness. Schematic of 5-layered WAAM part (a). Microstructural variations in high heat input low interlayer-temperature condition (b), high heat input high interlayer-temperature condition (c), low heat input low interlayer-temperature condition (d) and low heat input high interlayer-temperature condition (e).

5.2.3 Summary of microstructure evaluation for five layer structure

Dimensional variation of around 0.5 mm was reported as an effect of change of interlayer-temperature. Although, some of the studies might consider this marginal variation as an experimental error, however, a peculiar consistent pattern in dimensional change can be withdrawn and is displayed in this study. From the pattern identified in this study, it can be deduced that wider samples can be produced by applying high interlayer-temperature while for manufacturing of taller samples low interlayer-temperature can be applied.

Microstructures of columnar grains at central layer region and finer grains at the interlayer region with presence of porosity was found consistent throughout the wall structure in all samples irrespective interlayer-temperature, heat input or particular position in WAAM wall. Only the exception was top layer that showed equiaxed dendritic grains, however, it was consistent for each wall structure. There was variation in the size of dendritic structure with respect to interlayer-temperature and heat input. A further investigation related to the dendritic structure was not carried out because considering a WAAM

structure and product manufacturing, top layer is given a secondary importance. Most of the times, top layer of the forming object by WAAM is cut-off and does not remain a part of final object.

After deposition of subsequent layer, equiaxed grain structure at top layer reformed into columnar grains. Arc force, heat, liquid metal and penetration could be the reasons for destruction of equiaxed grains. Solidification rate and thermal gradient define the grain structure and grain morphology. These parameters vary at each layer from top to bottom. Bottom part that experiences greater temperature gradient forms columnar grains while top part solidifies as equiaxed grains. With further layer deposition, equiaxed grains remelted and forms and continues as columnar grains. The small grains at the interlayer region are formed with a difference mechanism.

5.3 Part – II Comparative investigation of pulsed-MIG and cold metal transfer (CMT)

The aim of this part was to understand the effect metal deposition variables on microstructure. The results of experiments from section 3.3.3 are discussed in detail in this section. This includes study of sixteen samples manufactured using two interlayer temperatures (50 and 100°C), two heat inputs (~120 and 280 J/mm), two MIG variants (pulsed MIG) and two interlayer dwell times (30 seconds and 2 minutes). Microstructural study using optical microscope and electron backscattered diffraction (EBSD) study using SEM was performed. Results obtained from infra-red camera for temperature variation across the wall structures were compared for different deposition conditions. The details were also used for calculations of cooling and solidification rates. Pulsed MIG processes samples were tensile and hardness tested as described in section 3.3.3.2. A comparative tensile test results are also discussed in this chapter (refer section 3.3.3.3).

5.3.1 Microstructure differences between pulsed MIG and cold metal transfer (CMT)

A wide difference in microstructure of pulsed MIG and CMT samples were observed while comparing at similar locations in deposited wall processed with similar deposition conditions. Microstructure with elongated grains in the heat flow direction can be seen in Figure 5.18. There was no difference between pulsed MIG and CMT samples as both revealed elongated grains, however, length of grains was seen much longer in pulsed MIG samples compared to other. A layer transition zone as shown in Figure 5.18a and b witnessed breakage of columnar grains at the interlayer region. Grains were more elongated in pulsed MIG samples and were much less compared the CMT samples. Pore can be seen at interlayer region. Microstructure shown in Figure 5.18c and d compares grains present at layer number six of manufactured wall. It can be argued that massive grains in pulsed MIG samples grew from lower end of a layer upto the top, however, the case was different in CMT samples. Although grains were found to be elongated in CMT, due to overall small dimensions, higher number of grains were present. Also, comparing overall grain size between pulsed MIG samples (Figure 5.18a and c) and CMT samples (Figure 5.18b and d), larger grains were observed at increase layer number (layer number 6) than lower layer number (layer number two).

Similarly, microstructures were obtained for high interlayer-temperature samples shown in Figure 5.19 at similar locations to that of shown in Figure 5.18. There was no appreciable difference between the morphology of the grains apart from the slightly larger grains were observed in Figure 5.19 than Figure 5.18. It was confirmed after the grains size measurements. Maximum average grain size measured for

CMT samples was 65 µm for microstructure shown in Figure 5.19d which was marginally greater than Figure 5.18d. Grains formed at interlayer region shown in Figure 5.18b and Figure 5.19b had average grain size 40 µm and 44 µm. Thus, grains at the interlayer regions and formed from the lower interlayer-temperature were comparatively smaller than grains at central region and formed by higher interlayer-temperature. Pulsed MIG samples also followed the similar trend. Largest grains were found in samples with high interlayer-temperature (109 µm) central of the layer whereas smallest were in low interlayer-temperature and from interlayer region (58 µm). Average grain size recorded for Figure 5.18c and Figure 5.19a were 85 µm and 81 µm.

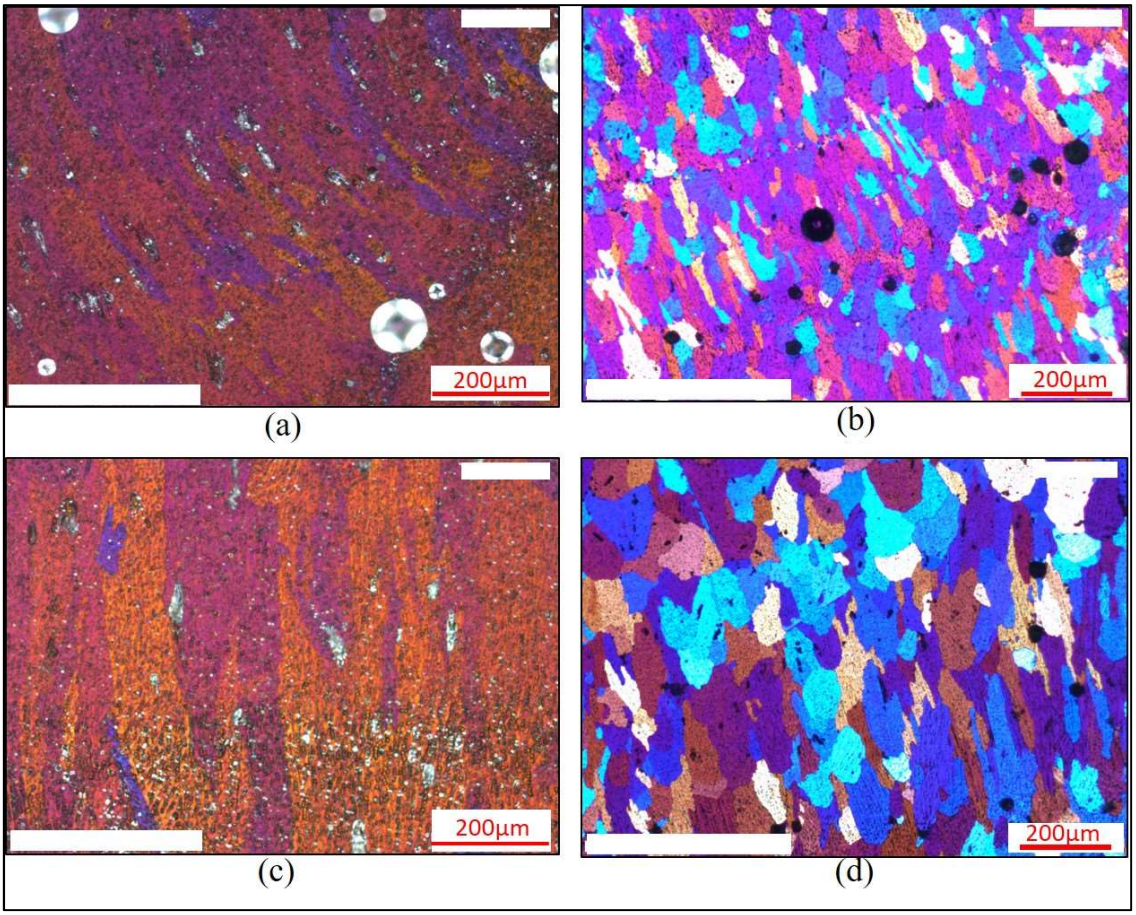

Figure 5.18 Microstructure in transverse direction of torch travel showing HH-T1 samples at layer transition from 2 to 3 shown for pulsed MIG (a) and CMT (b). Microstructure of layer 6 from pulsed MIG (c) and CMT (d).

Further, for low heat input conditions, it was observed that grains were relatively smaller than high heat input samples as can be seen in Figure 5.20 and Figure 5.21. Pulsed MIG samples showed larger grains compared to CMT and also, interlayer-temperature affected the grain size. Similar pattern as discussed earlier for high heat input samples was found reflecting in low hat input samples. For comparison, grains from layer 7 had average size around 86 µm for pulsed MIG samples which was around 52 µm for CMT for low heat input low interlayer-temperature condition. Similarly for high interlayer-temperature condition, average grain size was around 91 µm in pulsed MIG which was 64 µm for CMT samples.

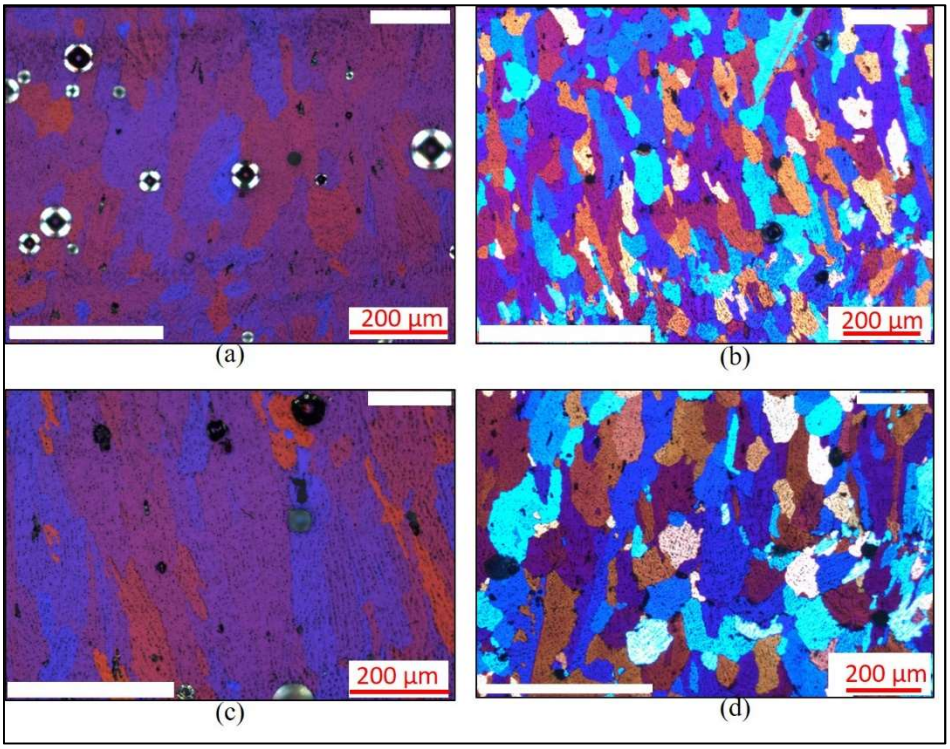

Figure 5.19 Microstructure in transverse direction of torch travel showing HH-T2 samples at layer transition from 2 to 3 shown for pulsed MIG (a) and CMT (b). Microstructure of layer 6 from pulsed MIG (c) and CMT (d).

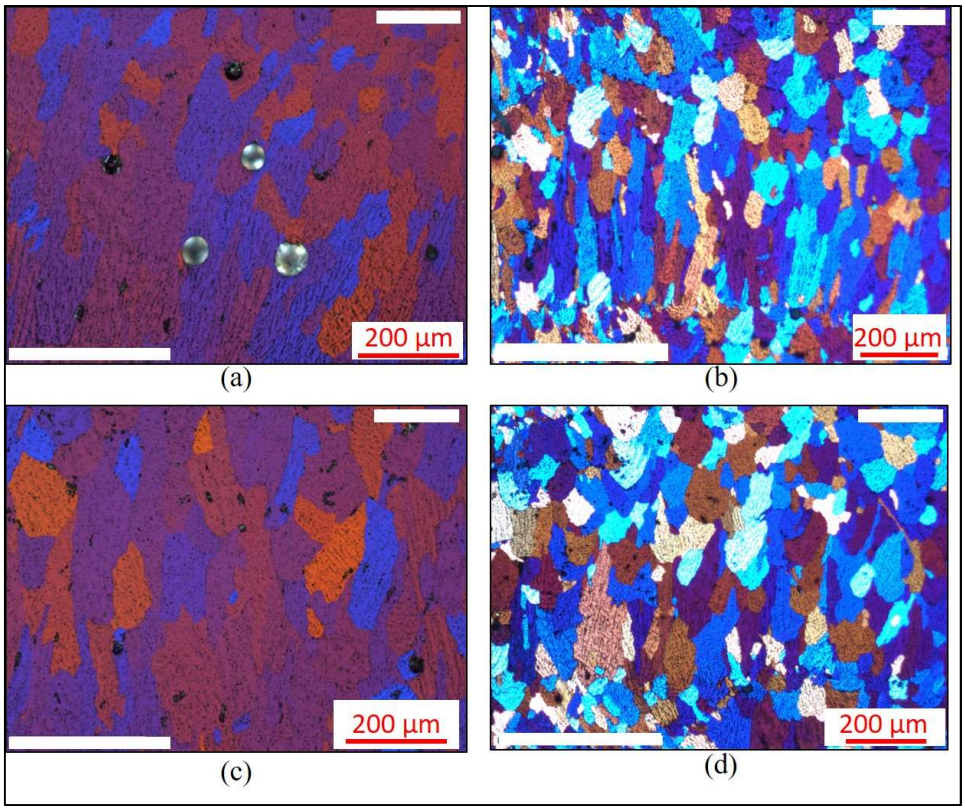

Figure 5.20 Microstructure in transverse direction of torch travel showing LH-T1 samples at layer transition from 2 to 3 shown for pulsed MIG (a) and CMT (b). Microstructure of layer 7 from pulsed MIG (c) and CMT (d).

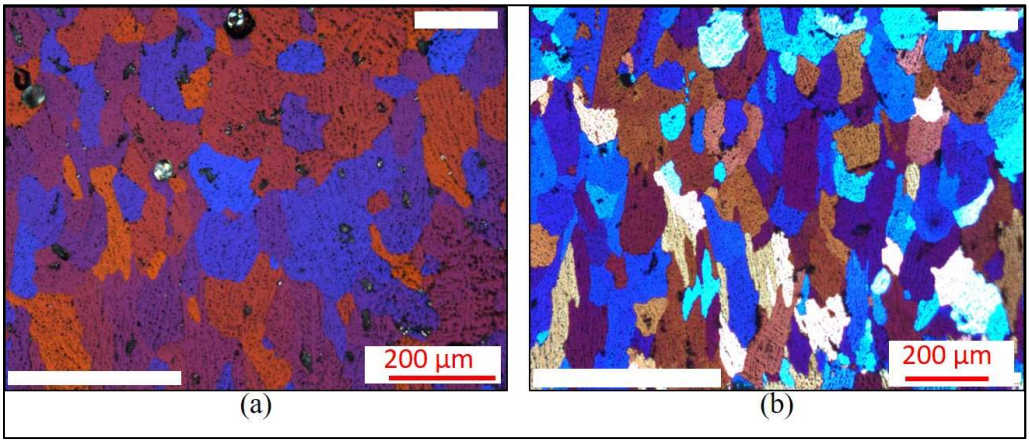

Figure 5.21 Microstructure in transverse direction torch travel showing LH-T2 samples of layer 7 produced using pulsed MIG (a) and CMT (b).

Thus, it can be argued that grains formed in pulsed MIG process were appreciably larger than found in CMT process. High heat input and interlayer-temperature condition of pulsed MIG process showed largest grains while statistically low heat input and interlayer-temperature of CMT samples produced smallest grains. There was no large difference in the average grain size for CMT samples (around 65 µm), however, low heat conditions further reduced grain size. Lower penetration, arc energy, heat input and short circuit transfer metal deposition continuously fragmented the forming larger grains in CMT resulting in smaller grains [80].

5.3.2 Microstructure throughout wall height (15 layers)

5.3.2.1 Microstructure along transverse direction of torch travel

It is common practice to produce a microstructure as a representative of entire area of interest; however, sometimes it may not represent the entire area, particularly in additive manufacturing where repeated heat addition imparts microstructural variations. In this consideration microstructure maps were prepared that will reveal the microstructural variation over the entire wall with 15 layers. Details regarding orientation of microstructural planes considered with respect to torch travel are provided in Figure 5.22

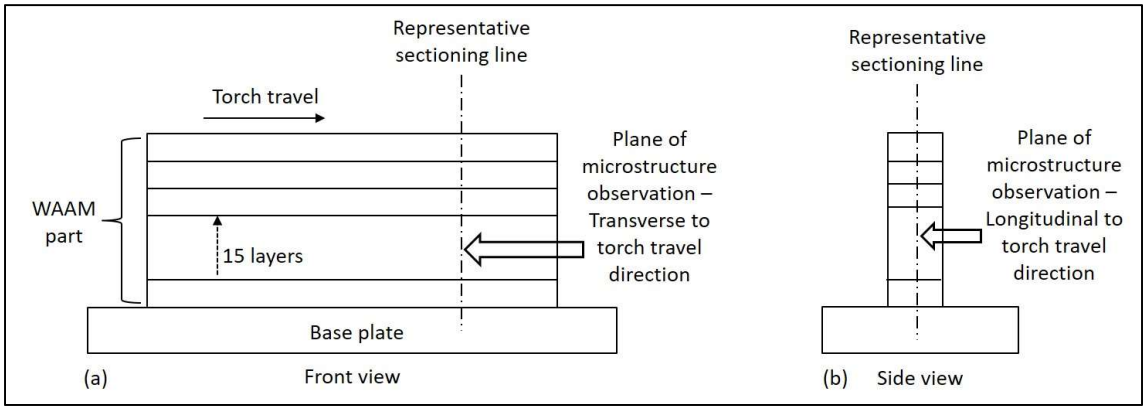

Figure 5.22 Illustration of planes considered for microstructure observations and their orientation with respect to torch travel direction. Microstructural plane perpendicular to torch travel direction i.e. transverse direction of torch travel (a) and microstructural plane parallel to torch travel direction i.e. longitudinal direction of torch travel (b)

Microstructure maps of CMT samples are shown in Figure 5.23 and Figure 5.24. A box shown in figures represents a continuous grain structure. All representative eight samples revealed roughly elongated grains in the build direction. As discussed earlier, grain sizes differed from high heat input to low heat input samples and grains were equiaxed at the top layer. Grains were comparatively smaller at the bottom layers which grew from layer 2 to 3 to its normal size. From previous discussion, grain size for these samples is varying from 50 to 65 μm.

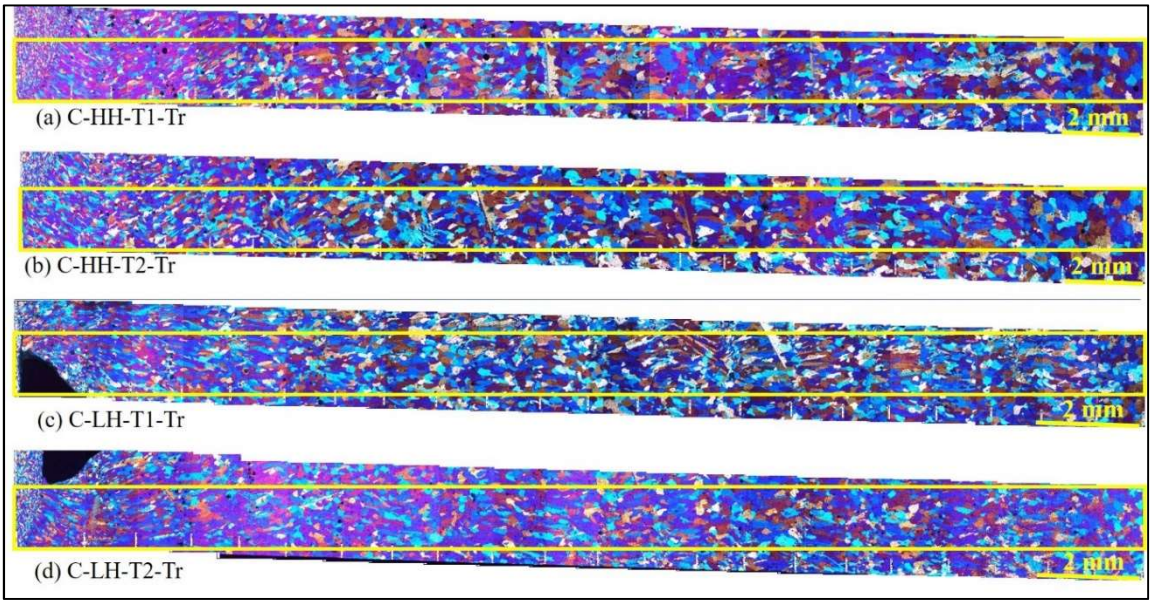

Figure 5.23 Microstructure map of entire built wall starting from bottom layer (left side) to top layer (right side) for interlayer-temperature based CMT samples taken in transverse direction of torch travel. Sample C-HH-T1 (a), C-HH-T2 (b), C-LH-T1 (c) and C-LH-T2 (d). Yellow box indicates continuous grains transformation.

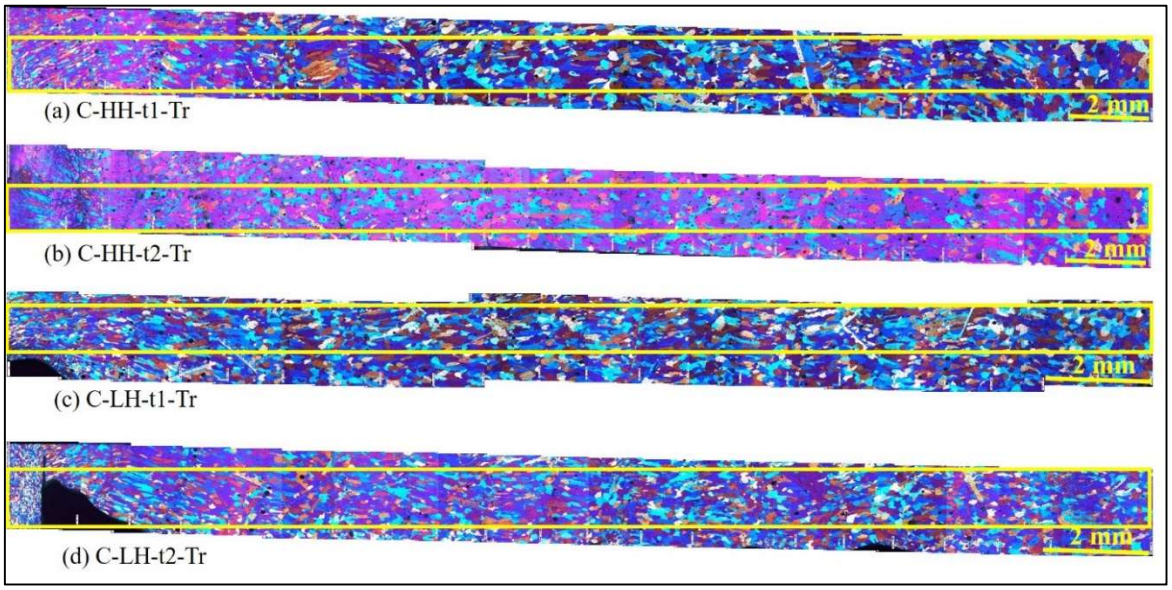

Figure 5.24 Microstructure map of entire built wall starting from bottom layer (left side) to top layer (right side) for interlayer-dwell-time based CMT samples taken in transverse direction of torch travel. Sample C-HH-t1 (a), C-HH-t2 (b), C-LH-t1 (c) and C-LH-t2 (d). Yellow box indicates continuous grains transformation.

For the comparison, similar microstructural maps were prepared for pulsed MIG samples which are shown in Figure 5.25. Similar to CMT samples, pulsed MIG samples also revealed variation in grain sizes with respect to heat input and interlayer-temperature. High heart input samples shown in Figure 5.25a and b, witnessed long columnar grains stretching throughout entire length of a layer. Thus, in some cases columnar grains possessed length of the order of 600 µm or more; however, no grain was found grown through the layers. This is contradictory to the epitaxial grain formation reported for Ti-6Al-4V alloy. Thus, at the end of every layer, a new grain formation was reported. In case of low heat input samples, overall grain size was smaller. Columnar grains with length of around 400 µm were found. Further it would be interesting to understand the nature of grains formed in three directions. At this point, it is clear that CMT samples possessed roughly equiaxed grains while pulsed MIG samples showed columnar grains when viewed in transverse direction of torch travel. Microstructural maps of entire wall taken in longitudinal direction are depicted in Figure 5.26 and Figure 5.27.

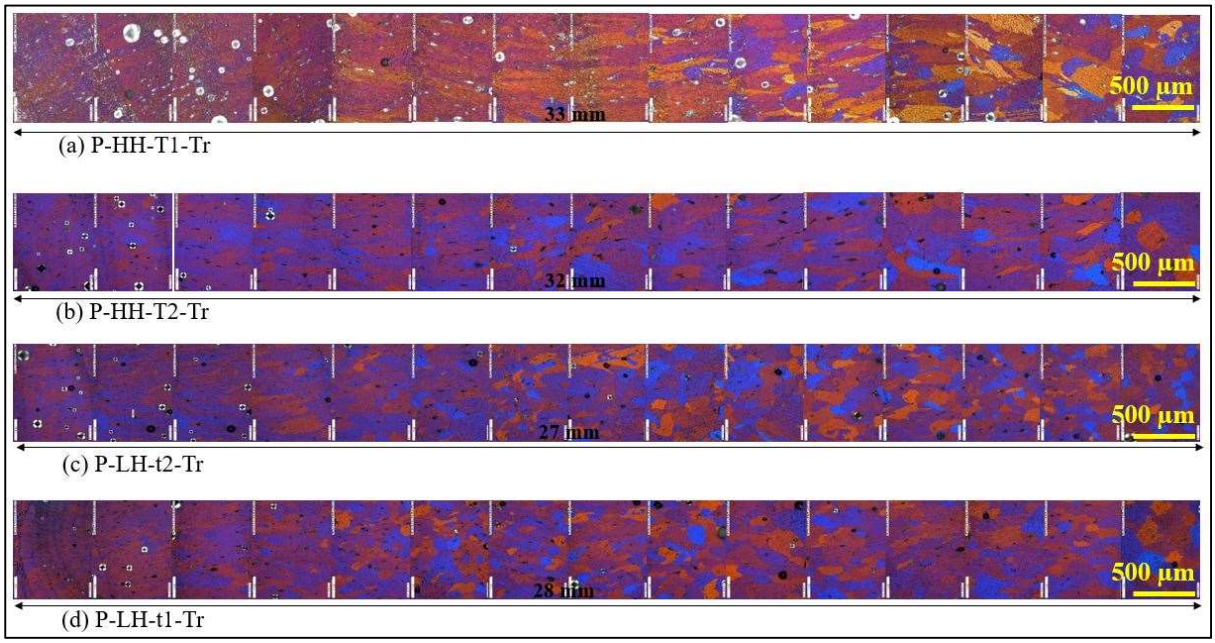

Figure 5.25 Microstructure map of entire built wall starting from bottom layer (left side) to top layer (right side) for pulsed MIG samples taken in transverse direction of torch travel. Total 15 micrographs represent microstructure of respective 15 layers sequentially from left to right (bottom to top). Sample P-HH-T1 (a), P-HH-T2 (b), P-LH-t1 (c) and P-LH-t2 (d).

5.3.2.2 Microstructure along longitudinal direction of torch travel

Microstructural study in the longitudinal direction of torch travel is not widely explored in the open literature. Many researchers studied microstructures only in transverse direction of torch travel [16,79,84,150]. A microstructural map taken in longitudinal direction of torch travel revealed a highly different microstructure taken in transverse direction of torch travel. Figure 5.26 and Figure 5.27 show microstructural map for CMT and pulsed MIG samples in longitudinal direction of torch travel respectively. Comparing Figure 5.26 with Figure 5.23 and Figure 5.24, it was clear that although the equiaxed grains were witnessed on the plane transverse to torch travel direction, grains were seen elongated on the plane longitudinal to torch travel direction. Following the map for single wall, for example Figure 5.26a, columnar grains can be clearly seen inclined at an angle 30° with vertical. A

growth of grains in this angle suggests the direction of torch travel. As discussed in methodology chapter, every successive layer was deposited such that start point of new layer was the end point of earlier layer. Therefore, deposited metal followed peculiar heat extraction pattern and heat flow [154]. Closely following Figure 5.26 and Figure 5.27, it was inferred that in WAAM deposition method, columnar grains were formed irrespective of the metal deposition methods such as pulsed MIG or CMT.

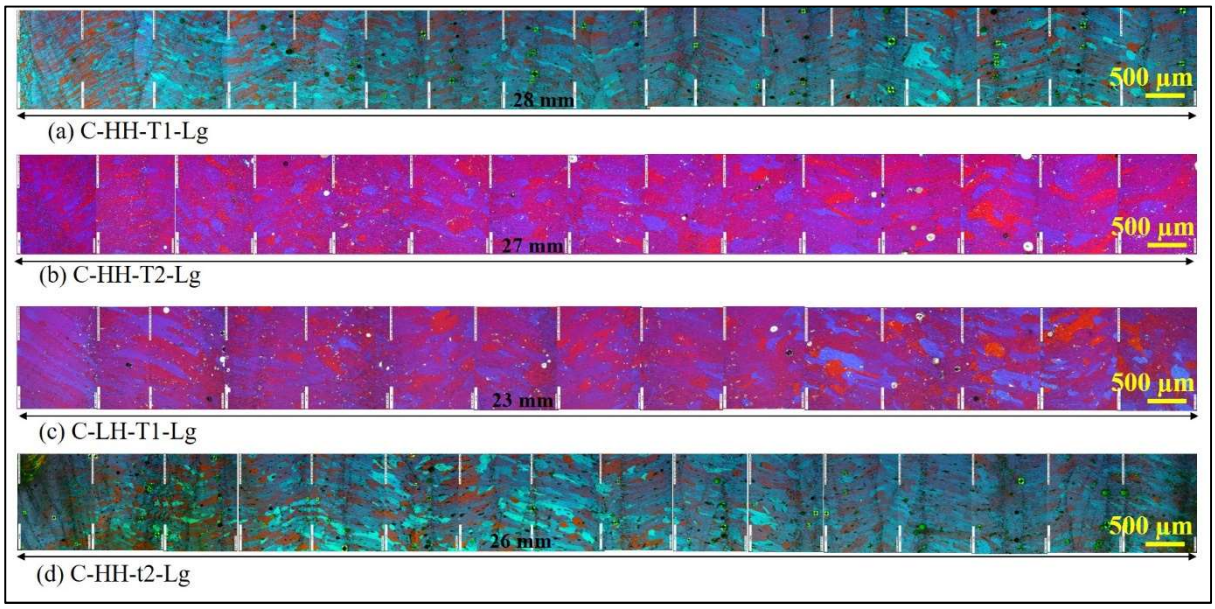

Figure 5.26 Microstructure map of entire built wall starting from bottom layer (left side) to top layer (right side) for CMT samples taken in longitudinal direction of torch travel. All micrographs are in sequential order representing microstructure of respective position in a wall from left to right (bottom to top). Sample C-HH-T1 (a), C-HH-T2 (b), C-LH-T1 (c) and C-HH-t2 (d).

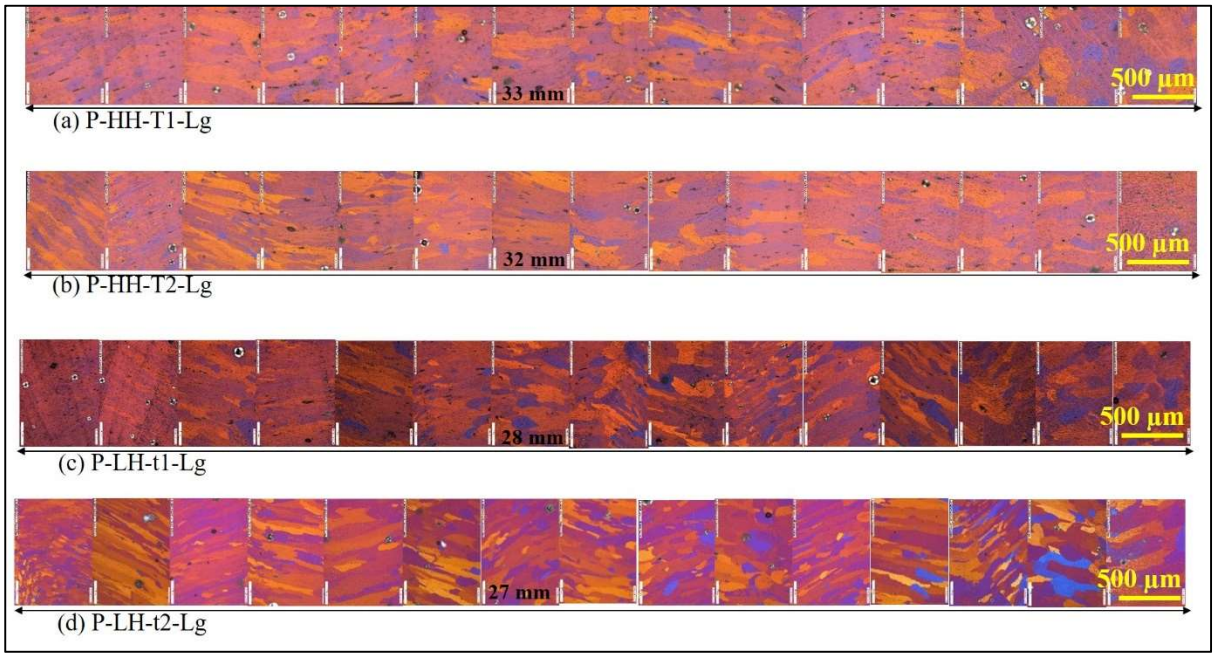

Figure 5.27 Microstructure map of entire built wall starting from bottom layer (left side) to top layer (right side) for pulsed MIG samples taken in longitudinal direction of torch travel. Total 15 micrographs represent microstructure of respective 15 layers sequentially from left to right (bottom to top). Sample P-HH-T1 (a), P-HH-T2 (b), P-LH-t1 (c) and P-LH-t2 (d).

5.3.3 Relation between interlayer-temperature and interlayer-dwell-time methods

Before proceeding with the calculations and discussion regarding cooling and solidification of metal, it is worthwhile to discuss the relationship between interlayer-temperature and interlayer-dwell-time control methods. Temperature of a top layer was maintained either 50 or 100°C for every layer in interlayer-temperature control method, however, it was important to find out the interlayer-temperature of each deposited layer for fixed interlayer-dwell-time that is either 30 or 120 seconds. Figure 5.28 confirms the increment in interlayer-temperature for each successive layer deposited in time-based deposition as discussed earlier [110,140,141]. The highest interlayer-temperature of 135°C was recoded for high heat input short interlayer-dwell-time method with highest rate of temperature rise. Least temperature, 40°C, was witnessed at the low heat input longer interlayer-dwell-time having gradual temperature rise. From the graph obtained, it can be said that for hot deposition condition interlayer-temperature would further rise if more layers were deposited, however, for least heat condition, temperature would rather remain similar for further layers. Also, high heat input longer interlayer-dwell-time control showed appreciable temperature reduction settling around 65°C for last four layers deposited. Comparatively, low heat input short interlayer-dwell-time followed similar pattern as that from high heat condition showing continual increment in interlayer-temperature. Thus, it can be asserted that longer interlayer-dwell-time samples showed lower interlayer-temperature compared to short interlayer-dwell-times. Thus, from the graph it can be concluded that longer interlayer-dwell-time supports in heat dissipation reducing the interlayer-temperature and achieving fairly similar interlayer-temperature after deposition of certain number of layers; however, short interlayer waiting time does not provide sufficient time for heat dissipation and compels heat accumulation ultimately continuously increasing the interlayer-temperature. Therefore, interlayer-dwell-time is one of the crucial factors in metal additive manufacturing that cannot be ignored. The more details about its effect on porosity can found in discussion part of porosity chapter.

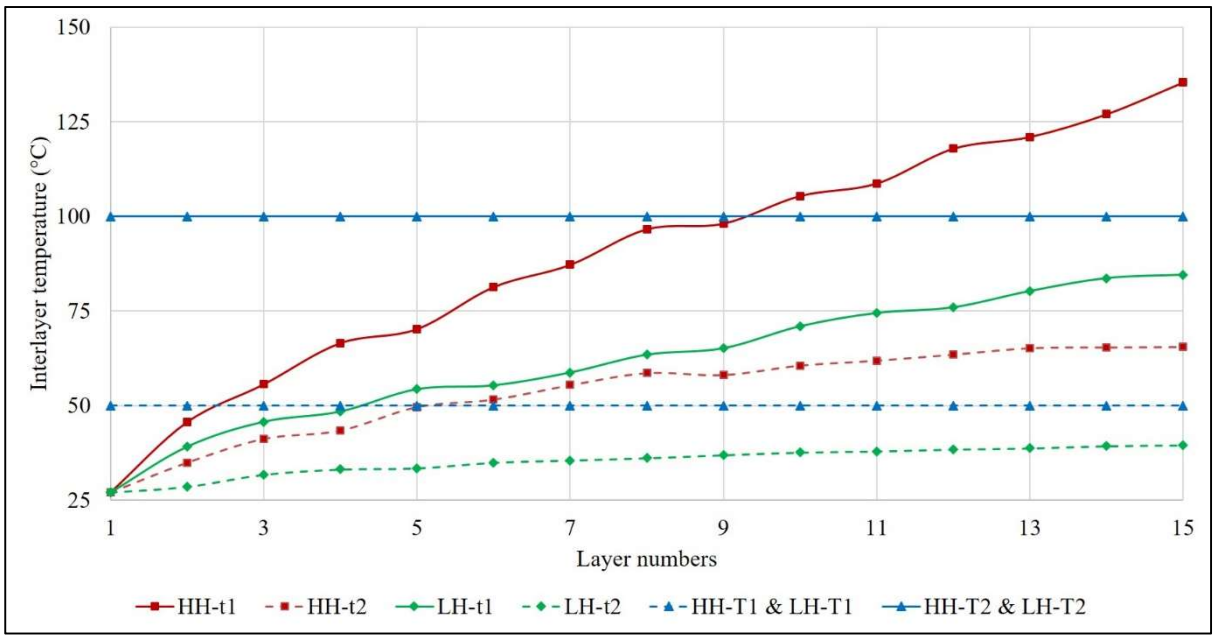

Figure 5.28 Interlayer-temperature measured for each depositing layer in interlayer-dwell-time based samples.

5.3.4 Quantification of metal solidification

Many researchers studied the unconventional solidification mode and heat transfer process involved in the metal additive manufacturing and many numerical and computational theories were developed [155–159]; however, the process is not fully understood and large amount of work is anticipated. As in this work, focus is directed towards the particular temperature maintenance, it was possible to calculate the liquid metal cooling and solidification rates. There are many mathematical models available, however, most of them are dedicated to carbon and alloys steels that considers typical critical cooling temperature range, 800 to 500°C. Therefore, classical established equations commonly employed in welding operations [160,161] were used for calculations of cooling rates and solidification times as shown equation 6 and 7 respectively.

$$R = \frac{2\pi k(Tc - To)^2}{Hnet} \qquad \text{Eq. (6)}$$

$$S = \frac{LHnet}{2\pi k\rho C(Tm - To)^2} \qquad \text{Eq. (7)}$$

Considering Eq.6, R is the cooling rate in °K/s, k is the thermal conductivity in J/m-s-°K, Tc is the temperature in °K at which cooling rate is calculated, To is the initial temperature in °K, $Hnet$ is the net heat input of the welding process taken in J/m. For Eq. 7, S is the solidification rate in seconds, L is the latent heat of fusion in J/m^3, ρ is the density of metal in kg/m^3, C is the specific heat of metal taken in J/kg-°K, Tm is the melting temperature, and $Hnet$, k and To are as above.

5.3.4.1 Cooling rates

The cooling rates were calculated for high and low heat input conditions. Pulsed MIG and CMT methods theoretically showed similar average heat inputs and hence, cannot be separately accounted for calculations. Graphical representation of cooling rates, shown in Figure 5.29 to Figure 5.31 essentially highlighted the effect of heat input on rate of cooling. Cooling rates calculated at different temperatures such as 638, 550, 450, 350, 250, and 160°C showed a vast difference. High heat input samples showed cooling rates between 1000 to 1500 °K/s while it was 2300 to over 3000 °K/s for low heat input samples when calculated at the melting point (638°C); however, the cooling rates were found varying from as low as 2.5 to 70 °K/s and 25 to 145 °K/s for high and low heat input samples respectively when calculated at stress relief temperature 160°C.

For fixed interlayer-temperature samples, cooling rate was unchanged for all 15 layers for a particular set. At the same time, samples with fixed interlayer-dwell-time showed varying cooling rates, maximum to minimum for increasing number of layers due to the different interlayer temperatures as discussed earlier. Therefore, the temperature difference between liquid aluminium and previously deposited layer gradually decreased with the increment in deposited layer, reducing the overall cooling rate. The condition holds true for both the heat inputs and thus, affected the microstructure. From Figure 5.29 to Figure 5.31, a close relation between interlayer-temperature and dwell-time can be drawn. In case of low heat input, cooling rates were found in proximity for 50°C interlayer-temperature and 120 seconds

interlayer-dwell-time for all the temperatures considered for cooling rate calculations. Also, 30 seconds interlayer-dwell-time samples with reducing cooling rates settled slightly higher than the lowest cooling rate shown by the 100°C interlayer-temperature samples at layer 15. Hence, curves did not cross showing lowest cooling rate by 100°C interlayer-temperature. Similarly, high heat input samples also showed matching cooling rates for 50°C interlayer-temperature and 120 seconds interlayer-dwell-time; however, unlike to low heat input samples, the reducing cooling curves of 30 seconds interlayer-dwell-time samples crossed the cooling curves of 100°C interlayer-temperature at around layer 9 for all the cases considered. Thus, heat accumulation in high heat input condition was high enough to reveal the cooling rate lower than possessed by 100°C interlayer-temperature samples beyond layer 9. Calculations are provided in Annexure II.

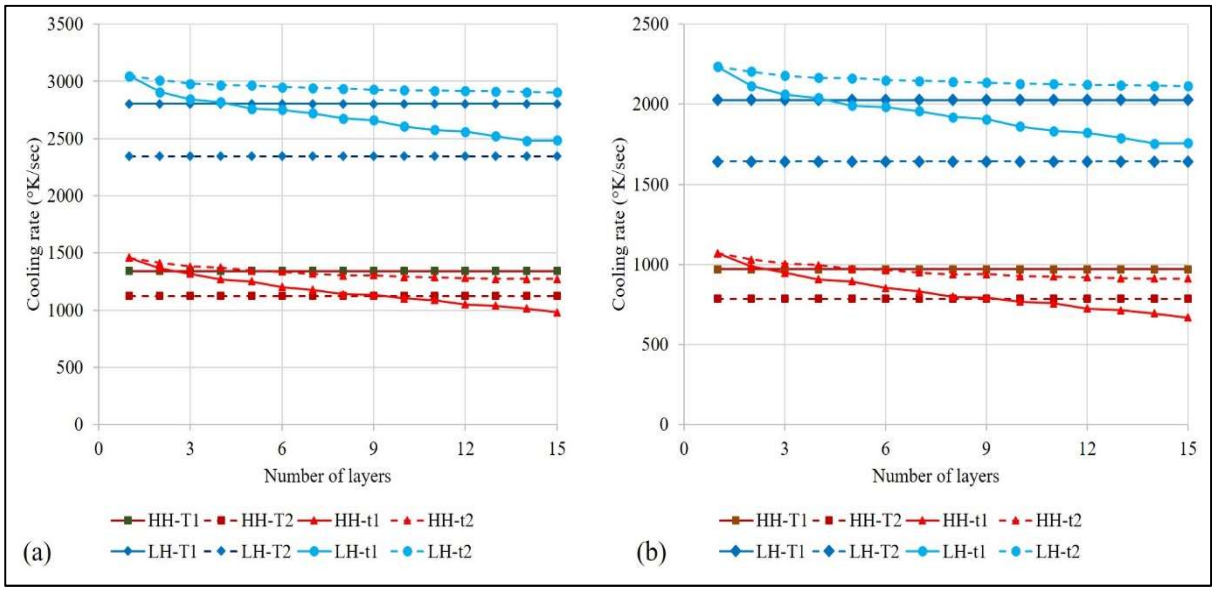

Figure 5.29 Calculated cooling rate at melting point (a) and at 550°C (b) of deposited aluminium.

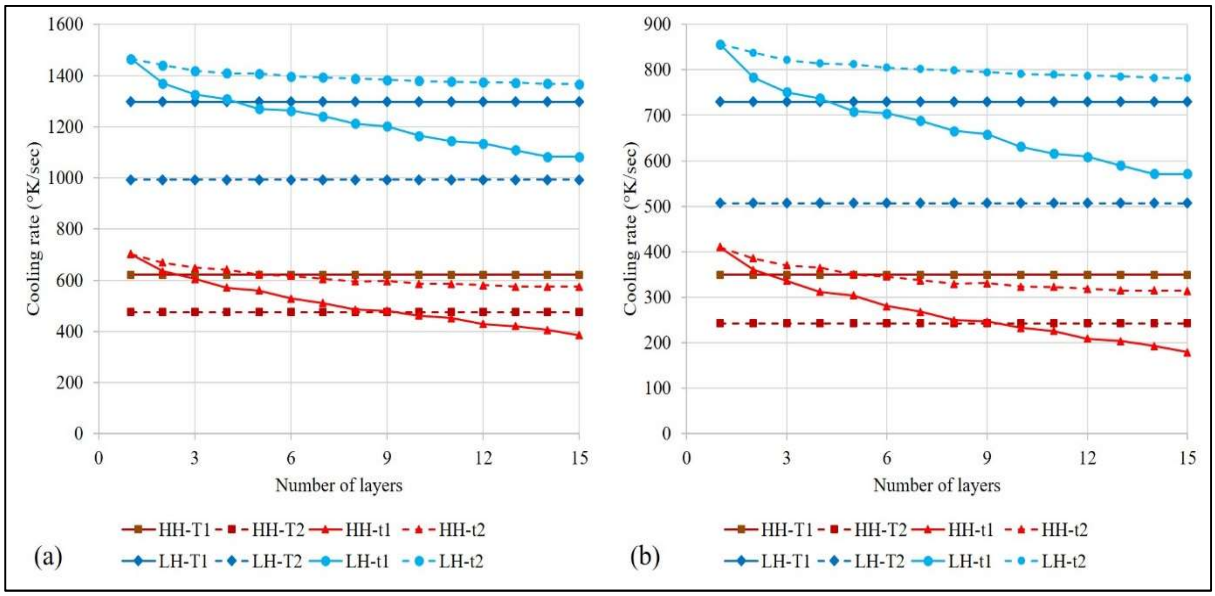

Figure 5.30 Calculated cooling rate at 450°C (a) and at 350°C (b) of deposited aluminium.

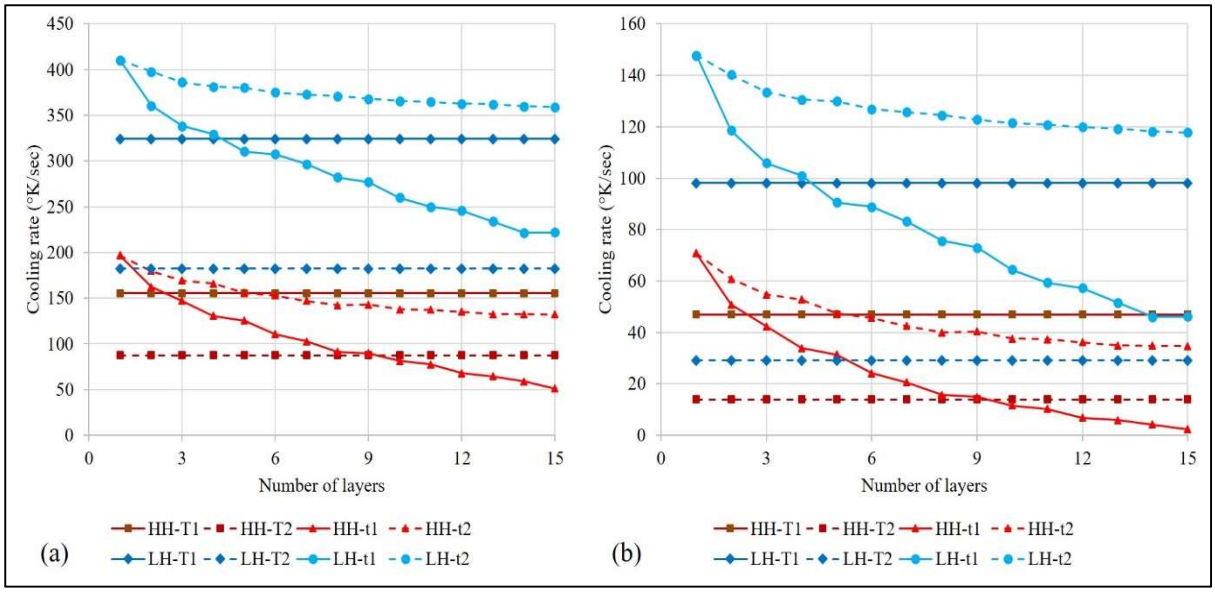

Figure 5.31 Calculated cooling rate at 250°C (a) and at 160°C (b) of deposited aluminium.

5.3.4.2 Solidification times and rates

Solidification times were calculated for eight different metal deposition conditions following Eq. 7 and graphically represented in Figure 5.32. Samples produced using low heat input showed lesser solidification time than high heat input. The fact was reflected from the cooling curves described earlier that cooling rate was higher for low heat input than high heat input suggested lesser solidification time for low heat input samples. Continuous increase in the solidification time was observed for 30 seconds interlayer-dwell-time samples due to accumulation of heat that reduced cooling rate and increased solidification time. Effect of heat accumulation was comparatively less in low heat input samples than high heat input. On a broader scale, low heat input samples revealed solidification time between 0.15 to 0.2 seconds while it was from over 0.3 to 0.45 seconds for high heat input samples that is approximately double, that essentially highlighted its impact on grain formation and grain growth. Again, comparing the solidification time for interlayer-temperature and interlayer-dwell-time control methods, similar results were obtained for high and low heat input samples. Thus, solidification time invariably affected the solidification rate depicted in Figure 5.33. Overall appearance of the curves showing solidification rate closely resembled to cooling curves where higher rates were witnessed at low heat input and lower at high heat input samples. Refer Annexure II for more details.

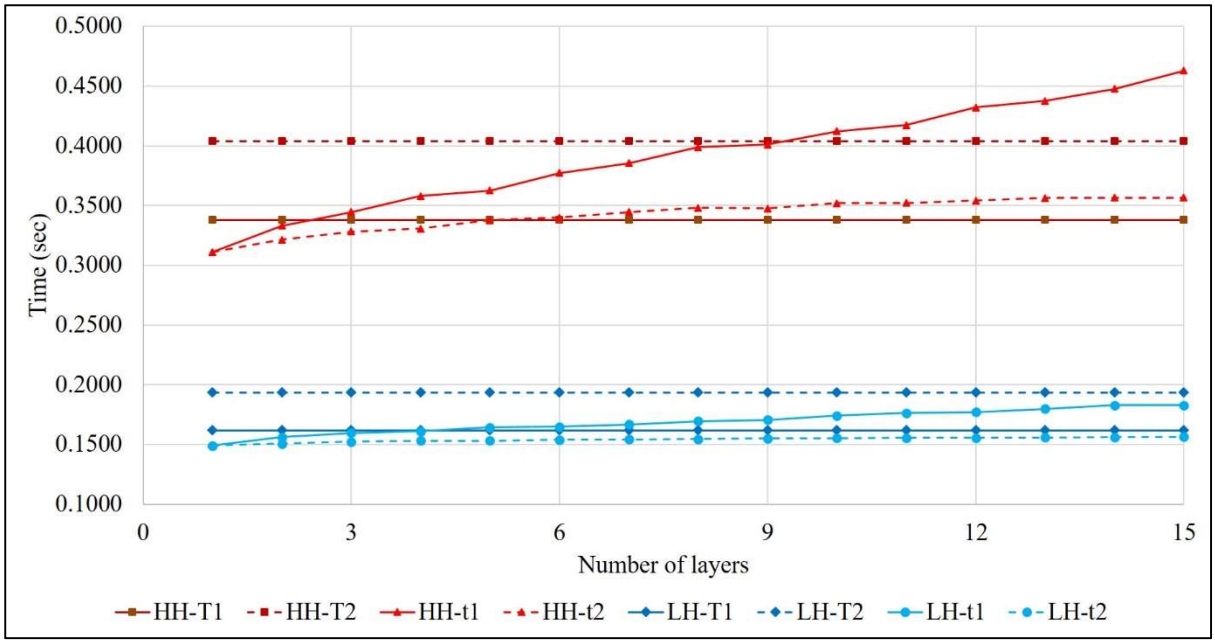

Figure 5.32 Calculated solidification time for deposited aluminium.

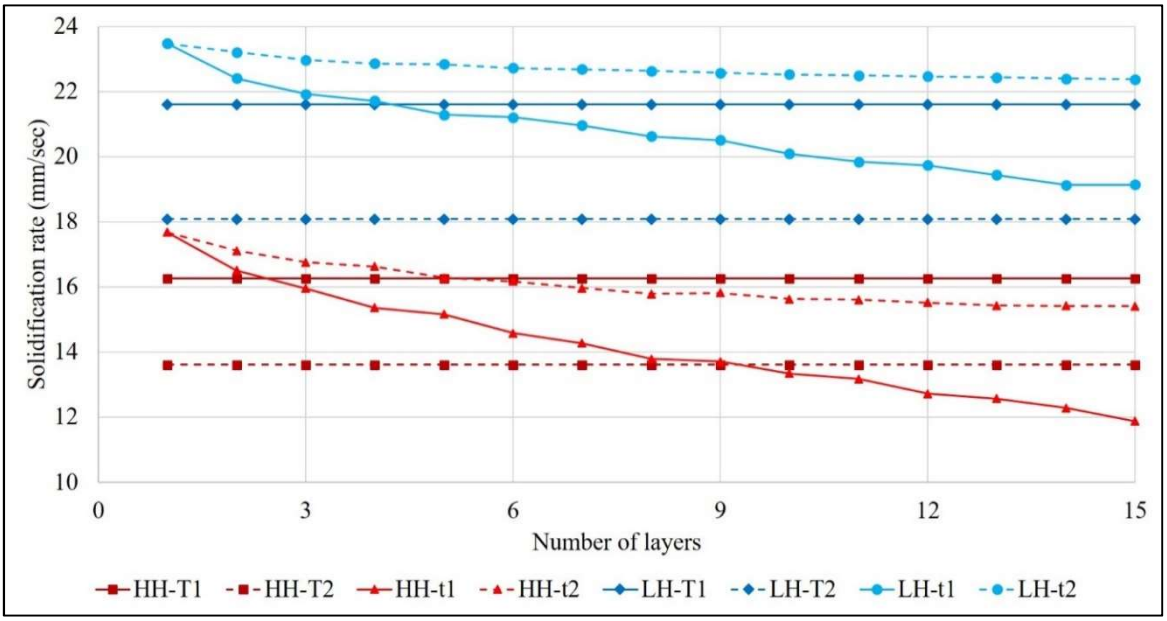

Figure 5.33 Calculated solidification rate for deposited aluminium.

From cooling and solidification curves, it can be conclude that heat input majorly affects the metal solidification phenomena. Also, interlayer-temperature and interlayer-dwell-time can also be the controlling factor defining specific cooling and solidification rates, thus ultimately controlling the microstructure.

5.3.5 Thermal imaging

In methodology chapter, details about temperature measurements of WAAM wall using thermal camera is described. This section presents the results and related discussion regarding the same. The images taken as a temperature recordings are shown in Figure 5.34a and b. The images are taken immediately after the end of deposition of layer 15. For temperature comparison, total 7 spots were chosen on a

deposited wall roughly at central region such that spot 1 represents temperature of layer 2, spot 2 represent layer 4, spot 3 shows layer 6 up to spot 7 showing temperature of layer 14. The analysis considers 530 and 0 °C maximum and minimum metal temperature which is a chosen predefined band of temperature measurement associated with the software employed. This band was chosen because the alloy of interest possesses melting temperature not far from the upper chosen temperature band limit.

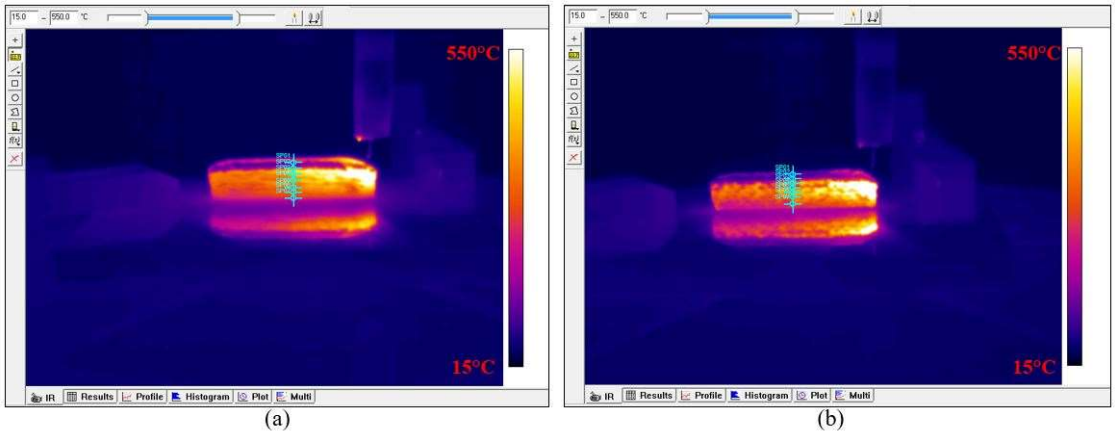

Figure 5.34 Thermal camera image showing temperature distribution in WAAM wall samples P-HH-T1 (a) and P-LH-t2 with seven spots starting from layer 2 up to layer 14.

Figure 5.35 to Figure 5.38 depicted the temperature variation at the central vertical part of a deposited wall from top to bottom at every alternative layer. Irrespective of metal deposition condition, all graphs revealed maximum temperature at the middle layers. Top and bottom layers witnessed relatively low temperatures. In all cases, temperature of the top layers was lesser than temperature of middle and initial layers suggesting faster cooling for top layers and heat accumulation at middle and initial layers. As expected, wide temperature variation was seen for different metal deposition conditions. From all the graphs it can be said that higher interlayer temperature samples witnessed increased overall temperature across the wall height. Regardless of temperature maintenance condition, pulse-MIG samples showed higher temperature with respect to comparable conditioned CMT samples. Samples prepared using 30 seconds interlayer-dwell-time showed higher temperature than samples prepared with 120 seconds. Also, higher heat input samples were found hotter than low heat input samples. Amongst all 16 samples, P-HH-t1 showed highest temperature for broader part of a wall while C-LH-T1 showed lesser temperature amongst all samples. The results are in coordination with earlier discussion from solidification and cooling rates sections where slowest cooling and solidification rate was recorded for pulsed-MIG sample with 30 seconds interlayer-dwell-time. Samples manufactured with 120 seconds interlayer-dwell-time and low heat input showed comparatively lower overall temperature of a wall in pulse-MIG mode. On the other hand, in CMT mode, high heat input and 30 second interlayer-dwell-time sample was recorded the highest temperature.

One of the important outcomes of the thermal camera recordings highlighted the fact that temperature of previously deposited layers is raised well above the recrystallisation temperature that is 300°C [134], therefore, microstructural changes are inevitable. This is important to note that the temperature of previously deposited layer is raised above recrystallisation temperature multiple times. The fact governs microstructure development and grain growth that will be discussed in later part of this chapter.

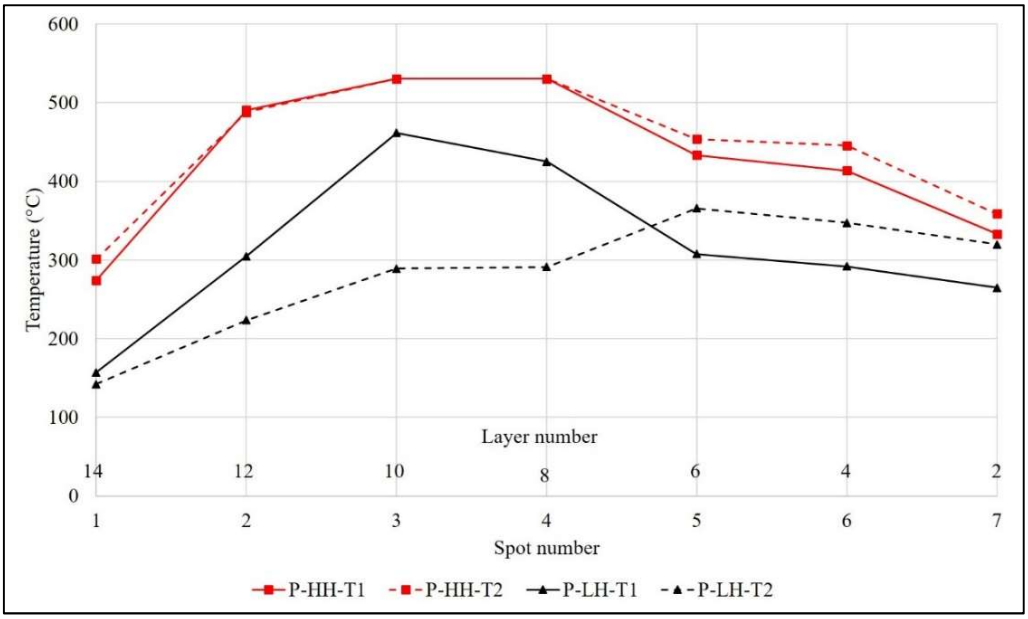

Figure 5.35 Temperature variation observed in pulsed-MIG interlayer-temperature based samples.

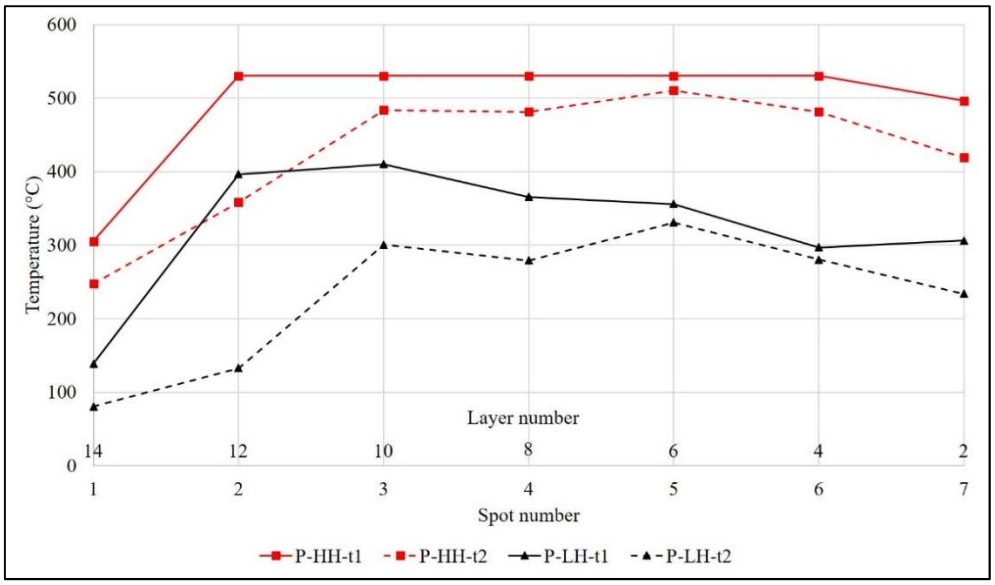

Figure 5.36 Temperature variation observed in pulsed-MIG interlayer-dwell-time based samples.

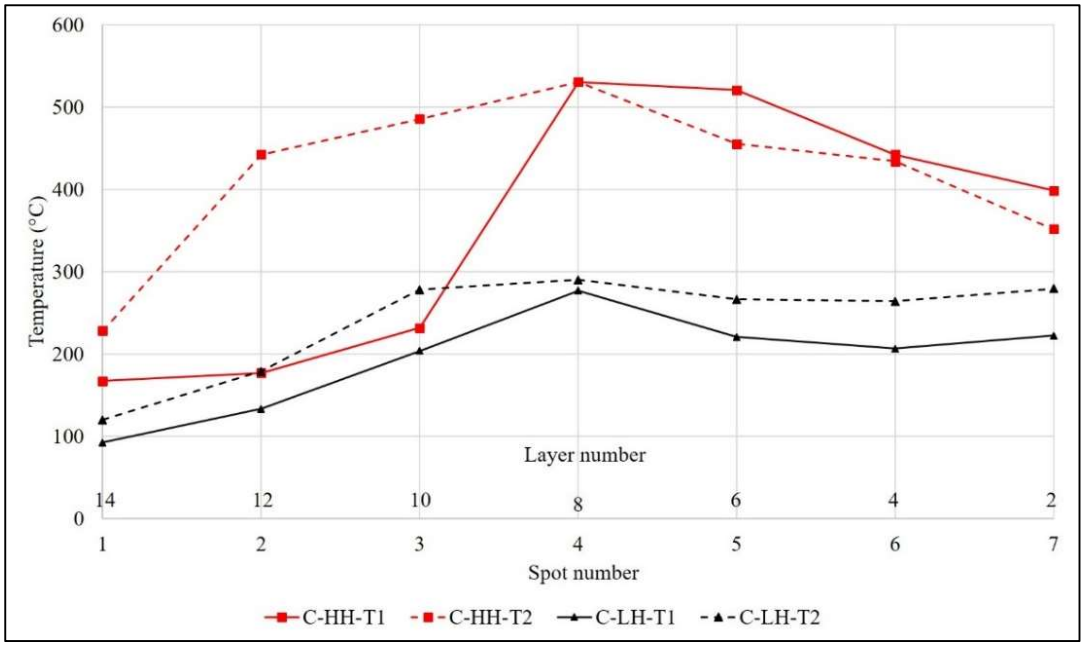

Figure 5.37 Temperature variation observed in CMT interlayer-temperature based samples.

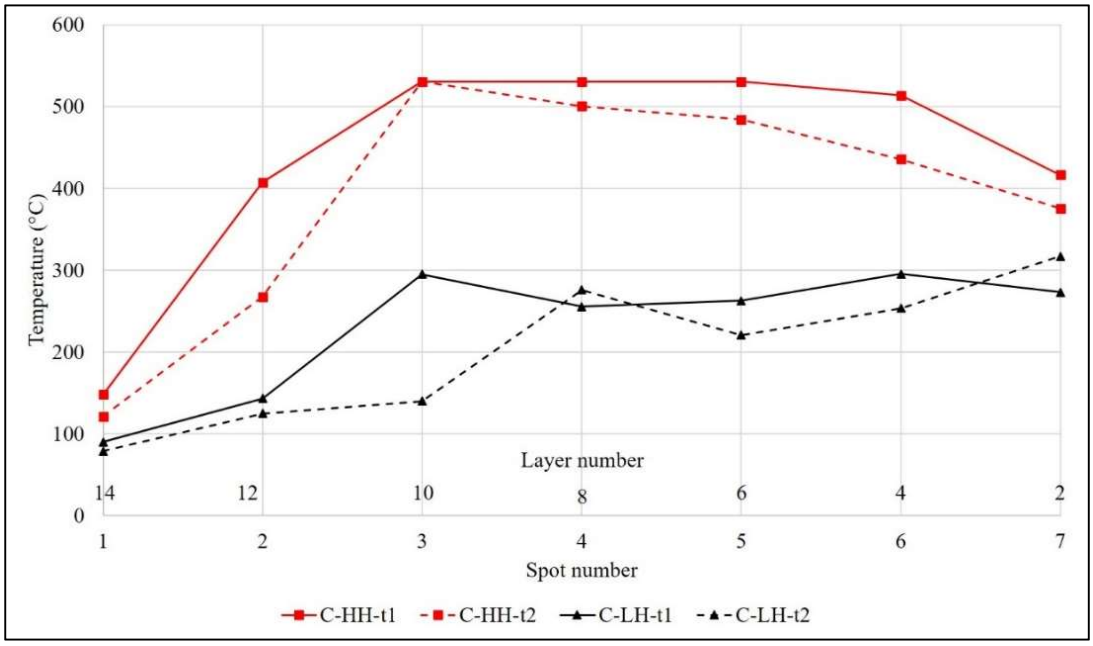

Figure 5.38 Temperature variation observed in CMT interlayer-dwell-time based samples.

5.3.6 Mechanical properties

5.3.6.1 Tensile properties

Samples prepared using pulsed-MIG process were tested for tensile strengths as discussed in Methodology chapter. A clear line can be drawn separating high and low heat input samples based on obtained strength values for respective samples from Table 5.1. Yield and ultimate tensile strengths of low heat input samples were found higher than high heat input samples. Average yield strengths of high and low heat input samples were around 126.5 and 134 MPa while ultimate tensile strengths were 276.5 and 285.5 MPa respectively. Hence, samples manufactured with low heat input possessed around 9 and

10 MPa higher yield and tensile strength than high heat input samples respectively. On the other hand, while comparing tensile test results based on sample locations it can be said that samples from top region of a wall had higher yield and tensile strength than samples representing bottom portion. Average tensile strengths of high heat input samples from bottom and top region of were around 275 and 284 MPa while for low heat input samples values were 277 and 286 MPa respectively. Similar trend was recorded for yield strength values with lower differences.

Table 5.1 Tensile test results of single bead-multilayer samples manufactured using pulsed-MIG.

Sample ID	Young's modulus (GPa)		Yield strength (MPa)		Ultimate Tensile Strength (MPa)		Elongation (%)	
	Bottom	Top	Bottom	Top	Bottom	Top	Bottom	Top
P-HH-T1	64.42	56.51	127.92	129.68	276.17	280.05	25	25
P-HH-T2	60.69	63.94	123.87	123.06	275.52	274.75	24	24
P-HH-t1	63.94	65.69	123.06	127.48	274.75	276.99	25	27.5
P-HH-t2	55.02	62.24	125.53	131.05	274.99	278.86	27.5	25
P-LH-T1	61.68	70.34	127.98	142.33	284.53	287.96	25	25
P-LH-T2	63.21	57.35	130.56	134.18	283.24	289.83	26.5	27.5
P-LH-t1	61.76	57.43	131.35	133.1	283.99	283.54	29	27.5
P-LH-t2	91.05	61.45	140.7	133.98	287.49	284.61	26.5	25

In an approach of multibead-multilayer wall manufacturing with different interlayer-temperatures as discussed in Methodology chapter, tensile tests were performed to understand any effect of interlayer-temperature variation on tensile properties. Results shown in Table 5.2 clearly divides horizontal and vertical samples. Horizontal samples witnessed higher average yield and tensile strengths compared to vertical samples by 3 and 49 MPa respectively. Results are similar to the results discussed in porosity chapter. When samples were compared for interlayer-temperature low heat input samples showed higher strengths than high heat input samples by marginal difference.

To better understand the effect of interlayer-temperature and its effect on tensile properties, chemical testing of all interlayer-temperature based samples were performed. Results for the same are presented in Table 5.3. Work hardening aluminium alloys obtain their strengths from solid solution strengthening effect produced due to the presence of alloying additions such as Mg for 5xxx series alloys [14,134]. Thus, the selected wire composition 5183 obtains its strength mainly from the Mg; however, elemental loss in aluminium alloys due to the exposure to a high temperature during arc metal deposition and its adverse effect on mechanical properties are widely discussed in literature [14]. In recent study, Yuan et al. [162] discussed the reduced strength of 5xxx series aluminium alloys in WAAM type deposition. According to authors, the rate of loss of Mg increased with increasing current and decreased with increasing travel speed. Thus, following the heat input formula, increase in current increases heat input while increase in travel speed decreases heat input [3,90].

Table 5.2 Tensile test results of multibead-multilayer samples manufactured using pulsed-MIG.

Sample ID	Young's Modulus (GPa)	Yield strength (MPa)	Ultimate Tensile Strength (MPa)
1-T1-A-H	74.2	135.09	289.36
1-T1-B-H	73.87	133.28	291.07
1-T1-C-H	64.87	134.17	292.46
2-T2-A-H	65.32	131.92	288.61
2-T2-B-H	68.23	131.53	285.2
2-T2-C-H	70.53	132.38	293.38
1-T1-A-V	68.5	132.75	266.94
1-T1-B-V	65.75	132.17	247.17
1-T1-C-V	67.19	131.86	211.3
2-T2-A-V	70.67	131.25	233.84
2-T2-B-V	68.85	132.26	264.6
2-T2-C-V	62.89	131.98	222.96

Initial feed stock wire 5183 possessed around 4.91% of Mg that found reduced irrespective of method used for deposition as per Table 5.3. Comparatively increased percentage of Mg was present in CMT samples (avg. 4.63%) than pulsed-MIG processed samples (avg. 4.58%). Figure 5.39 highlighted the increased Mg loss in pulse-MIG samples (avg. 6.61%) compared to CMT samples (avg. 5.65%). It can be argued that even though CMT and pulsed-MIG samples showed similar heat inputs by calculations, pulsed-MIG process was relatively hotter. This could be due to the longer ignited arc in pulse-MIG which was not the case of CMT where intermittent ignition and extinction of arc [3,163] reduced overall temperature and Mg loss. Further, considering the effect of interlayer-temperature and heat input on volatile Mg losses, similar results were obtained. Effect of heat input on Mg losses were prominent than effect of interlayer temperature in both pulsed-MIG and CMT processed samples. Highest heat content combination amongst eight samples that is pulsed-MIG and high interlayer-temperature showed lowest Mg content. CMT samples also showed the similar results for high heat input and 100°C interlayer temperature. The probable reason for low Mg percentage in samples could be the occurrence of higher temperature while metal deposition that guided Mg evaporation. Temperature of liquid aluminium raises above the melting point of Mg (1107°C [162]) in both CMT and pulsed-MIG processes; however, hotter pulsed-MIG could be responsible for raising temperature much higher that could not be achieved with CMT. Also, similar is the case with heat input where lower heat input raises the temperature above melting point of Mg but not as high as the temperature raise occurred at high heat input. Elemental Mg loss usually occurs at the top layer however, at very high temperature there are chances of additional Mg losses from the penultimate layer and that could be another field of study. This possibility is raised based on the results obtained for the thermal camera. Particularly for pulsed-MIG samples, high

penetration and heat input raises temperature of part of penultimate layer well above melting of aluminium. In this case it will be interesting to study the elemental loss that may affect the mechanical properties.

Table 5.3 Chemical analysis of deposited samples.

Elem-ents	Sample ID								
	Wire	C-HH-T1	C-HH-T2	C-LH-T1	C-LH-T2	P-HH-T1	P-HH-T2	P-LH-T1	P-LH-T2
Si	0.06	0.05	0.05	0.04	0.05	0.05	0.05	0.05	0.05
Mn	0.65	0.63	0.64	0.65	0.63	0.65	0.66	0.65	0.65
Mg	4.91	4.67	4.59	4.6	4.67	4.59	4.51	4.62	4.62
Cu	0.01	0.01	0.01	0.01	0.01	<0.01	0.01	<0.01	<0.01
Zn	<0.01	0.01	<0.01	<0.01	0.01	<0.01	<0.01	<0.01	<0.1
Fe	0.14	0.13	0.13	0.12	0.13	0.12	0.13	0.12	0.12
Ti	0.07	0.08	0.08	0.08	0.08	0.09	0.09	0.09	0.08
Cr	0.07	0.08	0.08	0.08	0.08	0.08	0.08	0.08	0.08
Al	Balance								

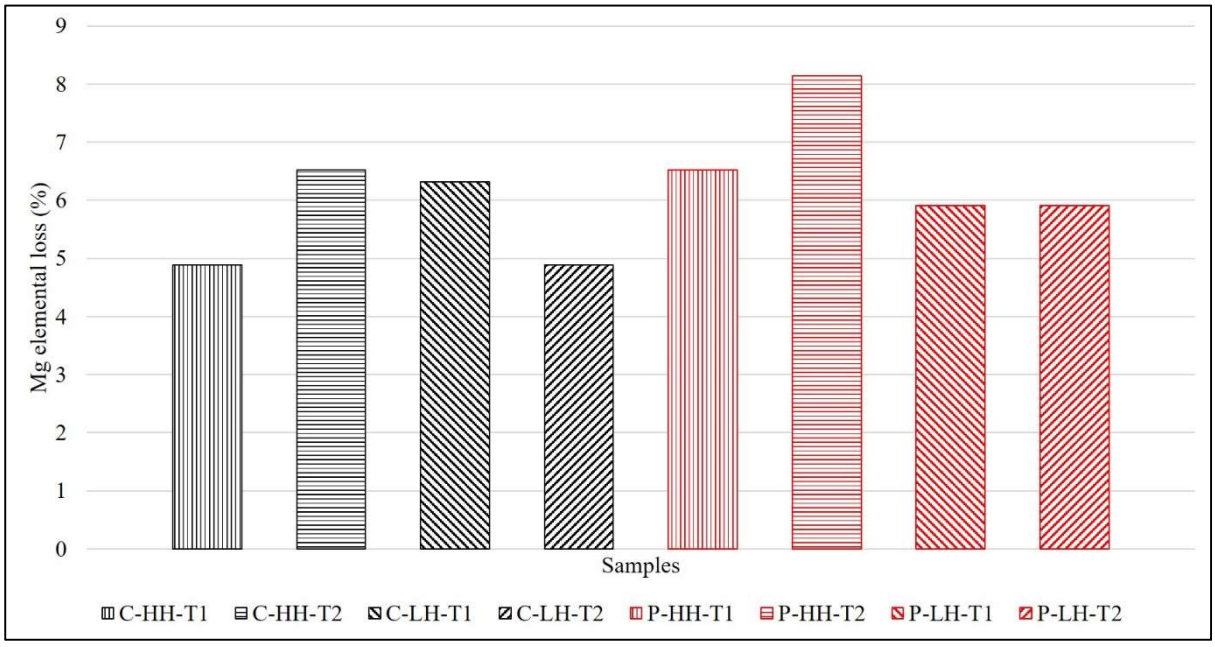

Figure 5.39 Percentage Mg elemental loss in CMT and pulse-MIG samples.

From the above discussion and results of chemical analysis it was clear that Mg, the main solid solution forming element responsible for strain hardening, was reduced compared to the feed stock wire. Therefore, the samples produced with low heat input, referring to Table 5.1, showed less tensile and yield strength than samples produced with high heat input. The similar results were reported by Fang et

al. [150] for CMT-P and CMT-ADV processes. Higher Mg loss witnessed by higher interlayer-temperature samples showed comparatively lesser yield and tensile strength than lower interlayer-temperature which was also found in Table 5.2. Additional factor while comparing horizontal and vertical tensile samples is the porosity present at the interlayer region. Detailed explanation regarding the strength reduction based on porosity is given in porosity and hydrogen dissolution chapter.

5.3.6.2 Hardness measurements

No appreciable differences in the hardness values were observed. In Figure 5.40 to Figure 5.43, hardness values were roughly above 75 Hv for almost all the samples. Hardness values close to the observed values were reported by Horgar et al [16]. There were few hardness values found as low as 50 Hv that can be ignored, however reported here, might be from the presence of porosity at the indentation area. Table 5.4 compares the average hardness of samples individually and in groups. There were hardly any variations evidenced in the hardness values, however, high heat input samples from both pulse-MIG and CMT processes possessed lower average hardness compared to low heat input samples. It should be noted that the difference between average hardness was marginal of 1.5 to 3 Hv, however, values cannot be ignored as average values considered roughly 200 individual hardness values for average calculations. One probable reason for the increased hardness for low heat input samples could be the higher cooling and solidification rate. Faster cooling forced the formation of smaller grains that can be held responsible for higher hardness [114] (refer Figure 5.18 to Figure 5.21). Also, it is believed that recrystallisation and annealing effect offered by high heat input in a layer type metal deposition extends to larger area of a forming part compared low heat input.

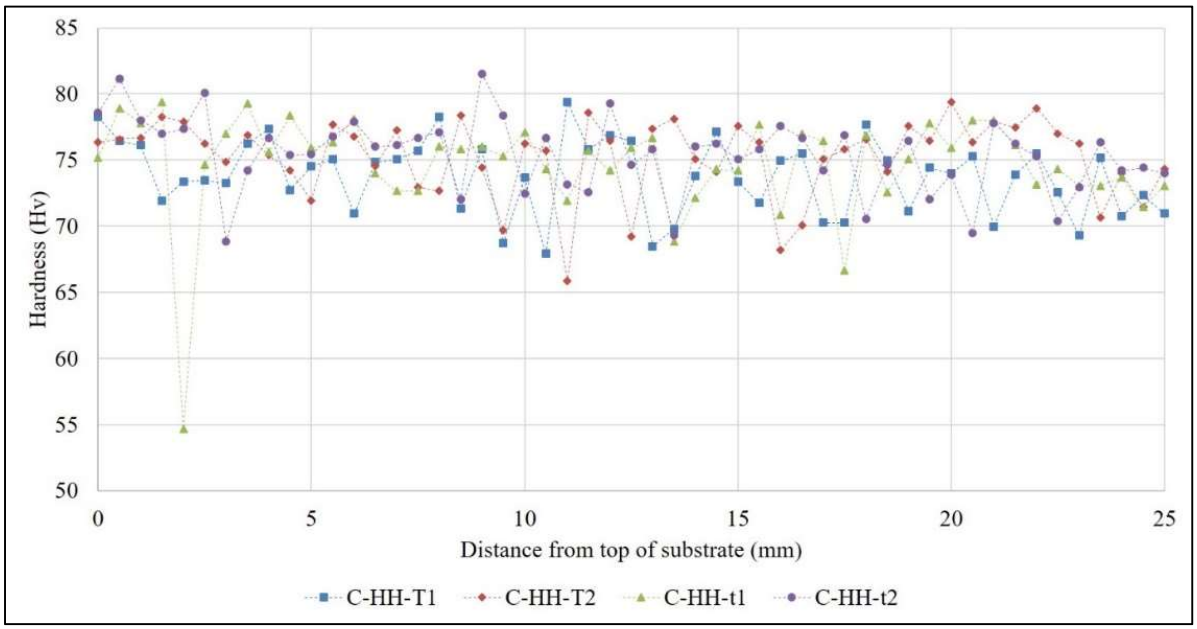

Figure 5.40 Hardness variation in CMT samples manufactured using high heat input condition.

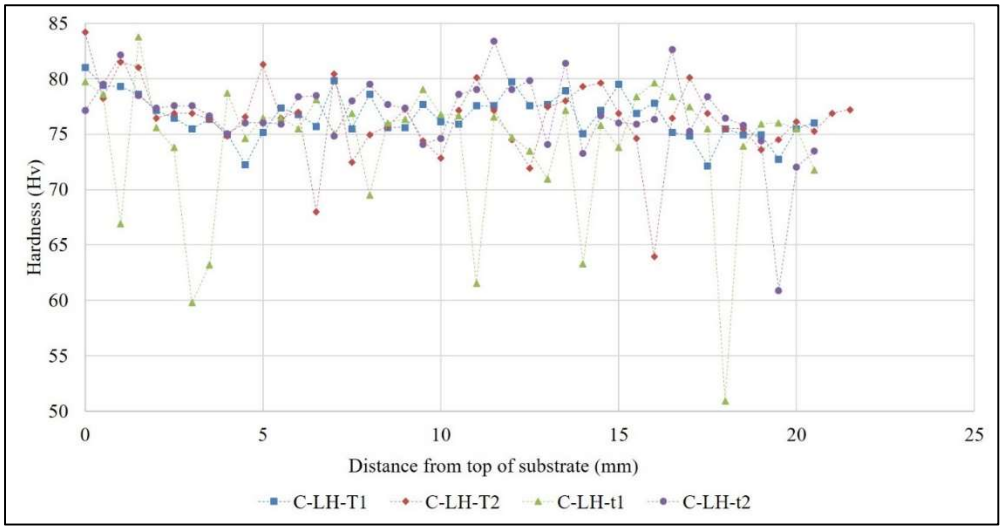

Figure 5.41 Hardness variation in CMT samples manufactured using low heat input condition.

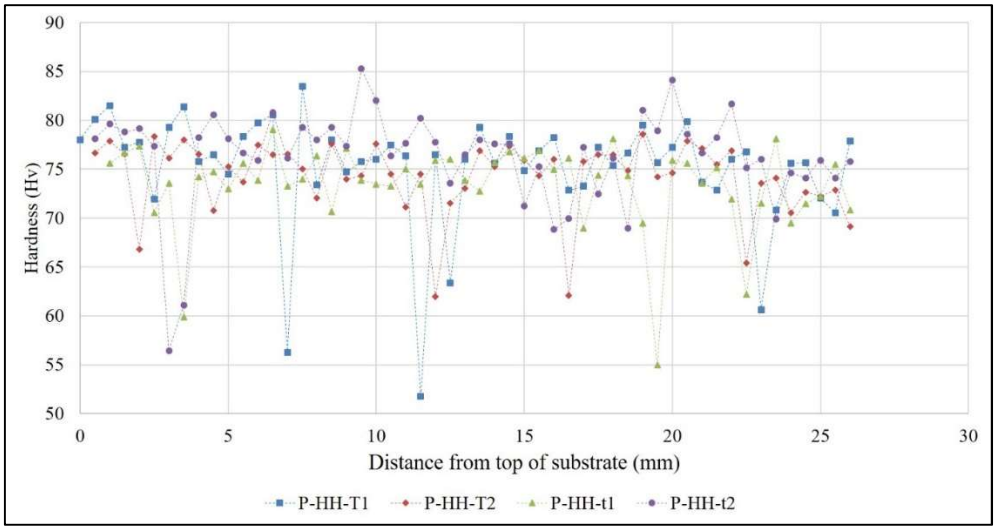

Figure 5.42 Hardness variation in pulsed-MIG samples manufactured using low heat input condition.

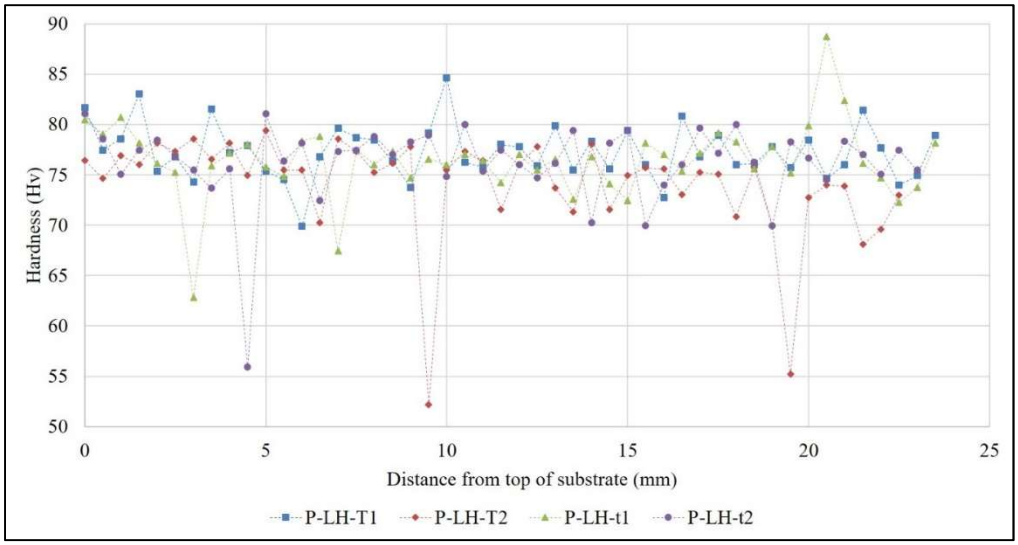

Figure 5.43 Hardness variation in pulsed-MIG samples manufactured using low heat input condition.

Table 5.4 Average hardness comparison of pulsed-MIG and CMT samples.

Sample ID	Average Hardness (Hv)			Sample ID	Average Hardness (Hv)		
P-HH-T1	75.19	74.73	74.8	C-HH-T1	73.66	74.34	74.57
P-HH-T2	74.25			C-HH-T2	75.04		
P-HH-t1	73.4	74.87		C-HH-t1	74.41	74.8	
P-HH-t2	76.31			C-HH-t2	75.2		
P-LH-T1	77.3	75.64	75.98	C-LH-T1	76.61	76.51	75.96
P-LH-T2	73.91			C-LH-T2	76.42		
P-LH-t1	76.44	76.32		C-LH-t1	74.0	75.39	
P-LH-t2	76.19			C-LH-t2	76.79		
Overall average	75.36			Overall average	75.18		

5.3.7 Effect of pulsing on microstructure

Most of the welding operations in recent time use current and voltage pulsing to reduce the heat input. It was evidenced that pulsing has positive effect in microstructure and mechanical properties [164–166]. In current investigation, pulsed-MIG samples witnessed effect of pulsing on microstructure. Open literature does not discuss the observed phenomena in details. The effect was noticed while understanding the microstructure taken in longitudinal direction as shown in Figure 5.26 and Figure 5.27. Microstructure of layer 1 taken in longitudinal direction is shown in Figure 5.44 and depositing parameters such as current, voltage and heat input is shown in Figure 5.45. A clear demarcation of disruption of columnar grains can be seen in a microstructure.

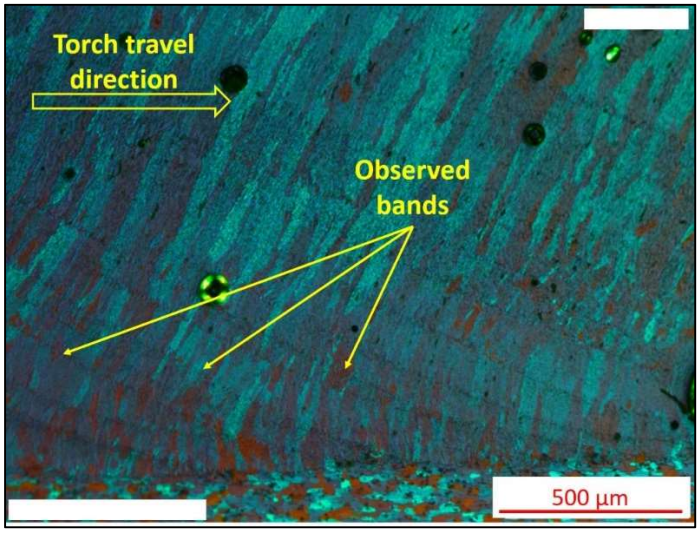

Figure 5.44 Microstructure of first layer of P-LH-t2 sample in longitudinal direction of torch travel revealing pulsing bands.

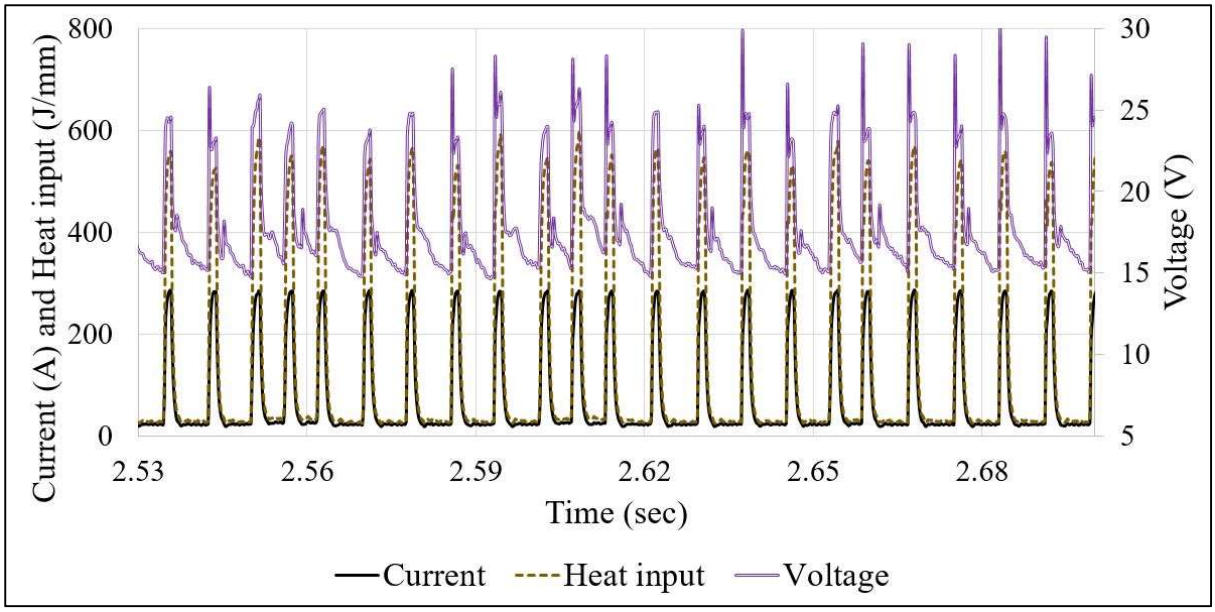

Figure 5.45 Current, voltage and heat input used while producing P-LH-t2 sample.

A distance between the observed bands was measured which found varying from 70 to 120 µm. Figure 5.45 showed around 7 to 8 peaks for every 0.05 seconds and torch forward travel was maintained at 0.6 m/min (10 mm/s). Form the calculations, torch should travel a distance of 0.5 mm in 0.05 seconds. Hence, while a torch traveling a distance of 0.5 mm in forward direction, power source induces around 7 to 8 pulses into depositing metal. Thus, 0.5 mm distance experienced around 8 pulses at a distance of every 80 µm. This distance roughly matches with the measured distance between the bands observed in microstructure.

It can be argued that pulsing not only supported in creating agitation into liquid weld metal but also depending upon solidification rate it disturbed the forming microstructure. The effect was studied at the bottom layer, however, similar pulsing effect can be observed at higher layers. In Figure 5.23 to Figure 5.27, columnar grains were observed disrupted at interlayer region, however, a close observation revealed that growth of columnar grains was also disturbed due to such a band formation as a result of pulsing.

5.3.8 Microstructure variation at interlayer region

Behaviour of metal at the interlayer region in metal additive manufacturing is interesting. Ti-6Al-4V shows centimetre scaled grains continuously grown through one layer to other [20,21]. No such abnormal growth of grains was reported in aluminium alloys [78,80,150]. Even long columnar grains were found interrupted at the interlayer region whereas part produced from CMT and CMT variants showed small sized grains [78,80]. In light with this, further part of this study highlights the microstructures from interlayer regions of the samples produced using pulsed-MIG and CMT processes.

For better understanding of metallic behaviour at the layer interface region, samples shown in Figure 5.46(a) were manufactured such that top layer covered only half of the total wall length and microstructure of that part was studied. SEM image of samples C-HH-t2 is shown in Figure 5.46(c) which demonstrated the existence of fine grains at the layer interface region. Upper and lower region

away from the interface clearly evidenced the presence of columnar grains. Microstructure showed similarity with the microstructures from Figure 5.26.

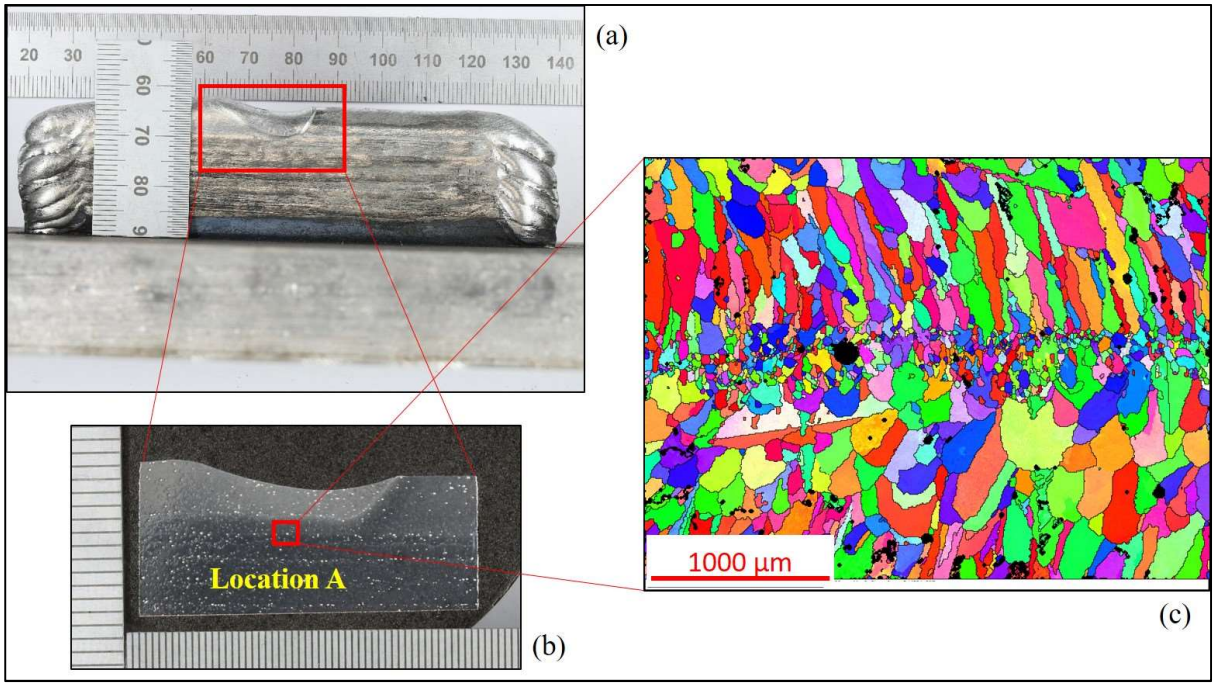

Figure 5.46 SEM image at location A. A full length sample C-HH-t2 – a front view (a), macro of a top part taken in longitudinal direction of torch travel (b) and SEM image at location A revealing macroscopic grains (c).

Orientation of columnar grains remained aligned with the torch travel direction. In Figure 5.46(c), upper region of layer interface showed penultimate layer in which metal deposition was started from right hand side and torch moved towards left hand side and reverse was the case of layer below it. Stretched columnar grains that did not show any dendritic nature could have been formed in particular direction of heat extraction forced by previously deposited layers. Heat flow in previously deposited layers remains the major source of extraction [110,113,141]. Heat released to the atmosphere by radiation cannot be as high as heat extraction by earlier layers. Equiaxed dendritic grains at the top layer completely eliminated and replaced by columnar grains, as discussed in Part-I of this chapter. Therefore, temperature gradient at the newly deposited layer and previous layers could be the driving force for the formation of columnar grains. The effect of heat addition during later layers deposition on the morphology of grains from earlier layers is a little discussed topic in the open literature.

From Figure 5.35 to Figure 5.38, it was proved that temperature of earlier layers was raised above the recrystallisation temperature of the alloy (~300°C [134]) multiple times. This fact must be taken in to consideration that the grain growth could occur stepwise. For example, grains formed at a layer number six may get affected not only while depositing layer number seven but also by layer number eight, nine, ten and so on depending upon shape and size of a part being manufactured, heat input of the process employed and metal's thermal properties. Thus, if temperature at the layer number six is raised above the recrystallisation temperature (that allowed grain boundary migration and grain growth) grain boundary migration can be expected in coordination with the heat flow. Thus, smaller columnar grains formed during the deposition of layer seven could be expected to grow in length after deposition of later

layer namely eight, nine *etc*. until temperature raise at layer six crosses recrystallisation temperature. At this point it should be noted that grains formed during deposition of seventh layer will remain the main grain structure and all the modification expected at later heating stages will not affect primary shape. Thus, grain modification could be the results of temperature gradient, one direction heat flow and raise of temperature above the recrystallisation temperature.

Zhang et al. [80] and Fang et al. [150] reported the existence of fine grained zone between two layers and probable reason authors discussed was the alternating polarity of CMT process that disturbed the dendrite growth disrupting overall grain growth forming fine grains. The postulations are relevant and therefore, it can be assumed that alternating polarity with reciprocating motion of feed stock wire was responsible for finer grain formation. Higher magnification SEM image shown in Figure 5.47(c) further emphasized the presence of finer grains in CMT samples. Thus, Figure 5.46(c) and Figure 5.47(c) observed finer grains at top region of a wall which did not undergo additional heat application. Therefore, following earlier discussion on grain growth, it is important to study the interlayer regions from the lower layers. Representative microstructures obtained from an optical microscopy of the lower layers are shown in Figure 5.48(a) and (b). Samples C-HH-T1 and C-HH-t2 both revealed finer grains at interlayer regions which experienced multiple heat treatments. Even after the repeated heat application, CMT samples evidenced finer grains at the interlayer region. The similar pattern of finer grains were observed in almost all the interlayer regions irrespective of layer numbers and deposition techniques.

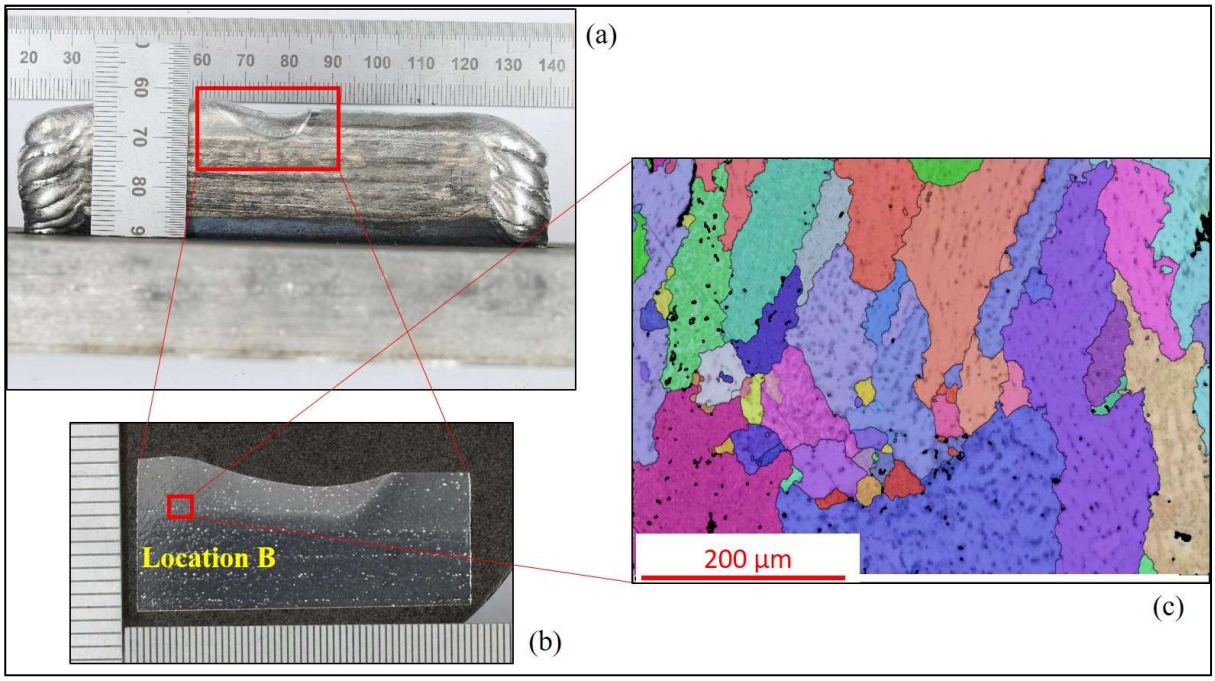

Figure 5.47 SEM image at location B. A full length sample C-HH-t2 – a front view (a), macro of a top part taken in longitudinal direction of torch travel (b) and SEM image at location B revealing macroscopic grains (c).

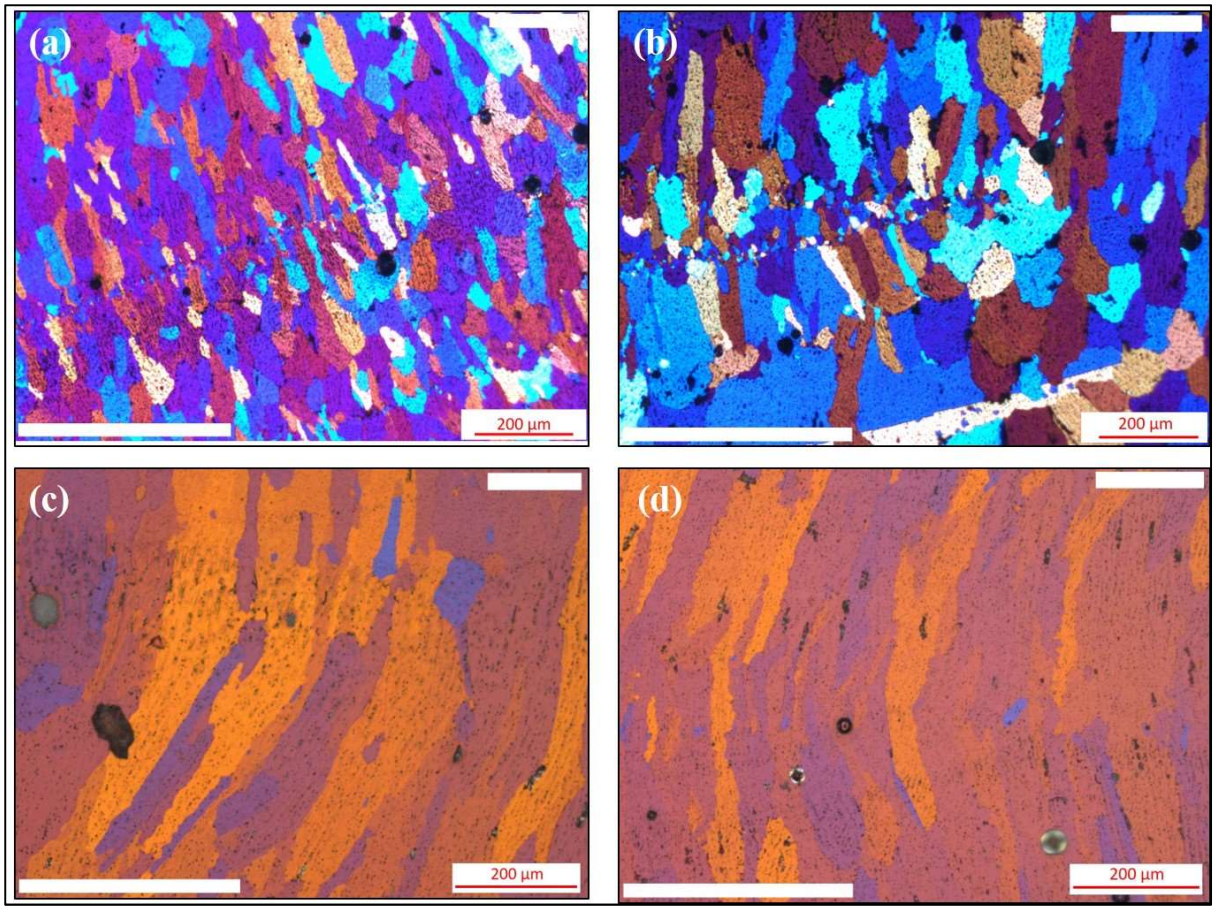

Figure 5.48 Microstructure in transverse direction of torch travel showing interlayer regions between layers 3 and 4 of sample C-HH-T1 (a), layers 7 and 8 of sample C-HH-t1 (b), layers 6 and 7 of sample P-HH-T1 and layers 7 and 8 for sample P-HH-T2.

On the contrary, pulsed-MIG samples with higher heat content showed continuation of grains through layers as can be seen in Figure 5.48(c) and (d). There were relatively less number of fine grains were present. The particular interlayer region with grain continuation can found at only in pulsed-MIG samples with high heat input. Samples from low heat input failed to reveal such a grain continuation through layers, hence, presented fine grains. It was discussed earlier that pulse-MIG process provides higher heat input than CMT process. Therefore, it can be concluded that high heat input in pulse-MIG raised temperature of the grains at an interlayer region above the recrystallisation temperature to a great extent number of times that supported in migration of grain boundaries of a fine grains in coordination with the heat flow direction that is down wards. It was observed that smaller grains converted and joined the larger columnar grains. Thus, formerly developed columnar grains had grown at an expense of finer grains at interlayer region ideally representing the epitaxial grain growth in aluminium. Only pulse-MIG high heat input samples showed such a grain growth that can be correlated with temperature rise displayed in Figure 5.35 and Figure 5.36. For example, sample P-HH-t1 showed temperature 530°C and above for layers 4 to 12 while depositing layer number 15. This high temperature showed lower cooling and solidification rate allowing more time for grain boundary migration. Also, temperature gradient created in the process further guides grain orientation. It is worthwhile to mention that finer pores at the interlayer region found drastically reduced which either got dissolved into solid solution during the process of grain migration or combined to form larger pores.

It should be noted that the size of columnar grains has grown only at a region close to interlayer region by joining of fine grains. Apart from this extension, there was hardly any dimensional change was noticed. Thus, rest of the grain portion remained unchanged. This particular fact of aluminium differentiates it from Ti-6Al-4V alloy where columnar grains witnessed changes at both ends solely depending upon temperature gradient. Therefore, at this point it will too early to term this growth as an epitaxial growth in aluminium; however, for high heat input considering high deposition process, it cannot be ignored.

Chapter 6: Residual Stress Analysis

6.1 Introduction

Considering the structural integrity of the additively manufactured parts, the process induced residual stresses cannot be ignored. Information about the magnitude and distribution of residual stresses is the critical factor in designing an engineering component and also to avoid in service damage of a functioning part [167]. To understand the presence and distribution of residual stresses, various computational modelling approaches [68,71,75,168] and practical experimentation such as neutron diffraction, contour residual stress measurement and hole-drilling method [65,66,72–74] have been undertaken. Additively manufactured part revealed residual stresses as high as the yield strength of a material [38,74] or higher [72] when measured in specific direction. To reduce the residual tensile stresses in a formed part, introduction of balancing compressive stresses by interlayer rolling process was experimented. The method had intended positive results of residual stress reduction [38,70]; however, the method found to be time consuming and difficult to implement for all shapes being formed via WAAM [131].

There is hardly any study available in the literature mentioning application of Contour method for residual stress measurement of WAAM object prepared by alloys other than Ti-6Al-4V and Ni-based super alloys. The method becomes suitable due to its simplicity of operation, requirement of standard equipment and obtaining 2D stress map of plane of interest [169]. Contour can measure stresses in thick components which is highly difficult through other methods. On the contrary, compared to other standard processes, contour results can have errors. Prime et al. [170] reported errors can be +/- 5 MPa while Zhang et al. [171] noticed variation of 20 MPa. Another study by Hosseinzadeh and Bouchard [172] suggested error can vary from 15 up to 30 MPa.

Researchers agreed on the fact that in layered metal deposition, the current layer releases residual stress of previous layers [65,75,111], however, top layer defines the state of overall residual stress and always have highest magnitude [65,75]. Raised temperature of a deposited part while depositing rear layer found to have an important effect of residual stress reduction in AM forming part [63,71,112]. Zhao et al. [65] and Li et al. [113] studied the effect of raised temperature at the forming part by correlating it with the interlayer dwell time, however, temperature of the part may not necessarily remain the same for different sized and shaped objects formed with same interlayer dwell time. Longer interlayer dwell time allowed increased cooling time for metal to contract and thus increased residual stresses compared to shorter dwell times that imparted relatively greater temperature of deposit and substrate before deposition of rear layer. Mughal et al. [63] reported the increased substrate temperature supported in reducing the distortion in continuous metal deposition approach. One of the important study from Vastola et al. [71] outlined that for every 50°C increase in preheating temperature of a substrate powder

bed, there was around 20% reduction of residual stresses due to the lower thermal gradients when powder bed temperature was higher and reduction in yield strength at higher temperature of a material.

There is little work published highlighting the application of maintenance of interlayer temperature in additive manufacturing (AM) and its effects on residual stresses, microstructure and mechanical properties. WAAMed aluminium parts were tested for residual stresses using the contour residual stress measurement method. Total two types of samples described in section 3.4 were studied for the better understanding of effect of variation of interlayer temperature, substrate thickness, number of layers and heat input on residual stress formation and distribution. There were eight samples from type 1 and one sample from type 2 considered. Refer section 3.4.4, Figure 3.25 and Figure 3.26. Thick (20 mm) and thin (6 mm) substrates, 35 and 18 mm deposit height, 280 and 120 J/mm heat input and 50 and 100°C interlayer temperature were the selected deposition parameters as described in section 3.4.4.

6.2 Understanding the stress distribution

As discussed in the experimental methodology chapter, a total 9 samples were tested for residual stress measurement by the contour method (refer Table 6.1). The stress distribution in all the samples at the cut plane including WAAM deposit and substrate plate is presented in Figure 6.1 to Figure 6.9. These 9 samples were classified into two categories – Type 1 with horizontal substrate and Type 2 with vertical substrate. Hence, Figure 6.1 to Figure 6.8 represent the Type 1 samples and Figure 6.9 represent the Type 2 sample. Details of samples are given in Table 6.1. From Figure 6.1 to Figure 6.9, all the samples revealed tensile as well as compressive residual stresses with varying magnitude; however, tensile stresses were found dominating compared to compressive stresses as discussed in further sections.

Table 6.1 Details of samples manufactured for residual stress measurement.

Sample Type	Sample number	Deposit height (mm)	Number of layers	Substrate thickness (mm)	Heat input (J/mm)	Interlayer temperature (°C)
Type 1	1	34-35	20	20	280	50
	2	17-18	10	20	280	50
	3	34-35	26	20	120	50
	4	34-35	20	20	280	100
	5	17-18	10	20	280	100
	6	34-35	26	20	120	100
	7	17-18	10	6	280	50
	8	17-18	10	6	280	100
Type 2	9	18-19	15	6	120	-

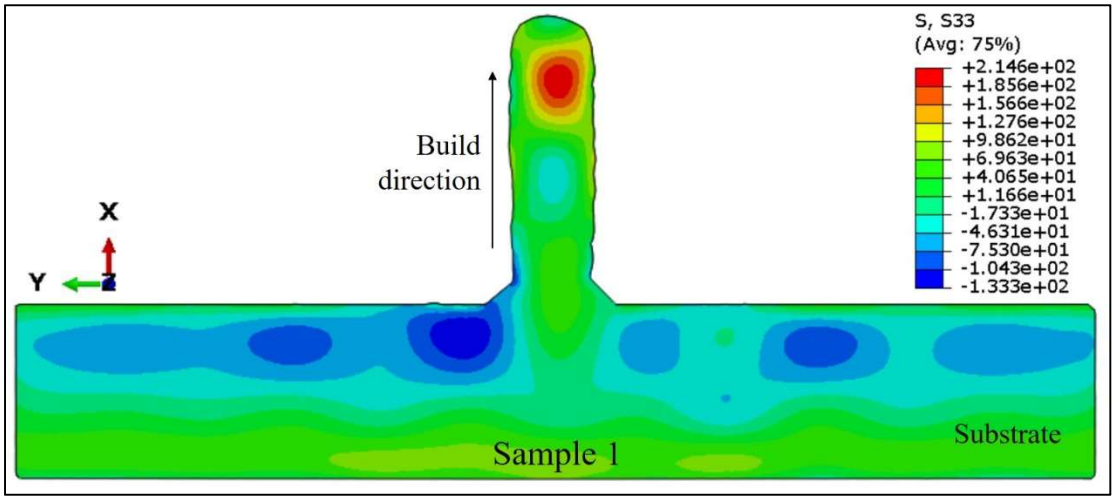

Figure 6.1 Distribution of residual stress in Sample 1 with 20 mm substrate thickness – Type 1. (Stress S_{33} shown in the figure is in the transverse direction to the plane and unit of stress is MPa).

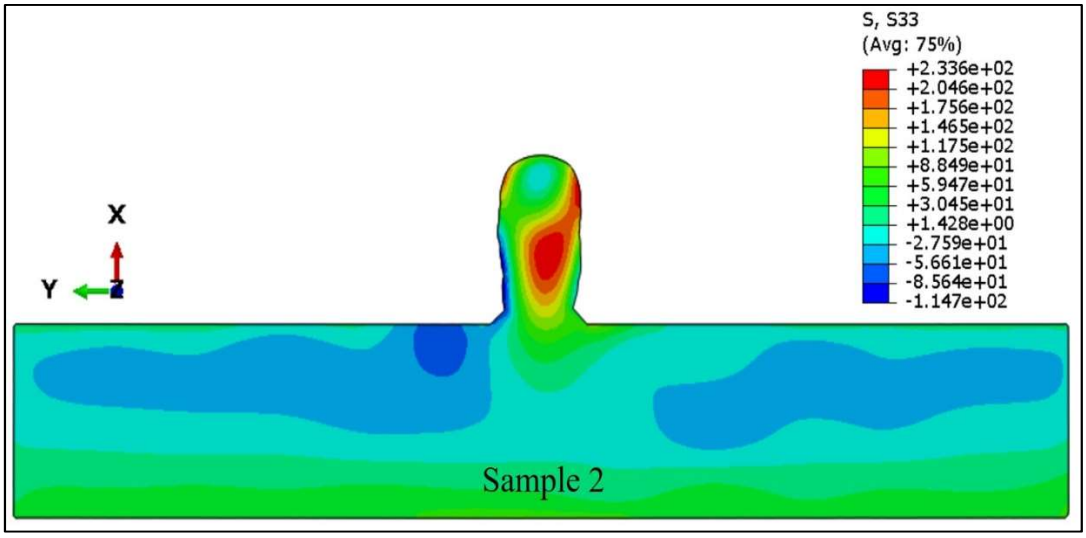

Figure 6.2 Distribution of residual stress in Sample 2 with 20 mm substrate thickness – Type 1. (Stress S_{33} shown in the figure is in the transverse direction to the plane and unit of stress is MPa).

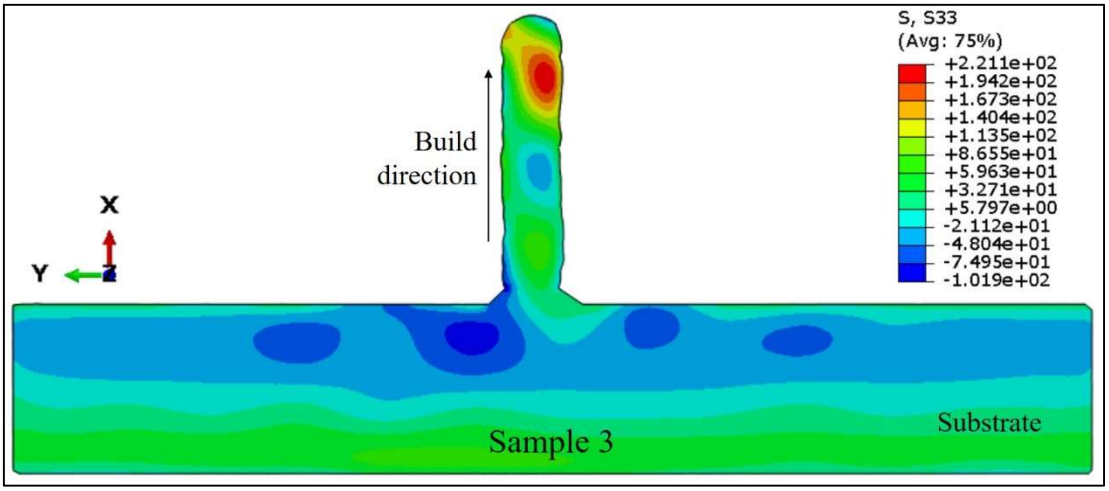

Figure 6.3 Distribution of residual stress in Sample 3 with 20 mm substrate thickness – Type 1. (Stress S_{33} shown in the figure is in the transverse direction to the plane and unit of stress is MPa).

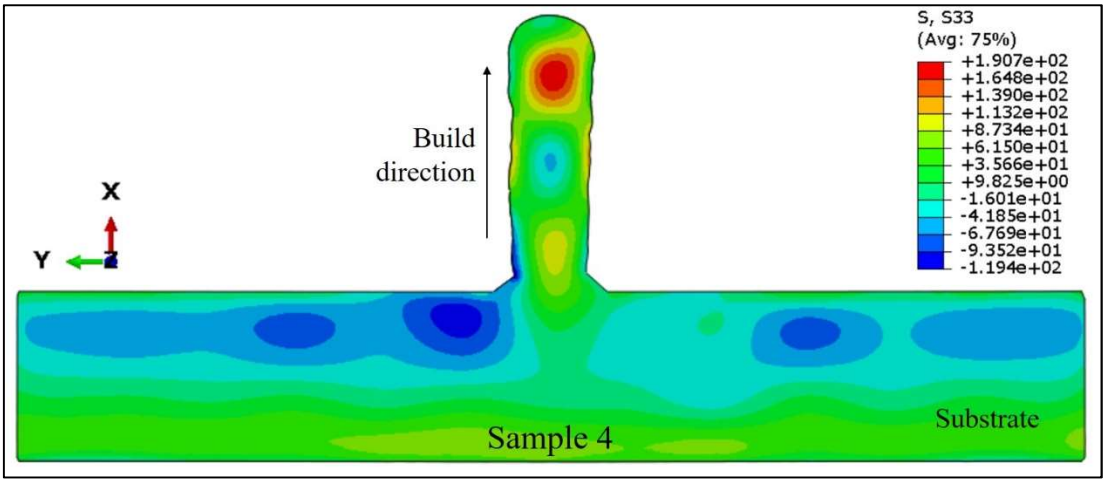

Figure 6.4 Distribution of residual stress in Sample 4 with 20 mm substrate thickness – Type 1. (Stress S_{33} shown in the figure is in the transverse direction to the plane and unit of stress is MPa).

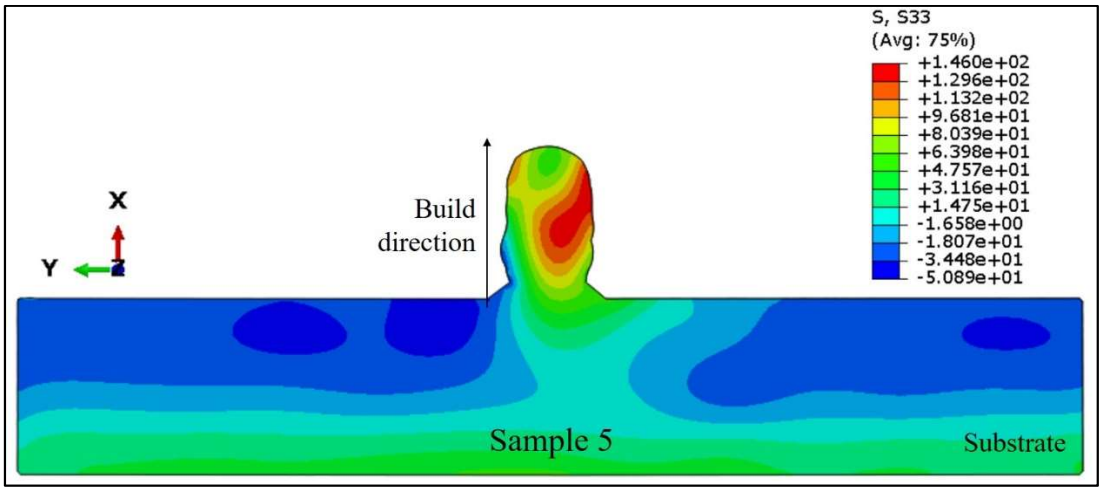

Figure 6.5 Distribution of residual stress in Sample 5 with 20 mm substrate thickness – Type 1. (Stress S_{33} shown in the figure is in the transverse direction to the plane and unit of stress is MPa).

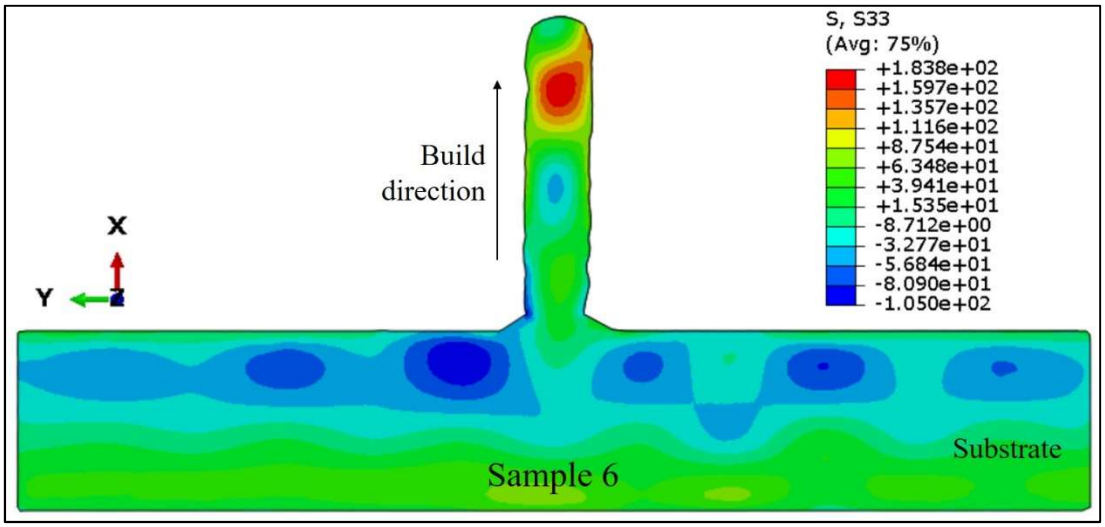

Figure 6.6 Distribution of residual stress in Sample 6 with 20 mm substrate thickness – Type 1. (Stress S_{33} shown in the figure is in the transverse direction to the plane and unit of stress is MPa).

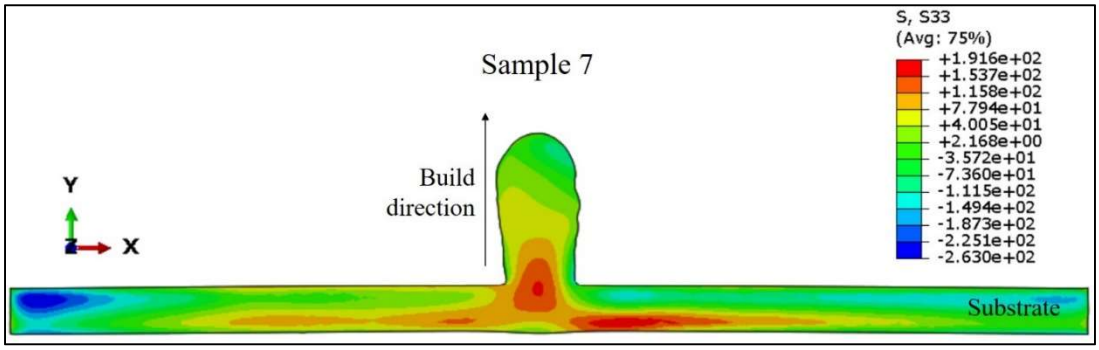

Figure 6.7 Distribution of residual stress in Sample 7 with 6 mm substrate thickness – Type 1. (Stress S_{33} shown in the figure is in the transverse direction to the plane and unit of stress is MPa).

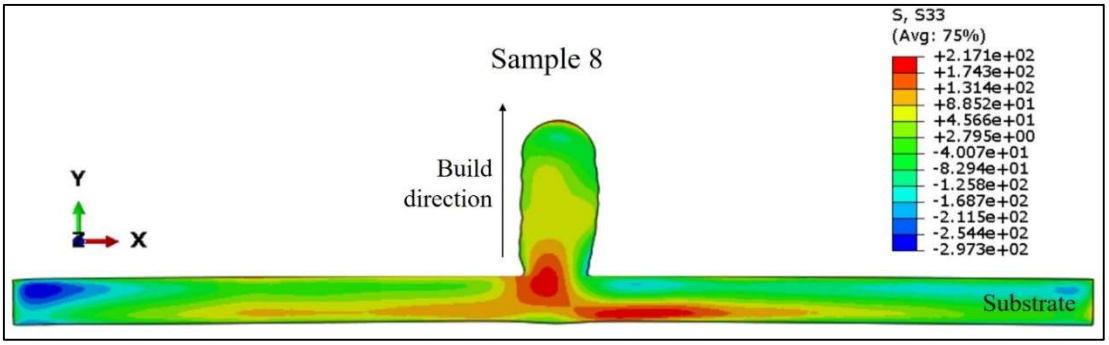

Figure 6.8 Distribution of residual stress in Sample 8 with 6 mm substrate thickness – Type 1. (Stress S_{33} shown in the figure is in the transverse direction to the plane and unit of stress is MPa).

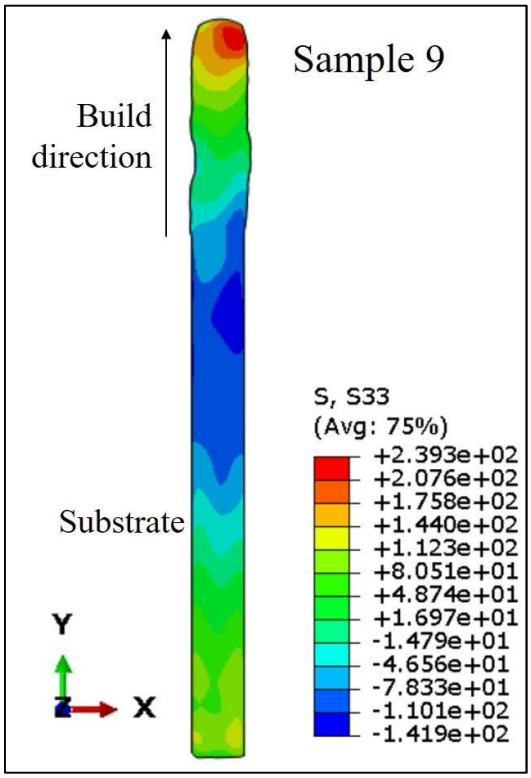

Figure 6.9 Distribution of residual stress in Sample 9 with 6 mm substrate thickness – Type 2. (Stress S_{33} shown in the figure is in the transverse direction to the plane and unit of stress is MPa).

The deposit and substrate parts of all samples can be separated in such a way that residual stress distribution in the two parts can be compared separately. Figure 6.10 illustrates the stress distribution in the deposits of all the Type 1 samples. Stress distribution in the substrate parts of Type 1 samples is shown in Figure 6.11. From Figure 6.10 and Figure 6.11 it can be inferred that all the deposits exhibited maximum tensile residual stresses and balancing compressive stresses were present in the substrate. Geometry of samples found to have impact of distribution of stresses.

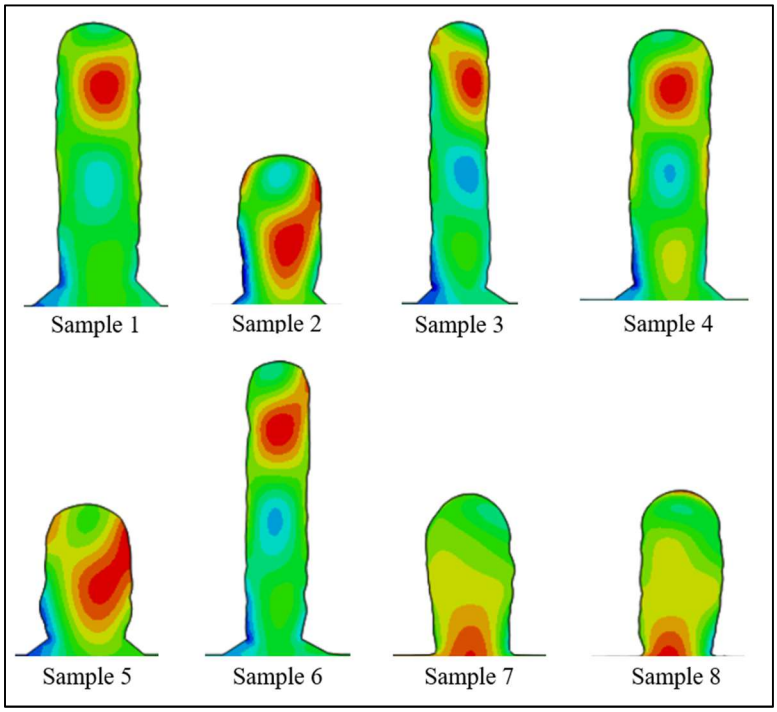

Figure 6.10 Deposit parts of samples 1 to 8, Type 1 having horizontal substrate. (Refer Figure 6.1 to Figure 6.8 for respective colour indices and stress values).

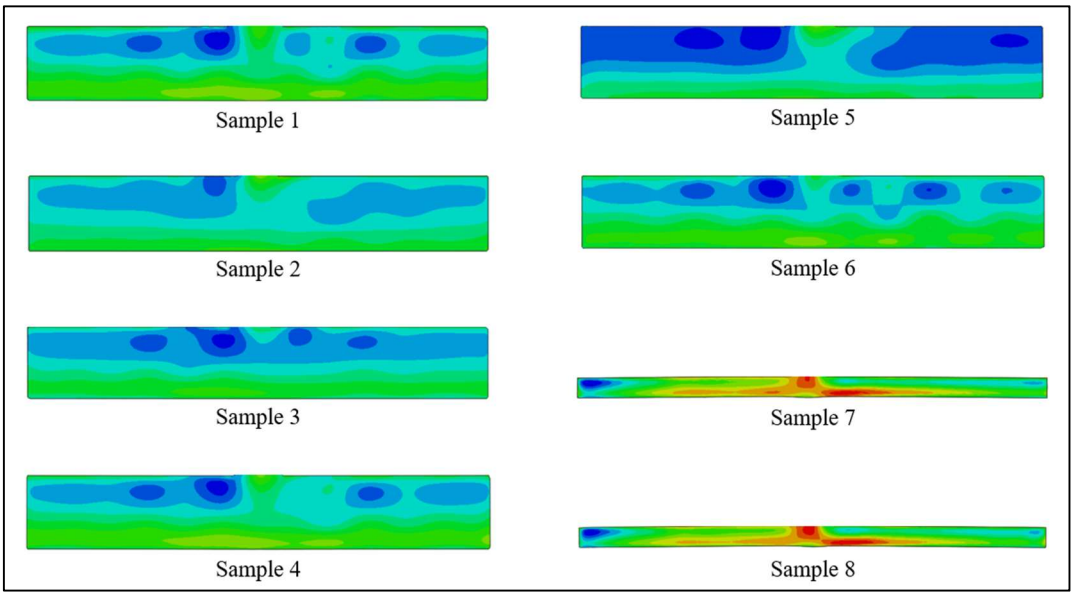

Figure 6.11 Substrate parts of samples 1 to 8, Type 1. Substrates of samples 1 to 6 showed 20 mm thickness and samples 7 and 8 showed 6 mm. (Refer Figure 6.1 to Figure 6.8 for respective colour indices and stress values).

6.2.1 Stress distribution in deposit of Type 1 samples

Figure 6.13 to Figure 6.20 show stress distribution in the deposit parts of Type 1 samples. All figures describe the actual residual stress following the central line of a deposit part. An average stress at each millimetre taken in horizontal direction is described in Figure 6.12. Comparison of the residual stress in a form of average stress taken across the deposit thickness at every 1 mm height difference is shown in Figure 6.21.

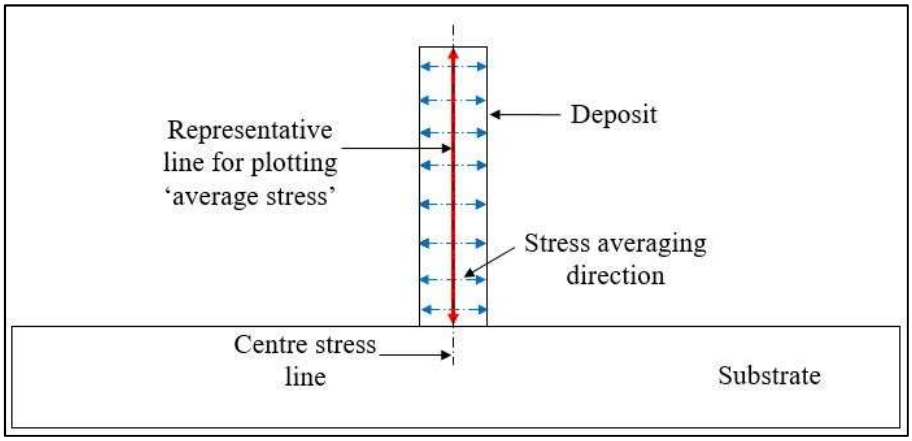

Figure 6.12 Schematic of WAAM describing stress averaging direction.

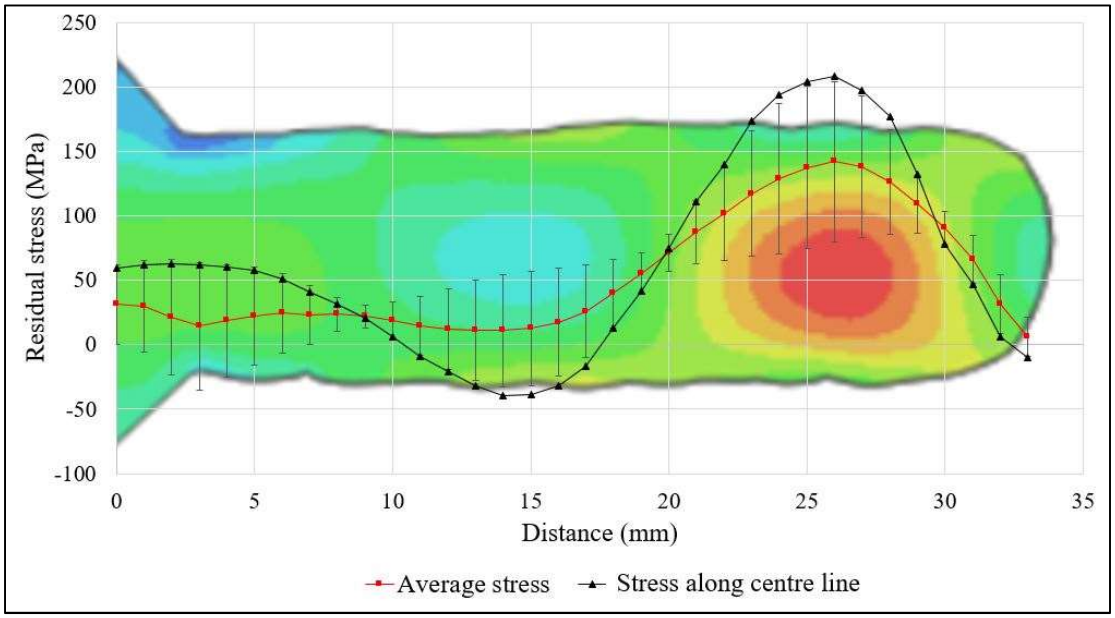

Figure 6.13 Distribution of average and centre line residual stress in deposit part of sample 1 having 35 mm height, 20 layers, 20 mm substrate thickness, 280 J/mm heat input and 50°C interlayer temperature.

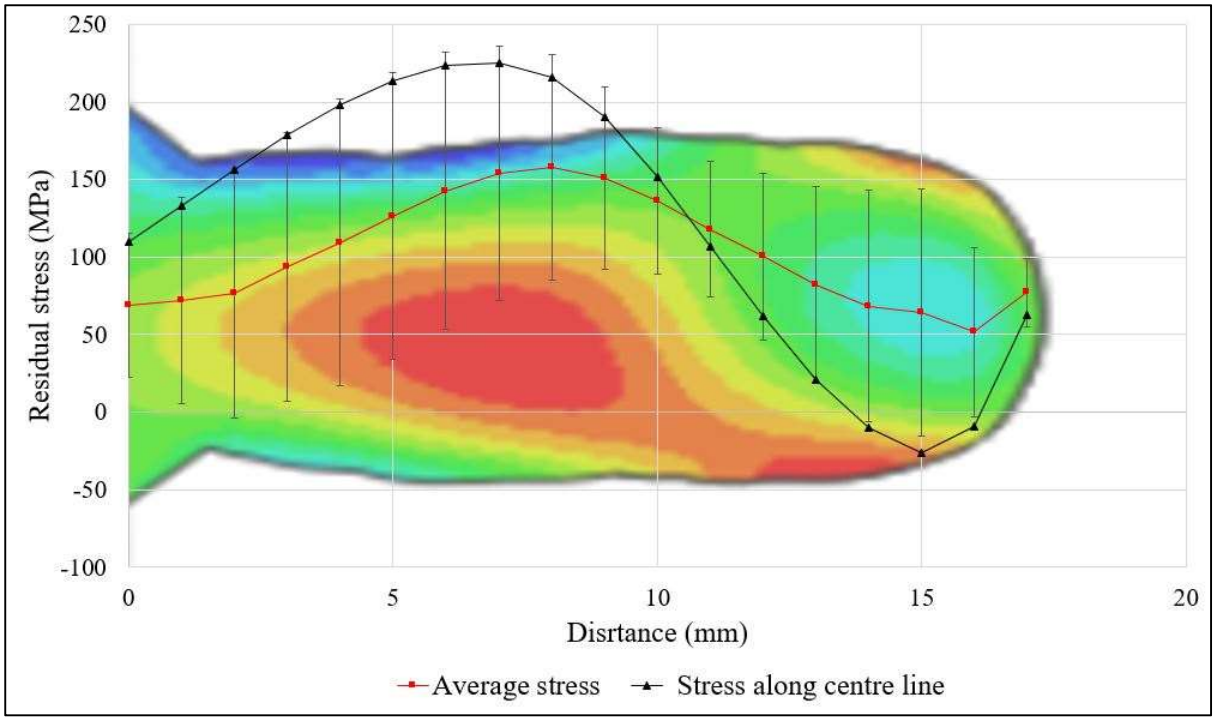

Figure 6.14 Distribution of average and centre line residual stress in deposit part of sample 2 having 18 mm height, 10 layers, 20 mm substrate thickness, 280 J/mm heat input and 50°C interlayer temperature.

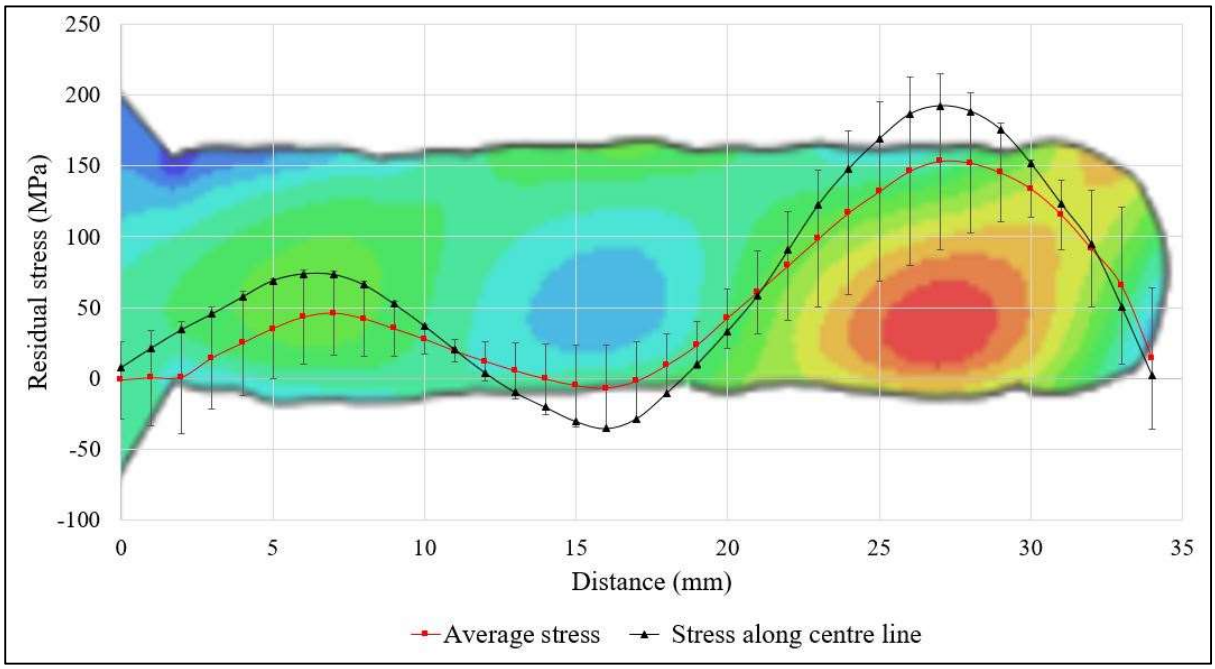

Figure 6.15 Distribution of average and centre line residual stress in deposit part of sample 3 having 35 mm height, 26 layers, 20 mm substrate thickness, 120 J/mm heat input and 50°C interlayer temperature.

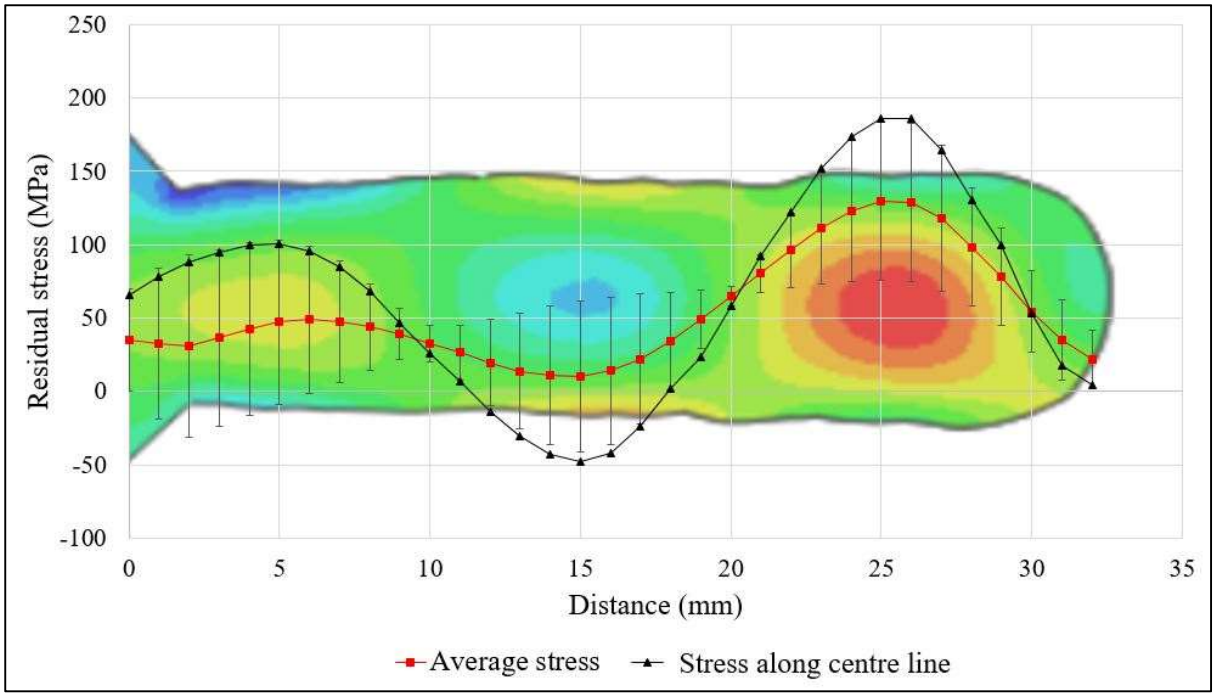

Figure 6.16 Distribution of average and centre line residual stress in deposit part of sample 4 having 35 mm height, 20 layers, 20 mm substrate thickness, 280 J/mm heat input and 100°C interlayer temperature.

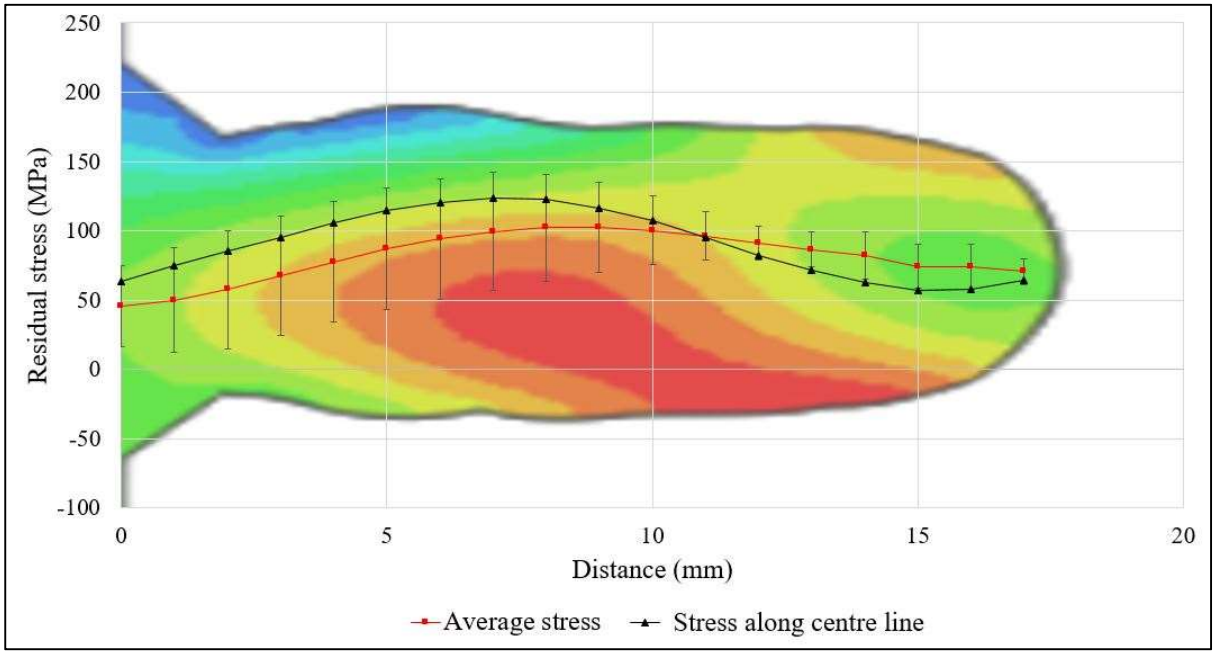

Figure 6.17 Distribution of average and centre line residual stress in deposit part of sample 5 having 18 mm height, 10 layers, 20 mm substrate thickness, 280 J/mm heat input and 100°C interlayer temperature.

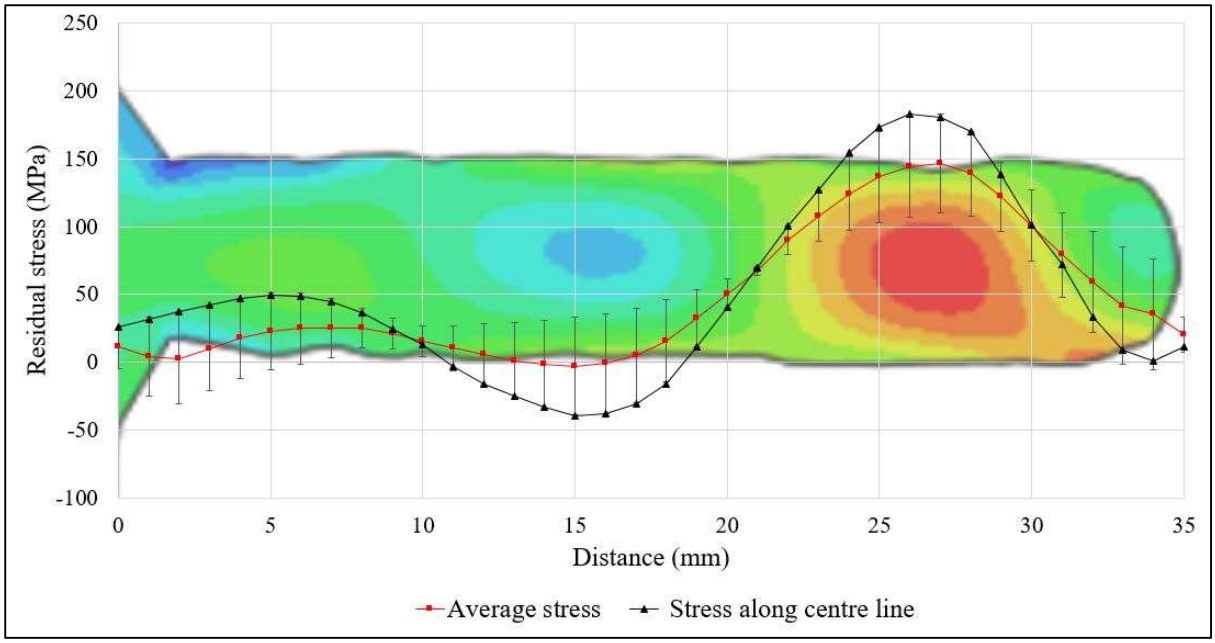

Figure 6.18 Distribution of average and centre line residual stress in deposit part of sample 6 having 35 mm height, 26 layers, 20 mm substrate thickness, 120 J/mm heat input and 100°C interlayer temperature.

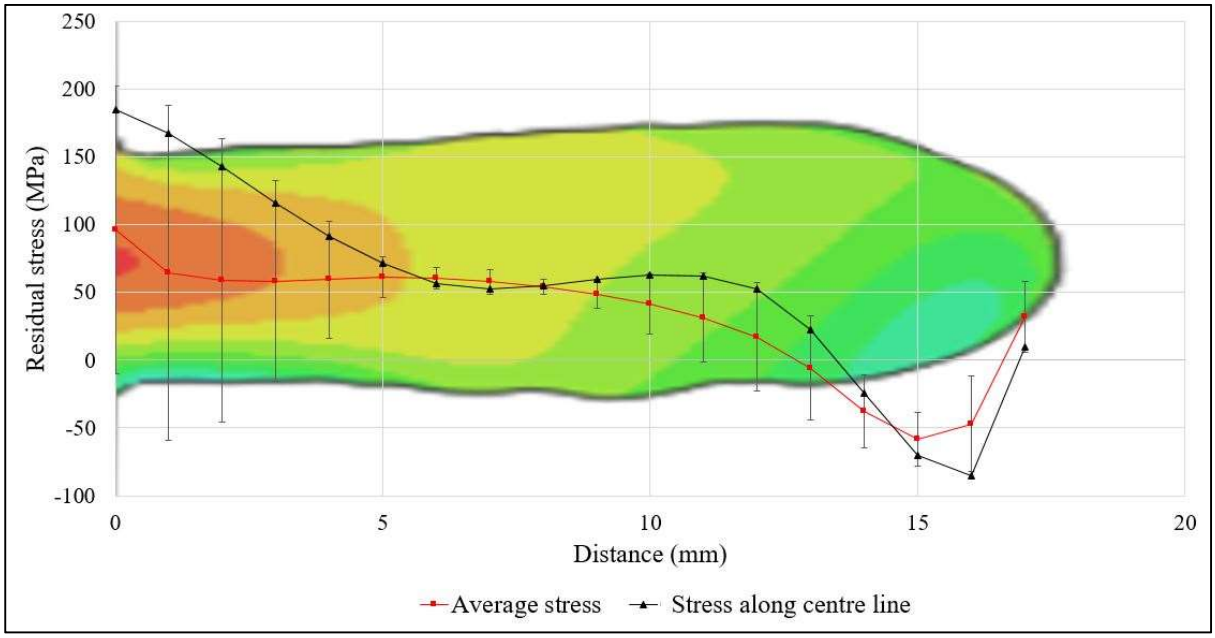

Figure 6.19 Distribution of average and centre line residual stress in deposit part of sample 7 having 18 mm height, 10 layers, 6 mm substrate thickness, 280 J/mm heat input and 50°C interlayer temperature.

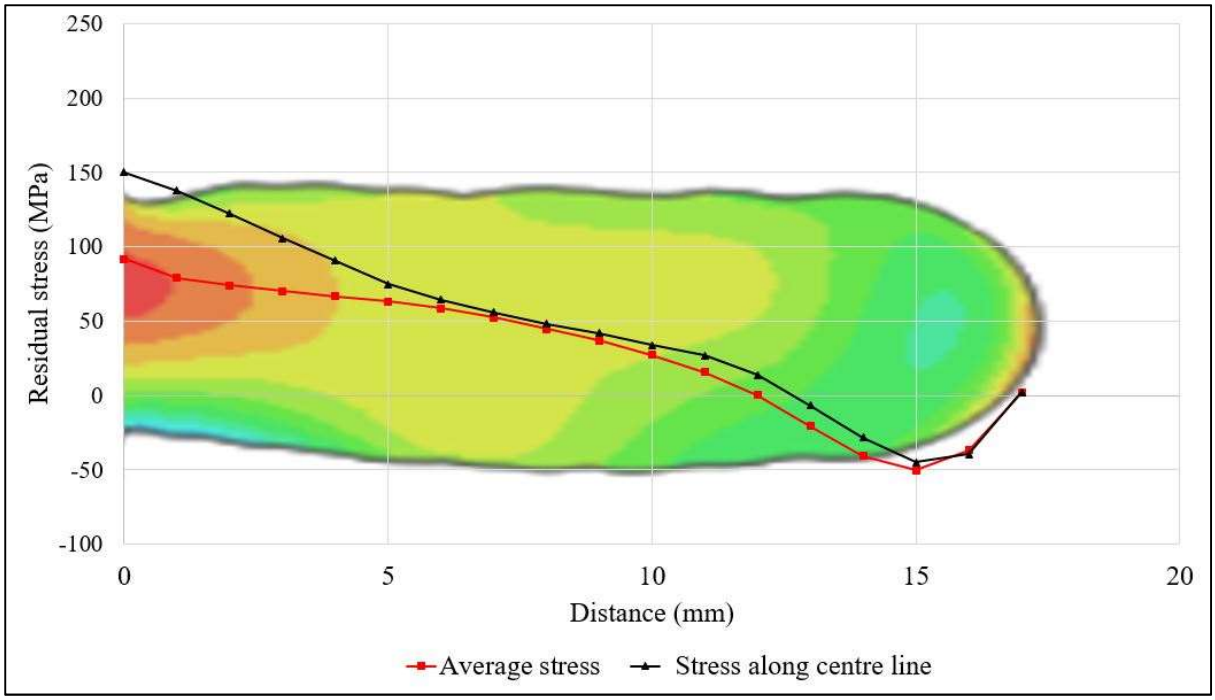

Figure 6.20 Distribution of average and centre line residual stress in deposit part of sample 8 having 18 mm height, 10 layers, 6 mm substrate thickness, 280 J/mm heat input and 100°C interlayer temperature.

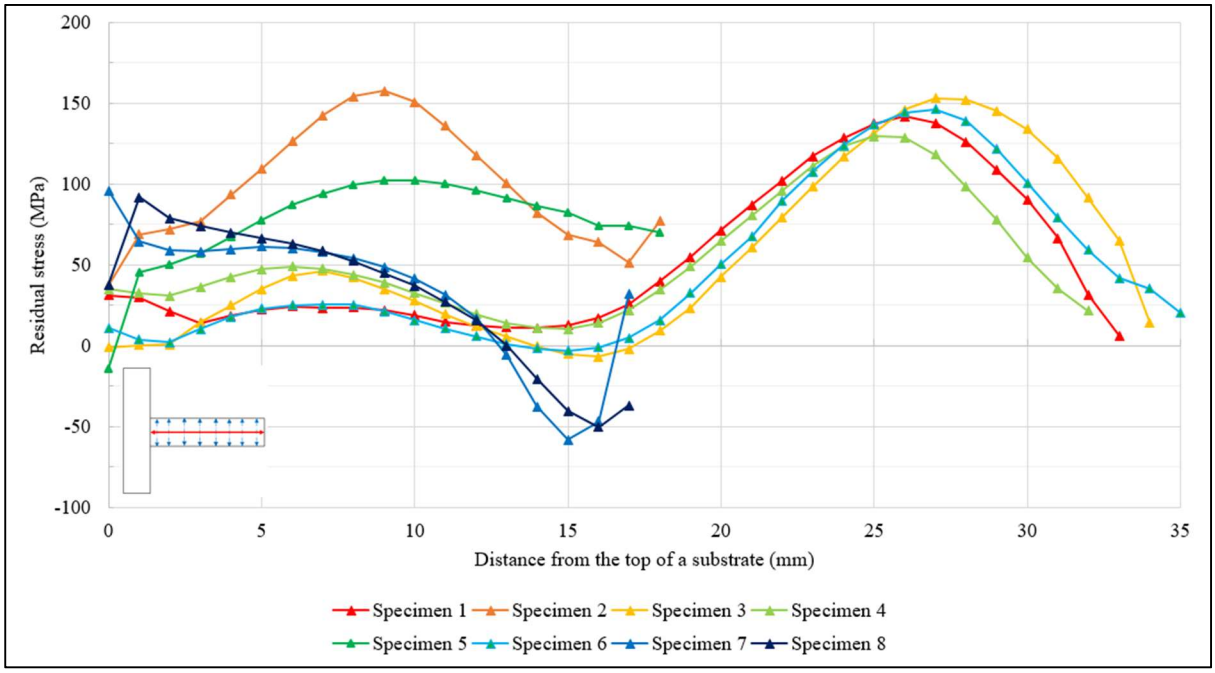

Figure 6.21 Average residual stress in deposit.

As described in Table 6.1, sample numbers 1, 3, 4 and 6 with 33-35 mm deposit height can be grouped together for comparison with sample numbers 2 and 5 that revealed 17-18 mm deposit height with comparable deposition conditions. Although, sample numbers 7 and 8 manufactured with short deposit height, their substrate thickness was different than taller deposit substrates, hence, sample 7 and 8 are not considered for this comparison. For the mentioned substrate thickness, sample 2 and 5 are compared

with sample 7 and 8. Further, samples 1, 2, 3 and 7 are compared with 4, 5, 6 and 8 respectively to understand the effect of interlayer temperature on residual stresses. Influence of number of layers can be obtained by comparing sample numbers 1 and 4 with samples 2 and 5 respectively. Lastly, maximum and minimum heat input can be compared for residual stresses by comparing sample numbers 1 with 3 and 4 with 6. Table 6.2 represents peak tensile stresses measured at a point in all samples.

Table 6.2 Maximum tensile stress measured in all samples at single point.

Sample	**1**	**2**	**3**	**4**	**5**	**6**	**7**	**8**	**9**
Maximum tensile stress measured (MPa)	212	233	215	186	137	182	193	150	238
Average of tensile stresses (MPa)	194						171		238

6.2.1.1 Effect of substrate thickness

The substrate thickness of the samples revealed major impact on the stress distribution. For a fair comparison, sample 2 is compared with sample 7 and sample 5 with sample 8 so that all the depositing parameters remains same except substrate thickness. Stress distribution of samples 2, 5, 7 and 8 are given in Figure 6.14, Figure 6.17, Figure 6.19 and Figure 6.20 respectively. Sample 2 showed majority of tensile stresses. Tensile stress at the start of deposit was 109 MPa which was increased by 114 MPa to reach a maximum value of 223 MPa at 6-8 mm deposit height while maximum compressive stress was 25 MPa at 2-3 mm from the top of deposit. Thus, within roughly 8-10 mm of deposit height, stress value changed by 245 MPa. Similar trend was monitored for sample 5 that showed 63 MPa initial stress and maximum of 123 MPa at the 6-8 mm distance from substrate. Sample 5 showed lowest tensile stress of 57 MPa at 2-3 mm below the top of deposit.

A situation was quite different as can be seen in Figure 6.19 and Figure 6.20, in case of sample number 7 and 8 where maximum stress of 185 and 150 MPa respectively was detected at the bottom of deposit next to substrate. Tensile stress reduced as deposit height increased up to 5-6 mm. Gradual reduction in tensile stress was observed in further deposit height up to around 11-12 mm from substrate. At the height of 15-16 mm that is 2-3 mm from deposit top, a plunge can be seen showing maximum compressive stress of 85 and 44 MPa. With further 2-3 mm height stress was found approaching towards tensile stress roughly reaching zero stress level. The stress distribution in sample 2 and 5 when compared with 7 and 8 was completely different. Sample 7 and 8 showed relatively consistent stress values and distribution than samples 2 and 5.

Noticeable change in stress distribution was clearly be seen in average stress distribution graph Figure 6.21. Comparing sample 2 and 7, maximum average stress in the sample 2 was 158 MPa at deposit height of 6-8 mm where as it was 91 MPa at the substrate-deposit interface for sample 7. As discussed above, average stress followed the actual central stress distribution and reached maximum average

compression of 50 MPa for sample 7, however, sample 2 did not reveal any compressive stress hence showed minimum average tensile stress of 51 MPa near the top of a deposit and 37 MPa at the deposit-substrate interface. Similar pattern was observed in samples 5 and 8. Sample 5 showed maximum average tensile stress 102 MPa at deposit height of 8-9 mm. Stress continuously reduced away from central area at both the ends of deposit such that at the deposit top average tensile stress reached 70 MPa and at deposit-substrate interface it was compressive with 14 MPa magnitude. Sample 8 followed sample 7 where maximum average compressive stress of 58 MPa was at 15-16 mm deposit height and maximum average tensile stress was 96 MPa.

The results showed that substrate thickness has appreciable influence on stress magnitude and distribution. More material available in the thick substrate could have offered greater resistance for deformation compared to thin substrate under the influence of repeated heating and cooling cycles influencing final state of residual stress. Also, difference in heat flow characteristics between thick and thin substrates and reduction in maximum temperature experienced at the substrate with every layer addition could have affected residual stress formation and distribution. A detailed discussion can be found in section 6.5.

6.2.1.2 Effect of interlayer-temperature

Sample number 7 and 8 are discussed as an example of effect interlayer temperature on distribution of residual stresses where sample 7 was manufactured using 50°C interlayer temperature and sample 8 had 100°C interlayer temperature. Figure 6.19 and Figure 6.20 show stress variation profiles in sample 7 and 8 respectively. Stress profiles of both the samples are discussed in section 6.2.1.1. Comparing these two samples it can be argued that sample 7 showed relatively higher magnitude of stress compared to sample 8. Starting with the maximum tensile residual stress at the deposit height of 0-1 mm, less interlayer temperature sample showed stress of 185 MPa whilst other sample with higher interlayer temperature showed around 150 MPa. After gradual reduction in stress intensity until up to around 50 MPa, a sharp plunge in sample 7 was noticed in which stress reached a maximum compressive 85 MPa while the reduction in stress was relatively smoother in sample 8 and maximum compressive stress was around 44 MPa, roughly half of the sample 7. The similar effect of interlayer temperature on stress magnitude can be found while comparing sample 3 and 6 (see Figure 6.15 and Figure 6.18) where sample 3 revealed maximum tensile stress 192 MPa which was 10 MPa more than maximum stress at sample 6. Maximum compressive stress was 35 MPa for sample 3 and 39 MPa for sample 6. Sample 4 (see Figure 6.16) showed relatively less maximum tensile stress 185 MPa compared to sample 1 (see Figure 6.13) that showed 208 MPa. Results from sample 2 and 5 were also in similar line (refer Figure 6.14 and Figure 6.17). Maximum tensile residual stress was 225 MPa while compressive was 25 MPa for sample 2 whilst sample 5 showed maximum 123 MPa tensile residual stress and no compressive stress was reported. Minimum tensile stress was 57 MPa for sample 5.

Average residual stress comparison between sample 7 and 8 also clearly revels the effect of temperature maintenance. Sample 7 showed greater average residual stress at tensile and compressive stress peaks compared to sample 8. The deposit height of 0-1 mm compared to sample 8. Sample 7 had 96 MPa tensile stress whereas sample 8 had marginally less 91 MPa. As deposit height increased, stress reduced and reversed into compressive. Higher average compressive stress showed by sample 7 which was 58 MPa, 8 MPa greater than sample 8. Similar trend of residual stress distribution was observed in sample

3 and 6 where sample 3 revealed greater peak stress values than sample 6. Maximum average tensile stress of sample 3 was 153 MPa whereas sample 6 showed 144 MPa. Comparing the average compressive stress, sample 3 displayed 7 MPa stress and sample 6 disclosed 2 MPa stress value. Tensile stress was also present at deposit height of 6-8 mm where sample 3 and 6 showed 46 and 25 MPa average stress respectively. Following sample 1 and 4, sample 1 showed higher peak tensile stress 142 MPa compared to sample 4 at 129 MPa. Also, sample 2 showed higher average peak tensile stress around 158 MPa than sample 5 that showed 102 MPa stress. Detailed discussion can be found in section 6.6 Effect of interlayer temperature.

6.2.1.3 Effect of deposit height

Considering total height of the deposition, two distinct patterns of stress distribution can be readily noticed. All the sample numbers 1, 3, 4 and 6 with deposition height of 33-35 mm followed peculiar pattern as can be seen in Figure 6.13, Figure 6.15, Figure 6.16 and Figure 6.18. Central stress along the deposition height varied from high tensile to considerable compressive stress. Residual stress near substrate in the deposit showed tensile stresses from 7 to 65MPa that further increased up to 49 to 100 MPa as distance from substrate increased and peaked at around 5 mm for all four samples. With further increased distance from a substrate, residual stresses reversed from tensile to compressive and reached maximum at around 15 mm distance from a substrate that is 17-18 mm from top of a deposit. Maximum compressive stress was 47 MPa for sample number 4 and minimum was 35 MPa for sample 3. Following a sharp surge, at the deposition height of around 25-27 mm from substrate that is 7-8 mm from top of deposit, all the samples showed highest tensile stress. Tensile stress of 208, 192, 185 and 182 MPa was recorded for samples 1, 3, 4 and 6 respectively. Thus, within the distance of 10 mm, residual stress reversed from compressive to tensile with a large change of around 230 MPa in magnitude. Reaching towards the top region of a deposit, residual stress plunged towards zero stress value. The similar variation in a stress can be seen in the graph showing average stress taken across the deposit thickness in Figure 6.21. Out of four samples discussed, two samples showed presence of compressive stress when cumulative effect was considered. Highest compressive and tensile stress was 7 and 153 MPa respectively shown by sample 3.

On the other hand, sample number 2 and 5 revealed different pattern of residual stress distribution than earlier described which can be seen in Figure 6.14 and Figure 6.17. Sample 2 and 5 showed tensile residual stress of 109 and 63 MPa at the start of the deposit close to substrate. In contrast to the taller deposit samples 1, 3, 4 and 6, highest residual stress was found at height 6-8 mm from substrate that is 10 mm from top of a deposit. Maximum tensile stress reported was 223 and 123 MPa for sample 2 and 5 respectively. In both the samples with short deposit height, low tensile or maximum compressive stress was observed at 15 mm away from the substrate that is 2-3 mm from deposit top. Sample 5 showed only tensile stresses with minimum value of 57 MPa at the mentioned location. Sample 2 showed highest compressive stress of 25 MPa at 2-3 mm below the top of a deposit. Lastly for both the samples, residual stress curve moved upward in tensile stress direction reaching 62 and 64 MPa for sample 2 and 5 respectively.

The similar trend of residual stress variation can be clearly seen in the form of an average stress variation (refer Figure 6.21); however, the maximum tensile average stress does not cross 160 MPa value for any of the tested sample. Similarly, maximum compressive stress was below 60 MPa. Considering high

deposit samples, sample numbers 1, 3, 4 and 6 showed their maximum average tensile stress at around 26 mm deposit height and it was highest for sample number 3 at around 153 MPa. The actual tensile stress at the same height was 192 MPa for the same. Sample 1 had highest tensile stress of around 208 MPa at the similar location, however, average stress dropped down to 142 MPa. Comparing compressive stress, only two samples out of four showed average compressive residual stress at around 15-16 mm from substrate. Sample 3 and 6 showed 7 and 3 MPa average compressive stress respectively. Other two samples, sample 1 and 4, had minimum average tensile stress 11 and 10 MPa at the similar deposit height. Shorter samples 2 and 5 showed all tensile average residual stresses with maximum average stress reaching as high as 158 MPa in sample 2. Maximum stress at the sample 5 did not exceed 105 MPa stress. Minimum average stress found in sample 2 was 51 MPa at the top of the deposit. More details and discussion is provided in section 6.7 effect of deposit height and number of layers.

6.2.1.4 Effect of number of layers

On a broader scale, effect of number of layers on the stress distribution was found similar to that of effect of height when difference in deposit height was considerably large (here 16-18 mm). While comparing sample 2 with sample 1 and 3 and sample 5 with sample 4 and 6, effect of number of layers and effect of deposit height was found similar. Further, samples with comparable heights are compared having different layer numbers such as sample 1 and 3 as well as sample 4 and 6. Marginal difference in the magnitude of peak stress was observed. Considering samples 1 and 3, maximum compressive stress was 39 MPa in sample 1 while it was 35 MPa in other. A peak tensile residual stress in sample 3 was 192 MPa which was lesser by 9 MPa in magnitude compared to sample 1. In second comparison, sample 4 and 6, maximum tensile residual stress was 185 MPa in sample 4 which reduced my 3 MPa in sample 6. Compressive residual stress in sample 6 was 39 MPa and sample 4 showed around 47 MPa. This indicated that higher number of layers reduced the peak magnitude of residual stress. Discussion on effect of number of layer can be found in section 6.7.

6.2.2 Hardness measurement at deposit of Type 1 samples

Hardness test was performed on the deposit parts shown in Figure 6.10 as well as on substrate displayed in Figure 6.11. Variation in the hardness across the deposit height was obtained and trend is displayed in graphs from Figure 6.22 to Figure 6.29. Average hardness of each sample is given in

Table 6.3. It can be observed that average hardness of all the samples falls within similar range; however, some plunge in hardness values were observed. The probable reason for reduced hardness could the presence of porosity. All the deposit parts formed by aluminium melting and solidification process possess porosity. One of the representative macro of the hardness samples as shown in Figure 6.30 revels the presence of porosity at testing surface that might have intervened hardness testing at the precise hardness test location. More details about porosity can be found in the chapter on porosity of this thesis. A single value plunge in a graph having hardness value below 60Hv are omitted from the calculations. The reason being the values below 60 Hv are far smaller than other observed hardness values which are around 75 Hv. The results are not far from the hardness values reported by Horgar et al. [16] for same 5183 aluminium alloy. Hardness values above 80 Hv were reported by Qi et al. [57] for Al-Cu-Mg alloys.

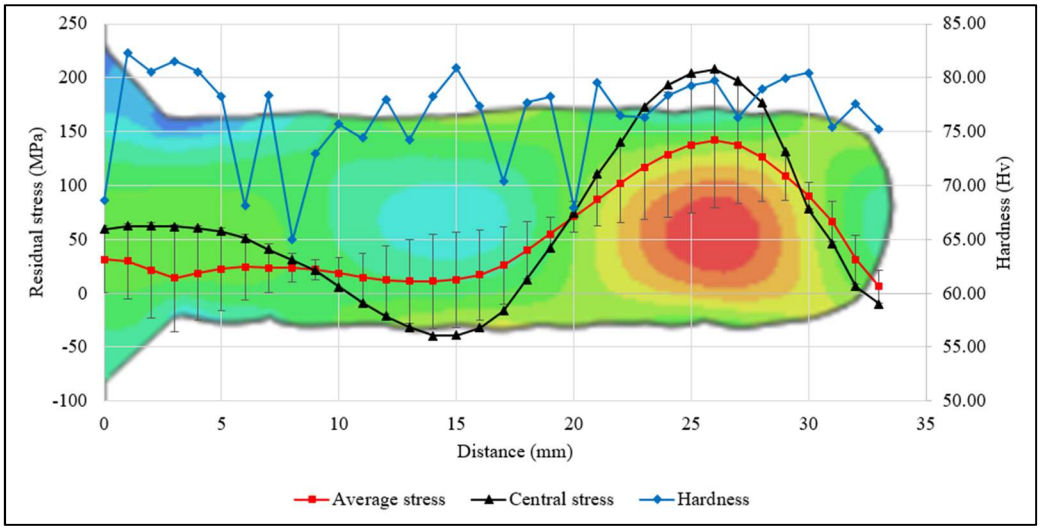

Figure 6.22 Distribution of residual stress and hardness along deposit height of sample 1.

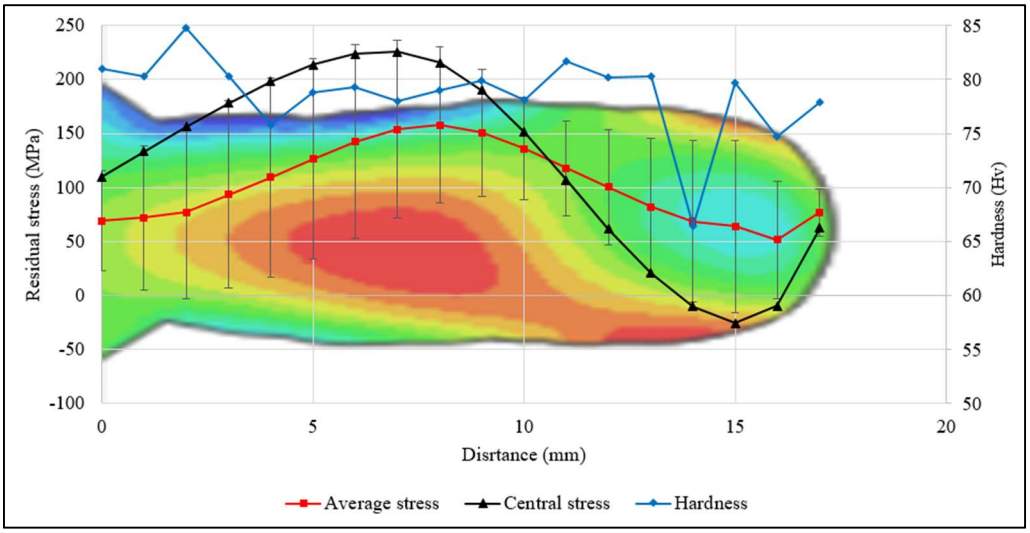

Figure 6.23 Distribution of residual stress and hardness along deposit height of sample 2.

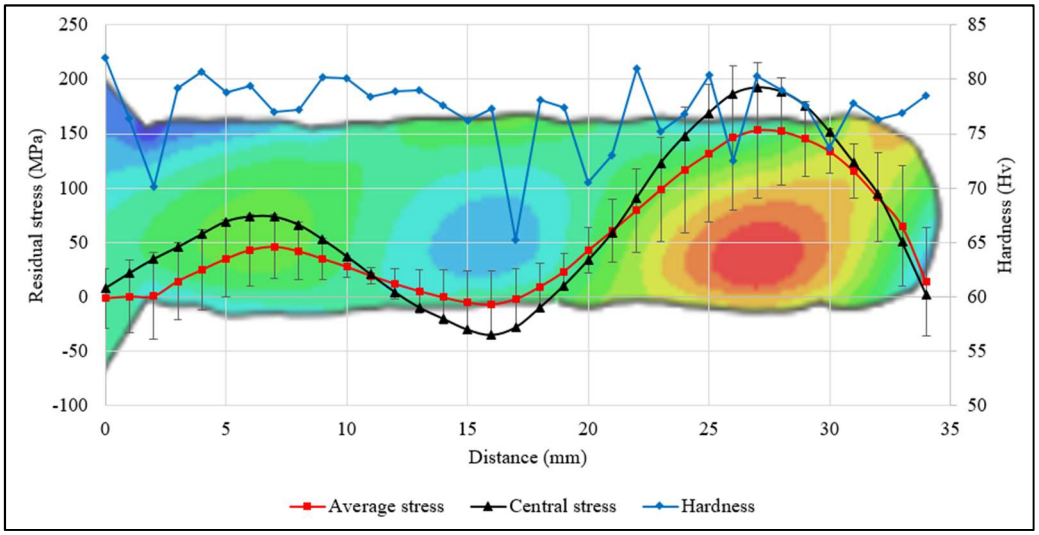

Figure 6.24 Distribution of residual stress and hardness along deposit height of sample 3.

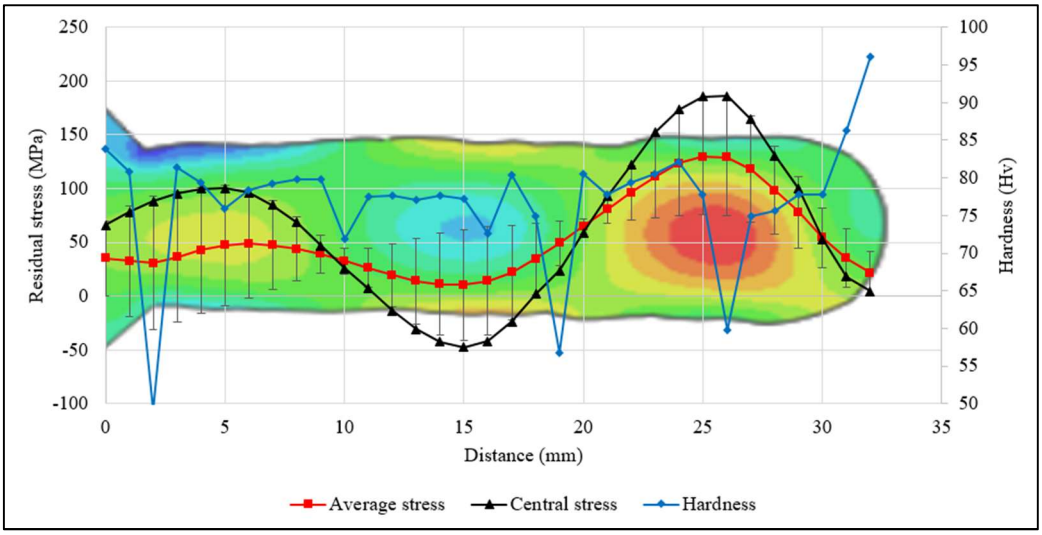

Figure 6.25 Distribution of residual stress and hardness along deposit height of sample 4.

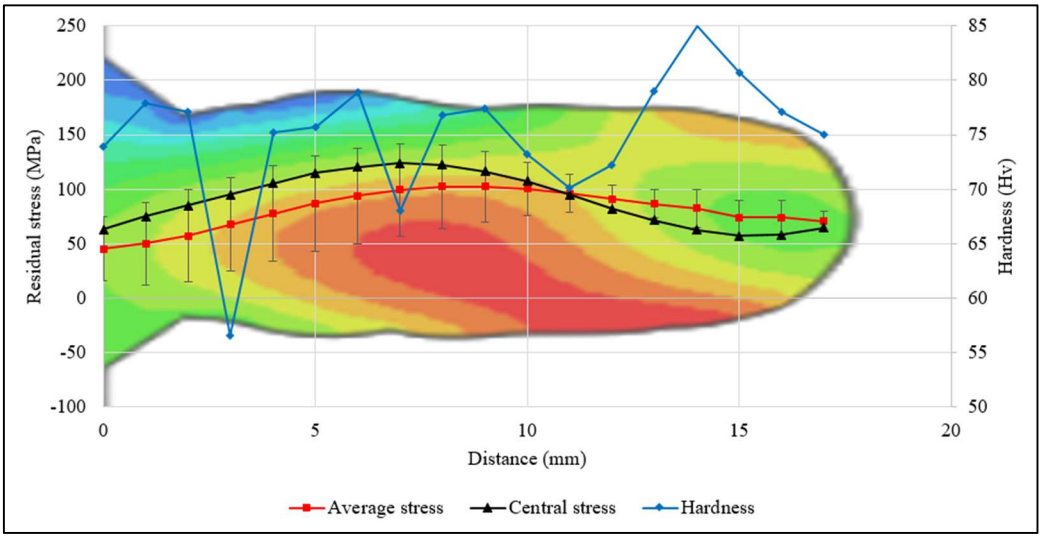

Figure 6.26 Distribution of residual stress and hardness along deposit height of sample 5.

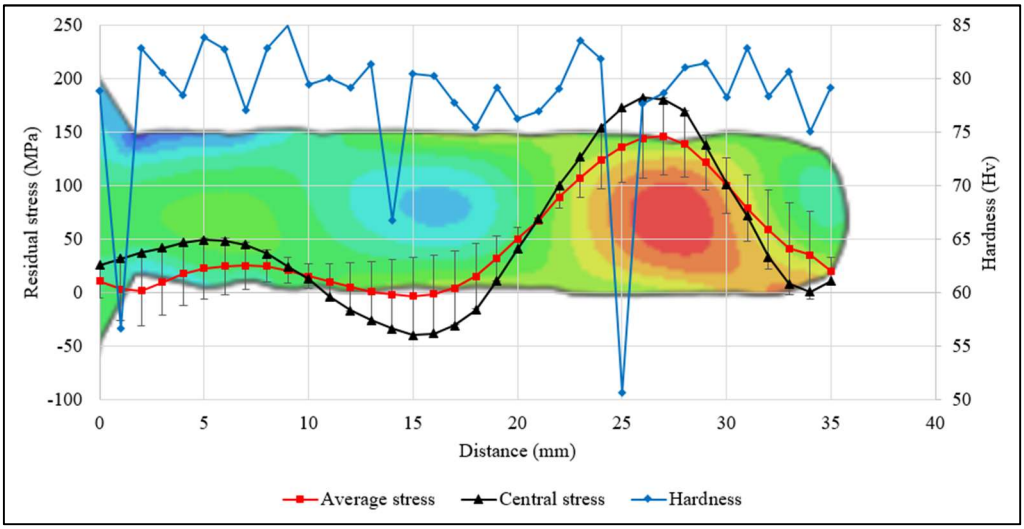

Figure 6.27 Distribution of residual stress and hardness along deposit height of sample 6.

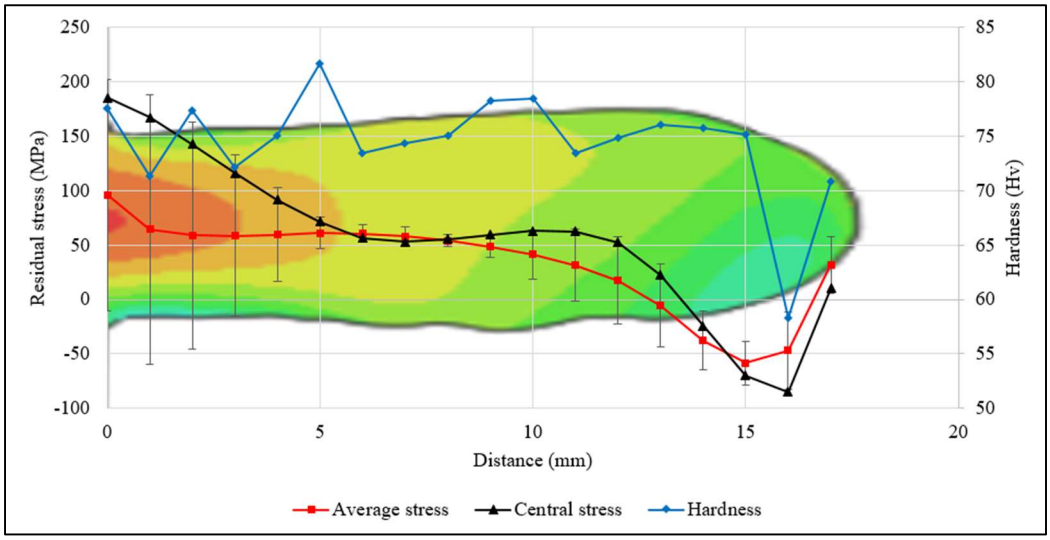

Figure 6.28 Distribution of residual stress and hardness along deposit height of sample 7.

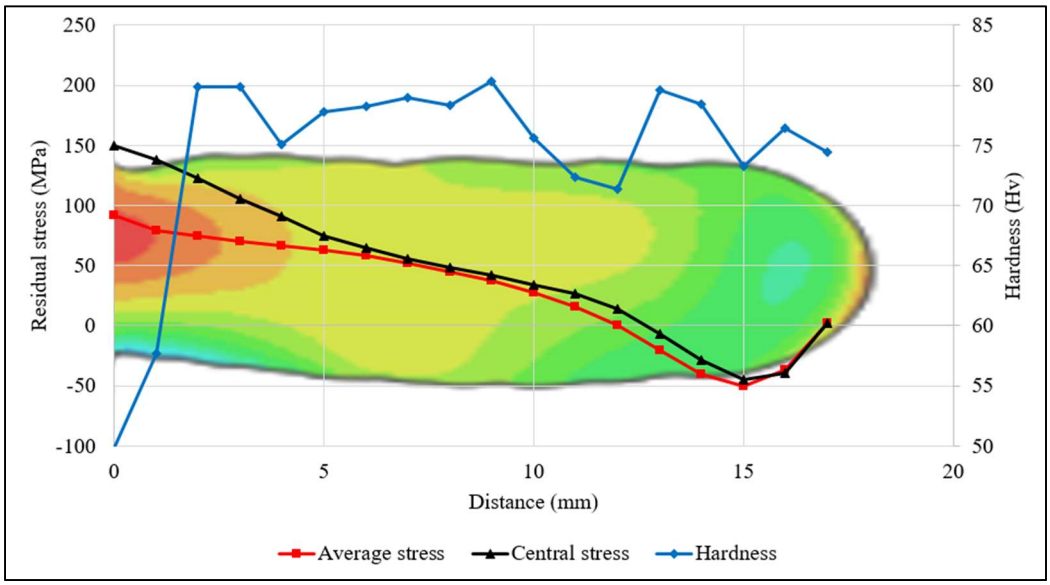

Figure 6.29 Distribution of residual stress and hardness along deposit height of sample 8.

Table 6.3 Average hardness of deposit and substrate.

Sample no.	**1**	**2**	**3**	**4**	**5**	**6**	**7**	**8**
Average hardness of deposit (Hv)	76.5	78.7	77.1	78.5	76.1	79.5	75.3	76.9
Average hardness of substrate (Hv)	88	87	86.5	85.5	85	86	78	79

Figure 6.30 Hardness test – sample 1 showing hardness locations throughout cross-section.

Following

Table 6.3 it was clear that average hardness values for deposits were varying between 75 to 80 Hv for all the samples; however, hardness of substrates were relatively high above 85 Hv for samples 1 to 6 and marginally below 80 Hv for samples 7 and 8. A particular trend similar to residual stresses was not observed for hardness. Effect of depositing parameters was less prominent on hardness; however, average hardness possessed by sample can be compared. Samples manufactured with low interlayer temperature 1, 3 and 7 showed comparatively lower average hardness compared to samples 4, 6 and 8 respectively. The percentage difference in average hardness was 2.44, 3.01 and 1.99% respectively. Samples with higher heat input having less number of layers showed lower average hardness than samples manufactures with lower heat input but increased number of layers.

6.2.3 Stress distribution in substrate of Type 1 samples

From Figure 6.21 it was clear that average residual stresses in deposits of samples were mostly tensile. The corresponding balancing compressive residual stresses were expected in respective sample substrates. The distribution of average residual stresses in the length direction in substrates of eight samples is given in Figure 6.31. Sample no. 1 to 6 with 20 mm substrate thickness revealed that majority of the compressive stresses were present at a region immediately below the top surface up to depth of around 12-13 mm. Further down the line compressive stresses were lowered and tensile stresses arose at most of the bottom half of substrate thicknesses. A trend of residual stress distribution in a substrate can be seen in Figure 6.11. Peak compressive stresses in six samples were found around 5 to 7 mm from substrate top and reached zero around 12-14 mm depth before reaching maximum tensile at 17-19 mm depth. Sample 1 showed highest compressive and tensile stresses around 60 and 66 MPa respectively amongst all six samples. Sample numbers 7 and 8 having 6 mm substrate thickness showed drastic changes in residual stresses. Thinner substrates followed similar stress distribution pattern that was observed in 20 mm thick substrates. Immediately at below the top surface, maximum compressive residual stress was observed while it reached maximum tensile just before the bottom end. This approach of averaging residual stresses broadly separates upper half of the substrate having compressive

stresses from bottom half revealing major tensile stresses; however, another approach shown in Figure 6.32 considers average taken in thickness direction. This approach of presenting residual stresses confirmed that central part of a substrate close to deposit possessed tensile stresses. Moving away from the central region, tensile stresses reduced and converted in to compressive stresses. The effect was predominantly seen in Figure 6.32a for samples 1 to 6. Major portion of a substrate apart from close to deposit and extreme ends revealed compressive residual stresses. Comparing all six samples, Sample 1 showed maximum average tensile stress just above 20 MPa at central part. In Figure 6.32b thinner substrates, samples 7 and 8, showed high tensile stresses reaching up to above 120 MPa at central region and above 100 MPa compressive away from central part. Intense stresses were seen in thinner substrates altering between tensile and compressive in nature.

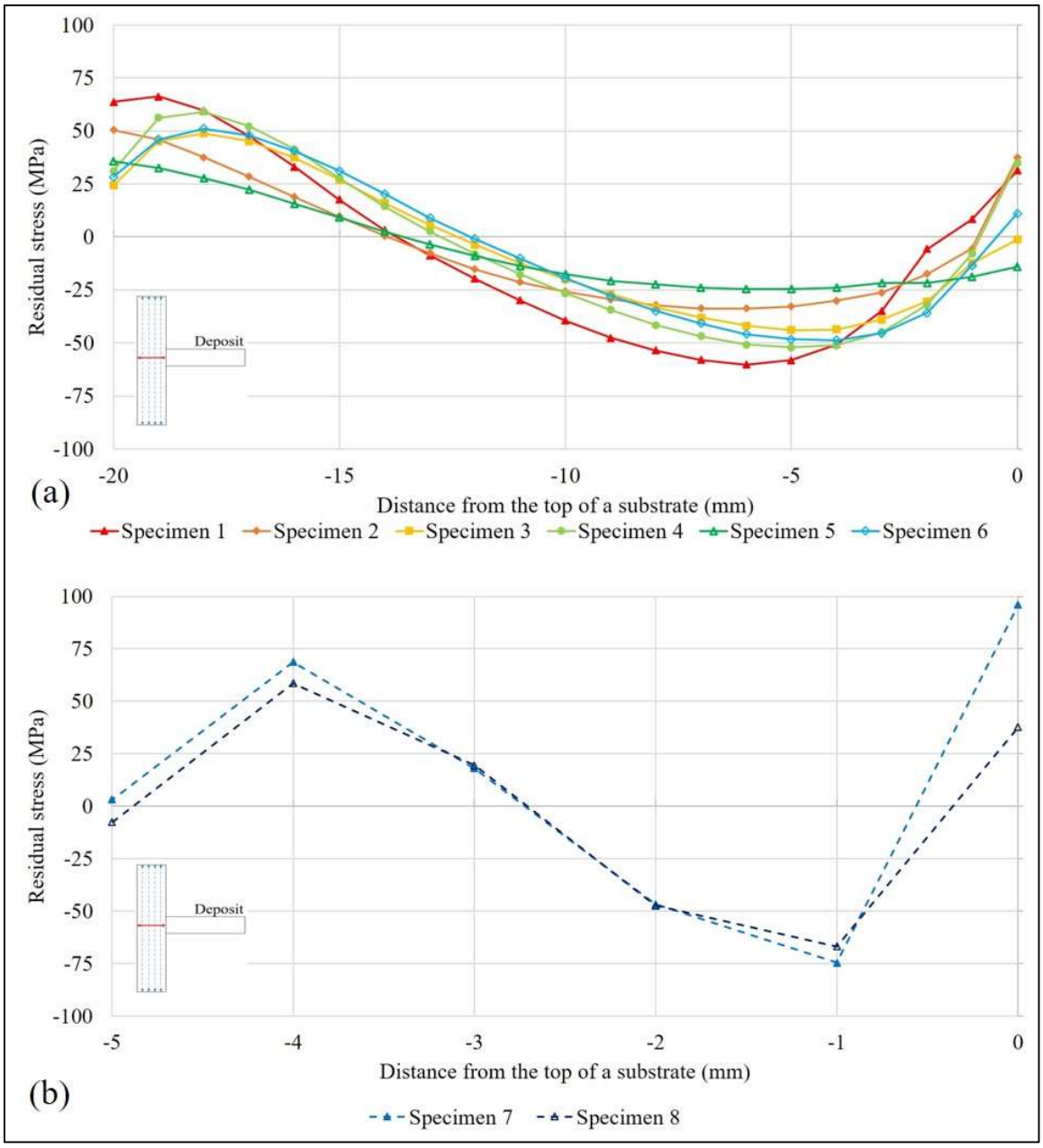

Figure 6.31 Average residual stress in substrate taken along length.

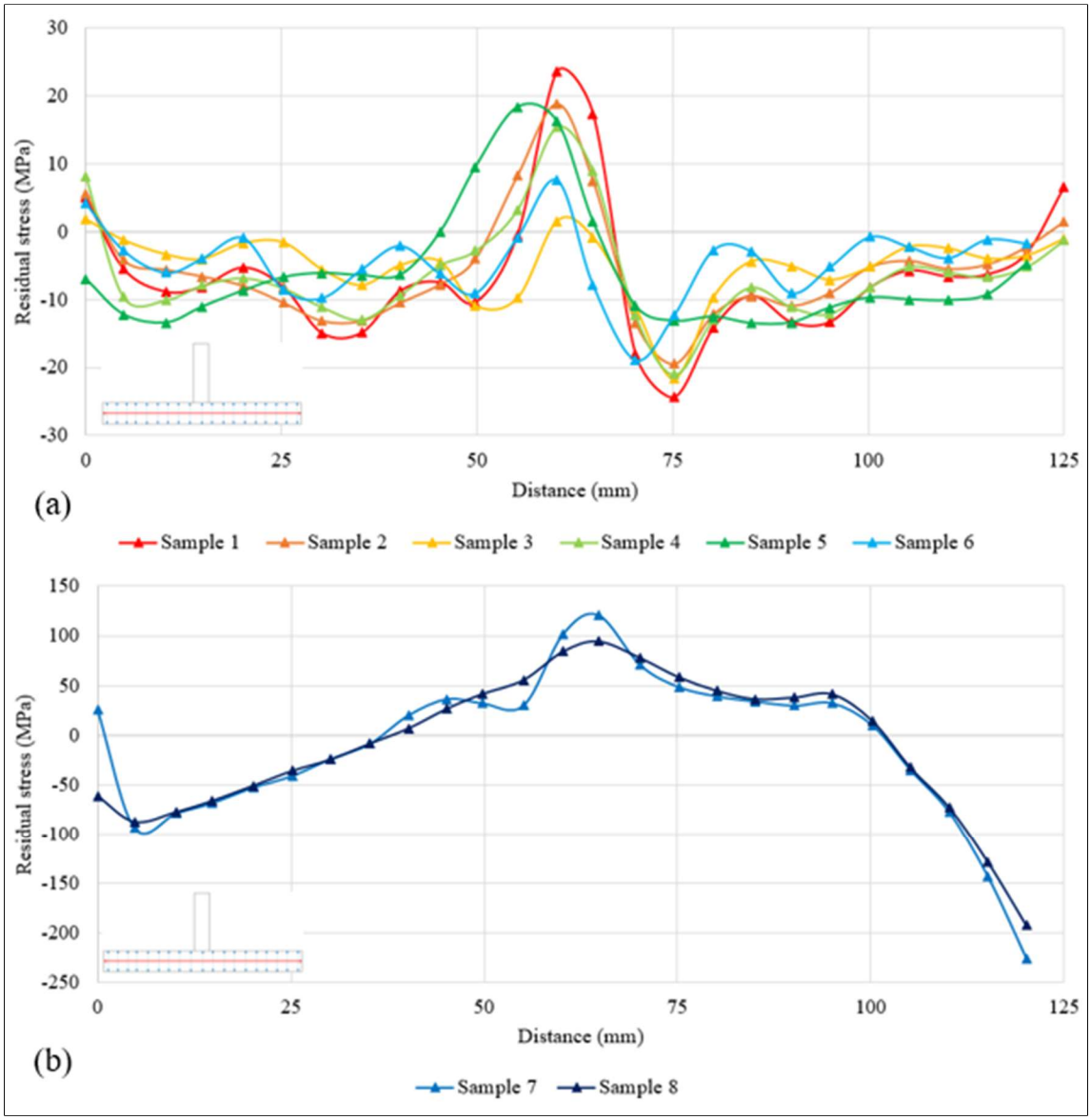

Figure 6.32 Average residual stress in substrate taken along thickness.

6.2.4 Stress distribution in Type 2 sample

Residual stress distribution in Type 2- samples number 9 is displayed in Figure 6.33. The deposit part of the sample showed high tensile stresses and substrate compressive stresses. Similar to Type 1 samples, tensile stresses were observed at the bottom of sample 9. Maximum tensile stress of around 215 MPa was present at the top region, mostly top layer of deposit that gradually reduced as height decreased and reached around 25 MPa compressive at the deposit substrate interface. Further maximum compressive stress of the order of 127 MPa was reported at around 10 – 12 mm from top surface in substrate. With further reduction of distance residual stress gradually increased reaching over 110 MPa at the bottom of substrate. Average stress distribution calculated followed the similar pattern.

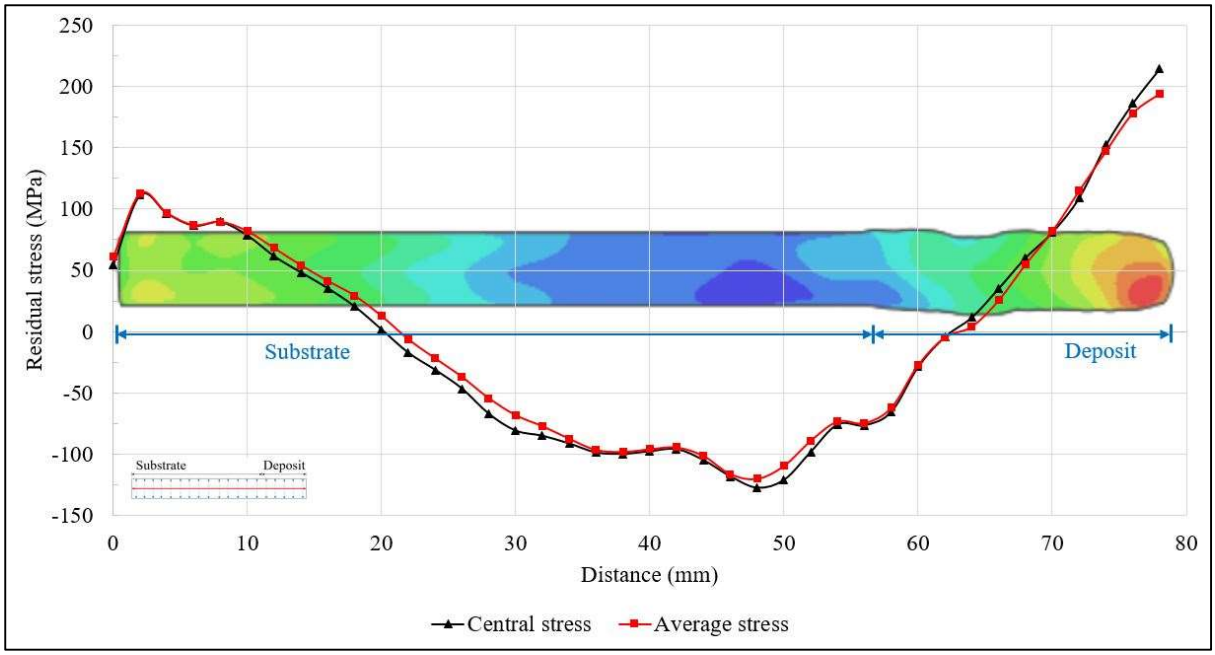

Figure 6.33 Distribution of residual stress in sample 9.

6.3 Magnitude of residual stresses

The results obtained from the contour testing highlight the presence of large tensile and compressive residual stresses in WAAM component. It is apparent that the magnitude of residual stresses was higher than the yield strength of the material composition 5183; however, the yield strength value considered for the comparison was obtained from tensile testing with uniaxial force. The properties of wire ER5183 provided by manufactures are given Chapter 3. Different tensile and yield strengths reported in literature and obtained during this study are reported in Table 6.4. From the date represented in the Table 6.4 confirms that the maximum tensile and yield strength did not cross 300 and 145 MPa respectively in deposited condition. Considering these results, plastic deformation of a deposit should start beyond 145 MPa of applied stress. Hence, residual stress higher than 145 MPa cannot be present; however, tensile residual stress as high as 200 MPa and compressive residual stress up to 50 MPa were apparent in graphs from Figure 6.13 to Figure 6.20. Hence, residual stresses are around 40% higher than the yield strength value provided my wire manufacturer.

There are many theories regarding establishing the relation between hardness, yield strength and tensile strength of different materials [173–176]. A simple relationship established by Tabor [177,178] in early studies mentioned yield strength is around one third of hardness.

$$\sigma_y = \hat{H}/3 \qquad \text{Eq. (8)}$$

where σ_y is yield strength and $\hat{H}$ is hardness

Table 6.4 Yield and ultimate tensile strengths from testing of wire 5183 after deposition from various sources.

Yield strength (MPa)	Tensile strength (MPa)	Deposit condition	Reported by
145	293	Additive manufacturing	Horgar et al. [16]
124	273	Additive manufacturing	Geng et al. [84]
146	283	Welding	Dutra et al. [179]
140	300	All weld test	Lincoln Electric [180]
141	287	Additive manufacturing	This study (refer Table 5.1)
131	284	Additive manufacturing	This study (refer Table 5.1)
130	283	Additive manufacturing	This study (refer Table 5.1)

Depending upon metals deformation characteristics during hardness test, different relations were established in later studies. Deviation of yield and hardness values from experimental observations led establishment of newer formulae for polymers, ceramics, and metals including ferrous and non-ferrous metals; however, very few relations drastically vary from Tabor's equation such as for ceramics and metallic glasses as derived by Zhang et al. [174]. From

Table 6.3 and as mentioned earlier, all hardness values of the deposits are varying from 75 to 80 Hv that is approximately 735 to 785 MPa (refer Appendix – III). Following simple relation given by Tabor [177,178], the expected yield strength of the material should vary from 245 to 260 MPa given that hardness values are around 735 to 785 MPa (75 to 80 Hv). Detailed calculations are provided in Appendix – III. On the other hand, if reverse calculations are made for hardness values considering 140 MPa yield strength, hardness values should fall around 43 Hv (420 MPa); however, all the hardness values reported earlier are around 80 Hv, well above 43 Hv for deposit of 5183 wire [16,179]. The calculations support the presence of residual stresses with value as high as 200 MPa. Maximum stress value reported in considering all the samples is 225 MPa in sample 2. From the hardness calculations maximum yield strength can be around 250 MPa. Hence, maximum stress observed in the deposit is less than the actual yield strength of a materials which support the possibility of presence of high residual stresses. The reason for large difference between the yield strengths obtained by tensile strength and calculations as per Tabor's equation can be the difference in material deformation after application of load. The load is unidirectional in case of tensile testing, however, indenter penetrates into materials surface in hardness testing. Different behaviours of different kinds of materials after application of load is discussed in detail by Zhang et al. [174]. Detailed discussion on the behaviour of aluminium 5183 wire deposit and its correlation with yield and tensile strength is out of scope of this study.

Leggatt [181] suggested a condition to check the possibility of presence of residual stresses with magnitude close to yield strength of material in a welded component. An equation can be written as –

$$\alpha\,(T_s - T_0) \geq \sigma_y / E \qquad \text{Eq. (9)}$$

where α is coefficient of thermal expansion, T_s is softening temperature usually taken at which yield strength drops to 10% of its ambient temperature (refer Figure 6.34), T_0 is ambient or interpass/layer temperature, σ_y is yield strength at ambient or interpass/layer temperature and E is young's modulus. As per the calculations in Appendix – III, both the types of samples, 50 and 100°C interlayer temperature, showed higher values for product of coefficient of thermal expansion and temperature difference than ratio of yield strength to young's modulus of deposit material. The values of the products were 0.00975 and 0.00845 for 50 and 100°C interlayer temperature respectively compared to the ratio 0.002. The calculations confirmed that residual stresses in a deposit could be close to yield strength of a material. Hence, it can be around 225 MPa as discussed earlier.

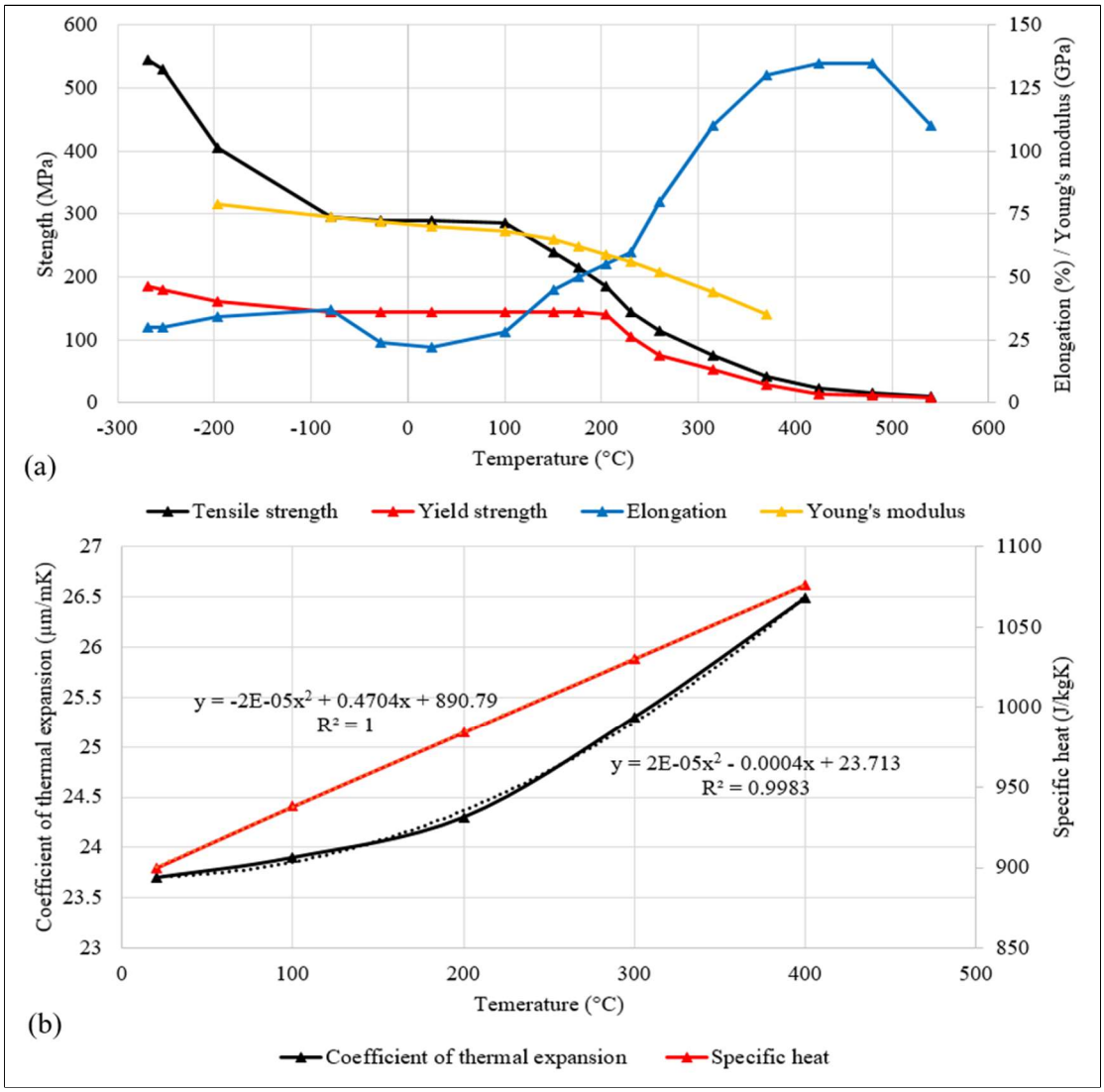

Figure 6.34 Material property variation as a function of temperature a) mechanical properties (from ASM Handbook [182]*) and b) thermal properties (from ASM Handbook* [127]*).*

Table 6.5 compares the maximum compressive stress measured at substrates of all samples. From the values it can be said that maximum compressive stress at a point in thick substrates (samples 1 to 6)

could not cross 135 MPa, however, thin substrate samples (samples 7 and 8) showed more than 250 MPa stress value. From these observations, thick samples showed comparatively lesser compressive stresses than thin samples. On an average maximum compressive stress in thick substrate samples was 92 MPa while it was 265 MPa for thin substrate samples. Maximum value shown by samples 7 was recorded at the one of the corners of substrate and can be considered overvalued or as a measuring irregularity. The magnitude of compressive stress recorded at samples number 8 agreed the presence of high stresses and it can be said that such a high stresses were responsible for distortion in thin substrates. Another argument could be the local change of mechanical properties of the substrate material due to high heat application at the area immediate to deposit region. More detailed explanation can be found in section 6.5.

Table 6.5 Maximum compressive stress measured in all samples at single point.

Sample	**1**	**2**	**3**	**4**	**5**	**6**	**7**	**8**	**9**
Maximum compressive stress measured (MPa)	132	74	88	108	50	104	281	250	140
Average of compressive stresses (MPa)	92						265		140

Several thermal cycles of expansion and contraction are believed to give rise to residual stresses in deposit. The amount of expansion and contraction can be measured using basic equation of coefficient of thermal expansion for volumetric scale.

$$(\nu_f - \nu_0) / \nu_0 = \alpha (T_0 - T_f) \qquad \text{Eq. (10)}$$

where ν_f and ν_0 are final and initial volumes, T_0 and T_f are initial and final temperatures and α is volumetric coefficient of thermal expansion. Previously deposited layers expand due to deposition of new layer. The layer immediately beneath newly depositing layer is expected to show highest dimensional changes compared to other layers due to experience of highest temperature. The effect of temperature on the dimensions of a deposit diminishes from top layer to bottom layer depending upon temperature gradient. From the Eq. 10, volume changes in a single layer can be calculated for heating and cooling cycles. Detailed calculations of volume expansion and contraction during temperature rise and temperature drop for two heat inputs used in the study are displayed in Appendix – III. According to the Appendix – III, samples manufactured with 50°C interlayer temperature showed around 4 % volume expansion and contraction, thus, during single layer deposition that is one heating cycle, the layer on which a new layer is deposited experienced total 8% of dimensional changes. In case of 100°C interlayer temperature samples, total dimensional changes were 7.5%, hence, around 3.75 % of volume expansion and contraction were observed. Hence, percentage strains expected were 4.1 and 3.7 % for 50 and 100°C interlayer temperature respectively (Appendix – III). The strain values are relatively high compared to other materials for example steel. Coefficient of linear thermal expansion of steel is roughly half of aluminium. Therefore, as per Appendix – III if linear expansions were calculated for

steel and aluminium considering 50 and 100°C interlayer temperature, aluminium showed roughly twice strain than steel. Thus, high coefficient of thermal expansion of a materials plays important role in controlling temperature dependent strains and thus ultimately residual stress formation. High strains in aluminium can be considered as a one of the important factors controlling and forming residual stresses.

At this point it can be argued that during and after every new layer deposition, heat flow exerts both positive and negative strain depending upon temperature rise and fall at particular location of a deposit. As number of layer increases, the temperature rise at layers far from the top layer reduces depending upon deposit's dimensions and material characteristics. Reduced strains are expected at the region having reduced temperature rise compared to large temperature rise. Hence, after metal deposition area close to top layer shows higher strains due to hotter regions and bottom area shows relatively lesser strains due to lower temperature. Only the top layer that is being deposited possesses increased free area for dimensional changes (contraction during metal solidification) due to absence of any layer on top and other layers starting from first layer on a substrate up to penultimate layer experiences restrictions as bottom and top part of layers are bound to adjacent layers. Hence, when temperature rises at any layer except top layer, metal expands more in less restricted region that is in horizontal direction and expands less in vertical direction as schematically shown in Figure 6.35. Thus, multiple layer deposition, restrictions to accommodate positive and negative strains and non-uniform expansion and contraction cycles across the deposit height enforces complex residual stresses a deposit.

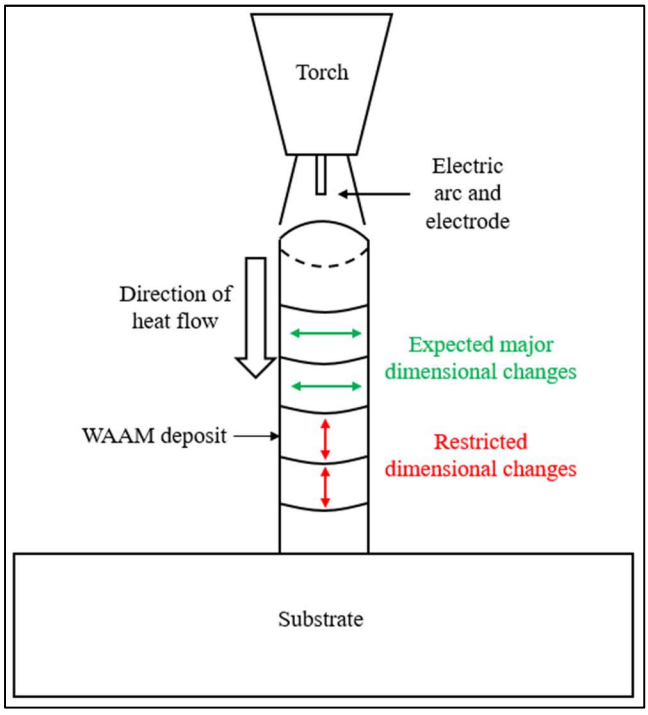

Figure 6.35 Schematic of expected and restricted strain directions in WAAM deposit.

In several studies on residuals stresses by contour method researchers revealed that the maximum stress in the component could be as high as yield strength of a material. Toparli and Fitzpatrick [183] reported as high as 250 MPa compressive stress in aluminium laser pinned part. Zhang et al. [171] reported maximum stress around 175 MPa whereas Liu and Yi [184] reported around 160 MPa residual stress in

aluminium component. The evidence supports the existence of high residual stresses in a fabricated part. In an additively manufactured part made of Ti-6Al-4V, residual stresses of the order of 500 MPa has been reported [87,185] by contour testing. In line with this, in a stainless steel weld, peak tensile stress was found around 320 MPa (roughly 40% higher than expected yield strength by tensile test) and compressive up to around 100 MPa. Residual stress study by contour method is not available in a literature for additively manufactured aluminium part. A computational study approach is advised in the case.

Contour testing assumes material deformation fully elastic with recognition of stresses only in normal direction to the cut surface and does not identify shear stresses and transverse displacements at the cut surface. Depending upon the magnitude of residual stresses, especially close to yield stress, plastic deformation may arise resulting errors in stress measured [186,187]. Also, internal imperfections affect contour cutting and stress relaxation. Errors in residual stress measurements could be +/-5 MPa as reported by Prime at el. [170], however, it was around +/-20 MPa for Zhang et al. [171]. Maximum error reported by Hosseinzadeh and Bouchard [172] was 15-30 MPa. These conditions could be valid for the obtained results as stresses are close to yield strength of a materials and porosity was found in the deposit as shown in Figure 6.36. It can argued that residual stresses in an additively manufactured part of aluminium could be as high as yield strength of a material.

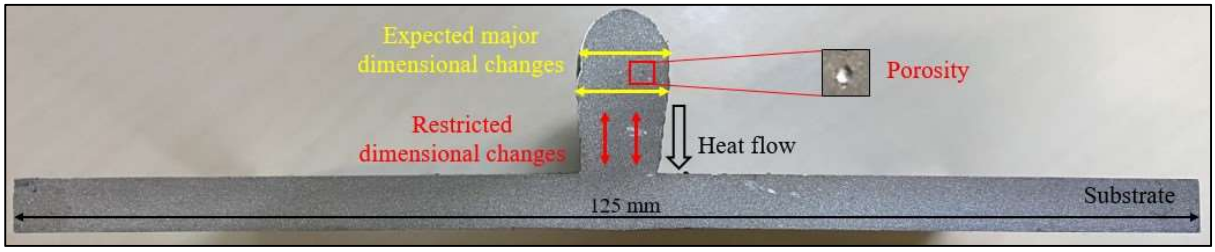

Figure 6.36 Expected and restricted dimensional changes in WAAM deposit and a porosity on cut surface.

6.4 Relation between hardness and residual stress

The hardness values showed hardly any relation with deposition parameters due to the frequent abrupt changes in hardness values in all samples. Surface imperfections could be the probable reason for the same. On the other hand, hardness values obtained are close to those reported by Horgar et al. [16] for WAAM using wire 5183 while Dutra et al. [179] for welding using the same wire. Processing the data obtained from Figure 6.22 to Figure 6.29 a rough correlation between hardness and residual stress can be determined as shown in Figure 6.37. The graph shows minimum hardness value for stress approaching zero and higher value for increased stress. The condition holds true for tensile as well as for compressive residual stresses. There is no large difference in the variation of hardness, however, pattern can be seen. From scattered data it can be said that for the increase of tensile stress from 0 to 225 MPa hardness increased from 75 to 79 Hv. In case of compressive stresses when increase from 0 to 50 MPa hardness rose from 77 to 79 Hv. Thus, direct relationship between residual stress and hardness can be easily obtained from the graph. The probable reason for hand in hand correlation between hardness and residual stress could be the increased strain at high stress regions provided increased resistance for the indenter penetration in to the deposit material. Higher the penetration greater

the materials deformation, hence, lower the hardness. Part of deposit material at high stress region possesses relatively higher strain should have revealed less deformation due to already existing increased strain and less stressed area have relatively less strained part of deposit that showed comparatively higher material deformation that is lesser resistance to deformation (penetration for indenter). Deposits and substrates of the same samples showed large difference in hardness values. This might be correlated to the increased surface imperfections at deposit compared to substrate. Another reason could be the mechanical deformation of wrought substrate material by rolling may have increased the hardness and minimised surface imperfections as compared to undeformed newly solidified deposit material.

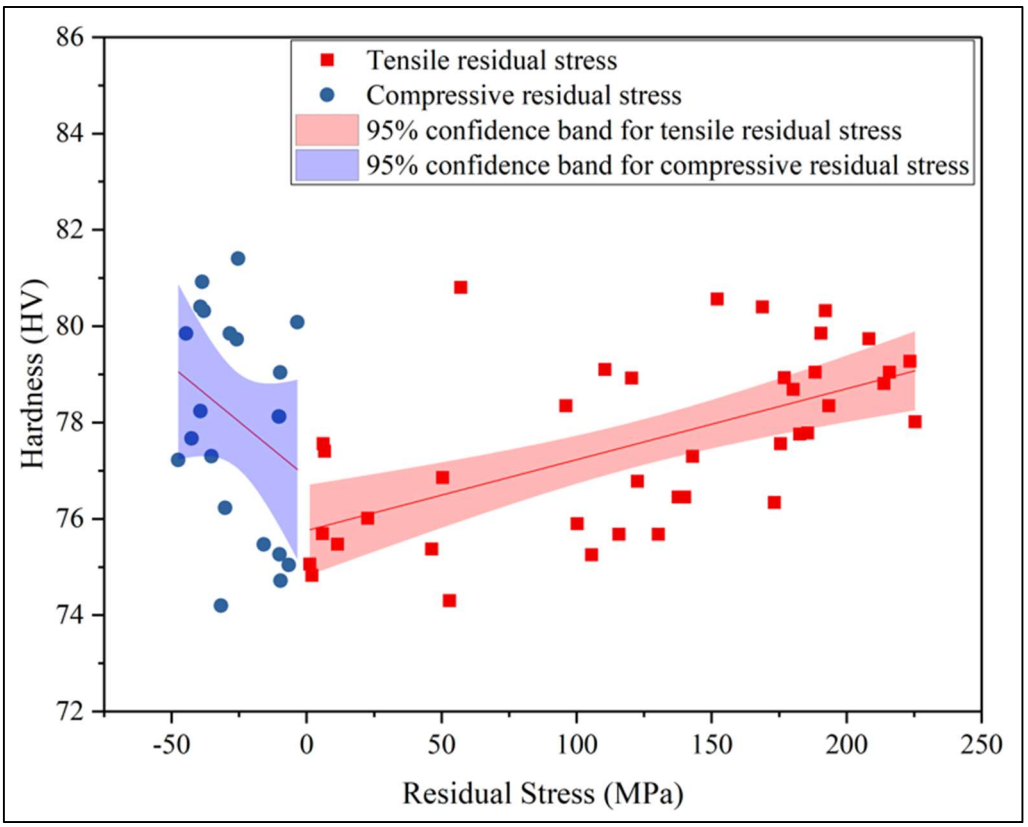

Figure 6.37 Correlation between hardness and residual stress.

6.5 Effect of substrate geometry

6.5.1 Type 1 samples

When liquid metal is deposited and gets solidified, due to metal contraction tensile stresses develop at the depositing metal and balancing compressive stresses in substrate [114]. Figure 6.13 to Figure 6.20 confirm that deposits possess majority tensile residual stresses and Figure 6.11, Figure 6.31 and Figure 6.32 suggests maximum balancing compressive stresses were produced in substrate. From Figure 6.32 a schematic of representing rough stress distribution in a WAAM part with thin and thick substrates can be drawn as shown in Figure 6.38. The representation resembles with the stress profile usually found in welded structure as described by Kou [114] and Dewald and Hill [188].

Residual stress measurement by contour method was experimented by Martina et al. [185] on WAAM part manufactured using Ti-6Al-4V material. Considering geometry of WAAM parts, overall stress

distribution pattern in the Ti-6Al-4V and all aluminium processed samples was expected similar apart from magnitude of stresses. Surprisingly, only samples with 6 mm substrate thickness, sample number 7 and 8, showed similarity with the titanium samples which had similar substrate thicknesses [38,185]. Rest of the six samples with 20 mm substrate thickness showed entirely different stress distribution pattern. As discussed earlier, maximum stress was present at the top region of deposit for six samples irrespective of the deposition conditions; however, samples 7 and 8 had peak stresses present at the portion close to substrate, similar titanium samples.

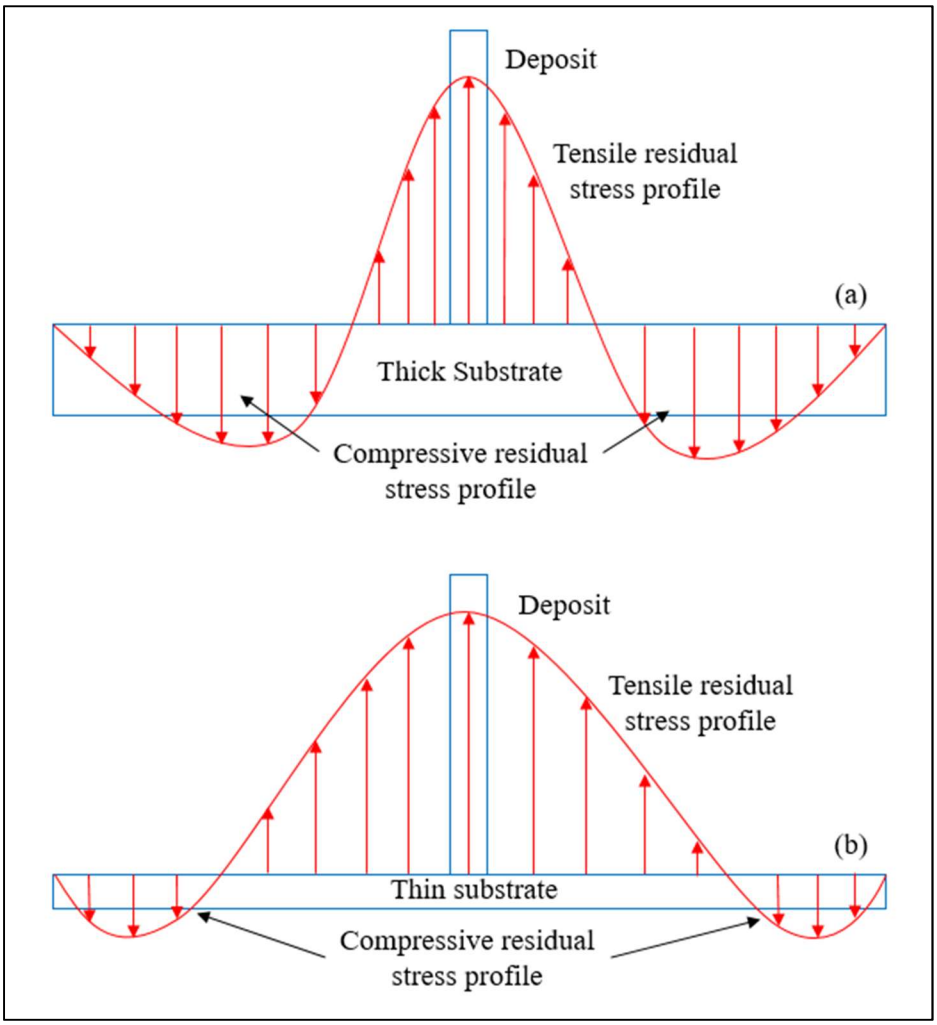

Figure 6.38 Schematic of residual stress distribution profile across WAAM part a) thin substrate b) thick substrate.

The probable reason for the difference in stress distribution between thin and thick substrate samples could be the availability of larger material volume at 20 mm thick substrate than 6 mm thick samples. Total volume of 20 mm thick substrate was 2.3 times greater than 6 mm thick substrate (refer Appendix – III). Thicker material shows higher stiffness compared to thinner material provided other dimensions are similar. Higher stiffness suggests higher resistance to deformation compared to less stiff material. Firstly, this fact highlights 20 mm thick substrate will have higher resistance to dimensional changes offered by addition of heat than 6 mm substrate. Further, stiffness of material is a function of temperature with inverse relation. Increased temperature eventually would reduce stiffness, young's modulus and yield and tensile strength (refer Figure 6.34). Thus, at high temperature material becomes

more susceptible to deformation. In one of the studies on effect of substrate thickness, Corbin et al. [189] reported considerably high temperature at the bottom surface of thin substrate than thick substrate after metal deposition at top surface. The results suggested that thin substrate gets heated up to high temperature throughout the thickness due to the presence of less material volume to spread heat compared to thick substrates. Higher thickness sample showed considerably less temperature at bottom surface indicating temperature gradient in cross section. This could be because higher material volume acts as a better heat sink than lesser volume. Hence, hotter thin substrate shows increased susceptibility for strain than thick substrate. This suggests that thinner substrate that has lower heat absorption capacity will respond more to the heat flowing down from a deposit. The response could be the formation of increased residual stresses due to higher temperature rise. Figure 6.39a and b illustrates the temperature distribution pattern expected in two different types of substrates.

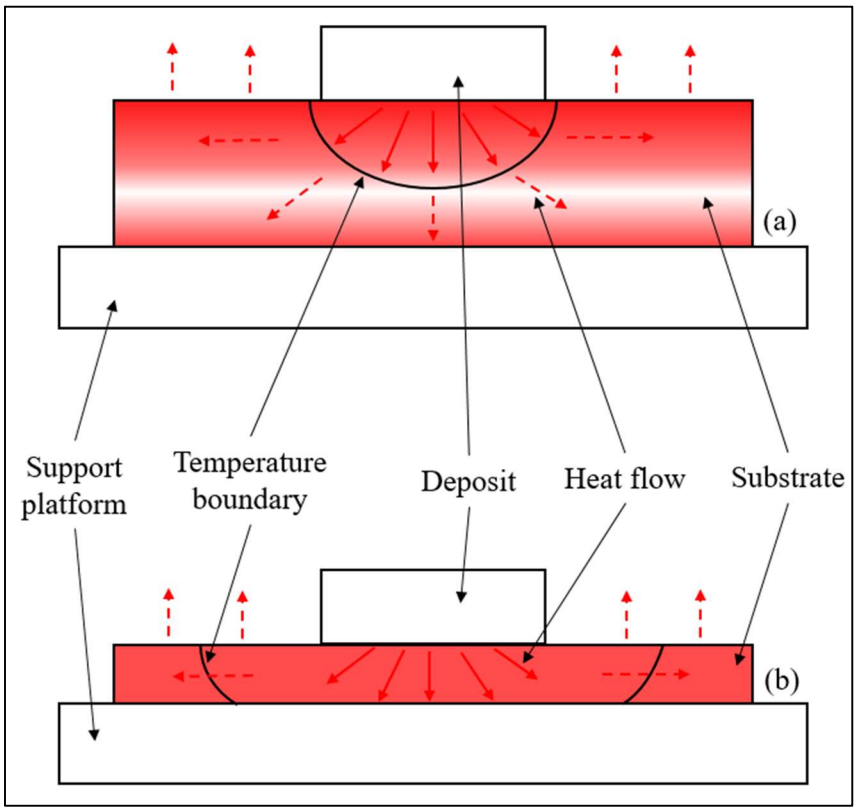

Figure 6.39 Temperature distribution in a) thick substrate and b) thin substrate.

As temperature increases beyond threshold value, stress relaxation temperature of a material, material alleviates plastic stress and strain due to local annealing effect. For the chosen aluminium alloy, stress relaxation process roughly begins from 160°C [190] which is around 0.25 time its melting point. Another reference [191] reported stress relaxation starts at temperature around 0.2 times the melting point of alloy. The temperature for Ti-6Al-4V is around 0.4 times of its melting point [189,192]. The difference could be due to different strengths, hardness and heat handling capacity. Figure 6.39 showed a temperature boundary that relates to stress relaxation temperature into substrate. When metal layer is deposited through arc, heat penetrates into substrate, however, due to heat absorption and dissipation temperature gradient always persists. Thus, temperature inside the curves in Figure 6.39 considers temperature higher than stress relaxation temperature.

6.5.1.1 Thin substrate

In case of thin substrate, the stress relaxation isotherm extends throughout the thickness as shown in Figure 6.39b. Material in this band should relieve stresses and strains by displaying a distortion. A close observation of the bottom part of substrates of samples 7 and 8 (refer Figure 6.7, Figure 6.8 and Figure 6.11) exactly beneath the deposit region revealed a small bulge which indicates dimensional change for stress accommodation due to heat application. A major distortion is expected in the region adjacent to deposit redistributing residual stresses. High tensile residual stresses shown in Figure 6.32b extend up to much wider part of a substrate away from deposit region confirmed temperature rise much above stress relaxation temperature in a wider region. It can be argued that temperature was high enough in the vicinity of the deposit part to produce considerable expansion which was later on cooling to room temperature produced appreciably high tensile residual stresses due to material contraction. The area outside of the isotherm that is extreme ends of substrate having less temperature rise will produce balancing compressive stresses which can observed in Figure 6.32b. From Figure 6.7 and Figure 6.8, it can be said that less material stiffness offered by 6 mm thick substrate and high temperature rise of a substrate cannon produce balancing compressive stresses in substrate thickness adjacent deposit region. Therefore, compressive stresses could be intensely present at the substrate ends where temperature rise is relatively less. It can be said that, for initial layers of metal deposition, compressive stresses were present in the substrate region close to deposit due to relatively less temperature of substrate balancing tensile stresses of deposit. Later, as number of layers increased, amount of heat flowing towards the substrate region gets dissipated in the vicinity of deposit increased enforcing thermal expansion. This could have shifted the compressive stresses towards the relatively colder part of a substrate. This could be due to heat sink/accumulation at the region close to deposit in substrate responsible for local area expansion following formation of tensile residual stresses. This explains the presence of high tensile stresses in the cross sectional part of thin substrates. Total ten number of layers were deposited making total height of deposit around 17-18 mm (refer Table 6.1) which might not be high enough to accommodate part of heat flowing towards the substrate reducing temperature at cross section. Rough residual stress profile across the WAAM parts of different substrate thicknesses observed is depicted in Figure 6.38. The residual stress distribution is not vastly different from that usually observed in the welded structure [114]. There will be heat conduction into the bottom metallic platform, however, this will not be enough to avoid the high temperature effects in the substrate.

6.5.1.2 Thick substrate

The stress relaxation temperature isotherm in case of thick substrate in contrast to thin substrate could not have reached bottom of a substrate as can be seen in Figure 6.39a. Also the area of isotherm in thick substrate in comparison to thin substrate must be smaller due to rapid heat conduction and dissipation in larger available material. A small bulge at the substrate beneath the deposit as observed in samples 7 and 8 was absent in thick substrates. This suggests that heat flowing from the top surface is not sufficient enough to produce any stains at the bottom part unlike samples 7 and 8. In contrast to thin substrates, compressive stresses were present in the vicinity of a deposit in substrate. From Figure 6.1 to Figure 6.6 it is clear that compressive stresses were distributed in roughly upper half part of substrate thickness. The fact suggested that sufficient stiffness offered by thick substrate and absence of heat accumulation at the part close to deposit provided enough balancing compressive stresses against the tensile stresses

forming due to molten metal solidification at deposit region. For the initial layers deposited on a top surface, deposit should show tensile stresses and balancing opposite stresses in adjacent substrate region as was discussed and expected at thin substrates. The effect of temperature rise at substrate is prominent for initial layers and diminishes as number of layers increases due to distance between heat source and substrate gradually increases. As number of layers increased, opposed to the fact observed in thin substrates, in thick substrate heat flowing from deposit was dissipated into the substrate. Thus, maximum tensile stress was created in deposit instead of deposit-substrate interface. From sample numbers 1 to 6 with deposit heights of around 18 mm and 35 mm (refer Figure 6.13 to Figure 6.18) it can be said that irrespective of deposit height, high and low tensile stresses were distributed across the section height except for very small part of compressive stress (refer Figure 6.40).

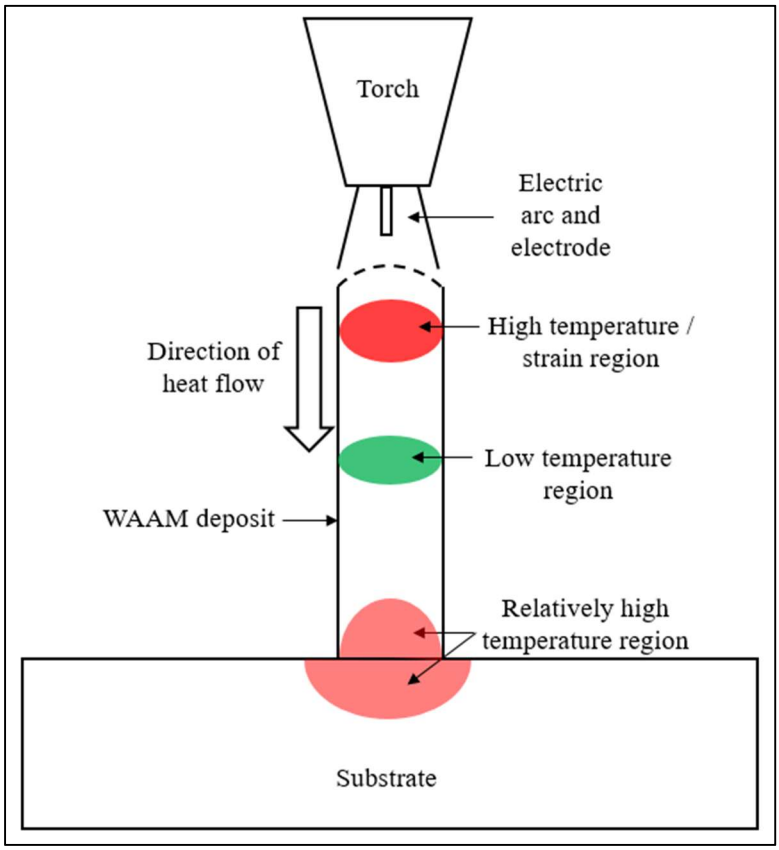

Figure 6.40 Temperature distribution in deposit and substrate after completion of metal deposition.

This could be because of strong support provided by the substrate by forming balancing compressive stresses in a substrate against all the tensile stresses forming during metal solidification in a deposit part. Heat added from the top of deposit with every layer of deposition is used partly for melting and raising temperature of the region immediate below the top layer and remaining heat conducted towards substrate. After depositing a layer, liquid metal gets rapidly solidified due to large temperature gradient between liquid metal and previously deposited layer and also due to heat loss to the atmosphere and previously deposited layers; however, after solidification of top layer, temperature of the deposit part beneath top layer (from results around 10 mm from top) remains high enough for longer duration to produce appreciable strain, expansion in this case, at the same region. This can be drawn from the results showing peak residual stresses in top region. After cooling the whole assembly to room temperature,

high strain produced high tensile stresses in the specific part of deposit. Temperature at the central part of deposit reduced relatively faster due heat extraction by substrate. This could be due to the geometry of a part being manufactured. Heat conduction from the central part of deposit towards the substrate is more practicable as high material volume substrate is expected to extract heat from the deposit than conducting heat upwards towards top layer. Further, after depositing 25 layers, it appears that substrate acted as a reservoir of heat. Bottom part of deposit remains relatively hot due to proximity to the hotter substrate. This might have created thermal expansions in the local region that after cooling to temperature gave rise to tensile stresses.

However, region of a substrate below the top surface adjacent to cross section predominantly showed compressive stresses (refer Figure 6.31a). Further, majority part of bottom half of thick substrate showed tensile stresses as discussed earlier in section 6.2.3 and following Figure 6.31. When the heat is introduced into the substrate it flows towards bottom surface which is in contact with steel support platform. Heat get accumulated at the bottom surface due to inability of free flow of heat from bottom surface to support platform opposed to free flow from top surface to bottom surface. Typical illustration of the same is shown in Figure 6.39. Therefore, heat accumulation is prominent at the bottom surface producing appreciable strain. Thus, as discussed earlier, strained region produced tensile stresses after cooling whole assembly to the room temperature. Top surface of substrate remained in contact with the atmosphere all the deposition time. It can be argued that heat at the top surface and immediately below it is transferred to atmosphere by convection. Therefore top surface could have revealed relatively cooler part of the assembly and hence showed compressive stresses. Hence overall stress distribution pattern in the WAAM manufactured part resembles that was found in welded structure and can be represented as per Figure 6.38a with comparatively increase compressive stresses spread over larger area compared to thin substrate.

Another possible explanation for the presence compressive stresses at the central part and tensile stresses at extreme ends could be the bending moment acting within the WAAM assembly. Sample number 2 and 5 with less deposit height showed only tensile stresses opposed to samples 1, 3, 4 and 6. The geometry of the part being manufactured found to have major impact on stress formation and distribution. Taller deposit height could be responsible for creating compressive stress area in central part of deposit. Tensile stresses development due to hot metal deposition at top, heat extraction and high stiffness offered by large material volume substrate producing balancing compressive stresses could be the affecting factors for stress formation and redistribution defining stress magnitude as well as location in WAAM part. The inverted t-shape of the assembly and increasing height of the part at centre with application heat could be affecting the stress distribution changing bending moment after particular deposit height. Specific study on the effect of work geometry on residual stress distribution is further recommended. Stress distribution in WAAM assembly changes due to unclamping [193] after completion of deposition. Also, EDM cutting of the samples might have affected stress redistribution. The extent of effect of unclamping and EDM cutting on stress redistribution can be more understood by computation study approach which is not the scope of this work.

6.5.2 Type 2 sample

Due to the unlike geometry of substrates of Type 1 and Type 2 samples, stress distribution in whole assembly appears completely different, however, close observations showed there was appreciable

similarity. Stress distribution in deposit shown by Figure 6.21 and in substrate as per Figure 6.31 can be combined and compared with Figure 6.33. Overall stress distribution confirmed that deposit part remains under tensile residual stresses while counteracting compressive stresses were created in substrate. Further, at the bottom part of the substrate tensile stresses were present. Considering overall stress distribution in Type 2 sample, the stress flow matches with one observed in Type 1 samples. The presence of large magnitude of stresses can be explained similar or previous discussion.

The phenomena of stress relaxation and heat dissipation to the substrate observed in Type 1 samples cannot be directly applied to Type 2 samples due to unalike substrate geometry and hence due to different heat flow conditions. Although, sample 9 didn't have horizontal substrate to spread the heat across, it had taller substrate with height of 60 mm; however, considering the overall dimensions of the substrate, total volume of Type 2 sample was only 0.12 and 0.4 times that of 6 and 20 mm thick substrates from Type 1 respectively (refer Appendix – III). The fact suggests that lesser material will have reduced heat extraction rate and heat absorbing capacity than larger material volume. Heat flowing into the substrate of Type 1 samples could spread in 3 dimensional space of the substrate as shown in Figure 6.41a.

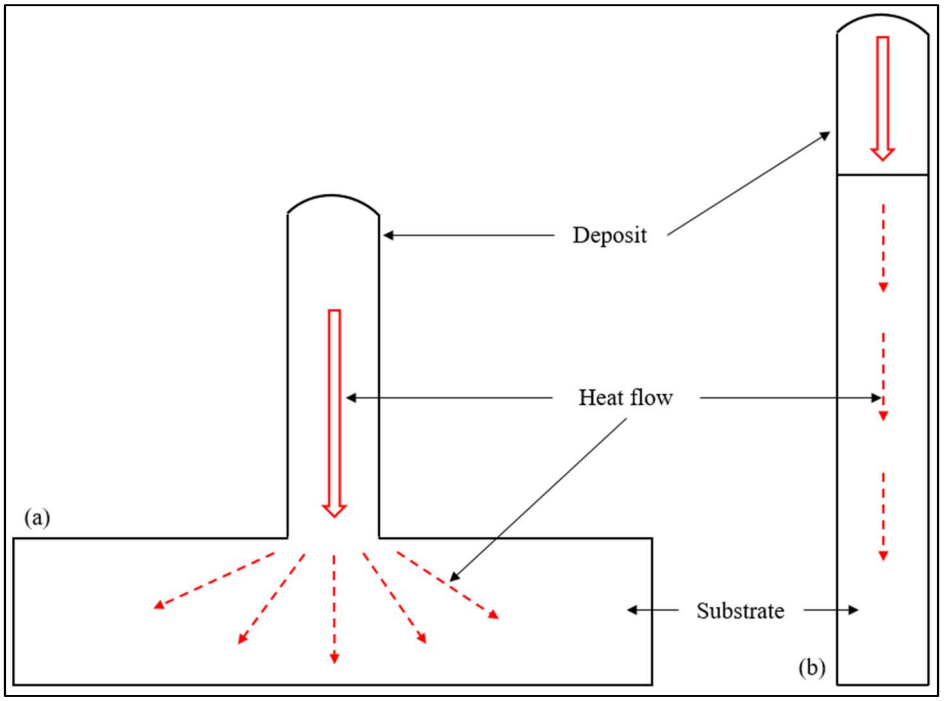

Figure 6.41 Schematic of heat flow in Type 1 and Type 2 samples.

Heat conduction is also possible from the bottom surface of a substrate having larger area to the metallic platform to a certain extend. Area of bottom surface of Type 1 samples was 18750 mm^2 (Please refer Appendix – III for area calculations). Also, area of the substrate available for heat convection to the atmosphere was 29750 and 22050 mm^2 for 20 and 6 thick substrate samples respectively. Considering Type 2 sample, heat flow remained restricted only in one direction that is from deposit at the top towards the bottom of substrate as shown in Figure 6.41b. Due to geometry, three dimensional heat flow in a substrate is not possible in Type 2 samples that is major restriction for heat extraction from deposit. Also, comparatively less area (750 mm^2) remained in contact with metallic platform which was only

0.04 times Type 1 samples. Further, Type 2 sample should experience heat loss due to convection to the atmosphere with calculated area of 15720 mm^2 which was again lesser than both of Type 1 samples. The fact explains that most of the heat being transferred to the substrate get accumulated preferably at the bottom of substrate. For initial layers heat extraction from substrate could be larger increasing overall temperature of substrate, however, with increased number of depositing layers temperature of substrate would have reached substantially high reducing heat extraction rate.

It is apparent that in sample 9 maximum compressive stresses were aggregated at the substrate immediately below substrate-deposit interface similar to Type 1 samples. Both the ends of WAAM assembly, top deposit and bottom substrate, revealed tensile residual stresses. The observations suggest that the heat flow greatly influenced stress distribution. There can be two reasons which further needs to be better understood through practical and/or computation approach. Firstly, after deposition of certain number of layers, bottom substrate remained hotter than central region. The reason being only available one-directional heat conduction towards the bottom portion, continuous exposure to heat and reduced heat losses from the portion supported in heat accumulation in the bottom region. Thus, it may have observed higher positive strains. During cooling, higher contraction at the bottom helped in forming tensile stresses. Presence of tensile stresses at top and bottom portion of assembly supported in formation compressive stresses at the central part balancing the overall bending moment in the manufactured assembly. Secondly, central area representing compressive residual stresses remained close to deposit part experiencing temperature rise at every layer deposition. Temperature remains higher than experienced by the bottom region of substrate. It can be argued that irrespective of relatively larger expansion experienced due to temperature rise at the region, relatively lower stiffness and strength of the central region may have incurred balancing compressive stresses due to the presence of high tensile stresses formed at the top deposit region. Also, due to geometry of the entire assembly bending moment acted in such a way that top and bottom portion of substrate represented tensile stresses and central weak part incurred balancing compressive stresses.

6.6 Effect of interlayer temperature

Beneficial effects of raised temperature of a substrate and previously deposited layers before deposition of subsequent layer in additive manufacturing on residual stress distribution and distortion is previously debated [63,71,75,112,194]. As discussed in section 6.2.1.2, sample manufactured with less interlayer temperature (sample 7) showed higher residual stress compared to sample prepared using higher interlayer temperature (sample 8). This temperature difference affected peak tensile and compressive stress values disclosing difference of 43 and 41 MPa respectively. Hence, there was 22% and 48% stress reduction after increasing the interlayer temperature. More details about percentage of reduction of residual stresses due to increased interlayer temperature measured for deposits are given in Table 6.6.

From Table 6.6 it is clear that as the interlayer temperature was increased, peak residual stress decreased. The results are in accordance with the previous results shown by Alimardani et al. [112] and Vastola et al. [71] mentioning inverse relation between preheat temperature and residual stresses in an additively formed part. The relation reported was not only valid for wire based additive manufacturing but also for power bed processes. Average decrement in the tensile residual stress was around 20% for four sets of samples while the same sets were compared for compressive stress, average stress reduction was around 25%. It can be argued at this point that around 20% stress reduction can be obtained after

increment of the interlayer temperature from 50 to 100°C. The results presented in Table 6.6 display a close relation with the observations reported by Vastola et al. [71] in a computational approach where researchers reported reduction of around 20% of Von Mises stresses for every 50°C temperature increment.

Table 6.6 Peak residual stess values and percentage differences for deposit.

Sample number	Interlayer temperature (°C)	Peak residual tensile stress [from Table 6.5] (MPa)	Peak residual compressive stress (MPa)	Percentage reduction in residual tensile stress (%)	Percentage reduction in residual compressive stress (%)
1	50	212	47	12	17
4	100	186	39		
2	50	233	25	41	–
5	100	137	-		
3	50	215	39	15	10
6	100	182	35		
7	50	193	85	22	48
8	100	150	44		
Average % reduction				22.5	25

It was noticed that solidification of metal affects residual stress formation [75]. Liquid metal solidification and contraction is responsible for stress formation. If heat input is kept constant, the temperature of a liquid metal falling through arc reaching deposition surface can be considered approximately constant. Temperature of liquid metal is not monitored in this study. The temperature gradient between molten metal and depositing surface changes when temperature of the depositing surface changes. This drives a change in the solidification rate. As discussed earlier in methodology chapter, theoretical approach revealed that the solidification times for deposited molten metal for high heat input samples were 0.274 and 0.328 sec for 50 and 100°C interlayer temperatures respectively. For the same, liquid metal cooling rates were 2141.3 and 1640.19 °C/sec and calculated solidification rates were 20.02 and 16.76 mm/sec for 50 and 100°C respectively. This explains relatively faster solidification at the samples manufactured with low interlayer temperature. Relatively rapid solidification should induce higher residual stresses compared to slower solidification [13].

6.7 Effect of deposit height and number of layers

Sections 6.2.1.3 and 6.2.1.4 confirmed that height of deposition affects stress distribution. Effect of substrate thickness on stress distribution is explained in section 6.5. Comparing samples 1 and 4 with samples 2 and 5 respectively it can be argued that combined effect of substrate thickness and number

of layers showed difference in presence of compressive stresses as well as stress field locations. Formation of high tensile stresses in deposit is inevitable, however, its location can be varied by controlling number of layers. For sample numbers 1, 3, 4 and 6 with deposit height of around 35 mm (refer Figure 6.13, Figure 6.15, Figure 6.16 and Figure 6.18) maximum tensile stress was observed at around 25 mm deposit height and for sample numbers 2 and 5 having around 18 mm deposit height maximum tensile stress was around 7-8 mm deposit height (refer Figure 6.14 and Figure 6.17). The fact indicates that smaller deposition height suppressed while taller deposits raised the location of high tensile stress area. In another words, irrespective of the deposit height, peak tensile stress was concentrated at around 10 mm distance from the top of a deposit. Additionally, fewer layer samples did not reveal presence of compressive stresses in deposit opposed to increased layer samples. A small region of compressive stress was only at the very top portion of deposit with roughly 2 mm height.

Chapter 7: Conclusions and Recommendations for Future Work

The current work explored influences of metal deposition parameters imposed during wire arc additive manufacturing (WAAM) on porosity and hydrogen dissolution, microstructure evolution, and residual stress distribution of aluminium. A new concept of interlayer-temperature that is fixed temperature maintenance for each layer deposition was introduced for its possible effects. After obtaining results and thoughtful discussions in Chapter 4 to 6, the current chapter provides important conclusions. The conclusions are subdivided as per the objectives of the work defined in Chapter 1. Further, this chapter recommends the future work in line with this study that will support in extending knowledge related to the introduced concept of interlayer temperature.

7.1 Porosity related

1. Samples processed with pulsed-MIG and cold metal transfer (CMT) showed an appreciable difference in pore count, pore volume and hydrogen dissolution characteristics highlighting pulsed-MIG hotter process than CMT. Continuous ignited arc of pulsed-MIG method showed increased overall energy, hotter deposit, higher arc penetration and lower cooling and solidification rates opposed to that of CMT technique which possessed high frequency oscillating motion of feed wire and arc on-off effects. These variations affected the hydrogen absorption, coalescence, pore formation and pore distribution.
2. Both pulsed MIG and CMT processes showed majority of small pores (0.11–0.20 mm diameter). Medium and large pores were relatively more in pulsed-MIG. Rapid reduction in temperature and increased solidification rate by CMT resulted into lesser absorption of hydrogen compared to pulsed-MIG, thus showed lesser pore count and overall pore volume fraction. Overall temperature increment of deposit was higher in pulsed-MIG that supported in coalescence of atomic hydrogen forming larger pores compared to CMT. Pulsed-MIG always showed higher pore count and overall pore volume fraction compared to CMT when similarly processes samples were compared.
3. Increased number of pores were present at the interlayer region compare to other parts of layer. A distinct band was pronounced in CMT samples than pulsed-MIG. Less penetration effect of CMT technique could be responsible for clear band formation. Drastic solidification rates encountered at solid-liquid interface while depositing liquid metal on previously solidified layer is the probable reason. Pore banding adversely affected tensile properties in built direction than torch travel direction due to the multiple occurrence after specific distance that is the layer height.

4. Comparatively, lower percentage of dissolved hydrogen was retained in solid solution by pulsed-MIG than CMT. Hotter and larger melt pool in pulsed-MIG helped in absorption of higher hydrogen and promoted atomic hydrogen movement in solid aluminium that supported in atomic hydrogen coalescence, finally forming pores. Therefore, more pore formation consumed more dissolved hydrogen in pulsed-MIG leaving behind lesser hydrogen in solid solution.
5. For processing conditions of low heat content that is low interlayer-temperature, low heat input and longer interlayer-dwell time control methods, pulsed-MIG showed higher total pore volume fraction compare to high heat processing conditions that is high interlayer-temperature, high heat input and shorter interlayer-dwell time. On the other hand, CMT showed a reverse trend. High heat condition of Pulsed-MIG enhanced hydrogen pore escape showing reduced pores. On the contrary, low heat CMT with low heat content had reduced hydrogen movement, forming relatively less pores and increased dissolved hydrogen in solid aluminium.

7.2 Microstructure related

1. Samples prepared with 50°C interlayer-temperature showed narrower and taller deposits compared with 100°C sample. This was due to the lower viscosity, higher spread of liquid aluminium and slower solidification encountered at 100°C interlayer-temperature.
2. Fine equiaxed grains were predominantly present at every interlayer region. This could be attributed to the number of forces acting on solidifying metal and absence of even conditions for metal solidification at solid-liquid interface.
3. The top layer of a multilayer wall deposition invariably possessed equiaxed grains; smaller for 50°C interlayer-temperature and larger for 100°C. Grain size was inversely proportional to the temperature difference between melting point and interlayer-temperature.
4. On a dimensional scale, there was no large variation in geometry of samples processed with 50°C and 100°C interlayer-temperatures; however, for manufacturing of large samples the fact cannot be ignored.
5. Grains produced by CMT process were smaller than pulsed-MIG for comparable conditions at any position in a deposit. This was the result of controlled metal deposition, faster solidification and cooling rate offered by CMT process.
6. Larger grains were observed for high heat input and interlayer-temperature samples than low heat input and interlayer-temperature samples. This was due to the temperature raise encountered at the high heat input and interlayer-temperature samples that lowered solidification rate providing increased time for grain growth.
7. In transverse direction of torch travel grains were columnar for pulsed-MIG while they were approximately equiaxed for CMT. In longitudinal direction of torch travel, grains were columnar not only for pulsed-MIG but also for CMT which is not discussed earlier. Speed of torch travel and single directional heat flow contributed for the formation of columnar grains in CMT. Higher heat content and heat flow in pulsed-MIG process supported columnar grain formation visible in transverse and longitudinal plane to torch travel.
8. The slowest cooling and solidification rate was reported for shorter interlayer-dwell-time that is 30 seconds, method for layer numbers above 10 in pulsed-MIG technique. In case of shorter

interlayer-dwell-time, heat addition after fixed time interval did not dissipate to the required extend showing heat built up raising interlayer-temperature of deposit higher for every new depositing layer.

9. Irrespective of metal deposition condition, temperature of at least top two layers was raised above the recrystallisation temperature of the alloy affecting overall grain formation and growth. The effect was pronounced in pulsed-MIG, could be the reason for the formation of columnar grains as discussed earlier
10. Low heat input samples with smaller grains showed relatively higher tensile strength than high heat input samples having larger grains in pulsed MIG. Horizontal tensile samples (longitudinal to torch travel direction) showed higher tensile strength than vertical tensile samples (transverse to torch direction). Multiple occurrence of interlayer regions with porosity and incongruent microstructure and presence of columnar grains in built direction were responsible for lower tensile strength of vertical samples. Relatively higher number of grain boundaries in horizontal samples supported in increased tensile properties. Also, volatile element Mg, the main strengthening element in alloy 5183, loss in high heat condition found lowering the tensile strength.
11. Grain growth at interlayer region was witnessed for high heat condition of pulsed-MIG suggesting possibility of formation of epitaxial grains. Uncommon phenomena observed in WAAM of aluminium suggested a threshold heat content that may drive epitaxial grain growth.

7.3 Residual stress related

1. Substrate geometry, number of layers that is deposit height, interlayer-temperature and heat input appreciably affected the residual stresses in a WAAM part.
2. Deposit part showed majority tensile stresses while compensating compressive stresses were accumulated at the substrate. Tensile stress formation was attributed to the liquid metal experiencing contraction during solidification. A substrate of WAAM part under restricted movement possessed counter compressive stresses balancing the formed tensile stresses.
3. Tensile residual stresses with magnitude over yield strength of alloy 5183 were found in the deposit. Origin of high strain due to repeated cycles of thermal expansion and contraction in aluminium could be responsible for the presence of high magnitude residual stresses.
4. For all samples with deposit thickness around 35 mm, high magnitude and peak tensile residual stresses were concentrated near top region. Active bending moment shifted the high magnitude tensile stresses at the top of deposit where shape and size of the part contributed to the major extent.
5. Thicker substrates showed tensile stresses near deposit and compressive in rest part, however, thinner substrate showed compressive stresses concentrated at extreme ends and majority of central portion showed tensile stresses. The difference in stiffness and heat flow characteristics offered by thick and thick substrates in relation with positive and negative strains as a result of temperature variation and active bending moment controlled stress variation. Temperature rise near deposit area at thin substrate, thus strain, was higher than thick substrate that controlled stress distribution.

6. Hardness values found increased with increasing tensile as well compressive residual stresses. The increased strain at high stress regions could have provided increased resistance for indenter penetration in to the deposit material.

7.4 Recommendations for Future Work

In light of the current findings on porosity and hydrogen dissolution [149,195], microstructural investigations and residual stress understanding related with WAAM of aluminium; the author would like to propose the following tasks as a future continuation of this work:

1. Author proposes a computational approach to understand the effect of variation of interlayer-temperature, heat input, and interlayer-dwell-time on microstructural variations. This is for the better understanding of grain growth in CMT which showed columnar grains similar to pulsed-MIG. Also, computational study of high heat samples from pulsed-MIG process that showed epitaxial grain growth similar to commonly found in Ti-6Al-4V alloy is recommended.
2. The presence of similar to epitaxial grain growth in pulsed-MIG high heat samples can be further chased with thermo-kinetics and mathematical approach. Forming of epitaxial grains due to application of heat above the threshold value of that material will be interesting and important field of study that may reveal material's fundamental property to react to the heat flow and may enlighten the basics of columnar grain growth.
3. Formation of nearly equiaxed fine grains at the interlayer region and columnar grains through layer thickness is not fully understood which may need a thermodynamic and thermo-kinetics approach.
4. Effect of interlayer-temperature on dimensions of a large structure need to be investigated to avoid major dimensional variations from the intended shape.
5. Loss of elemental Mg at each layer for different interlayer temperatures would highlight the effect of repeated heat application on Mg content ultimately affecting mechanical properties.
6. As more than 90% of absorbed hydrogen remains dissolved in solid solution of aluminium alloy 5183, the similar study can be extended to the cast and weld products. Hydrogen coalescence and pore formation during high temperature application of the formed products could be crucial.
7. Materials behaviour under different loading conditions such as uniaxial and multiaxial loads needs further understanding. The fact interfered in study and understanding of residual stresses.
8. A relation between residual stress and hardness at the location of indenter penetration needs further investigation.
9. Computer simulation approach could strongly support in fundamental understanding of residual stress distribution and profound effect of other deposition variables such as substrate dimensions and deposit height and overall shape. This could allow increased flexibility for deposition parameters.
10. For residual stress study, distortion measurement was not considered. It would be appropriate to consider distortion measurements and correlate with residual stresses along with the consideration of parametric effects.

Appendix – I

Calculations for dissolved hydrogen in sample C-LH-T2 –

(1) Total volume of sample measured by X-CT scan = 1440 mm^3
Mass of sample can be calculated such as –
Mass = density x volume
= 2.7 x 10^{-3} (g/mm^3) x 1440 mm^3
= 3.888 g

(2) Total volume of the pores found in 1440 mm^3 (3.888 g) of samples volume = 0.44 mm^3

(3) Weight of the samples tested for dissolved hydrogen = 0.402 g
Thus, corresponding volume of the pores in samples of weight 0.402 g can be calculated as –
= 0.402 (g) x 0.44 (mm^3) / 3.888 (g) = 0.04549 mm^3

(4) Total hydrogen detected after dissolved hydrogen test 0.834 ppm
ppm to ml conversion can be as follows –
1 ppm = 1.12 (ml) / 100 (g)
Thus, 0.834 ppm are –
= 0.834 (ppm) x 1.12 (ml / 100 g) / 1 (ppm) = 0.93408 ml / 100 g
Hence, 0.93408 ml of hydrogen per 100 g of metal.

(5) Weight of the samples for dissolved hydrogen test was 0.402 g.
Thus, total hydrogen for 0.402 g of metal can be calculated as –
= 0.93408 (ml) x 0.402 (g) / 100 (g) = 0.003755 ml
Hence, 0.402 g of tested samples showed 0.003755 ml (375.5 x 10^{-5} ml) of total detected dissolved hydrogen.

(6) From point (3), we know that 0.402 g of samples showed 0.04549 mm^3 of pore volume. Here we are assuming that all the pores are completely filled with hydrogen.
Therefore, converting pore volume from mm^3 to ml, we get –
= 0.04549 (mm^3) = 4.549 x 10^{-5} (ml)
Hence, in a sample of weight 0.402 g with 0.04549 mm^3 of pore showed 4.549 x 10^{-5} ml of hydrogen.

(7) From point (5) we know that total hydrogen in sample was 375.5 x 10^{-5} ml.
From point (6) it was clear that hydrogen in the pore was 4.549 x 10^{-5} ml.
Thus, dissolved hydrogen can be calculated as –

= (375.5 – 4.549) x 10^{-5}

= 370.951 x 10^{-5} ml

Dissolved hydrogen in the sample was 0.00370951 ml (370.951 x 10^{-5} ml)

(8) Percentage of dissolved hydrogen with respect to total hydrogen in sample –

= (370.951 x 10^{-5}) / (375.5 x 10^{-5}) x 100

= 98.78 %

Thus, samples C-LH-T2 showed 98.78% of dissolved hydrogen and 1.22% of hydrogen in pores.

Similar calculations were made for remaining the samples. The obtained values of dissolved hydrogen are tabulated in Table A.

Table A Details of dissolved hydrogen values samples wise.

Samples ID	**Weight of samples consumed in dissolved hydrogen test (g)**	**Total detected hydrogen in sample (ml)**	**Expected total hydrogen in samples of 100 g (ml)**	**Volume of hydrogen at pores (%)**	**Dissolved hydrogen volume in solid sample (%)**
C-LH-T1	0.402	0.003755	0.934	1.22	98.78
P-LH-T1	0.5659	0.006293	1.112	5.06	94.94
C-LH-t2	0.2899	0.003311	1.142	1.25	98.75
P-LH-t2	0.5015	0.007021	1.4	4.48	95.52

Appendix – II

Cooling rate

For the calculations of cooling rate as per Eq. 6, following values were used as materials properties of wire composition of 5183 wherever possible. Otherwise, properties of wrought plate composition 5083 was considered as a closest chemical composition to 5183 alloy.

k = 205 J/m-s-°K [127,135,196]

Tc = 911 °K for wire composition of 5183 taken from the equilibrium diagram [196,197]

To = 323 and 373 °K as per interlayer-temperature maintained

$Hnet$ = 155 × 10^3 and 350 × 10^3 J/m for low and high heat input respectively. The values were calculated as described in porosity chapter.

Solidification time

For the calculations of solidification time as per Eq. 7, following values were used as materials properties of wire composition of 5183 wherever possible. Otherwise, properties of wrought plate composition 5083 was considered as a closest chemical composition to 5183 alloy.

k = 205 J/m-s-°K [127,135,196]

To = 323 and 373 °K as per interlayer-temperature maintained

$Hnet$ = 155 × 10^3 and 350 × 10^3 J/m for low and high heat input respectively. The values were calculated as described in porosity chapter.

Ĺ = 1.179 × 10^9 J/m^3 (Calculations are as per following equation) [135,196]

$$\acute{L} = \frac{Latent\ heat}{Molar\ volume}$$

$$\acute{L} = \frac{10.79\ kJ/mol}{10^{-5}\ m^3/mol}$$

ρ = 2700 kg/m^3 [127,196]

C = 880 J/kg-K

Tm = 911 °K for wire composition of 5183 taken from the equilibrium diagram [196,197]

Solidification rate

A common approach was adopted for the calculation of solidification rate. Deposition characteristics of pulsed MIG confirms layer height and penetration around 5.5 mm. The value depends upon number of factors such as current, voltage, torch travel speed; however, considering values used in this study, total metal penetration and metal build up is around 5.5 mm. For better comparison, a common values is considered.

Therefore, calculations for high heat input low interlayer-temperature follows as –

$$Solidification\ rate\ (mm/s) = \frac{Distance\ (mm)}{solidification\ time\ (seconds)}$$

$$Solidification\ rate = \frac{5.5}{0.3382}$$

$$Solidification\ rate = 16.26\ mm/s$$

Appendix – III

Calculations for hardness conversion

Hardness values in Hv can be expressed in kg/mm^2 by following conversion as –

1 Hv = 1 kg/mm^2

This further can be converted into MPa by following the conversion factor –

1 kg/mm^2 = 9.806 MPa [198]

Therefore, 76.5 Hv = 76.5 kg/mm^2

Hence 76.5 x 9.806 = 715.15 MPa

Following the conversion factor, hardness is expressed in MPa as in Table B.

Table B Average hardness of deposits samplewise.

Sample no.	**1**	**2**	**3**	**4**	**5**	**6**	**7**	**8**
Average hardness of deposit expressed in Hv	76.5	78.7	77.1	78.5	76.1	79.5	75.3	76.9
Average hardness of deposit expressed in MPa	750.1	771.7	756.0	769.7	746.2	779.5	738.1	754.0

Calculations for yield strength from hardness values

$$\sigma_y = \hat{H}/3 \qquad \text{Eq. (11)}$$

where σ_y is yield strength and $\hat{H}$ is hardness.

Table C Yield strengths calculated from hardness.

Sample no.	**1**	**2**	**3**	**4**	**5**	**6**	**7**	**8**
Average hardness of deposit expressed in MPa	750.1	771.7	756.0	769.7	746.2	779.5	738.1	754.0
Yield strength MPa	250	257.2	252	256.5	248.7	259.8	246	251.3

Calculations for possibility check of high residual stresses

A condition for the presence of residual stress with magnitude close to yield strength of a material is as follows –

$$\alpha (T_s - T_0) \geq \sigma_y / E \text{ [181]} \quad \text{Eq. (12)}$$

where α is coefficient of thermal expansion, T_s is softening temperature usually taken at which yield strength drops to 10% of its ambient temperature (refer Figure 6.34), T_0 is ambient or interpass/layer temperature, σ_y is yield strength at ambient or interpass/layer temperature and E is young's modulus.

Case 1 – Calculations for 50°C interlayer temperature

From Eq. 12,

$\alpha (T_s - T_0) = 26 \times 10^{-6} \times (425 - 50)$
$\alpha (T_s - T_0) = 26 \times 375 \times 10^{-6}$
$\alpha (T_s - T_0) = 0.00975$
And,
$\sigma_y / E = 145 / 70000$
$\sigma_y / E = 0.002$

This satisfies the Eq. 12 as $0.00975 > 0.002$

Case 2 – Calculations for 100°C interlayer temperature

From Eq. 12,

$\alpha (T_s - T_0) = 26 \times 10^{-6} \times (425 - 100)$
$\alpha (T_s - T_0) = 26 \times 325 \times 10^{-6}$
$\alpha (T_s - T_0) = 0.00845$
And,
$\sigma_y / E = 145 / 70000$
$\sigma_y / E = 0.002$

This satisfies the Eq. 12 as $0.00845 > 0.002$

Calculations for volumetric expansion

Expected volumetric expansion of a single layer a deposited part can be calculated from formula –

$$\Delta \nu / \nu_0 = \alpha \Delta T \text{ [198]}$$
$$\text{that is } (\nu_f - \nu_0) / \nu_0 = \alpha (T_0 - T_f) \text{ [198]} \quad \text{Eq. (13)}$$

where ν_f and ν_0 are final and initial volumes, T_0 and T_f are initial and final temperatures and α is coefficient of thermal expansion.

$\alpha = 70 \times 10^{-6} K^{-1}$ (adopted from [127])
ν_1 = volume of a single layer deposited with low heat input can be calculated as –
length = 100 mm
width = 8 mm
height = 2.3 mm (35 mm / 15 layers)
volume (ν) = length x width x height = 1840 mm^3
ν_2 = volume of a single layer deposited with high heat input can be calculated as –
length = 100 mm

width = 9.5 mm
height = 2.2 mm (33 mm / 15 layers)
volume (ν) = length x width x height = 2090 mm^3

Therefore, ν = 1840 mm^3 and 2090 mm^3 for low and high heat input manufactured parts respectively.

For the alloy Al-Mg with wire 5183 composition, liquidus temperature is around 638°C that is 911 K.

Case 1 – Calculations for 50°C interlayer temperature and low heat input

Change in dimensions due to rise in temperature from 50 to 638°C

T_0 = 50°C
T_f = 638°C

From Eq. 13,

$(\nu_f - 1840) / 1840 = 70 \times 10^{-6} \times (638 - 50)$
$\nu_f = (70 \times 10^{-6} \times 588 \times 1840) + 1840$
$\nu_f = 75.734 + 1840$
$\nu_f = 1915.73\ mm^3$

Hence, expansion of volume was 75.73 mm^3

Change in dimensions due to reduction in temperature from 638 to 50°C

T_f = 50°C
T_0 = 638°C
From Eq. 13,
$(\nu_f - 1840) / 1840 = 70 \times 10^{-6} \times (50 - 638)$
$\nu_f = [70 \times 10^{-6} \times (-588) \times 1840] + 1840$
$\nu_f = - 75.734 + 1840$
$\nu_f = 1764.266\ mm^3$

Hence, contraction of volume was 75.73 mm^3

Case 2 – Calculations for 100°C interlayer temperature and low heat input

Change in dimensions due to rise in temperature from 100 to 638°C

T_0 = 100°C
T_f = 638°C
From Eq. 13,
$(\nu_f - 1840) / 1840 = 70 \times 10^{-6} \times (638 - 100)$
$\nu_f = (70 \times 10^{-6} \times 538 \times 1840) + 1840$
$\nu_f = 69.2944 + 1840$
$\nu_f = 1909.29\ mm^3$

Hence, expansion of volume was 69.29 mm^3

Change in dimensions due to reduction in temperature from 638 to 100°C

$T_f = 100°C$
$T_0 = 638°C$

From Eq. 13,

$(\nu_f - 1840) / 1840 = 70 \times 10^{-6} \times (100 - 638)$
$\nu_f = [70 \times 10^{-6} \times (-538) \times 1840] + 1840$
$\nu_f = - 69.2944 + 1840$
$\nu_f = 1770.7\ mm^3$

Hence, contraction of volume was 69.29 mm^3

Case 3 – Calculations for 50°C interlayer temperature and high heat input

Change in dimensions due to rise in temperature from 50 to 638°C

$T_0 = 50°C$
$T_f = 638°C$

From Eq. 13,

$(\nu_f - 2090) / 2090 = 70 \times 10^{-6} \times (638 - 50)$
$\nu_f = (70 \times 10^{-6} \times 588 \times 2090) + 2090$
$\nu_f = 86.0244 + 2090$
$\nu_f = 2176.0244\ mm^3$

Hence, expansion of volume was 86.02 mm^3

Change in dimensions due to reduction in temperature from 638 to 50°C

$T_f = 50°C$
$T_0 = 638°C$

From Eq. 13,

$(\nu_f - 2090) / 2090 = 70 \times 10^{-6} \times (50 - 638)$
$\nu_f = [70 \times 10^{-6} \times (-588) \times 2090] + 2090$
$\nu_f = - 86.0244 + 2090$
$\nu_f = 2003.97\ mm^3$

Hence, contraction of volume was 86.02 mm^3

Case 4 – Calculations for 100°C interlayer temperature and high heat input

Change in dimensions due to rise in temperature from 100 to 638°C

$T_0 = 100°C$

$T_f = 638°C$

From Eq. 13,

$(\nu_f - 2090) / 2090 = 70 \times 10^{-6} \times (638 - 100)$

$\nu_f = (70 \times 10^{-6} \times 538 \times 2090) + 2090$

$\nu_f = 78.7094 + 2090$

$\nu_f = 2168.7094\ mm^3$

Hence, expansion of volume was 78.7 mm^3

Change in dimensions due to reduction in temperature from 638 to 100°C

$T_f = 100°C$

$T_0 = 638°C$

From Eq. 13,

$(\nu_f - 2090) / 2090 = 70 \times 10^{-6} \times (100 - 638)$

$\nu_f = [70 \times 10^{-6} \times (-538) \times 2090] + 2090$

$\nu_f = -78.7094 + 2090$

$\nu_f = 2011.2904\ mm^3$

Hence, contraction of volume was 78.7 mm^3

From above calculations, total change in dimensions assuming 100 mm wall length is tabulated in Table D.

Table D Total volumetric dimensional changes due to thermal cycles.

Control conditions		**Expansion**		**Contraction (mm^3)**		**Total change in dimensions (mm^3)**	
		mm^3	**%**	**mm^3**	**%**	**mm^3**	**%**
50°C interlayer temperature	Low heat input	75.734	4.11	75.734	4.11	151.468	8.22
	High heat input	86.024	4.11	86.024	4.11	172.048	8.22
100°C interlayer temperature	Low heat input	69.294	3.76	69.294	3.76	138.588	7.52
	High heat input	78.709	3.76	78.709	3.76	157.418	7.52

Calculations for volumetric percentage strain

Percentage volumetric strain can be calculated using the formula –

$$\varepsilon = \alpha \Delta \check{T} \text{ [13]} \qquad \text{Eq. (14)}$$

where ε is strain, α is volumetric coefficient of thermal expansion and $\Delta \check{T}$ is temperature change.

Case 1 – Calculations for 50°C interlayer temperature

From Eq. 14

$\varepsilon = 70 \times 10^{-6} \times (638 - 50)$
$\varepsilon = 70 \times 588 \times 10^{-6}$
$\varepsilon = 0.0411$
$\% \varepsilon = 4.11$

Case 2 – Calculations for 100°C interlayer temperature

From Eq. 14

$\varepsilon = 70 \times 10^{-6} \times (638 - 100)$
$\varepsilon = 70 \times 538 \times 10^{-6}$
$\varepsilon = 0.0376$
$\% \varepsilon = 3.76$

Calculations for length based percentage strain

Percentage linear strain can be calculated using the formula –

$$\varepsilon = \alpha \Delta \check{T} \text{ [13]} \qquad \text{Eq. (15)}$$

where ε is strain, α is linear coefficient of thermal expansion and $\Delta \check{T}$ is temperature change.

$\alpha_{al} = 23.5 \times 10\text{-}^{6} K^{-1}$ (for aluminium [127])
$\alpha_{st} = 12 \times 10^{-6}$ (for steel [127])

Case 1 – Calculations for 50°C interlayer temperature

Aluminium,

$\varepsilon = 23.5 \times 10^{-6} \times (638 - 50)$
$\varepsilon = 23.5 \times 588 \times 10^{-6}$
$\varepsilon = 0.01381$
$\% \varepsilon = 1.381$

Steel,

$\varepsilon = 12 \times 10^{-6} \times (638 - 50)$
$\varepsilon = 12 \times 588 \times 10^{-6}$
$\varepsilon = 0.007056$
$\% \varepsilon = 0.705$

Case 2 – Calculations for 100°C interlayer temperature

Aluminium,

$\varepsilon = 23.5 \times 10^{-6} \times (638 - 100)$

$\varepsilon = 23.5 \times 538 \times 10^{-6}$

$\varepsilon = 0.012643$

$\% \varepsilon = 1.264$

Steel,

$\varepsilon = 12 \times 10^{-6} \times (638 - 100)$

$\varepsilon = 12 \times 538 \times 10^{-6}$

$\varepsilon = 0.006456$

$\% \varepsilon = 0.645$

Table E Percentage strain comparison in aluminium and steel.

Control condition	Material	% Strain
50°C interlayer temperature	Aluminium	1.381
	Steel	0.705
100°C interlayer temperature	Aluminium	1.264
	Steel	0.645

Substrate volume calculation

Type 1 samples

Case 1 – 6 mm thin substrate

Volume (v) = length x width x height

= 150 x 125 x 6 mm^3

= 112500 mm^3

Case 2 – 20 mm thick substrate

Volume (v) = length x width x height

= 150 x 125 x 20 mm^3

= 375000 mm^3

Type 2 sample

Volume (v)= length x width x height

= 125 x 6 x 60 mm^3

= 45000 mm^3

Surface area calculation

Type 1 samples

Case 1 – 6 mm thick substrate

Total surface area (TSA) = 2(length x width) + 2(width x height) + 2(height x length)

= 2(150 x 125) + 2(125 x 6) + 2(6 x 150)

= 40800 mm^2

Surface area in contact with metallic platform (SAP) = length x width

= 150 x 125

= 18750 mm^2

Surface area in contact with atmosphere (SAA) = TSA – SAP

= 40800 – 18750

= 22050 mm^2

Case 2 – 20 mm thick substrate

Total surface area (TSA) = 2(length x width) + 2(width x height) + 2(height x length)

= 2(150 x 125) + 2(125 x 20) + 2(20 x 150)

= 48500 mm^2

Surface area in contact with metallic platform (SAP) = length x width

= 150 x 125

= 18750 mm^2

Surface area in contact with atmosphere (SAA) = TSA – SAP

= 48500 – 18750

= 22050 mm^2

Type 2 sample

Total surface area (TSA) = 2(length x width) + 2(width x height) + 2(height x length)

= 2(125 x 6) + 2(6 x 60) + 2(60 x 125)

= 17220 mm^2

Surface area in contact with metallic platform (SAP) = length x width

= 125 x 6

= 750 mm^2

Surface area in contact under deposit (SAD) = length x width

= 125 x 6

= 750 mm^2

Surface area in contact with atmosphere (SAA) = TSA – (SAP + SAD)

= 48500 – (750 + 750)

= 15720 mm^2

References

[1] Ford S, Despeisse M. Additive manufacturing and sustainability: an exploratory study of the advantages and challenges. J Clean Prod 2016;137:1573–87. doi:10.1016/j.jclepro.2016.04.150.

[2] Thompson MK, Moroni G, Vaneker T, Fadel G, Campbell RI, Gibson I, et al. Design for Additive Manufacturing: Trends, opportunities, considerations, and constraints. CIRP Ann - Manuf Technol 2016;65:737–60. doi:10.1016/j.cirp.2016.05.004.

[3] Derekar KS. A review of wire arc additive manufacturing and advances in wire arc additive manufacturing of aluminium. Mater Sci Technol (United Kingdom) 2018;34:895–916. doi:10.1080/02670836.2018.1455012.

[4] Hascoet JY, Karunakaran KP, Marya S. Additive Manufacturing Viewed from Material Science: State of the Art & Fundamentals. Mater Sci Forum 2014;783–786:2347–52. doi:10.4028/www.scientific.net/MSF.783-786.2347.

[5] Labonnote N, Rønnquist A, Manum B, Rüther P. Additive construction: State-of-the-art, challenges and opportunities. Autom Constr 2016;72:347–66. doi:10.1016/j.autcon.2016.08.026.

[6] Roy R, Stark R, Tracht K, Takata S, Mori M. Continuous maintenance and the future – Foundations and technological challenges. CIRP Ann - Manuf Technol 2016;65:667–88. doi:10.1016/j.cirp.2016.06.006.

[7] Gao W, Zhang Y, Ramanujan D, Ramani K, Chen Y, Williams CB, et al. The status, challenges, and future of additive manufacturing in engineering. Comput Des 2015;69:65–89. doi:10.1016/j.cad.2015.04.001.

[8] Frazier WE. Metal additive manufacturing: A review. J Mater Eng Perform 2014;23:1917–28. doi:10.1007/s11665-014-0958-z.

[9] America Makes & ANSI Additive Manufacturing Standardization Collaborative (AMSC). Standardization Roadmap for Additive Manufacturing 2017:Public Draft.

[10] Lloyd's Register Foundation. Roadmap for additive manufacturing - Safe adoption of additive manufacturing for safety-critical assets 2016;2.

[11] World Aluminum. Int Alum Inst 2020. http://www.world-aluminium.org/statistics/ (accessed 15 January 2020).

[12] Helms, Hinrich; Krack J. Energy savings by light - weighting - 2016 Update 2016;49:0–69.

[13] Totten G, Scott M, editors. Handbook of Aluminum - Vol 1 Physical Metallurgy and Processes. US: Marcel Dekker Inc; 2003.

[14] Mathers G. The welding of aluminium and its alloys. Cambridge UK: Woodhead publishing limited, Cambridge England; 2002. doi:10.1533/9781855737631.1.

[15] Yousefian P, Tiryakioğlu M. Pore Formation During Solidification of Aluminum: Reconciliation of Experimental Observations, Modeling Assumptions, and Classical Nucleation Theory. Metall Mater Trans A Phys Metall Mater Sci 2018;49:563–75. doi:10.1007/s11661-017-4438-6.

[16] Horgar A, Fostervoll H, Nyhus B, Ren X, Eriksson M, Akselsen OM. Additive manufacturing using WAAM with AA5183 wire. J Mater Process Technol 2018;259:68–74. doi:10.1016/j.jmatprotec.2018.04.014.

[17] Baker R. Method of Making Decorative Articles. US Pat 1920:1–3.

[18] Eschholz OH. Ornamental arc welding 1920:1–3.

[19] Ujiie A. United States Patent. US3558846A, 1971.

[20] Donoghue J, Antonysamy AA, Martina F, Colegrove PA, Williams SW, Prangnell PB. The effectiveness of combining rolling deformation with Wire-Arc Additive Manufacture on β-grain refinement and texture modification in Ti-6Al-4V. Mater Charact 2016;114:103–14. doi:10.1016/j.matchar.2016.02.001.

[21] Martina F, Colegrove PA, Williams SW, Meyer J. Microstructure of Interpass Rolled Wire + Arc Additive Manufacturing Ti-6Al-4V Components. Metall Mater Trans A Phys Metall Mater Sci 2015;46:6103–18. doi:10.1007/s11661-015-3172-1.

[22] Song Y-A, Park S, Chae S-W. 3D welding and milling: part II—optimization of the 3D welding process using an experimental design approach. Int J Mach Tools Manuf 2005;45:1063–9. doi:10.1016/j.ijmachtools.2004.11.022.

[23] Nobel P. Method and apparatus for electric arc welding. US1898060A, 1919.

[24] Carpenter O, Kerr H. Method and apparatus for metal coating metal pipes by electric fusion. US2427350A, 1943.

[25] White W. Pressure roller and method of manufacture. US3156968A, 1962.

[26] Brandi H, Luckow H. Method of making large structural one-piece parts of metal, particularly one-piece shafts. US3985995A, 1976. doi:10.1145/634067.634234.

[27] Hitoshi T. Production of powder of metal or nonmetal or alloy thereof. JP19830003867 19830113, 1984.

[28] Ayres P, Edmonds D, Hartwig D, Merker D, Weber C. Method and apparatus for controlling weld bead shape to eliminate microfissure defects when shape melting austenitic materials. US4782206A, 1987.

[29] Doyle T, Ryan P. Method and apparatus for automatic vapor cooling when shape melting a component. US4857694A, 1988.

[30] Shockey H. Machine for reclaiming worn brake drums. US1886503A, 1930.

[31] Muscato G, Spampinato G, Cantelli L. A closed loop welding controller for a rapid manufacturing process. IEEE Int Conf Emerg Technol Fact Autom ETFA 2008:1080–3. doi:10.1109/ETFA.2008.4638529.

[32] Irving R. An all electroslag welded vessel. Iron Age 1970;205.

[33] Ujiie A. Process and apparatus for tripple-electrode MIG welding using short-circuit and spray-arc deposition. US3746833A, 1972. doi:10.1016/j.scriptamat.2005.10.045.

[34] K. Kussmaul, F.W. Schoch HL. High quality large components ‘“shape welded”’ by a SAW process. Weld J 1983;62:17–24.

[35] Dickens PM, Pridham MS, Cobb RC, Gibson I, Dixon MG. Rapid Prototyping Using 3-D Welding. Proc 3rd Symp Solid Free Fabr Austin, Texas, Austin, Texas: 1992, p. 280–90.

[36] Ribeiro F. Metal Based Rapid Prototyping for More Complex Shapes. Bienn Int Conf "Computer Technol Weld, Cambridge UK: The Welding Institute; 1996, p. 1–11.

[37] Zhang YM, Li P, Chen Y, Male AT. Automated system for welding-based rapid prototyping. Mechatronics 2002;12:37–53. doi:10.1016/S0957-4158(00)00064-7.

[38] Colegrove PA, Martina F, Roy MJ, Szost BA, Terzi S, Williams SW, et al. High Pressure Interpass Rolling of Wire + Arc Additively Manufactured Titanium Components. Adv Mater Res 2014;996:694–700. doi:10.4028/www.scientific.net/AMR.996.694.

[39] Martina F, Williams SW, Colegrove P. Improved microstructure and increased mechanical properties of additive manufacture produced Ti-6Al-4V by interpass cold rolling. SFF Symp

2013:490–6. doi:10.1007/s13398-014-0173-7.2.

[40] Million K, Zimmerman H. Method of preparing structural components having a symmetrically curved wall by buildup welding 1985:1–8.

[41] Piehl K. Shape welding of heavy components. Tech Berichte-Thyssen 1989;21:53–71.

[42] Spencer DJ, Dickens PM WC. Rapid prototyping of metal parts by three dimentional welding. Mech E J Eng Manuf 1998;212:175–82.

[43] McAninch M, Dale M, Marcel R. Building workpieces by deposit welding 1990;0375114:375114.

[44] Zhang YM, Chen Y, Li P, Male AT. Weld deposition-based rapid prototyping: A preliminary study. J Mater Process Technol 2003;135:347–57. doi:10.1016/S0924-0136(02)00867-1.

[45] Mehnen J, Ding J, Lockett H, Kazanas P. Design for Wire and Arc Additive Layer Manufacture. Glob Prod Dev 2011:721–7. doi:10.1007/978-3-642-15973-2.

[46] Kazanas P, Deherkar P, Almeida P, Lockett H, Williams S. Fabrication of geometrical features using wire and arc additive manufacture. Proc Inst Mech Eng Part B J Eng Manuf 2012;226:1042–51. doi:10.1177/0954405412437126.

[47] Mehnen J, Ding J, Lockett H, Kazanas P. Design study for wire and arc additive manufacture. Int J Prod Dev 2014;19:2–20. doi:10.1504/IJPD.2014.060028.

[48] Ding D, Pan Z, Cuiuri D, Li H. A tool-path generation strategy for wire and arc additive manufacturing. Int J Adv Manuf Technol 2014;73:173–83. doi:10.1007/s00170-014-5808-5.

[49] Newman ST, Zhu Z, Dhokia V, Shokrani A. Process planning for additive and subtractive manufacturing technologies. CIRP Ann - Manuf Technol 2015;64:467–70. doi:10.1016/j.cirp.2015.04.109.

[50] Venturini G, Montevecchi F, Scippa A, Campatelli G. Optimization of WAAM Deposition Patterns for T-crossing Features. Procedia CIRP 2016;55:95–100. doi:10.1016/j.procir.2016.08.043.

[51] Adinarayanappa SM, Simhambhatla S. Determination of process parameter for twin-wire weld-deposition based additive manufacturing. ASME 2014 Int Des Eng Tech Conf Compture Inf Eng Conf IDETC/CIE 2014, Buffalo, New York, USA: ASME; 2014, p. V004T06A003-V004T06A003.

[52] Yang D, Wang G, Zhang G. A comparative study of GMAW- and DE-GMAW-based additive manufacturing techniques: thermal behavior of the deposition process for thin-walled parts. Int J Adv Manuf Technol 2017;91:2175–84. doi:10.1007/s00170-016-9898-0.

[53] Somashekara MA, Suryakumar S. Studies on Dissimilar Twin-Wire Weld-Deposition for Additive Manufacturing Applications. Trans Indian Inst Met 2017;70:2123–35. doi:10.1007/s12666-016-1032-3.

[54] Yang D, He C, Zhang G. Forming characteristics of thin-wall steel parts by double electrode GMAW based additive manufacturing. J Mater Process Technol 2016;227:153–60. doi:10.1016/j.jmatprotec.2015.08.021.

[55] Li F, Chen S, Shi J, Tian H, Zhao Y. Evaluation and Optimization of a Hybrid Manufacturing Process Combining Wire Arc Additive Manufacturing with Milling for the Fabrication of Stiffened Panels. Appl Sci 2017;7:1233. doi:10.3390/app7121233.

[56] Prado-Cerqueira JL, Diéguez JL, Camacho AM. Preliminary development of a Wire and Arc Additive Manufacturing system (WAAM). Procedia Manuf 2017;13:895–902. doi:10.1016/j.promfg.2017.09.154.

[57] Qi Z, Cong B, Qi B, Sun H, Zhao G, Ding J. Microstructure and mechanical properties of double-wire + arc additively manufactured Al-Cu-Mg alloys. J Mater Process Technol 2018;255:347–

53. doi:10.1016/j.jmatprotec.2017.12.019.

[58] Wang F, Williams S, Colegrove P, Antonysamy AA. Microstructure and Mechanical Properties of Wire and Arc Additive Manufactured Ti-6Al-4V. Metall Mater Trans A 2013;44:968–77. doi:10.1007/s11661-012-1444-6.

[59] Zhang J, Wang X, Paddea S, Zhang X. Fatigue crack propagation behaviour in wire+arc additive manufactured Ti-6Al-4V: Effects of microstructure and residual stress. Mater Des 2016;90:551–61. doi:10.1016/j.matdes.2015.10.141.

[60] Zhang J, Zhang X, Wang X, Ding J, Traoré Y, Paddea S, et al. Crack path selection at the interface of wrought and wire + arc additive manufactured Ti–6Al–4V. Mater Des 2016;104:365–75. doi:10.1016/J.MATDES.2016.05.027.

[61] Zhang X, Martina F, Ding J, Wang X, Williams S. Fracture toughness and fatigue crack growth rate properties in wire + arc additive manufactured Ti-6Al-4V. Fatigue Fract Eng Mater Struct 2017;40:790–803. doi:10.1111/ffe.12547.

[62] Mughal MP, Mufti RA, Fawad H. The mechanical effects of deposition patterns in welding-based layered manufacturing. Proc Inst Mech Eng Part B J Eng Manuf 2007;221:1499–509. doi:10.1243/09544054JEM783.

[63] Mughal MP, Fawad H, Mufti RA, Siddique M. Deformation modelling in layered manufacturing of metallic parts using gas metal arc welding: Effect of process parameters. Model Simul Mater Sci Eng 2005;13:1187–204. doi:10.1088/0965-0393/13/7/013.

[64] Ding J, Colegrove P, Mehnen J, Ganguly S, Almeida PMS, Wang F, et al. Thermo-mechanical analysis of Wire and Arc Additive Layer Manufacturing process on large multi-layer parts. Comput Mater Sci 2011;50:3315–22. doi:10.1016/j.commatsci.2011.06.023.

[65] Zhao H, Zhang G, Yin Z, Wu L. Effects of interpass idle time on thermal stresses in multipass multilayer weld-based rapid prototyping. J Manuf Sci Eng Trans ASME 2013;135. doi:10.1115/1.4023363.

[66] Colegrove PA, Coules HE, Fairman J, Martina F, Kashoob T, Mamash H, et al. Microstructure and residual stress improvement in wire and arc additively manufactured parts through high-pressure rolling. J Mater Process Technol 2013;213:1782–91. doi:10.1016/j.jmatprotec.2013.04.012.

[67] Williams SW, Martina F, Addison AC, Ding J, Pardal G, Colegrove P. Wire + Arc Additive Manufacturing. Mater Sci Technol 2016;32:641–7. doi:10.1179/1743284715Y.0000000073.

[68] Somashekara MA, Naveenkumar M, Kumar A, Viswanath C, Simhambhatla S. Investigations into effect of weld-deposition pattern on residual stress evolution for metallic additive manufacturing. Int J Adv Manuf Technol 2017;90:2009–25. doi:10.1007/s00170-016-9510-7.

[69] Colegrove PA, Donoghue J, Martina F, Gu J, Prangnell P, Hönnige J. Application of bulk deformation methods for microstructural and material property improvement and residual stress and distortion control in additively manufactured components. Scr Mater 2017;135:111–8. doi:10.1016/j.scriptamat.2016.10.031.

[70] Szost BA, Terzi S, Martina F, Boisselier D, Prytuliak A, Pirling T, et al. A comparative study of additive manufacturing techniques: Residual stress and microstructural analysis of CLAD and WAAM printed Ti-6Al-4V components. Mater Des 2016;89:559–67. doi:10.1016/j.matdes.2015.09.115.

[71] Vastola G, Zhang G, Pei QX, Zhang YW. Controlling of residual stress in additive manufacturing of Ti6Al4V by finite element modeling. Addit Manuf 2016;12:231–9. doi:10.1016/j.addma.2016.05.010.

[72] Brown DW, Bernardin JD, Carpenter JS, Clausen B, Spernjak D, Thompson JM. Neutron diffraction measurements of residual stress in additively manufactured stainless steel. Mater Sci Eng A 2016;678:291–8. doi:10.1016/j.msea.2016.09.086.

[73] Martina F, Roy MJ, Szost BA, Terzi S, Colegrove PA, Williams SW, et al. Residual stress of as-deposited and rolled wire+arc additive manufacturing Ti–6Al–4V components. Mater Sci Technol (United Kingdom) 2016;32:1439–48. doi:10.1080/02670836.2016.1142704.

[74] Ghasri-Khouzani M, Peng H, Rogge R, Attardo R, Ostiguy P, Neidig J, et al. Experimental measurement of residual stress and distortion in additively manufactured stainless steel components with various dimensions. Mater Sci Eng A 2017;707:689–700. doi:10.1016/j.msea.2017.09.108.

[75] Li R, Xiong J, Lei Y. Investigation on thermal stress evolution induced by wire and arc additive manufacturing for circular thin-walled parts. J Manuf Process 2019;40:59–67. doi:10.1016/j.jmapro.2019.03.006.

[76] Almeida P, Williams S. Innovative process model of Ti–6Al–4V additive layer manufacturing using cold metal transfer (CMT). Solid Free Fabr Symp 2010:25–36.

[77] Wagiman A, Bin Wahab MS, Mohid Z, Mamat A. Effect of GMAW-CMT Heat Input on Weld Bead Profile Geometry for Freeform Fabrication of Aluminium Parts. Appl Mech Mater 2013;465–466:1370–4. doi:10.4028/www.scientific.net/AMM.465-466.1370.

[78] Cong B, Ding J, Williams S. Effect of arc mode in cold metal transfer process on porosity of additively manufactured Al-6.3%Cu alloy. Int J Adv Manuf Technol 2014;76:1593–606. doi:10.1007/s00170-014-6346-x.

[79] Cong B, Qi Z, Qi B, Sun H, Zhao G, Ding J. A Comparative Study of Additively Manufactured Thin Wall and Block Structure with Al-6.3%Cu Alloy Using Cold Metal Transfer Process. Appl Sci 2017;7:275. doi:10.3390/app7030275.

[80] Zhang C, Li Y, Gao M, Zeng X. Wire arc additive manufacturing of Al-6Mg alloy using variable polarity cold metal transfer arc as power source. Mater Sci Eng A 2018;711:415–23. doi:10.1016/j.msea.2017.11.084.

[81] Xiong J, Zhang G. Adaptive control of deposited height in GMAW-based layer additive manufacturing. J Mater Process Technol 2014;214:962–8. doi:10.1016/j.jmatprotec.2013.11.014.

[82] Xiong J, Zhang G, Zhang W. Forming appearance analysis in multi-layer single-pass GMAW-based additive manufacturing. Int J Adv Manuf Technol 2015;80:1767–76. doi:10.1007/s00170-015-7112-4.

[83] Ding D, Pan Z, Cuiuri D, Li H. A multi-bead overlapping model for robotic wire and arc additive manufacturing (WAAM). Robot Comput Integr Manuf 2015;31:101–10. doi:10.1016/j.rcim.2014.08.008.

[84] Geng H, Li J, Xiong J, Lin X, Zhang F. Geometric Limitation and Tensile Properties of Wire and Arc Additive Manufacturing 5A06 Aluminum Alloy Parts. J Mater Eng Perform 2017;26:621–9. doi:10.1007/s11665-016-2480-y.

[85] Xiong J, Yin Z, Zhang W. Forming appearance control of arc striking and extinguishing area in multi-layer single-pass GMAW-based additive manufacturing. Int J Adv Manuf Technol 2016;87:579–86. doi:10.1007/s00170-016-8543-2.

[86] Xiong J, Lei Y, Chen H, Zhang G. Fabrication of inclined thin-walled parts in multi-layer single-pass GMAW-based additive manufacturing with flat position deposition. J Mater Process Technol 2017;240:397–403. doi:10.1016/j.jmatprotec.2016.10.019.

[87] Martina F, Roy M, Colegrove P, Williams S. Residual Stress Reduction in High Pressure Interpass Rolled Wire+arc Additive Manufacturing Ti-6Al-4V Components. Solid Free Fabr Proc, Austin, Texas: 2014, p. 89–94.

[88] Honnige J, Williams S, Roy M, Colegrove P, Ganguly S. Residual Stress Characterization and Control in the Additive Manufacture of Large Scale Metal Structures. Mater reseach Proc, 2016, p. 455–60. doi:10.21741/9781945291173-77.

[89] Gu J, Ding J, Williams SW, Gu H, Bai J, Zhai Y, et al. The strengthening effect of inter-layer cold working and post-deposition heat treatment on the additively manufactured Al-6.3Cu alloy. Mater Sci Eng A 2016;651:18–26. doi:10.1016/j.msea.2015.10.101.

[90] Gu J, Ding J, Williams SW, Gu H, Ma P, Zhai Y. The effect of inter-layer cold working and post-deposition heat treatment on porosity in additively manufactured aluminum alloys. J Mater Process Technol 2016;230:26–34. doi:10.1016/j.jmatprotec.2015.11.006.

[91] Gu J, Wang X, Bai J, Ding J, Williams S, Zhai Y, et al. Deformation microstructures and strengthening mechanisms for the wire+arc additively manufactured Al-Mg4.5Mn alloy with inter-layer rolling. Mater Sci Eng A 2018;712:292–301. doi:10.1016/j.msea.2017.11.113.

[92] Cong B, Ouyang R, Qi B, Ding J. Influence of Cold Metal Transfer Process and Its Heat Input on Weld Bead Geometry and Porosity of Aluminum-Copper Alloy Welds. Rare Met Mater Eng 2016;45:606–11. doi:10.1016/S1875-5372(16)30080-7.

[93] Wang P, Hu S, Shen J, Liang Y. Characterization the contribution and limitation of the characteristic processing parameters in cold metal transfer deposition of an Al alloy. J Mater Process Technol 2017;245:122–33. doi:10.1016/j.jmatprotec.2017.02.019.

[94] Wiktorowicz R, Melton G. Shielding gas selection for controlled dip transfer (short arc) welding. TWI Bull 2013.

[95] Consonni M. The 2017 edition of BS EN ISO 15614-1: review of the changes and their practical implications 2018.

[96] Melfi T. ASME IX Heat Input Code Changes 2010.

[97] Pickin CG, Young K. Evaluation of cold metal transfer (CMT) process for welding aluminium alloy. Sci Technol Weld Join 2006;11:583–5. doi:10.1179/174329306X120886.

[98] Pickin CG, Williams SW, Lunt M. Characterisation of the cold metal transfer (CMT) process and its application for low dilution cladding. J Mater Process Technol 2011;211:496–502. doi:10.1016/j.jmatprotec.2010.11.005.

[99] Kumar NP, Arungalai Vendan S, Siva Shanmugam N. Investigations on the parametric effects of cold metal transfer process on the microstructural aspects in AA6061. J Alloys Compd 2016;658:255–64. doi:10.1016/j.jallcom.2015.10.166.

[100] Ola OT, Doern FE. A study of cold metal transfer clads in nickel-base INCONEL 718 superalloy. Mater Des 2014;57:51–9. doi:10.1016/j.matdes.2013.12.060.

[101] Elrefaey A. Effectiveness of cold metal transfer process for welding 7075 aluminium alloys. Sci Technol Weld Join 2015;20:280–5. doi:10.1179/1362171815Y.0000000017.

[102] Gungor B, Kaluc E, Taban E, SIK Ş.Ş A. Mechanical and microstructural properties of robotic Cold Metal Transfer (CMT) welded 5083-H111 and 6082-T651 aluminum alloys. Mater Des 2014;54:207–11. doi:10.1016/j.matdes.2013.08.018.

[103] Cao R, Wen BF, Chen JH, Wang PC. Cold Metal Transfer joining of magnesium AZ31B-to-aluminum A6061-T6. Mater Sci Eng A 2013;560:256–66. doi:10.1016/j.msea.2012.09.065.

[104] Liu YB, Sun QJ, Sang HB, Feng JC. Microstructure and mechanical properties of cold metal transfer welded aluminium/nickel lap joints. Sci Technol Weld Join 2015;20:307–12. doi:10.1179/1362171815Y.0000000011.

[105] Adebayo a, Mehnen J, Tonnellier X. Limiting Travel Speed in Additive Layer Manufacturing. Trends Weld Res Proc 9th Int Conf 2013;3:1038–44.

[106] Wei PS. Thermal Science of Weld Bead Defects: A Review. J Heat Transfer 2011;133:031005. doi:10.1115/1.4002445.

[107] Wei PS, Yeh JS, Ting CN, DebRoy T, Chung FK, Lin CL. The effects of Prandtl number on wavy weld boundary. Int J Heat Mass Transf 2009;52:3790–8.

doi:10.1016/J.IJHEATMASSTRANSFER.2009.02.020.

[108] Gratzke U, Kapadia PD, Dowden J, Kroos J, Simon G. Theoretical approach to the humping phenomenon in welding processes. J Phys D Appl Phys 1992;25:1640–7. doi:10.1088/0022-3727/25/11/012.

[109] Nguyen TC, Weckman DC, Johnson DA, Kerr HW. The humping phenomenon during high speed gas metal arc welding. Sci Technol Weld Join 2005;10:447–59. doi:10.1179/174329305X44134.

[110] Xiong J, Li R, Lei Y, Chen H. Heat propagation of circular thin-walled parts fabricated in additive manufacturing using gas metal arc welding. J Mater Process Technol 2018;251:12–9. doi:10.1016/j.jmatprotec.2017.08.007.

[111] Zhao H, Zhang G, Yin Z, Wu L. Three-dimensional finite element analysis of thermal stress in single-pass multi-layer weld-based rapid prototyping. J Mater Process Technol 2012;212:276–85. doi:10.1016/j.jmatprotec.2011.09.012.

[112] Alimardani M, Toyserkani E, Huissoon JP. A 3D dynamic numerical approach for temperature and thermal stress distributions in multilayer laser solid freeform fabrication process. Opt Lasers Eng 2007;45:1115–30. doi:10.1016/j.optlaseng.2007.06.010.

[113] Lei Y, Xiong J, Li R. Effect of inter layer idle time on thermal behavior for multi-layer single-pass thin-walled parts in GMAW-based additive manufacturing. Int J Adv Manuf Technol 2018;96:1355–65. doi:10.1007/s00170-018-1699-1.

[114] Kou S. Metallurgy Second Edition Welding Metallurgy. vol. 822. 2003. doi:10.1016/j.theochem.2007.07.017.

[115] Martina F, Williams S. Wire + arc additive manufacturing vs . traditional machining from solid: a cost comparisonfrom solid : 2015.

[116] Gu D. Laser Additive Manufacturing (AM): Classification, Processing Philosophy, and Metallurgical Mechanisms. 2015. doi:10.1007/978-3-662-46089-4_2.

[117] Xiong J, Zhang G. Online measurement of bead geometry in GMAW-based additive manufacturing using passive vision. Meas Sci Technol 2013;24. doi:10.1088/0957-0233/24/11/115103.

[118] Geng H, Li J, Xiong J, Lin X, Zhang F. Optimization of wire feed for GTAW based additive manufacturing. J Mater Process Technol 2017;243:40–7. doi:10.1016/j.jmatprotec.2016.11.027.

[119] Herzog D, Seyda V, Wycisk E, Emmelmann C. Additive manufacturing of metals. Acta Mater 2016;117:371–92. doi:10.1016/j.actamat.2016.07.019.

[120] Withers PJ, Bhadeshia HKDH. Residual stress. Part 1 – Measurement techniques. Mater Sci Technol 2001;17:355–65. doi:10.1179/026708301101509980.

[121] Withers PJ, Bhadeshia HKDH. Residual stress. Part 2 – Nature and origins. Mater Sci Technol 2001;17:366–75. doi:10.1179/026708301101510087.

[122] Moore P, Addison AC, Nowak M. Mechanical Performance of Wire Plus Arc Additive Manufactured Steel and Stainless Steel Structures(Paper). FIRST Int Congr WELDING, Addit Manuf Assoc NON Destr TESTING, ICWAM 2017, Metz, France: 2017, p. 1–9.

[123] Fu Y, Zhang H, Wang G, Wang H. Investigation of mechanical properties for hybrid deposition and micro-rolling of bainite steel. J Mater Process Technol 2017;250:220–7. doi:10.1016/j.jmatprotec.2017.07.023.

[124] Kotecki D, Armao F. Stainless steels properties - how to weld them where to use them 2003.

[125] Ji L, Lu J, Liu C, Jing C, Fan H, Ma S. Microstructure and mechanical properties of 304L steel fabricated by arc additive manufacturing. MATEC Web Conf 2017;128:03006. doi:10.1051/matecconf/201712803006.

[126] Wang H, Jiang W, Ouyang J, Kovacevic R. Rapid prototyping of 4043 Al-alloy parts by VP-GTAW. J Mater Process Technol 2004;148:93–102. doi:10.1016/j.jmatprotec.2004.01.058.

[127] ASM Handbook (Vol.2) - Properties and Selection: Nonferrous alloys and Special-purpose materials. 10th ed. Materials Park, Ohio USA: ASM International; 1990.

[128] Fixter J, Gu J, Ding J, Williams SW, Prangnell PB. Preliminary Investigation into the Suitability of 2xxx Alloys for Wire-Arc Additive Manufacturing. Mater Sci Forum 2016;877:611–6. doi:10.4028/www.scientific.net/MSF.877.611.

[129] Gu J, Cong B, Ding J, Williams SW, Zhai Y. Wire+Arc Additive Manufacturing of Aluminium. Proc 25th Annu Int Solid Free Fabr Symp, Austin, Texas: 2014, p. 4–6.

[130] Ding Y, Muñiz-Lerma JA, Trask M, Chou S, Walker A, Brochu M. Microstructure and mechanical property considerations in additive manufacturing of aluminum alloys. MRS Bull 2016;41:745–51. doi:10.1557/mrs.2016.214.

[131] Silva CMA, Bragança IMF, Cabrita A, Quintino L, Martins PAF. Formability of a wire arc deposited aluminium alloy. J Brazilian Soc Mech Sci Eng 2017;39:4059–68. doi:10.1007/s40430-017-0864-z.

[132] Standard welding terms and definitions, AWS A3.0;2001. Miami, Florida: American Welding Society; 2001.

[133] ASME Boiler and Pressure Vessel Code - Sec IX. New York, US: ASME; 2010.

[134] Lumley R. Fundamentals of aluminium metallurgy. First. UK: Woodhead Publishing Limited; 2010.

[135] Davis J. ASM Specialty Handbook - Aluminum and aluminium alloys. USA: ASM International; 2010.

[136] Devletian J, Wood W. Factors affecting porosity in aluminum welds - A review. Weld Res Counc 1983;290:1–18.

[137] Geng H, Li J, Xiong J, Lin X. Optimisation of interpass temperature and heat input for wire and arc additive manufacturing 5A06 aluminium alloy. Sci Technol Weld Join 2017;22:472–83. doi:10.1080/13621718.2016.1259031.

[138] Bai J, Ding H, Gu J, Wang X, Qiu H. Porosity evolution in additively manufactured aluminium alloy during high temperature exposure. 1st Int Conf New Mater Chem Ind, 2017.

[139] Gao YX, Yi JZ, Lee PD, Lindley TC. The effect of porosity on the fatigue life of cast aluminium-silicon alloys. Fatigue Fract Eng Mater Struct 2004;27:559–70. doi:https://doi.org/10.1111/j.1460-2695.2004.00780.x.

[140] Wu B, Ding D, Pan Z, Cuiuri D, Li H, Han J, et al. Effects of heat accumulation on the arc characteristics and metal transfer behavior in Wire Arc Additive Manufacturing of Ti6Al4V. J Mater Process Technol 2017;250:304–12. doi:10.1016/j.jmatprotec.2017.07.037.

[141] Xiong J, Lei Y, Li R. Finite element analysis and experimental validation of thermal behavior for thin-walled parts in GMAW-based additive manufacturing with various substrate preheating temperatures. Appl Therm Eng 2017;126:43–52. doi:10.1016/j.applthermaleng.2017.07.168.

[142] Grigorenko G. Formation of pores in welds. Avtom Svarka 1970;10:13–7.

[143] Ryan EM, Sabin TJ, Watts JF, Whiting MJ. The influence of build parameters and wire batch on porosity of wire and arc additive manufactured aluminium alloy 2319. J Mater Process Tech 2018;262:577–84. doi:10.1016/j.jmatprotec.2018.07.030.

[144] Gu JL, Ding JL, Cong BQ, Bai J, Gu HM, Williams SW, et al. The Influence of Wire Properties on the Quality and Performance of Wire+Arc Additive Manufactured Aluminium Parts. Adv Mater Res 2014;1081:210–4. doi:10.4028/www.scientific.net/AMR.1081.210.

[145] Hasegawa M. Ellingham Diagram. vol. 1. Elsevier Ltd.; 2014. doi:10.1016/B978-0-08-096986-

2.00032-1.

[146] Hashimoto E, Kino T. Hydrogen diffusion in aluminium at high temperatures. J Phys F Met Phys 1983;13:1157–65. doi:10.1088/0305-4608/13/6/013.

[147] Chalmers B. Principles of Solidification. Appl solid state Phys, Springer, Boston, MA; 1970, p. 161–70. doi:10.1007/978-1-4684-1854-5_5.

[148] Llnderoth S. Hydrogen diffusivity in aluminium. Philos Mag Lett 1988;57:229–34. doi:10.1080/09500838808214712.

[149] Derekar K, Lawrence J, Melton G, Addison A, Zhang X, Xu L. Influence of Interpass Temperature on Wire Arc Additive Manufacturing (WAAM) of Aluminium Alloy Components. MATEC Web Conf, vol. 269, 2019, p. 05001. doi:10.1051/matecconf/201926905001.

[150] Fang X, Zhang L, Chen G, Dang X, Huang K, Wang L, et al. Correlations between microstructure characteristics and mechanical properties in 5183 aluminium alloy fabricated by wire-arc additive manufacturing with different arc modes. Materials (Basel) 2018;11. doi:10.3390/ma11112075.

[151] Zhang C, Gao M, Zeng X. Workpiece vibration augmented wire arc additive manufacturing of high strength aluminum alloy. J Mater Process Tech 2019;271:85–92. doi:10.1016/j.jmatprotec.2019.03.028.

[152] Gomez Ortega A, Corona Galvan L, Deschaux-Beaume F, Mezrag B, Rouquette S. Effect of process parameters on the quality of aluminium alloy Al5Si deposits in wire and arc additive manufacturing using a cold metal transfer process. Sci Technol Weld Join 2018;23:316–32. doi:10.1080/13621718.2017.1388995.

[153] Wu B, Pan Z, Ding D, Cuiuri D, Li H, Fei Z. The effects of forced interpass cooling on the material properties of wire arc additively manufactured Ti6Al4V alloy. J Mater Process Technol 2018;258:97–105. doi:10.1016/j.jmatprotec.2018.03.024.

[154] Wei HL, Mazumder J, Debroy T. Evolution of solidification texture during additive manufacturing. Nature Publishing Group; 2015. doi:10.1038/srep16446.

[155] Rai A, Helmer H, Körner C. Simulation of grain structure evolution during powder bed based additive manufacturing. Addit Manuf 2017;13:124–34. doi:10.1016/j.addma.2016.10.007.

[156] Liu J, To AC. Quantitative texture prediction of epitaxial columnar grains in additive manufacturing using selective laser melting. Addit Manuf 2017;16:58–64. doi:10.1016/j.addma.2017.05.005.

[157] Li X, Tan W. Numerical investigation of effects of nucleation mechanisms on grain structure in metal additive manufacturing. Comput Mater Sci 2018;153:159–69. doi:10.1016/j.commatsci.2018.06.019.

[158] Liu P, Wang Z, Xiao Y, Horstemeyer MF, Cui X, Chen L. Insight into the mechanisms of columnar to equiaxed grain transition during metallic additive manufacturing. Addit Manuf 2019;26:22–9. doi:10.1016/j.addma.2018.12.019.

[159] Knapp GL, Raghavan N, Plotkowski A, Debroy T. Experiments and simulations on solidification microstructure for Inconel 718 in powder bed fusion electron beam additive manufacturing. Addit Manuf 2019;25:511–21. doi:10.1016/j.addma.2018.12.001.

[160] Messler RJ. Principles of welding. Singapore: WILEY-VCH Verlag GmbH & Co; 2004.

[161] Messler RJ. Joining of materials and structures. USA: Elsevier Butterworth-Heinemann; 2004.

[162] Yuan T, Yu Z, Chen S, Xu M, Jiang X. Loss of elemental Mg during wire + arc additive manufacturing of Al-Mg alloy and its e ff ect on mechanical properties. J Manuf Process 2020;49:456–62. doi:10.1016/j.jmapro.2019.10.033.

[163] Feng J, Zhang H, He P. The CMT short-circuiting metal transfer process and its use in thin

aluminium sheets welding. Mater Des 2009;30:1850–2. doi:10.1016/j.matdes.2008.07.015.

[164] Wang P, Hu S, Shen J, Liang Y, Pang J. Effects of electrode positive/negative ratio on microstructure and mechanical properties of Mg/Al dissimilar variable polarity cold metal transfer welded joints. Mater Sci Eng A 2016;652:127–35. doi:10.1016/j.msea.2015.11.080.

[165] Praveen P, Yarlagadda PKDV, Kang MJ. Advancements in pulse gas metal arc welding. J Mater Process Technol 2005;164–165:1113–9. doi:10.1016/j.jmatprotec.2005.02.100.

[166] Praveen P, Yarlagadda PKDV. Meeting challenges in welding of aluminum alloys through pulse gas metal arc welding. J Mater Process Technol 2005;164–165:1106–12. doi:10.1016/j.jmatprotec.2005.02.224.

[167] Webster GA, Ezeilo AN. Residual stress distributions and their influence on fatigue lifetimes. Int J Fatigue 2001;23:375–83.

[168] Megahed M, Mindt H-W, N'Dri N, Duan H, Desmaison O. Metal additive-manufacturing process and residual stress modeling. vol. 5. Integrating Materials and Manufacturing Innovation; 2016. doi:10.1186/s40192-016-0047-2.

[169] Hosseinzadeh F, Kowal J, Bouchard PJ. Towards good practice guidelines for the contour method of residual stress measurement 2014. doi:10.1049/joe.2014.0134.

[170] Prime MB, Gnäupel-Herold T, Baumann JA, Lederich RJ, Bowden DM, Sebring RJ. Residual stress measurements in a thick, dissimilar aluminum alloy friction stir weld. Acta Mater 2006;54:4013–21. doi:10.1016/j.actamat.2006.04.034.

[171] Zhang Y, Ganguly S, Edwards L, Fitzpatrick ME. Cross-sectional mapping of residual stresses in a VPPA weld using the contour method 2004;52:5225–32. doi:10.1016/j.actamat.2004.07.045.

[172] Hosseinzadeh F, Bouchard PJ, Keynes M, Uk MK. Mapping Multiple Components of the Residual Stress Tensor in a Large P91 Steel Pipe Girth Weld Using a Single Contour Cut 2013:171–81. doi:10.1007/s11340-012-9627-z.

[173] Hawk J, Frank R, Wilsdorf H. Yield stress as determined from hardness measurements for mechanically alloyed aluminium base alloys. Metall Trans A 1988;19A:2363–6.

[174] Zhang P, Li SX, Zhang ZF. General relationship between strength and hardness. Mater Sci Eng A 2011;529:62–73. doi:10.1016/j.msea.2011.08.061.

[175] Busby JT, Hash MC, Was GS. The relationship between hardness and yield stress in irradiated austenitic and ferritic steels. J Nucl Mater 2005;336:267–78. doi:10.1016/j.jnucmat.2004.09.024.

[176] Cahoon J, Broughton W, Kutzak A. The determination of yield strength from hardness measurements. Metall Trans 1971;2:1979–83.

[177] Tabor D. A simple theory of static and dynamic hardness. Proc R Soc London Ser A Math Phys Sci 1948;192:247–74.

[178] Tabor D. The hardness of solids. Rev Phys Technol 1970;1:145–79. doi:10.1088/0034-6683/1/3/i01.

[179] Dutra JC, e Silva RHG, Savi BM, Marques C, Alarcon OE. Metallurgical characterization of the 5083H116 aluminum alloy welded with the cold metal transfer process and two different wire-electrodes (5183 and 5087). Weld World 2015;59:797–807. doi:10.1007/s40194-015-0253-0.

[180] Inspection certificate 3.1. Sheffield, UK: 2018.

[181] Leggatt RH. Residual stresses in welded structures 2008;85:144–51. doi:10.1016/j.ijpvp.2007.10.004.

[182] Kaufman G, editor. Properties of aluminium alloys - Tensile, creep, and fatigue data at high and low temperatures. USA: ASM International, The Aluminium Association; 1999.

[183] Toparli MB, Fitzpatrick ME. Development and Application of the Contour Method to Determine the Residual Stresses in Thin Laser-Peened Aluminium Alloy Plates 2015. doi:10.1007/s11340-015-0100-7.

[184] Liu C, Yi X. Residual stress measurement on AA6061-T6 aluminum alloy friction stir butt welds using contour method. Mater Des 2013;46:366–71. doi:10.1016/j.matdes.2012.10.030.

[185] Martina F, Roy MJ, Szost BA, Terzi S, Colegrove PA, Williams SW, et al. Residual stress of as-deposited and rolled wire+arc additive manufacturing Ti–6Al–4V components. Mater Sci Technol (United Kingdom) 2016;32:1439–48. doi:10.1080/02670836.2016.1142704.

[186] Hosseinzadeh F, Kowal J, Bouchard J. Towards good practice guidelines for the contour method of residual stress measurement. J Eng 2014;8:453–68. doi:10.1049/joe.2014.0134.

[187] Prime MB. Cross-sectional mapping of residual stresses by measuring the surface contour after a cut. J Eng Mater Technol Trans ASME 2001;123:162–8. doi:10.1115/1.1345526.

[188] DeWald AT, Hill MR. Residual stress in a thick weld determined using the contour method. Davis: 2001.

[189] Corbin DJ, Reutzel EW, Beese AM. Effect of Substrate Thickness and Preheating on the Distortion of Laser Deposited Ti – 6Al – 4V 2018;140:1–9. doi:10.1115/1.4038890.

[190] Tellkamp VL, Dallek S, Cheng D, Lavernia E. Grain growth behavior of a nanostructured 5083 Al – Mg alloy. J Mater Res 2001;16:938–44. doi:10.1557/JMR.2001.0133.

[191] Totten G, MacKenzie S, editors. Handbook of Aluminum - Vol 2 Alloy Production and Materials Manufactruing. US: Marcel Dekker Inc; 2003.

[192] Denlinger ER, Jarred H, Panagiotis M. Residual stress and distortion modeling of electron beam direct manufacturing Ti-6Al-4V. Proc Inst Mech Eng , Part B J Eng Manuf 2015;229:1803–13. doi:10.1177/0954405414539494.

[193] Brice CA, Hofmeister WH. Determination of Bulk Residual Stresses in Electron Beam Additive-Manufactured Aluminum. Metall Mater Trans A 2013;44:5147–53. doi:10.1007/s11661-013-1847-z.

[194] Lu X, Lin X, Chiumenti M, Cervera M, Hu Y, Ji X, et al. Residual stress and distortion of rectangular and S-shaped Ti-6Al-4V parts by Directed Energy Deposition: Modelling and experimental calibration. Addit Manuf 2019;26:166–79. doi:10.1016/j.addma.2019.02.001.

[195] Derekar KS, Addison A, Joshi SS, Zhang X, Lawrence J, Xu L, et al. Effect of pulsed metal inert gas (pulsed-MIG) and cold metal transfer (CMT) techniques on hydrogen dissolution in wire arc additive manufacturing (WAAM) of aluminium. Int J Adv Manuf Technol 2020;107:311–31. doi:10.1007/s00170-020-04946-2.

[196] Brandes EA, Brook GB. Smithells Metals Reference Book. Seven. UK: Butterworth-Heinemann; 1992.

[197] Baker H. ASM Handbook: Alloy Phase Diagrams. Ohio, USA: ASM International; 1992.

[198] Callister W, Rethwisch D. Materials Science and Engineering - An Introduction. Eight. US: John Wiley & Sons, Inc; 2010.